Improving Sound Systems by Electrical Means

Schneider, Henrik

Publication date:
2015

Document Version
Publisher's PDF, also known as Version of record

Technical University of Denmark

Henrik Schneider

Improving Sound Systems by Electrical Means

PhD Thesis, March 2015

DTU Electrical Engineering
Department of Electrical Engineering

Henrik Schneider

Improving Sound Systems by Electrical Means

PhD Thesis, March 2015

Improving Sound Systems by Electrical Means

This PhD Thesis was prepared by
Henrik Schneider

Supervisors
Michael A. E. Andersen
Arnold Knott

Release date:	22^{nd} March 2015
Category:	1 (public)
Edition:	Final
Comments:	This thesis is submitted in partial fulfillment of the requirements for obtaining the PhD degree at the Technical University of Denmark.

Department of Electrical Engineering
Electronics Group (ELE)
Technical University of Denmark
Oersteds Plads bygning 349
DK-2800 Kgs. Lyngby
Denmark
www.ele.elektro.dtu.dk
Tel: (+45) 45 25 25 25
Fax: (+45) 45 88 01 17

Preface and Acknowledgment

This PhD thesis “Improving Sound Systems by Electrical Means” has been carried out at the Electronics group, Department of Electrical Engineering, Technical University of Denmark (DTU) during the period December 2011 to March 2015. The project has been partially funded by the Danish Sound Innovation Network and carried out in co-operation with Pascal Audio A/S and LoudSoft A/S. A special thanks to Jesper Lind Hansen from Pascal Audio for valuable information and fruitful discussions and to Peter Larsen from LoudSoft for his great patience with me regarding transducer and loudspeaker knowledge.

I want to express my greatest gratitude to my PhD supervisors Prof. Michael A. E. Andersen and Assoc. Prof. Arnold Knott for giving me this great opportunity and for their trust in me. They have provided a solid and inspiring base for my research and fully supported me during busy and troublesome periods. Also a big thanks for all the constructive suggestions and discussions during paper writing and seminar presentations.

In order to learn about transducers I have been following the courses "Electroacoustic Transducers and Systems" and "Advanced Loudspeaker Models" which is being taught by Assoc. Prof. Finn Agerkvist at the Acoustic technology department at DTU. The content of the courses created a strong foundation for my research and ever since I have been working closely with Finn Agerkvist and the acoustic department on several projects.

I would also like to thank Wolfgang Klippel who I meet during his course in Dresden University titled ”Sound Quality of Audio Systems”. He and his team was truly processional and inspirational.

The results presented in this PhD thesis could not have been done without fruitful collaboration with both colleagues and students. I would therefore like to thank Thomas Andersen, Prasanth Thummula, Lars Press Petersen, Lasse Crone Jensen, Zhe Zhang, Ziwei Ouyang, Lina Huang, Michey Pierre Madsen, Jacob Dølner Mønster, Emilio Pranjic, Anders M. Madsen, Ruben Bjerregaard, Akira Yamauchi and Ivan H. H Jorgensen.

I have also enjoyed many fun and constructive moments with Jeppe Arnsdorf Pedersen, Kristian Lindberg Poulsen, Maria del Carmen Mira Albert, Juan Carlos Hernandez Botella, Riccardo Pittini, and Dennis Nielsen.

I have always liked the atmosphere in the Electronics Group at DTU. One of many reasons is the kind assistance of our technical staff Henriette D. Wolff, Bertil Morelli, Allan Jørgensen and Dorte Bettina Svejstrup. They are all extremely professional, helpful and service minded.

Last but not least I want to thank my wife, my two daughters and closest family for their great love and support during my PhD work. They helped me countless times whenever I was working late, travelling to conferences or was trying to reach some deadline in the middle of a holiday.

Lyngby March 22, 2015

Henrik Schneider

Abstract

The availability and flexibility of audio services on various digital platforms have created a high demand for a large range of sound systems. The fundamental components of sound systems such as docking stations, sound bars and wireless mobile speakers consists of a power supply, amplifiers and transducers. Due to historical reasons the design of each of these components are commonly handled separately which are indeed limiting the full performance potential of such systems. To state some examples the requirements of the amplifier distortion could be relaxed if the distortion of the transducer was considered, the power requirement of the power supply could be relaxed if the acoustical power requirement was known, the total sound system efficiency could be optimized which would properly require a radical design change for all the components, communication between the components could lead to intelligent control and protection functionality and so on. In this work different strategies towards improvements of sound systems by electrical means was investigated considering the interfaces between each component and the performance of the full system. The strategies can be categorized by improvements of sound quality, efficiency, size and cost as well as production.

The transducer is considered the weakest component when it comes to sound quality which is especially apparent for micro-speakers. Historically the common voltage drive of a transducer has been challenged by the alternative current drive in relation to sound quality. Prior research points out that current drive provides a more direct control of the force applied to the moving parts of a transducer resulting in less distortion and thus improved sound quality but the information is quite sparse. In this work multi-tone distortion related to voltage and current drive of transducers with different characteristics were investigated using a non-linear transducer model. The goal was to predict if and when current drive is advantageous. Current drive was found to be most effective at higher audio frequencies where the non-linear voice coil inductance has a major effect on distortion. At lower audio frequencies transducer related distortions are more pronounced and an old motional feedback technique was revisited. An accelerometer is mounted on the moving parts of the transducer enabling motional control which lead to a 14 dB distortion reduction in the best case. This technology is very promising since it compensates for most distortion mechanisms of the transducer such as non-linearities, production variation, wear-n-tear, temperature changes and so on. Furthermore the accelerometer output can be used for protection purposes. The only disadvantages are challenges in terms of cost and system complexity. The noise floor of the accelerometer prevents

motional control at very low displacements.

The main advantage of Class-D audio amplifiers is high efficiency which is often stated to be more than 90 %. This is only true at high power levels but at low power levels the efficiency unfortunately drops due to severe switching losses in the semiconductors. This efficiency characteristic is an environmental concern since the amplifier is operating at low power levels for background music in more than 89 % of the time and thus a lot of energy is wasted considering the amount of sound systems around the world. Even when the music is played at higher levels the average power is still quite low due to the dynamic behavior of music. In this work energy consumption and sound quality for Class-D audio amplifiers using a peak-tracking power supply scheme was investigated as a means to reduce these losses. It was proven that the efficiency of a class-d amplifier could be increased from approximately 55 % to 90 % at 1 W output power without sacrificing the distortion. A full tracking power supply scheme would further improve these numbers but the efficiency of the power supply also needs to be taken into account which should be addressed in future work.

Power requirements of a sound system have been a large part of this project. There is a surprisingly big lack of scientific information regarding this topic and the goal has thus been to develop an intelligent approach to estimate the power requirements to obtain a size and cost reduction. The greatest challenge was to develop an analyzing tool to estimate the worst case power scenario versus time for a given loudspeaker application. Models including the influence of the enclosure and the most critical non-linearities were derived and experimental verified. Since the power requirement is related to the music material more than 400 music tracks were analyzed and it was proven that full power capability is only needed for a few milliseconds which inspire radical design changes and large reduction of size and cost for the power supply, the amplifiers and the transducers. The work on a power supply based on this research was performed showing a 5 times size reduction compared to a commercial power supply. Future work should expand this analysis to a range of different sound system applications and audio material.

An alternative production method for the Class-D amplifier output inductor has been proposed and investigated. A hybrid winding concept for toroids were proposed where the traces in a printed circuit board completes the winding of bended copper foil cut-outs placed in a handy former. The main potential is expected to be production related and faster time to market since the former including the foil cut-outs can be pre-fabricated and pre-shipped to different suppliers around the world. A dynamic 3D model made in matlab and finite element analyses were used to optimize the shape of the bended copper foils to optimize the DC resistance. The DC resistance was reduced by 30 % compared to the starting point for a 10 turn toroidal inductor using this method.

The combined work indicate that large sound system improvements are in reach by use of electrical means. Innovative solutions have been investigated and improvements of sound quality, efficiency, size and cost as well as production have been demonstrated.

Resumé

Tilgængeligheden og fleksibiliteten af audio tjenester på forskellige digitale platforme har skabt en stor efterspørgsel til en lang række forskellige lydsystemer. De fleste af disse lydsystemer såsom dockingstationer, lydbarer og trådløse mobile højttalere indeholder en strømforsyning, forstærkere og højtalerenheder. Af historiske årsager bliver designet af hver a disse komponenter almindeligvis håndteret separat, hvilket begrænser systemets fulde ydeevne. For eksempel kunne forvrængningskrav til forstærkeren reduceres hvis forvrængingen af højtaleren blev taget i betragtning, strømforsyningens effektkrav kunne reduceres hvis det aktuelle akustiske effektkrav var kendt, effektiviteten af det samlede lydsystem kunne forbedres hvilket ville kræve radikale design ændringer af alle komponenterne, kommunikation mellem hver enkelt komponent kunne tilføre intelligente styrrings- og beskyttelses-funktioner o.s.v. Dette arbejde præsenterer forskellige strategier til forbedringer af lydsystemer ad elektrisk vej og grænsefladerne mellem hver komponent samt det samlede systems ydelse er blevet taget med i overvejelserne. Strategierne kan kategoriseres under forbedring af lydkvalitet, effektivitet, størrelse og omkostninger samt produktion.

Højtalerenheden betragtes som den svageste komponent når det kommer til lydkvalitet, hvilket især er tydeligt med mikro-højttalere. Historisk er spændingsstyrrede højtalere blevet udfordret af den alternative strømstyrring i forhold til lydkvalitet. Tidligere forskning peger på, at strømstyrring giver en mere direkte kontrol af kræftoverførslen til de bevægelige dele af en højtaler hvilket resulterer i mindre forvrængning og dermed bedre lydkvalitet, men oplysningerne er ganske sparsomme. I dette arbejde blev multi-tone forvrængning undersøgt i relation til spændings- og strøm-styrring af højtalere med forskellige karakteristika ved anvendelse af en ulineær højtaler model. Målet var at forudsige i hvilke sammenhænge strømstyrring kunne vise sig fordelagtig. Strømstyrring viste sig at være mest effektiv ved højere audio frekvenser, hvor den ulineære svingspoleinduktans har stor betydning for forvrængning. Ved lavere audio frekvenser er en højtalers forvrænginger mest udtalte og en gammel teknik baseret på positionsstyrrings blev derfor undersøgt. Et accelerometer er monteret på de bevægelige dele af en højtalerenhed hvilket muliggør præcis positionsstyrring, som i bedste tilfælde førte til 14 dB mindre forvrængning. Denne teknologi er meget lovende, da den kompenserer for mange forvrængningsmekanismer såsom ulineariteter, variationer i produktionen, slitage, temperaturpåvirkninger m.m. Accelerometermålingen kan ydermere bruges til beskyttelses funktioner. De største udfordringer angår pris og systemkom-

pleksitet. Accelerometerets støjgulv forhindre brug af motional feedback ved lave lydniveauer.

Den største fordel ved klasse-D forstærkere er høj effektivitet som ofte angives at være højere end 90 % hvilket kun gælder for høje effektniveauer. Effektiviteten er væsentlig lavere ved lave effektniveauer på grund af alvorlige skiftetab i halvlederkomponenter. Dette er en miljømæssig bekymring, idet forstærkeren arbejder ved lave effektniveaur i mere end 95 % af tiden under afspilning af baggrundsmusik. Dermed går en masse energi tabt når det totale antal af verdens lydsystemer tages i betragtning. Selv når musikken afspilles med højere lydstyrker er den gennemsnitlige effekt og effektivitet stadig relativ lav på grund af musikkens dynamik. I dette arbejde er energiforbrug og lydkvalitet for klasse-D forstærkere blevet undersøgt i relation til en metode hvor forstærkerens forsyningsspænding ændres som funktion af lytteniveauet. En effektivitetsforbedring fra ca. 55 % til 90 % blev påvist ved en udgangseffekt på 1 Watt uden særlig nedgradering af forstærkerens forvrængning.

En stor del af dette arbejde har fokuseret på lydsystemers effektkrav. Der er overraskende lidt videnskabelig information om dette emne og målet har derfor været at udvikle en intelligent fremgangsmåde til at estimere effektbehovet for at opnå en størrelses og pris gevinst. Den største udfordring var udviklingen af et analyseredskab til at estimere det værst tænkelige effektkrav som funktion af afspilningstid for en given højtalerapplikation. Modeller som inkluderer indflydelsen af kabinettet og de mest kritiske ulinearitet blev udviklet og verificeret eksperimentelt. Da effektkravet er relateret til audio materialet blev mere end 400 musik numre analyseret og det blev bevist at høj effekt kun kræves i få millisekunder hvilket kan medfører radikale design ændringer og en stor reduktion i størrelse og pris af strømforsyningen, forstærkerne og højtaleren. Et design af en strømforsyning baseret på denne viden resulterede i en 5 gange mindre strømforsyning sammenlignet med en kommerciel strømforsyning. Fremtidigt arbejde burde udvide analysen til en større variation af lydsystemer og audio-materiale.

En mere snæver forskningsindsats blev udført inden for en alternativ produktionsmetode af klasse-d udgangsspoler. En hybrid viklingsmetode for ringkerner blev foreslået hvor banerne i et printkort fuldender viklingen af en mængde bukkede kobber stykker placeret i en simpel holder. Potentiallet forventes at være produktionsrelateret og mulighed for en kort produkt til markeds tid da holderen med alle kobber stykkerne kan præfabrikeres og være til rådighed hos forskellige distributører rundt omkring i verden på forhånd. En 3D model baseret på matlab og "finite element" analyse blev brugt til at optimere formen af de bukkede kopper stykker i forhold til DC-modstanden. DC-modstanden blev med denne metode reduceret med 30 % i forhold til udgangspunktet for en ringkernespole med 10 viklinger. Det samlede arbejde indikere at store forbedringer af lydsystemer er i rækkevidde ved brug af elektriske midler. Innovative løsninger er blevet undersøgt og forbedringer af lydkvalitet, effektivitet, størrelse og pris samt produktion er blevet påvist.

Contents

List of Figures

List of Tables

?

Chapter 1

Introduction

1.1 Background and Motivation

Originally two ideas gave hope and motivation for sound systems improvements by electrical means. One concerning size and cost improvements of amplifiers using a novel current driven class-d topology. The other concerning sound quality improvements by a change of the transducer driving principle from voltage to current drive. Since the start of the project several additional ideas have occurred and the main observations and considerations that this work is based upon are:

- The force acting on the moving parts of a transducer is proportional to the voice coil current. Why don't we control the voice coil current instead of the voltage?
- The distortion of a transducer is displacement dependent. Why not use a motion sensor to retain control of the moving parts?
- Loudspeakers cover a large power range. How is the actual power requirements of a sound system determined?
- The power supply in mains connected sound systems is much larger than the amplifiers. What is the reason and can it be improved?
- The idle losses of class-d amplifiers are high? How can it be reduced?
- The winding fill factor of a typical inductor used in class-d amplifiers seems low. What options exists to improve it?

These and more questions were asked and have been investigated in this work since no satisfactory answers were found in the sparse literature dealing with these subjects. As a matter of fact these questions are very hard to answer because a correct answer depends on a vast number of variables. Furthermore the answers require a full system understanding which require a wide electrical, mechanical and

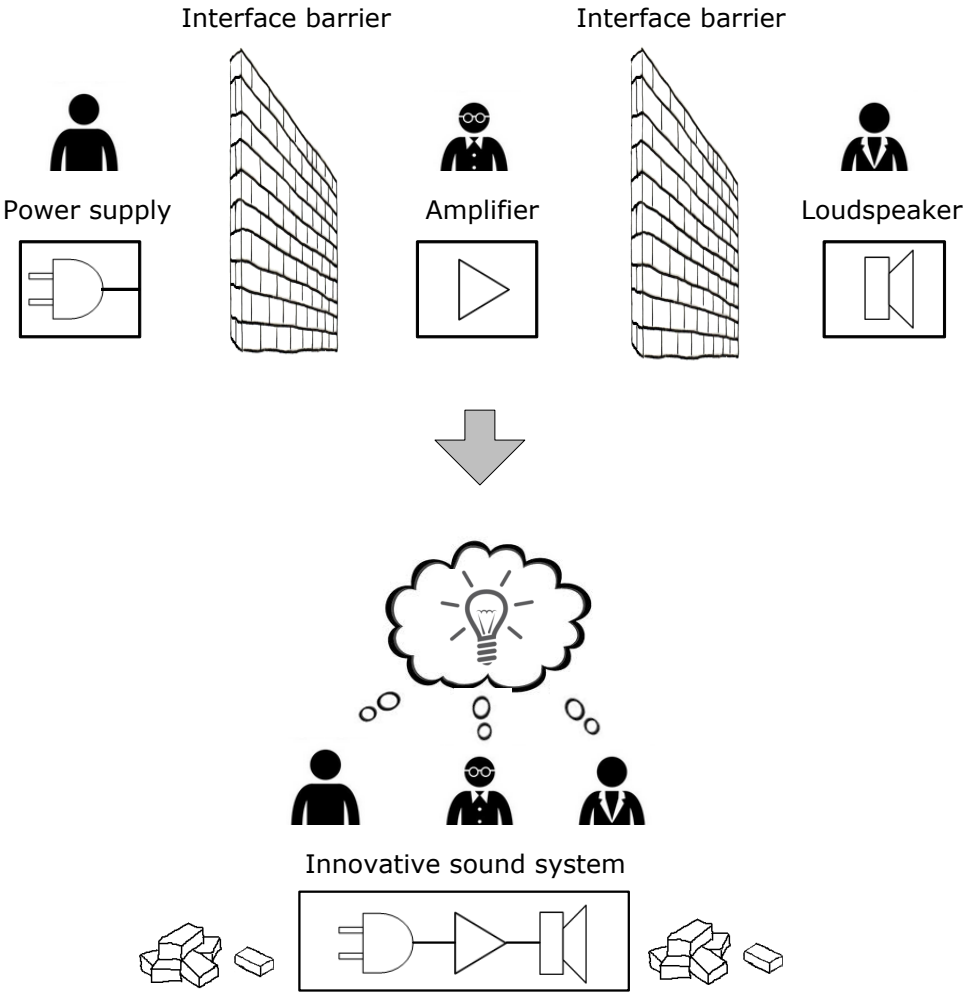

Figure 1.1: Trend towards intelligent sound system design

acoustical understanding. This is however not supported by the traditional sound system design practice where the power supply design, the amplifier design and the loudspeaker design are split up and performed by specialists as illustrated in the top of figure 1.1. In this work steps towards a holistic sound system design have been taken as illustrated in the bottom of figure 1.1.

1.2 Thesis structure and content

The structure and content of this PhD thesis are visualized in figure 1.2. A short introduction is followed by an overview and state-of-the-art chapter. The main content are supplementing the already published information from scientific articles. The work was naturally split into chapters related to improving of sound systems by electrical means. The chapter titles are Sound Quality, Efficiency, Cost and Size and Production. Each chapter starts with a short introduction to the topic, presents the research in a condensed form and finishes with a discussion. At last an overall conclusion and future work are presented. Relevant publications are included in the appendix.

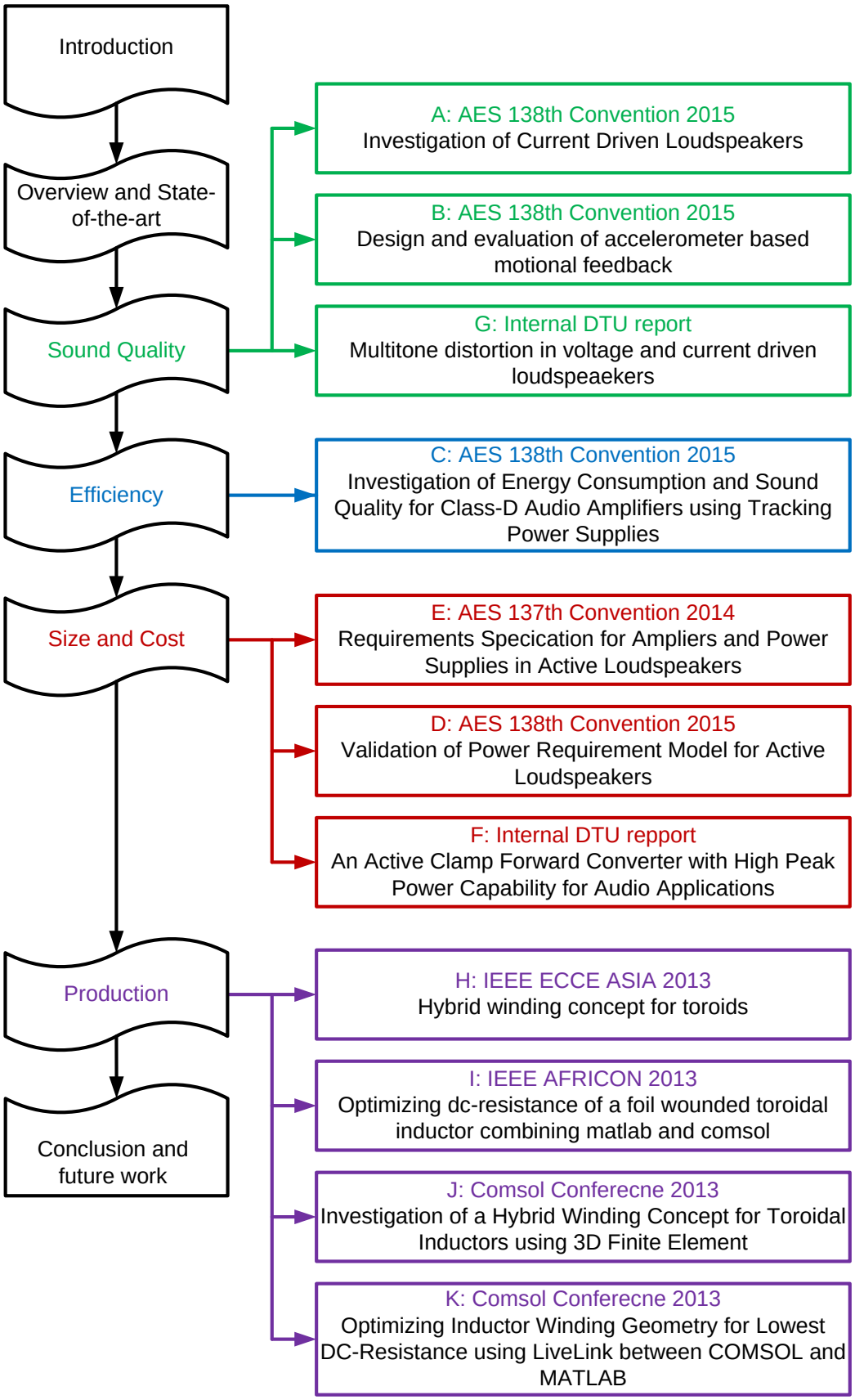

Figure 1.2: Thesis structure

Chapter 2

Overview and State-of-the-art

2.1 Power supplies and amplifiers

State-of-the-art amplifiers are shown in figure 2.1a and 2.1c. Figure 2.1a shows a single 400 W amplifier from Hypex and figure 2.1c shows a 2 times 50 W amplifier with integrated power supply from Bang & Olufsen IcePower. The total harmonic distortion is 0.001 % and 0.002 % respectively at 1 W and 100 Hz. The switching frequencies is about 500 kHz and the efficiency is above 90 % at full power for both. A disadvantage of these amplifiers is a relative high idle loss which is addressed in chapter 4. Figure 2.1d shows a 2 times 50 W amplifier designed during this work. The amplifier is optimized for a small size by consideration of the dynamic behaviour of music. The amplifier is based on a Texas Instrument chip where semiconductors, control and protection are integrated in a single chip. The inductors are high current power inductors from coilcraft, the components are placed on both sides of the printed circuit board and no heatsinks are utilized. As a consequence the amplifer occupies very little space which encourage a small power supply.

State-of-the-art power supplies from Hypex and Bang & Olufsen IcePower are shown in figure 2.1b and 2.2c respectively. Since music is very dynamic the ratio of the peak to average power is high and the full power capability is only needed in short periods of time. This is apparent from the specifications where high power ratings are given for time periods spanning from 80 to 90 seconds. The efficiency of the Hypex power supply is just stated to be high and only the total efficiency of 80 % including amplifiers are given for the IcePower module. The switching frequencies are around 100 kHz which is low compared to state-of-the-art power supplies for LED (light emitting diode) applications where switching frequencies of hundreds of Mhz are applied. Figure 2.2e shows a power supply designed during this work. The power capability is based on a power requirement analysis described in chapter 5 and the peak power is only rated for 40 ms. The efficiency is 84 % at the maximum continuous power level and the switching frequency is 500 kHz which is 5 times higher than the state-of-the-art power supplies shown here. As a consequence the size of the magnetic components are decreased, semiconductors with lower continuous ratings are used and there is no need for heatsinks.

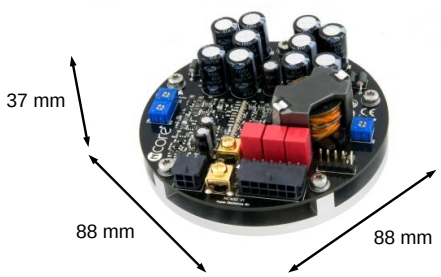

a) From www.hypex.nl

Hypex amplifier (1 ch.)

Specification for NC400
Power 400 W @ 4Ω
THD: 0.0011% @ 1 W
IMD: 0.0007% @ 200 W
AMP fsw: 470 kHz – 530 kHz
Efficiency: up to 93 %
Supply rejection ratio: 80 dB

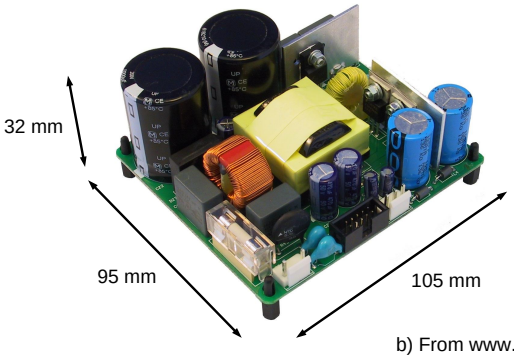

b) From www.hypex.nl

Hypex power supply

Specification for SMPS400
Input voltge: 90-264 V
Vout: 47 V
Vaux: ±21 V
Power (90 sec.): 550 W
Power (5 min.): 350 W
Power continuous: 240 W
SMPS fsw: 125 kHz
Efficiency: High!

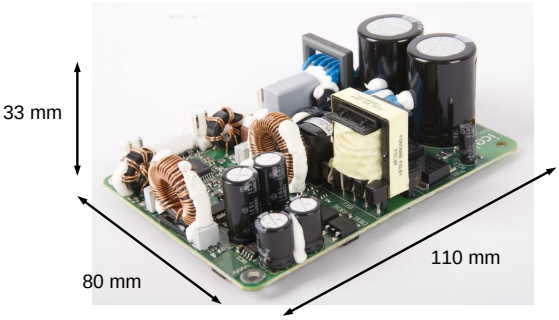

c) From www.icepower.bang-olufsen.com

IcePower power supply + amplifier (2 ch.)

Specification for 50ASX2
Input voltge: 85-264 V
Vout: ±25 V
Power (120 sec.): 170 W
Power continuous: 43 W
SMPS fsw: 100 kHz
AMP fsw: 90 kHz – 600 kHz
THD: 0.002 @ 1 W, 100 Hz
IMD: 0.0007 % 10 W
Total efficiency: up to 80%

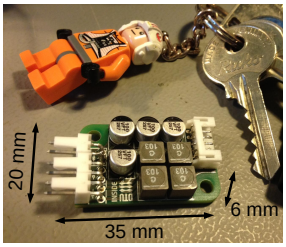

d)

DTU amplifier (2 ch.)

Specification
Power 2x50 W @ 4Ω
THD: 0.1% @ 25 W, 1 kHz
AMP fsw: 400 - 1200 kHz (selectable)
Efficiency: up to 90 %
Supply rejection ratio: 70 dB

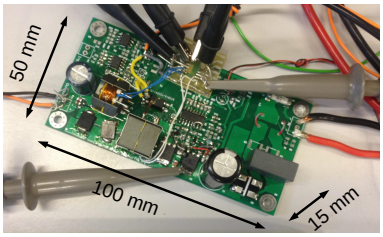

e)

DTU power supply

Specification
Input voltge: 90-264 V
Vout: 25 V
Vaux: ±12 V (Independent)
Power (40 ms): 200 W
Power continuous: 25 W
SMPS fsw: 500 kHz
Efficiency: 84% @ 25 W

Figure 2.1: Overview of state-of-the-art power supplies and amplifiers

2.2 Transducers and loudspeakers

The principle behind the electro dynamic transducer has not changed since it was invented in the 1930ies but all the processes from design to fabrication to evaluation have been greatly improved. Figure 2.2a shows how the entire transducer is drawn in 2D during the design phase which enables the designer to predict the performance of a transducer and change the design before a prototype is build. Figure 2.2b shows how the break up of the cone can be simulated which can lead to an optimized cone shape. The fabrication is very critical when it comes to transducers. Figure 2.2c show the crude manual fabrication done in 1954 and 2.2d shows the precise and consistent automatic fabrication of today. When it comes to measuremnts and evaluation of a transducer much has happened. Figure 2.2e shows a typical set up for a laser displacement measurement. This kind of measurement can be used to measure the characteristics of a transducer such as the cone break up modes. Figure 2.2f shows a measurement of a breakup mode which can be used to evaluate the accuracy of the initial design. Listening tests as shown in figure 2.2g are still a very important test when it comes to evaluation of a transducer. Often trained listeners and standardized test procedures and listening environments are used. A new measuring method where a laser is used to measure how sound propagates is shown in figure 2.2h. To conclude, a state-of-the-art transducer and loudspeaker utilize the latest knowledge and best design, fabrication and measurement techniques of today. The transducers used in most applications are however far from state-of-the-art transducers and the loudspeaker is thus often referred to as the weakest link in a sound system. This issue is addressed in chapter 3.

2.3 Discussion

Figure 2.3 shows four sound systems that have emerged during the last decade. It is not hard to imagine that size and cost of the power supply, the amplifiers and the transducers are very critical. In portable sound systems the efficiency is of equal importance because the operating time depends on it. Another matter is the sound quality which is a great challenge due to size constraints. To deal with all of these challenges, this work presents several sound system improvements concerning sound quality, efficiency, cost and size as well as production.

Design

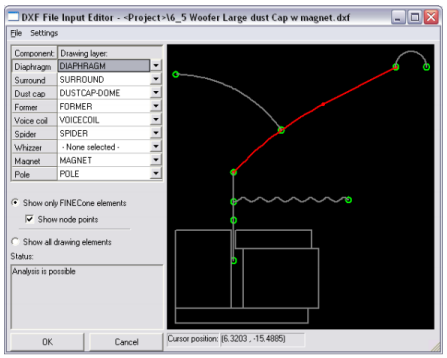

a) From LoudSoft A/S

Simulation

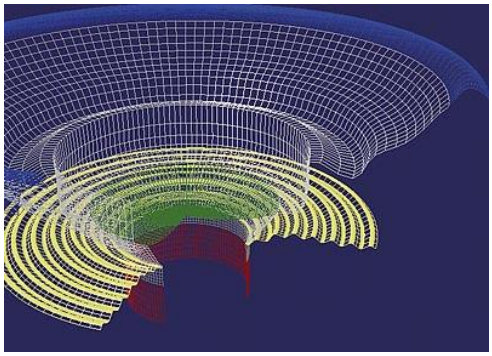

b) From LoudSoft A/S

Fabrication

c) From www.audioholics.com

d) From www.lavocespeakers.com

Measurements and evaluation

e) From www.klippel.de

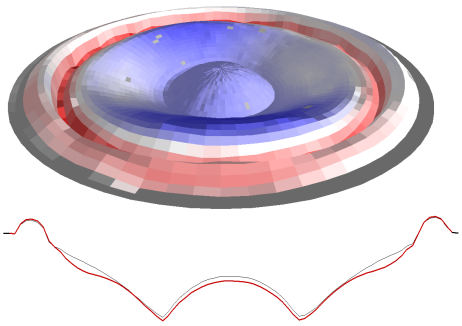

f) From www.klippel.de

g) From www.elektro.dtu.dk

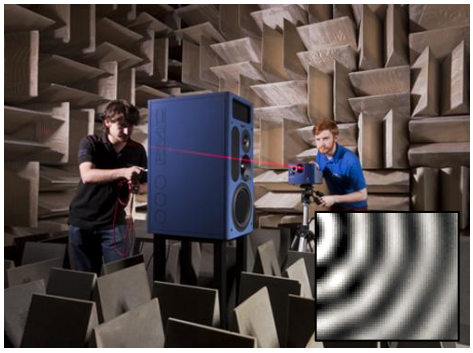

h) From www.phys.org

Figure 2.2: Overview of state-of-the-art transducer design

Figure 2.3: Overview of challenging loudspeaker applications

Chapter 3

Sound Quality

3.1 Introduction

The rating of sound quality is typically limited to ”bad”, ”good enough” and ”hi fidelity” justified by terms like ”clear”, ”boomy”, ”crisp”, ”dry”, ”musical” and so on. The judgement is made while listening to a variety of well known music. Unfortunately such listening tests are not accurate and efficient enough to be used during a development phase. Instead engineers analyse the distortion which is naturally related to sound quality and simple sine tones are used instead of music signals due to simplicity. The most popular measurements are total harmonic distortion (THD) and intermodulation distortion (IMD). THD is a ratio between the fundamental and the harmonic content in a system excited by a pure sine signal. If a signal is measured by voltages the THD is given by

$$THD = \frac{\sqrt{\sum_{n=2}^{\infty} V_n^2}}{V_1} \tag{3.1}$$

The ratio is mostly presented in percentage and a low THD means low distortion. More tones are typically present at one time in musical signals which is why the two-tone IMD measure is popular. Two tones excites both difference and summed frequency components of the original signal which reveal far more distortion. IMD can be specified as the RMS value of the various sum-and-difference signals as a percentage of the RMS voltage of the original signal. A multi-tone signal resembles a music signal even better but is far more complex to analyse suggesting a graphical or statistical analysis. These methods does however not relate well to the perceived sound quality [3, 4] which makes it difficult to rate a sound system due to a given change in the design or to compare two systems in terms of these distortion measures. A lot of work have been done to solve this issue but due to the complexity of the human hearing system no well proven solution is available today [5–14]. The following was stated in 1953 and restated in 2001 in papers from the

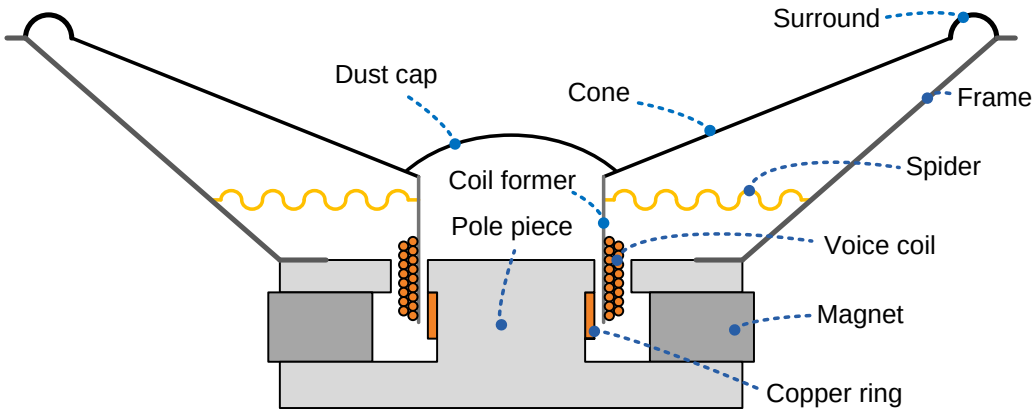

Figure 3.1: Cross-sectional view of an electro-dynamic transducer

Audio Engineering Society [5, 15]: "if any manufacturer or group of manufacturers can carry out the necessary research required to correlate listening tests with various methods of measuring nonlinear distortion, it will be a great and valuable service to the industry. Until such a time, however, in the last analysis, the only best test is to listen". These words are just as pertinent today and this must be kept in mind when talking about sound quality referred to measurements of THD, IMD and alike.

The transducer is considered the weakest link in a sound system when it comes to distortion and has thus been in focus. In this chapter the most critical distortion mechanism of the electro-dynamic transducer is presented in addition to an investigation of the driving scheme and motional feedback.

3.2 Non-linear distortion mechanisms in the electro-dynamic transducer

An electro-dynamic transducer converts an electrical signal into sound waves. A typical construction is seen in figure 3.1. An electrical coil referred to as the "voice coil" is wound on a cylindrical coil former which is attached to a cone. A dust cap finishes the moving assembly. Two suspensions referred to as the "surround" and the "spider" secures the moving assembly to a frame and provide linear guidance. The voice coil is suspended in a gab of a magnet system consisting of a permanent magnet and a pole piece made of steel. Sometimes a copper ring is incorporated in the pole piece to reduce eddy current effects. When an alternating current is applied to the voice coil a Lorentz force will push and pull the moving assembly back and forth and in that way sound waves are generated.

A linear lumped model of the electro-dynamic transducer is shown in figure 3.2. $u(t)$ is the voice coil voltage, R_e is the voice coil resistance, L_e is the voice coil inductance, R_2 and $L2$ models the eddy current effect, $i(t)$ is the voice coil current, u_{emf} is the voltage induced by the back electromotive force, Bl is the force factor (flux in the gap times the length of the wire in the gap), $v(t)$ is the velocity of the cone, R_{ms} is the suspension related loss due to friction, M_{ms} is the mass of the

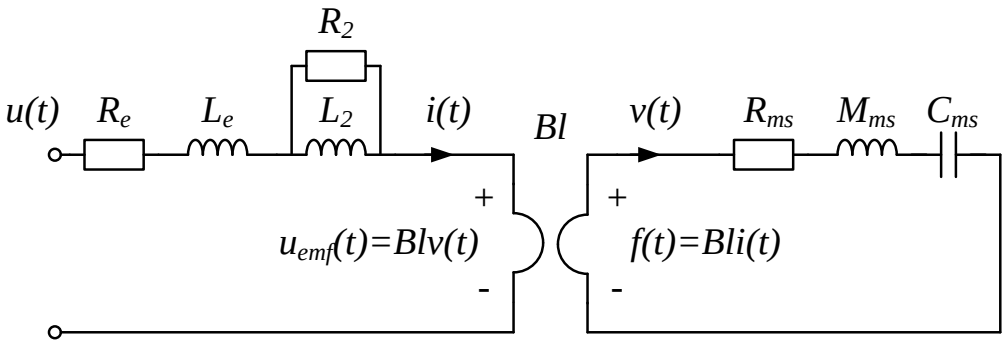

Figure 3.2: Electrical equivalent circuit diagram of a linear transducer.

moving assembly, C_{ms} is the compliance of the suspension and $f(t)$ is the Lorentz force applied to the moving assembly.

The following fundamental equations can be derived by Kirchhoff's voltage law and Laplace transformation

$$u(s) = R_e i(s) + sL_e i(s) + \frac{R_2 sL_2}{R_2 + sL_2} i(s) + sBlx(s) \tag{3.2}$$

$$f(s) = Bl \cdot i(s) \tag{3.3}$$

$$f(s) = M_{ms} s^2 x(s) + R_{ms} sx(s) + \frac{1}{C_{ms}} x(s) \tag{3.4}$$

The most critical distortions are displacement related and originates from the non-linearity of the suspension compliance, the force factor and the voice coil inductance. The dependency of the displacement x can be fitted to polynomials by

$$L_e(x) = \sum_{n=0}^{N-1} a_n x^n \quad Bl(x) = \sum_{n=0}^{N-1} a_n x^n \quad C_{ms}(x) = \sum_{n=0}^{N-1} a_n x^n \tag{3.5}$$

where N is the order of the polynomial and a_n is the n^{th} coefficient of the polynomial.

Figure 3.3 shows the polynomials of a 6.5" woofer extracted from measured data using the Klippel analyser. The dashed lines are mirrored data which were added to aid in the visualising of unsymmetrical characteristics. Symmetrical and unsymmetrical characteristics will generate uneven and even harmonics respectively. The voice coil inductance is thus expected to generate even harmonic distortion. A non-linear Matlab Simulink model of a transducer was created based on equation (3.2) - (3.4) and C_{ms}, Bl and L_e was made dependent on the displacement x by use of the polynomial regression in 3.5. The linear and non-linear parameters were extracted from measurements done on a Klippel analyzer. The non-linear model has been very intuitive to work with since the voice coil voltage and current as well as the velocity, acceleration and displacement are easily available. The added input

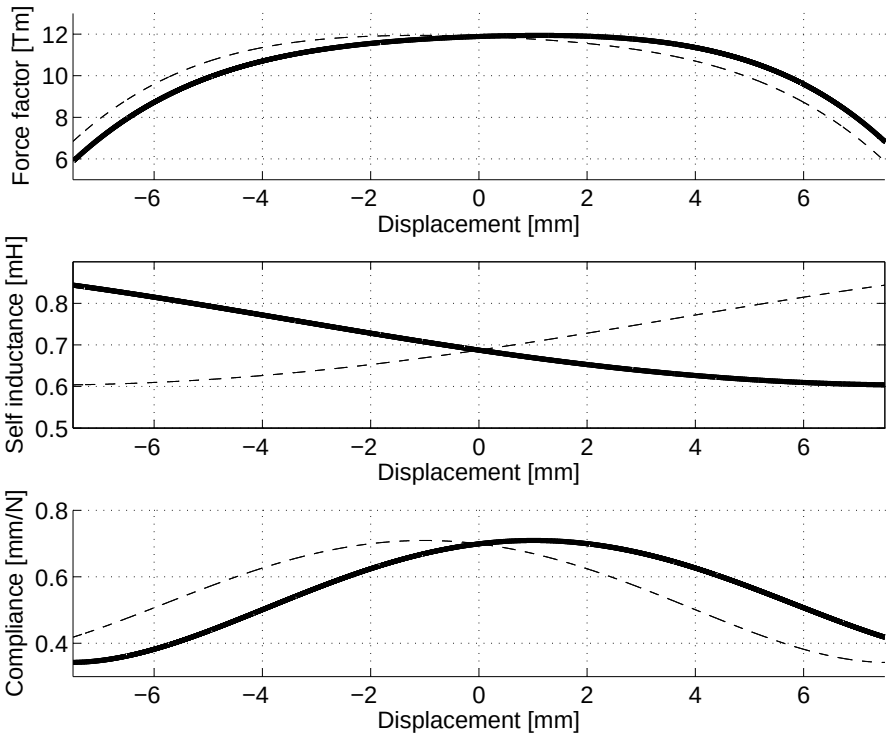

Figure 3.3: Non-linear polynomials based on Klippel measurement (solid). Mirrored values (dashed)

filter of the non-linear model can be used to apply a cross-over filter in addition to equalization.

A Polytec Doppler laser was used to evaluate the accuracy of the model and the experimental setup is shown in figure 3.5. A comparison of the measured and simulated harmonic and intermodulation distortion is shown in figure 3.6. The test signal consisted of a low frequency tone of 16 Hz (half the resonance frequency) mixed with a high frequency tone of 648 Hz. At this voltage level both harmonic and intermodulation distortion are generated. It is noted that the simulation overestimates uneven harmonics and underestimates the even harmonics which indicates that there is a higher degree of asymmetry in the non-linear values than expected. A range of measurements were taken with various input voltages and frequencies. Later on THD and IMD were analysed based on modelled and measured data and the comparisons are shown in figure 3.7 and 3.8. In 3.7 it is noted that the simulation underestimates the THD at low input voltages. A possible explanation is that the noise floor of the measurements effect the calculated THD. In 3.8 it is noted that the IMD is underestimated when the low frequency tone is twice the resonant frequency of the transducer. At higher frequencies and lower displacements the distortions are lower and thus the simulation result is more sensitive to model inaccuracies. This analysis however show that it is possible to predict the non-linear distortion quite well using only 3 displacement dependent non-linearities. Based on this experience the model was used to investigate the individual influence of

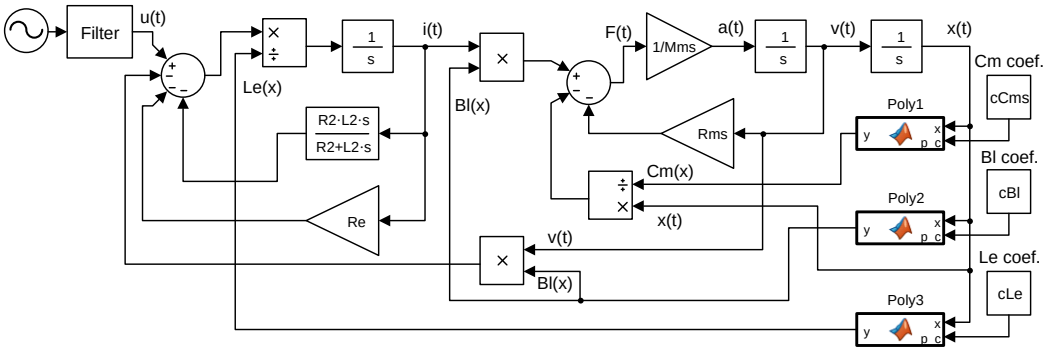

Figure 3.4: Non-linear voltage driven transducer model in Matlab Simulink

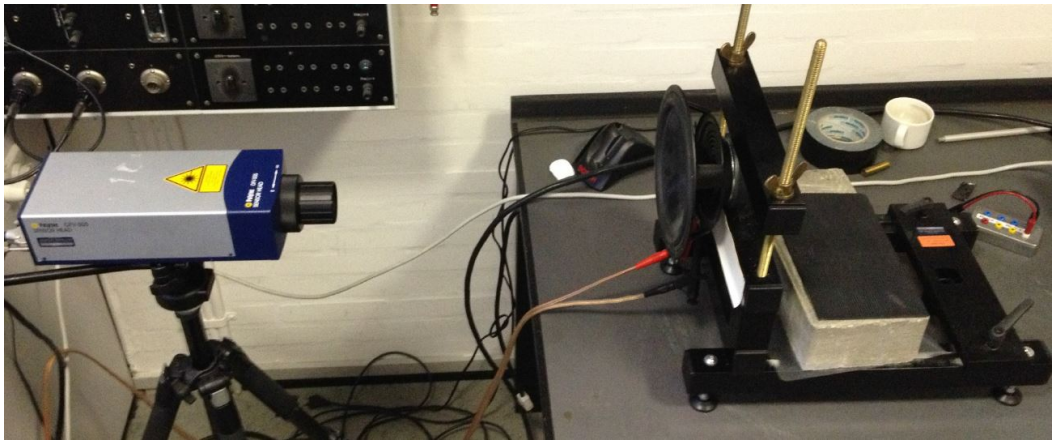

Figure 3.5: Experimental set up with the laser and the woofer

each non-linearity with similar test signal as used previously. The following was concluded.

- The force factor generates large harmonic- as well as intermodulation distortion.
- The self inductance generates low harmonic distortion and large intermodulation distortion.
- The compliance generates large harmonic distortion and low intermodulation distortion.

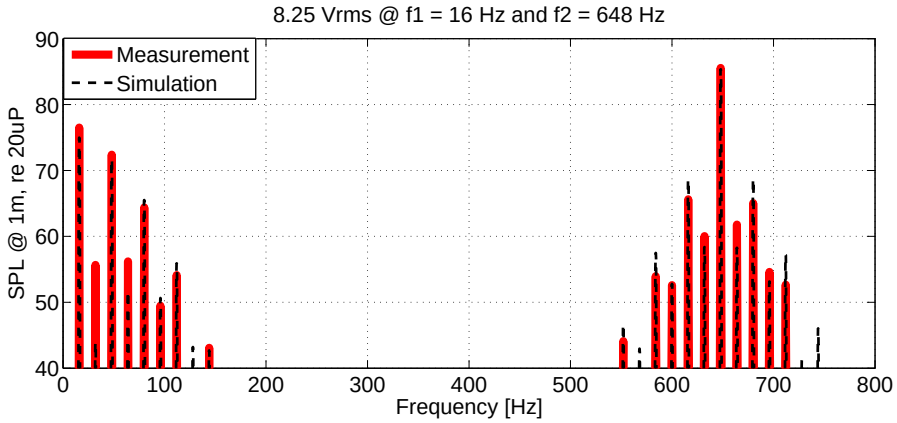

Figure 3.6: Comparison plot of measured and simulated harmonic and intermodulation distortion

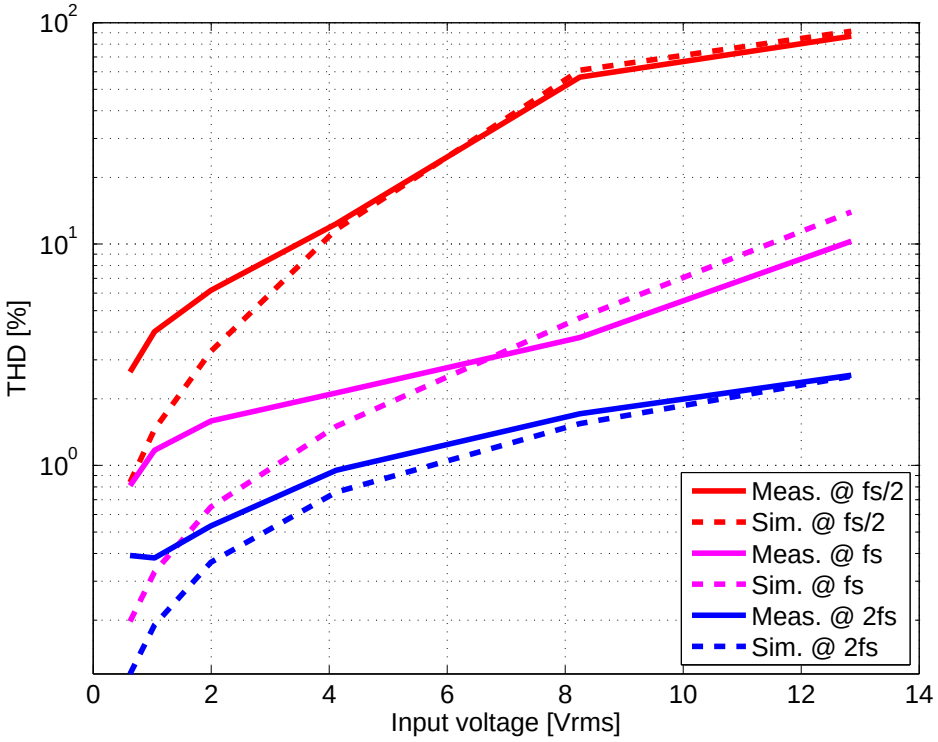

Figure 3.7: Total harmonic distortion vs. input voltage at $f_s/2$, f_s and $2f_s$

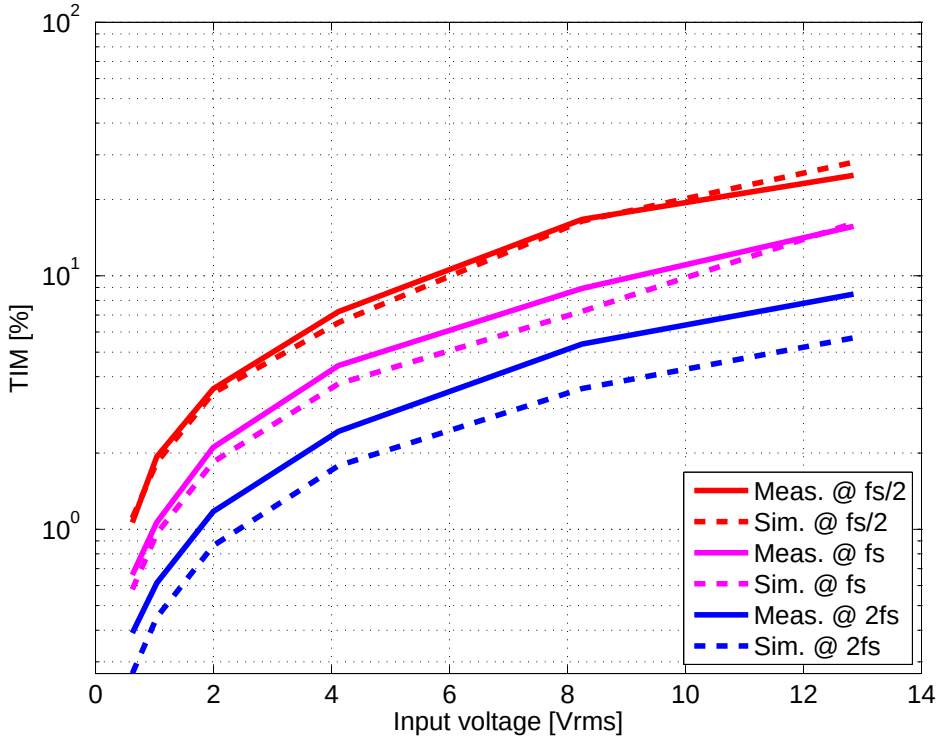

Figure 3.8: Intermodulation distortion vs. input voltage. $f_1 = \{f_s/2, f_s, 2f_s\}$, $f_2 \approx 25f_s$

3.3 Current Driven Transducers

Traditionally transducers are driven by voltage controlled amplifiers but from time to time a simple question pops up: Would current drive be more beneficial? When this work begun that exact question came up in relation to the sound quality of microspeakers. At first a literature study was performed on current driven transducers in general but the literature was found to be very sparse and sufficient answers were not found. Later on it became clear that the advantages of the driving scheme are very application dependent and thus it is difficult to provide a set of general guidelines. A number of publications address current control [16–23] and speak about all the advantages such as reduced compression caused by voice coil heating, elimination of the back electromotive voltage and reduced harmonic distortion and inter modulation distortion due to elimination of the non-linear inductance effect. Unfortunately the disadvantages are not sufficiently highlighted and delt with which casts a shadow over the full potential of current feedback. This work make use of a non-linear transducer model to analyse a range of 5" woofers with distinct characteristics under voltage and current drive. Figure 3.9 shows the 3 most critical non-linearities as a function of displacement. The difference between Woofer 1 an Woofer 2 is that a copper shorting ring has been implemented in Woofer 2 to reduce the effect of eddy currents. Thus the voice coil inductance of Woofer 2 is more linear than Woofer 1. The 3rd woofer has very different non-linear characteristics and in the displacement range used for comparison test (-5.7 mm to 5.7 mm) it behaves very linear and symmetrical.

The model in figure 3.4 was used to simulate voltage drive and the model in figure 3.10 was used to simulate current drive. The main difference of the models is that the current is directly controlled in the case of current drive. As a result the distortion contribution from the non-linear inductor is removed and the distortion contribution from the force factor is reduced.

The acceleration which is proportional to the sound pressure level can be described by equation 3.6 and 3.7 for voltage- and current-drive respectively. It is noted that the acceleration due to current drive is independent of L_e, R_e and less independent of Bl.

$$Z_{(a/v)} = \frac{Bls^2}{Bl^2 s + (sL_e + R_e)(s^2 M_{ms} + sR_{ms} + \frac{1}{C_{ms}})} \tag{3.6}$$

$$Z_{(a/i)} = \frac{Bls^2}{(s^2 M_{ms} + sR_{ms} + \frac{1}{C_{ms}})} \tag{3.7}$$

In 3.11 the calculated SPL is shown for the two driving schemes. The amplitude of the sinusoidal signal used to calculate the SPL's were 1 for both voltage and current drive which explains the difference in SPL's. In order to compare voltage and current drive the power applied to the woofer in both driving schemes have to be equalized, thus the SPL's have to match. This is achieved using the filter

shown in figure 3.12 and by applying the filter the resulting SPL's optain the form of a 4th order bandpass filter as shown in figure 3.13 The chosen bandpass characteristic resembles a typical crossover design for a woofer in a 2 way loudspeaker. Implementation of the filters makes it possible to use a signal with the same amplitude as input for both voltage and current drive and it enables comparison of the two driving schemes. The filters are designed to obtain a maximum SPL within the maximum limits of the displacements just bellow x_{MAX} (determined by the Klippel measurement). In figure 3.14, 3.15 and 3.16 the simulated sound pressure level of Woofer 1, Woofer2 and Woofer 3 are shown respectively. A multi-tone test signal is used in the evaluation of the driving schemes since it resembles audio signals to a higher degree than the signals used to predict THD and IMD as mentioned previously. It is clearly seen that current drive is very effective on Woofer 1 where attenuation in the order of 10 dB is obtained. The effect is less on Woofer 2 and negligible on Woofer 3.

3.3.1 Discussion

Now, is current drive more beneficial than voltage drive? In theory current drive seems advantageous compared to voltage drive even if a shorting ring is implemented since current drive effectively eliminates inductor related distortions and reduces the distortion contribution from the non-linear force factor. On the positive side the cost of current controlled amplifiers is not expected to increase. However if the transducer is highly linear the driving scheme seems irrelevant and voltage control is thus sufficient. Even though current drive seems very attractive it has several shortcomings. The filter applied to equalize the SPL under current drive is not a valid solution in real applications since the resonant frequency tends to drift as a function of usage, temperature and ageing. Only one viable but unproven control solution to handle this problem could be found [24] and further work in this topic is thus needed. The distortion levels from the non-linear compliance and the force factor are however still high despite that current control was successfully implemented. In micro-speakers the compliance related distortion is very severe because space dos not allow for two suspensions and thus the spider is sacrificed. Due to this reason and the fact that displacement related distortion is less critical in high frequency transducers, current drive is not advantageous when it comes to tweeters and micro-speakers as indicated in [23]. This is backed up by Klippel who have rated the effect of different non-linearities for different tranducer types as follows:

Woofers:

- 1. Force factor $Bl(x)$
- 2. Compliance $C_{ms}(x)$
- 3. Inductance $L_e(x)$
- 4. Flux modulation $L_e(i)$

Tweeters

- 1. Compliance $C_{ms}(x)$

Micro speakers

- 1. Force factor $Bl(x)$
- 2. Compliance $C_{ms}(x)$
- 3. Mechanical resistance $R_{ms}(x)$

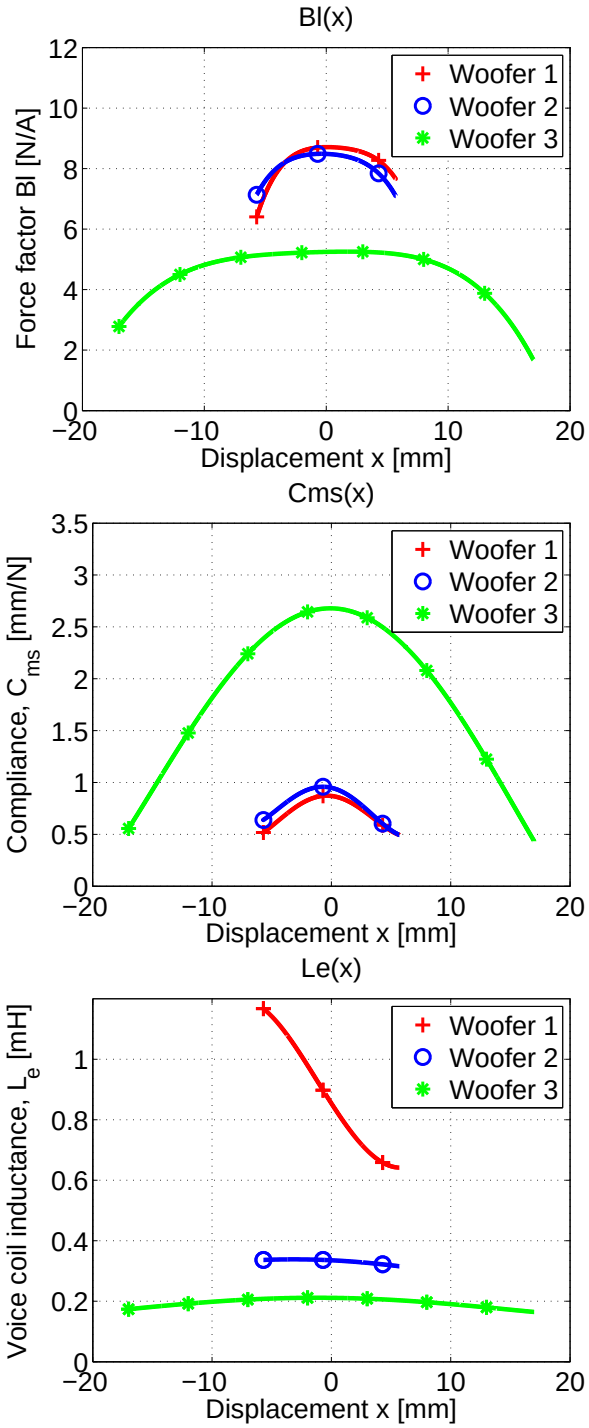

Figure 3.9: Critical non-linear components

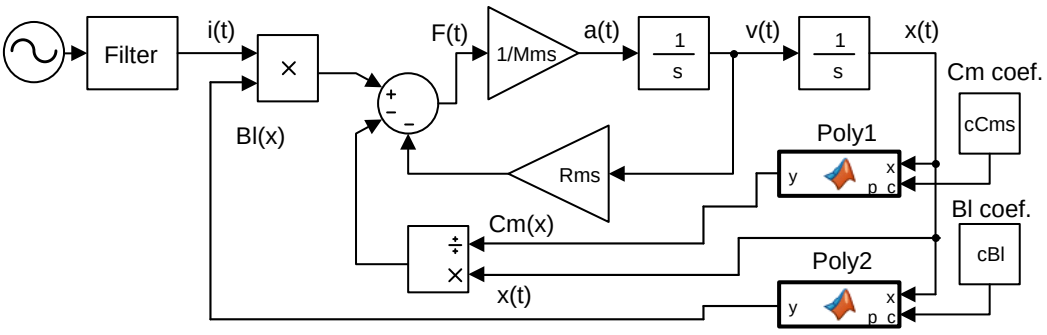

Figure 3.10: Non-linear current driven transducer model in Matlab Simulink

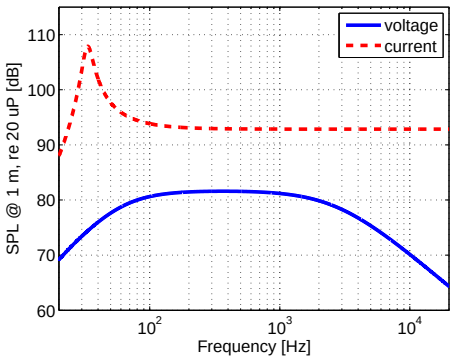

Figure 3.11: SPL

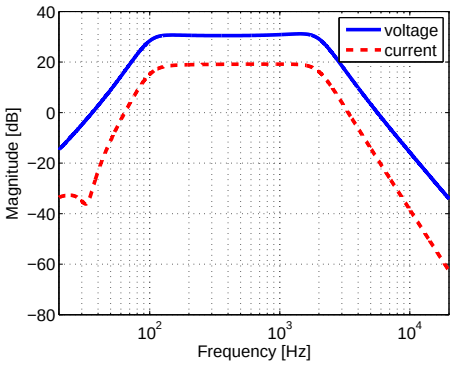

Figure 3.12: Applied filter

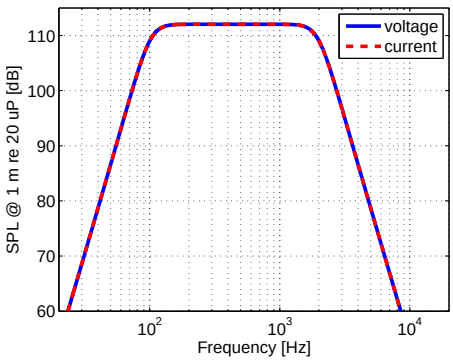

Figure 3.13: Resulting response

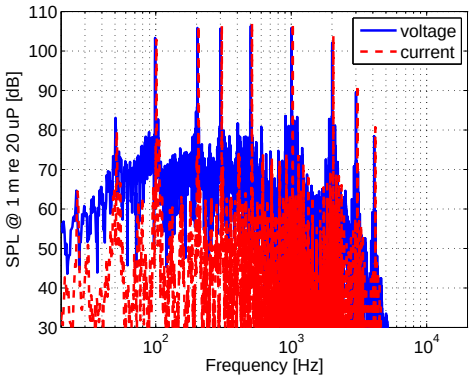

Figure 3.14: Woofer 1

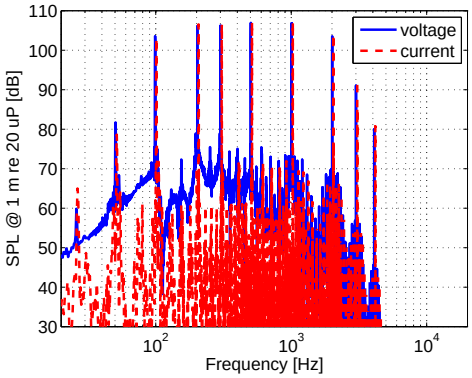

Figure 3.15: Woofer 2

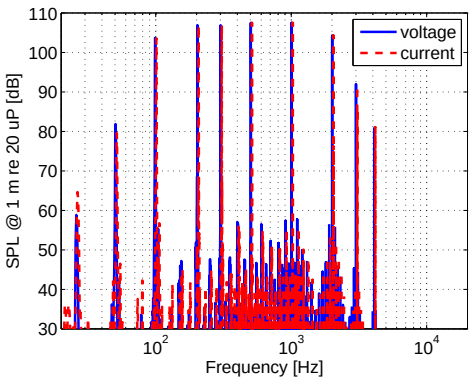

Figure 3.16: Woofer 3

3.4 Motional feedback

Motional feedback is an old concept which have been used in conjunction with voltage drive as well as current drive. In principal a motional sensor is sensing the movement of the cone which is compared to the input signal and any error between the two is corrected by a controller leading to an accurate and close to distortion free audio reproduction. This is however only applicable for low frequencies due to problems with cone breakup at higher frequencies. The alternative feedforward methods have received a lot of focus in recent years due to advances in digital processors, loudspeaker characterization methods and loudspeaker modelling [25–27]. The feed-forward method avoids a motional sensor but requires an accurate model of the transducer that incorporates the non-linearities and adapts to system changes caused by usage, temperature, ageing, production spread and so on [28]. Even though feedforward compensation has come a long way and seems very promising the alternative MFB technique is revisited in this work. The output or motion of the loudspeaker can either be captured as acceleration [29–31], velocity [32–37], pressure [38] or position [39–41]. Motional feedback is normally implemented on closed box systems because only a single sensor is necessary to sense the output. Attempts with higher order systems including passive radiators have also been successfully implemented [42]. In [18, 21, 43] motional feedback was alternatively used to control the undamped mechanical resonance of a current driven loudspeakers. Loudspeaker protection using feedforward or feedback has also been proposed [44, 45].

Despite the fact that both feed-forward and motional feedback have been investigated intensively, this kind of active distortion cancellation is very rarely found in commercial products. The motivation was to answer the question: Why is motional feedback not used to improve the sound quality of woofers and subwoofers today?

A simplified schematic of the motional feedback implementation is shown in figure 3.17. The output of the accelerometer is DC-biased since the electronics are supplied by a single supply voltage. Then the output is filtered by a forth order

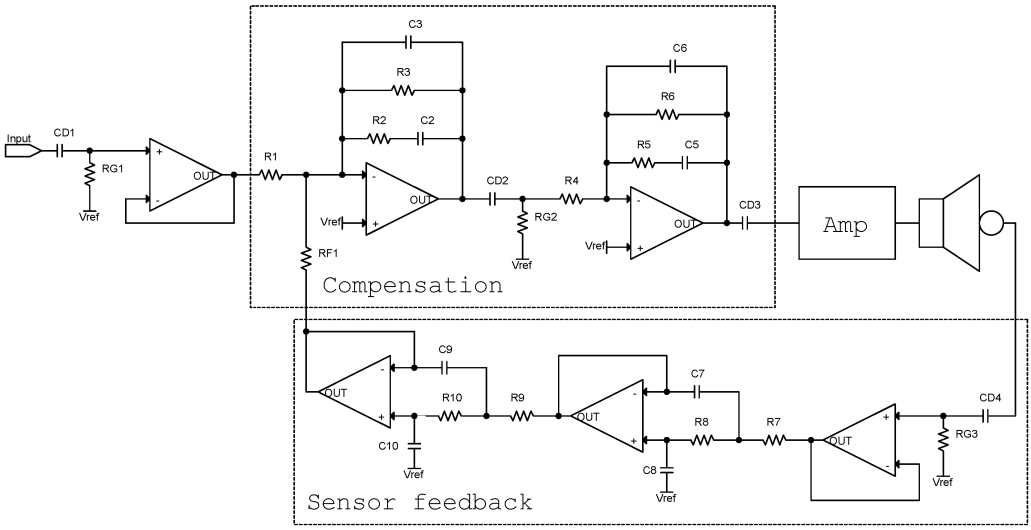

Figure 3.17: Simplified motional feedback schematic

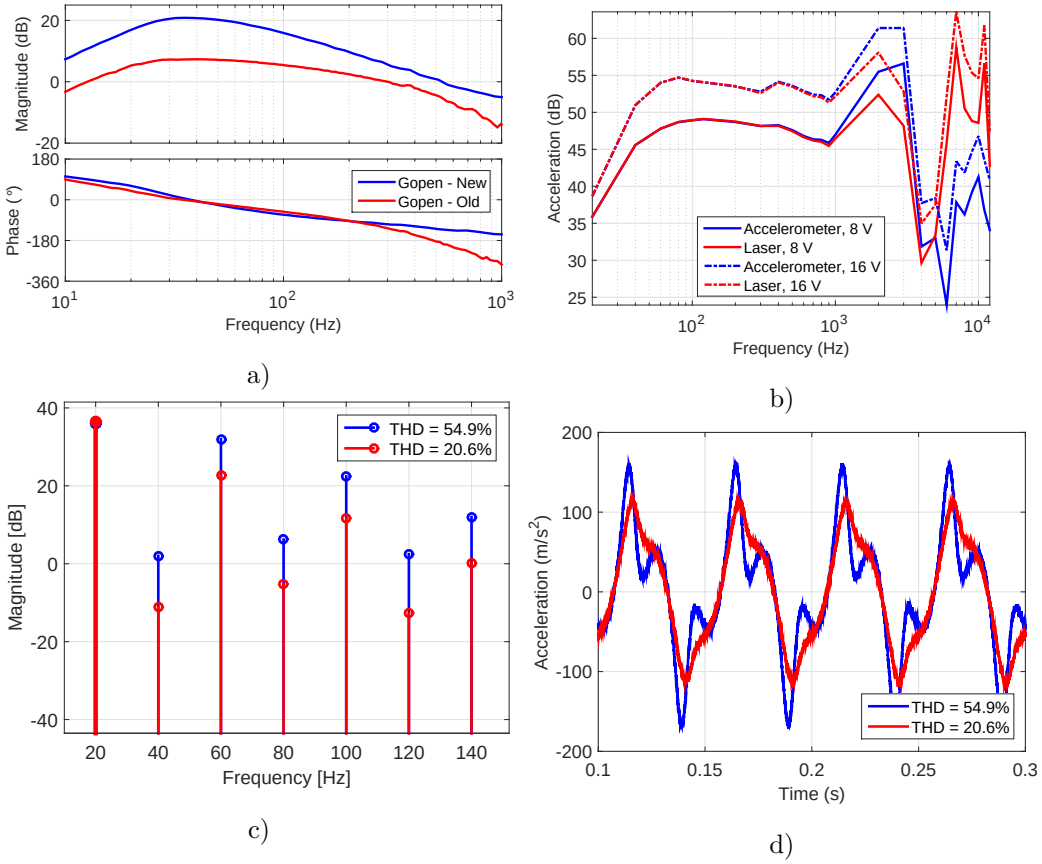

Figure 3.18: Various measurements

lowpass filter to remove any high frequency noise and unwanted artefacts of the accelerometer. The input signal is also DC-biased and compared to the filtered accelerometer ouput. A compensation circuit is designed to obtain a desired open loop response by considering the additional transfer functions of the amplifier and the transducer. In this work two compensation circuits were designed and tested and the measured open loop response of the first (old) and the second (new) is shown in figure 3.18.a. The cone acceleration was measured with a Polytec Doppler laser in order to validate the accuracy of the accelerometer. A comparison at differen input voltage levels are shown in figure 3.18.b. A good coherence is seen up to 1 kHz where cone break-up start to occur. Figure 3.18.c and 3.18.d shows the measured frequency spectrum and the measured accelerometer output with and without the first "old" compensation. During the measurements the transducer was feed with a $8V_{RMS}$, 20 Hz sine wave signal. The effect of the motional feedback implementatoin is clearly visible. Table 3.1 list the final improvements in terms of THD obtained by the second "new" compensation. It is clearly seen how the THD decrease as a function of frequency and voltage level. A 5 time reduction of THD is obtained in the best case.

Frequency (Hz)	THD w/o. / w. (%)		
	$2\,V_{rms}$	$4\,V_{rms}$	$8\,V_{rms}$
20	5.3 / 1.1	15.0 / 1.3	54.9 / 9.1
30	2.4 / 0.4	5.6 / 0.5	22.0 / 2.1
40	1.3 / 0.3	2.5 / 0.5	7.0 / 1.6
50	0.9 / 0.5	1.5 / 0.8	3.2 / 0.5

Table 3.1: Laser based THD measurements with and without compensation

3.4.1 Discussion

Based on this work it can be concluded that motional feedback is very straight forward to implement and that it greatly improves total harmonic distortion. The full potential of motional feedback in terms of transient response, perceived sound quality, cost and power requirements is however still to be revealed. Future work should include a way to adjust the amount of motional feedback as a function of the displacement level in order to improve the signal to noise ratio. A digital implementation would probably be advantageous in terms of added functionality. Listening tests and transient response tests should also be conducted. The sound quality and power requirements vs. enclosure size is another very interesting topic to explore. To the authors opinion there is no good reason why motional feedback is not being used to improve the sound quality of woofers and subwoofers today.

Chapter 4

Efficiency

4.1 Introduction

4.2 Tracking power supply

Class-D amplifiers are known to be highly efficient compared to traditional linear amplifiers [46–50]. On the other hand the efficiency advantage is relatively poor at idle and at low power levels as indicated by the measured efficiency shown in figure 4.1.

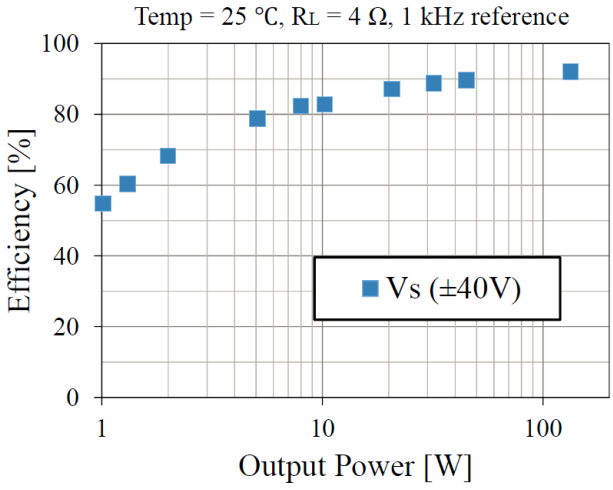

Figure 4.1: Measured efficiency of a 130 W class-D amplifier with a 1 kHz reference and a supply voltage of ± 40 V

In previous research the generalized distribution of volume control positions in time and the corresponding output power have been analysed [48]. The research showed that the users were listening to background music in 89 % of the time corresponding to a peak power of 1.3 W. This coupled with the fact that the average power is much lower than the peak power when it comes to music indicate that the efficiency

of a sound system should be optimized for lower power levels. An efficiency below 60 % at the background music level is actually an environmental concern when all the sound systems around the world is considered.

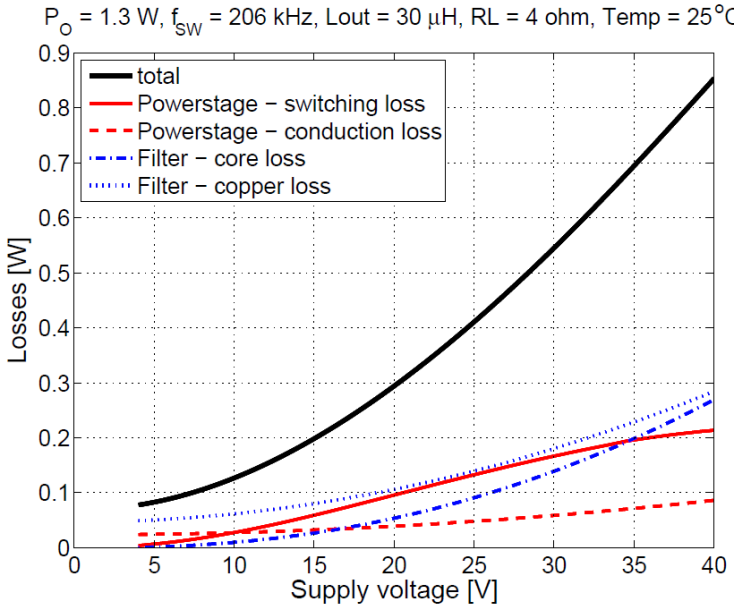

Figure 4.2: Power losses analysis vs. supply voltage at 1.3 V constant output power in 4 Ω load

In [51] a detailed loss analysis of class-D amplifiers is presented. In this work that model is used to predict the losses in a class-d amplifier driving 1.3 W constant output power into a 4 Ω load as a function of the supply voltage - see figure 4.2. As seen both power stage switching losses as well as the filter conduction and switching losses are greatly decreased by lowering the supply voltage. Figure 4.3 shows a handful of different power supply schemes. In order to illustrate the dynamics of each supply scheme the left side show a high signal level and the right side show a medium signal level. Figure 4.3.a shows a common fixed voltage supply that leaves a large headroom when the audio signal is low. A few amplifiers control the supply voltage as a function of the volume controller as shown in figure 4.3.b. This is a huge improvement but due to the high peak to average content of audio material a large headroom is still present. In figure 4.3.c a 2 level supply scheme is shown. The advantage of this approach is a relative simple implementation that changes the gain of the feedback loop in the power supply based on a simple trigger circuit. When the user listens to background music the supply voltage will be low and the supply voltage will go to its maximum level at other volume settings. Figure 4.3.d shows a peak and hold supply voltage scheme where the supply voltage is turned up during the peaks of the audio signal and is hold for a while before it begins to fall again until it finds the next peak. This scheme is also quite simple to implement using a peak and hold circuit but it will properly require more from the feedback loop of the amplifier because the amplifier have to adjust its gain to the constantly changing supply voltage. Figure 4.3.e illustrate a fast tracking power supply. This is the ultimate scheme in terms of minimum supply voltage but on the other hand it requires a lot from the control loop of both the amplifier and the power supply. A fast and fully tracking power supply was presented in [52, 53]

The goal of this work was to investigate the real efficiency improvement of a peak and hold based tracking power supply and to investigate if the total harmonic distortion of the amplifier is affected. The peak and hold based tracking power supply was not implemented but the efficiency of a class-D amplifier as a function of the output power was measured and for each power level the supply voltage was adjusted to the peak value the amplifier output voltage. Figure 4.4 compares the measured efficiency with and without a "peak and hold based tracking power supply". As seen the efficiency is drastically improved at 1 W. If the power supply rejection ratio of the amplifier is high due to a well designed feedback loop then the total harmonic distortion should not be altered which is also the case for the measured THD curves shown in figure 4.5.

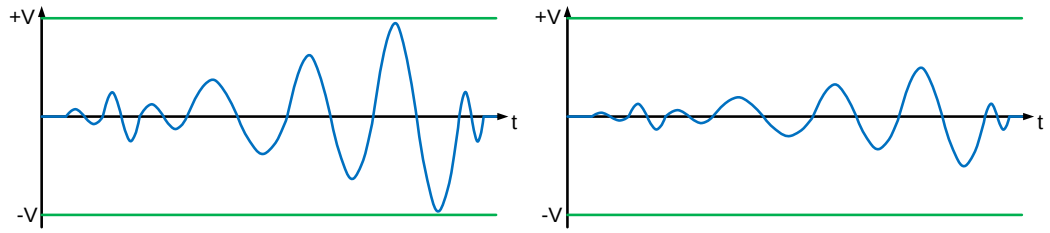

a) Fixed supply voltage

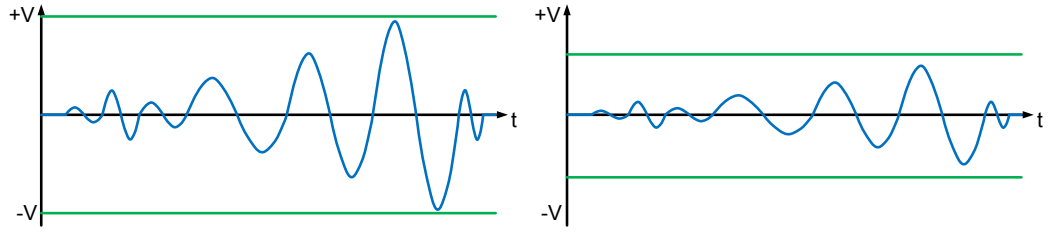

b) Supply voltage proportional to volume level setting

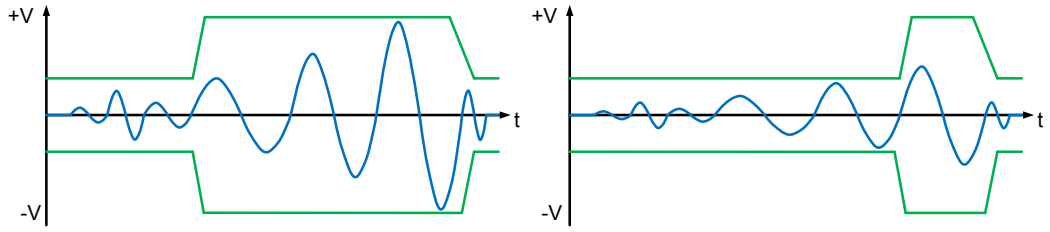

c) 2-level supply voltage with fixed treshold

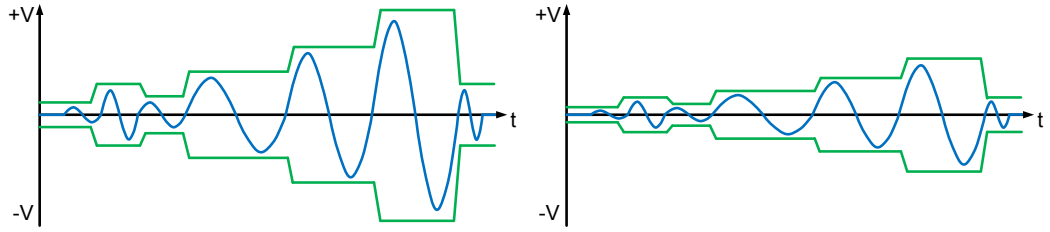

d) Peak and hold supply voltage

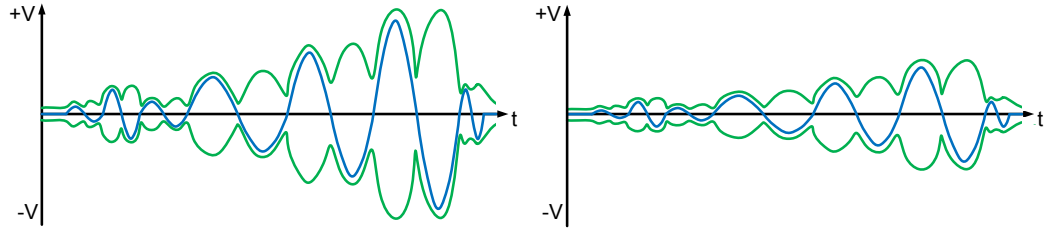

e) Tracking supply voltage

Figure 4.3: Amplifier supply voltage schemes. Left: High signal level, Right: Low signal level, supply voltage (green), signal (blue)

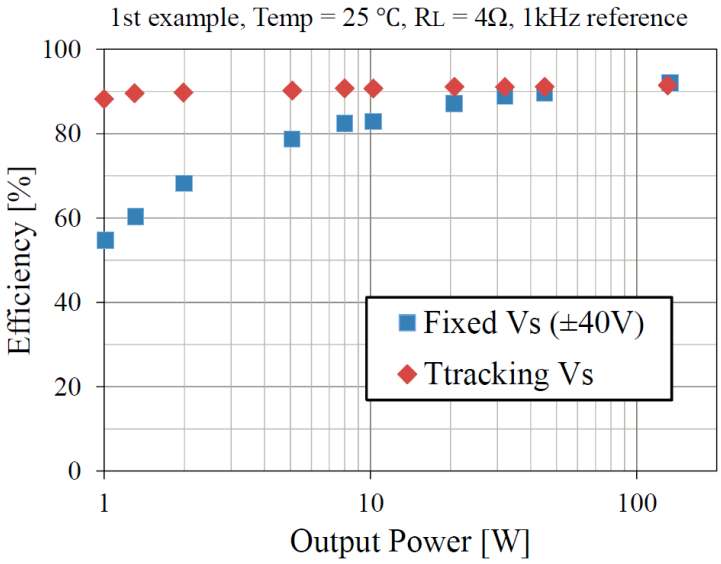

Figure 4.4: Comparison of measured efficiency with an without peak tracking power supply

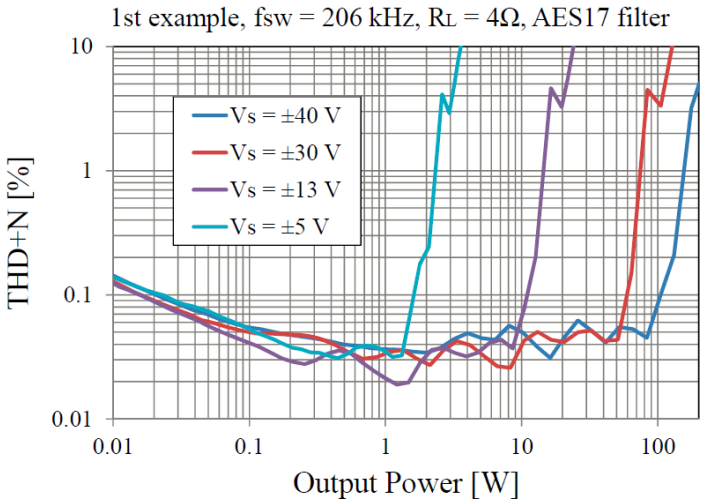

Figure 4.5: THD vs. power for different supply voltages

4.2.1 Discussion

This work demonstrate that the efficiency of a class-D amplifier can be significantly improved at low power levels by the use of a peak and hold based tracking power supply. In theory the amplifier efficiency could be further improved if a fast tracking power supply scheme was applied. In future work the efficiency of the tracking power supply should however be considered since a higher conversion ratio could counteract the gained efficiency improvement to some extend. Previous research has investigated the possibility of integrating the power supply and the amplifier in a single stage but it seems like that approach has to many disadvantages [54]. To the authors knowledge the literature regarding this subject is very sparse and a fixed supply voltage is common practice for class-D amplifiers.

4.3 Non-linear transducer and electrical compensation

This chapter describes a interesting concept for efficiency improvement that was not investigated or published due to lack of time. It is well known that the transducer is the weakest component in the sound reproduction chain as mentioned before. The passband efficiency for a transducer is given by

$$\eta = \frac{Bl^2}{R_e M_{ms}^2} \frac{\rho_0 S_d^2}{2\pi c} \tag{4.1}$$

To state an example the efficiency of the 8” woofer (HiVi-M8N) used in the work on motional feedback [B] is

$$\eta_{woofer} = \frac{9.6^2}{6.5 \cdot 0.0365^2} \frac{1.18 \cdot 0.0214^2}{2\pi 345} \cdot 100 = 0.27\% \tag{4.2}$$

The efficiency of a 1” tweeter (BC25SC06-04) is a little higher

$$\eta_{tweeter} = \frac{1.7^2}{2.9 \cdot 0.00027^2} \frac{1.18 \cdot 0.00068^2}{2\pi 345} \cdot 100 = 0.35\% \tag{4.3}$$

It seems very challanging to improve the efficiency when looking at equation 4.1. The force factor Bl can be increased by the use of a larger and stronger magnet but a physical limit exists and strong neodymium magnets are already applied. Further more a larger magnet takes up more space inside the loudspeaker enclosure which decrease the efficiency below the resonance frequency of the transducer. A larger magnet also increase the weight of the transducer which is a disadvantage when it comes to handling and shipping. The effective cone area S_d is constrained by the size of the final loudspeaker design. Even if a larger cone area would be an option the larger cone would increase the mass M_{ms}. The mass could be reduced by using a thin and lightweight material and apply cone optimization to avoid break up. This approach has already been applied and there is a physical limit as well as a economic limit to the choice of material and the fabrication. The mass could also be reduced by the use of a lighter conductor such as alluminium but that would cause the resistance to increase. The resistance could be lowered by adding fewer

turnes, decreasing the diameter of the voice coil or by increasing the diameter of the wire or by improving the fill factor using rectangular wire. The last two options increase the mass and the two first options decrease the force factor Bl. The task is thus to balance all of these parameters to optimize the efficiency of a transducer. This task is actually very limited by the fact that the transducer needs to be linear in a certain displacement range and due to the fact that the DC-resistance of the voice coil R_e needs to be fixed at 4Ω or 8Ω.

Klippel and Agerkvist have however showed that a non-linear transducer motor can improve the efficiency at certain displacement ranges but non-linear compensation methods such as motional feedback are required [1, 2]. A range of motor topologies are shown in figure 4.6. Each topology produce a unique force factor characteristic as shown in figure 4.7.

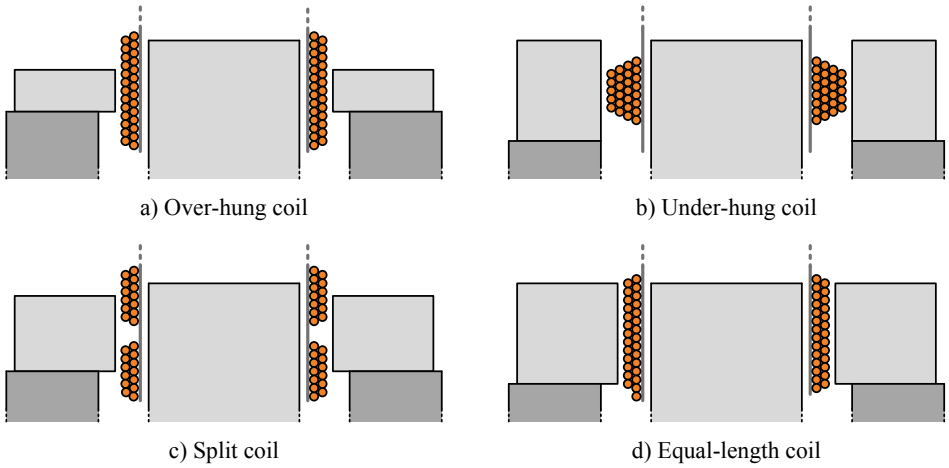

Figure 4.6: Motor topologies

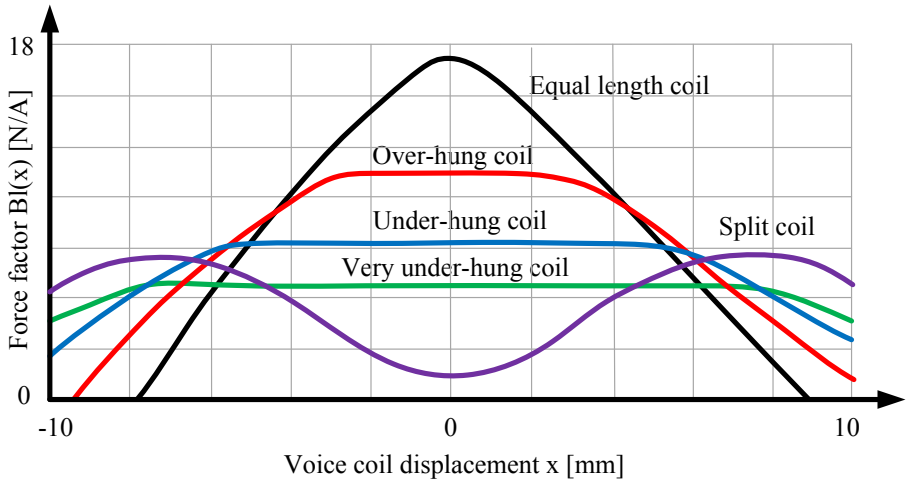

Figure 4.7: Illustration of force factor vs. displacement for different motor topologies. The curves are based on work by Klippel and Agerkvist [1, 2]

4.3.1 Discussion

Considering the behavior of the listener and the behavior of music the displacement is most frequently operating in the low range. Thus the equal length coil motor topology is most attractive in terms of efficiency. Future work should focus on the tradeof between a high force factor vs. a decreased number of turns leading to lower voice coil resistance, lower DC resistance and lower voice coil inductance. In professional audio equipment where the loudness level is constantly high the split coil motor topology could be of interest. In both cases non-linear control is required.

Chapter 5

Cost and size

5.1 Introduction

For many years it seemed like the saying ”more is better” applied for amplifier power in a sound system. In recent years the game has changed since many new sound systems integrate the power supply, the amplifiers and the transducers in a single unit leaving all of the technical details to the engineers - it just have to play loud enough! New design possibilities arise as a consequence of the integration but at the same time size and cost of the main components is a major challenge. Present design practices relying on sinusoidal test signals and resistive amplifier loads which are far from the actual audio signals and amplifier loads are hindering improvements in this area [55–61]. The motivation has thus been to develop an intelligent approach to estimate the realistic power requirements of a given sound system to avoid over dimensioned sound systems and to obtain a highly appreciated size and cost reduction [D,E].

5.2 Modeling of requirements specification

The power required during audio reconstruction is mainly a function of the audio material being reproduced, the loudness level and the efficiency of the loudspeaker. A more detailed scheme for estimation of the power requirements is shown in figure 5.1. The model uses a large database of music files (400 music tracks in total), the music tracks are loudness normalized to enable a fair comparison of the individual power requirements of each track, the same amount of gain is then applied to each track to bring the loudness level to a specific loudness limit, the music is filtered by a cross-over filter and the resulting signals are applied to a linear model of specific transducers/drivers that are to be used in the given application.

The model used was similar to the Matlab simulink model shown in figure 3.4 but with the non-linear dependencies of the displacement disabled. From the simulations the voice coil voltage and current of each music track was stored. It was then

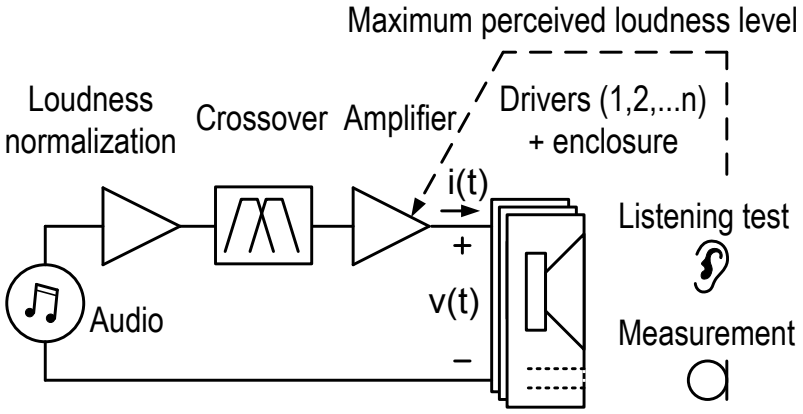

Figure 5.1: Scheme for power requirement estimation

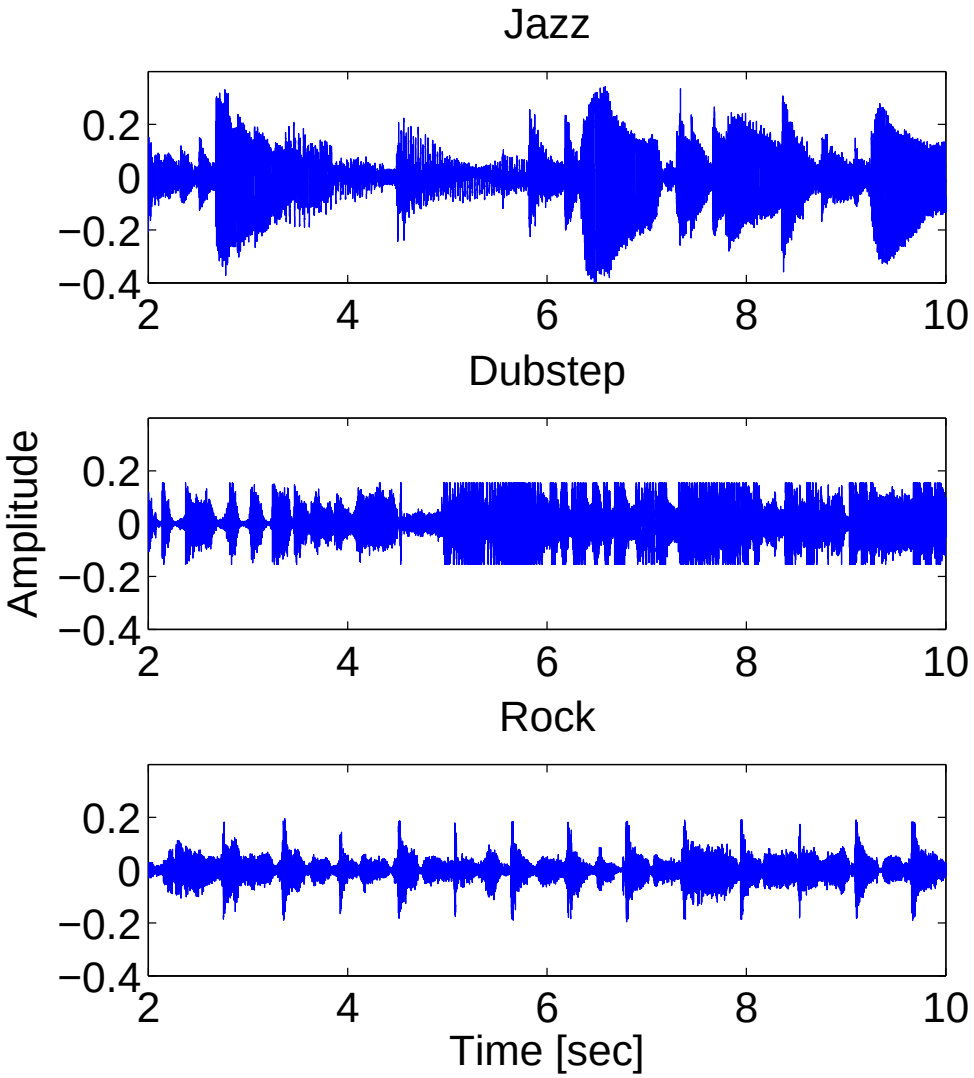

Figure 5.2: 3 genres of music with applied loudness normalization

relatively simple to extract the worst case peak voltage and current and to calculate the worst case peak power and the apparent power for each track. The result are shown in figure 5.3. As seen the peak voltage, the peak current and thus the peak power was highest for the woofer. The average apparent power was however higher for the subwoofer for less than half of the songs and it is noted that the worst case peak power is approx. 100 times higher than the average apparent power. This knowledge can be used to determine the supply voltage of the amplifier and the ratting of the components in the power supply and the amplifiers. From these results it is clear that the power requirement is related to the audio material. Figure 5.2 show 3music tracks of individual genres with applied loudness normalization. These tracks sound equally loud despite their different characteristics. By eye inspection the Dubstep track sees to have the highest average power requirement whereas the Jazz track seems to have the highest peak power requirements. It is however hard to distinguish the worst case power requirements for the woofer and the tweeter.

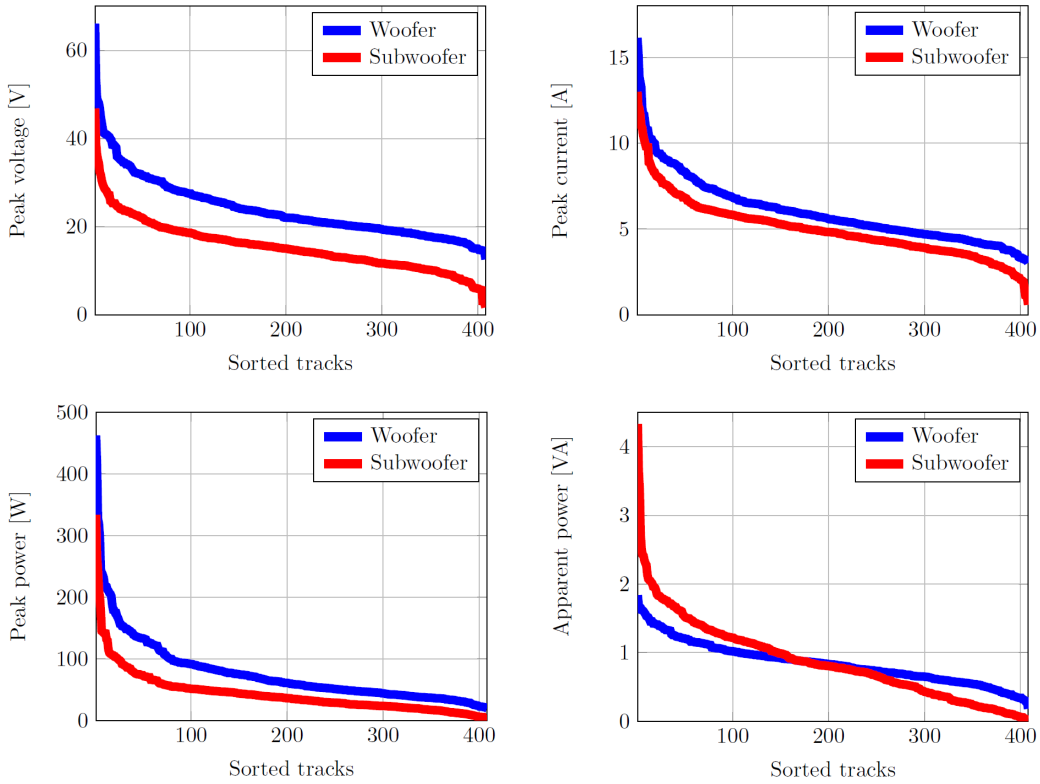

Figure 5.3: Analyse of worst case peak voltage, peak current, peak power and apparent power

The most important information is however missing. What is the worst case power requirement scenario during playback of these music tracks? How fast does the high power levels decay? How frequently is the high power levels required? There is no simple way to answer these questions and therefore the power vs. time for each track had to be analyzed in more detail. Figure 5.4 illustrate the presented analyzing scheme. The stored data of the voltage and current from the simulation were multiplied to form the power signal. Then the power signal was multiplied in the time domain with a square window with stepwise logarithmically increasing window width. For each window width the window was moved forward with 1 sample until

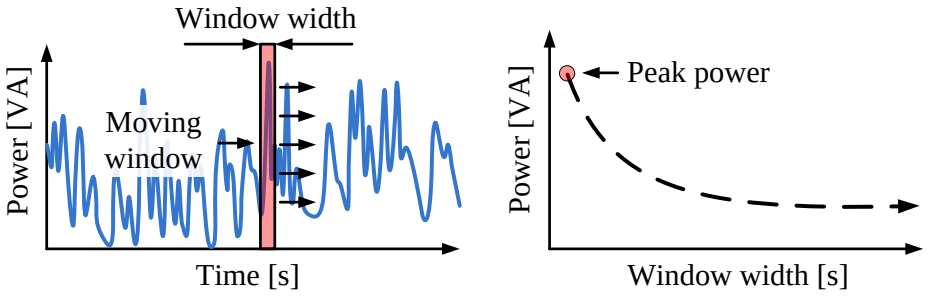

a) Short window

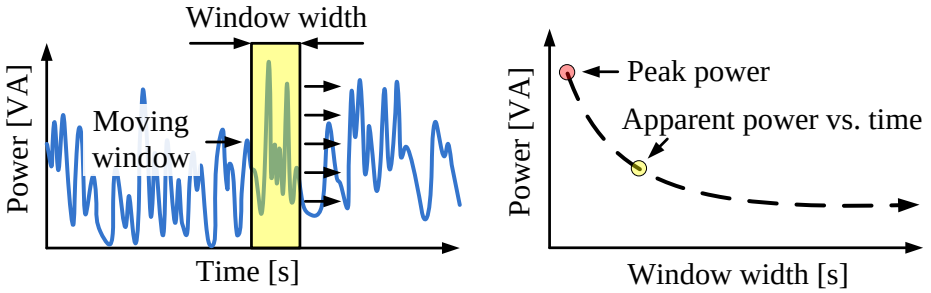

b) Medium window

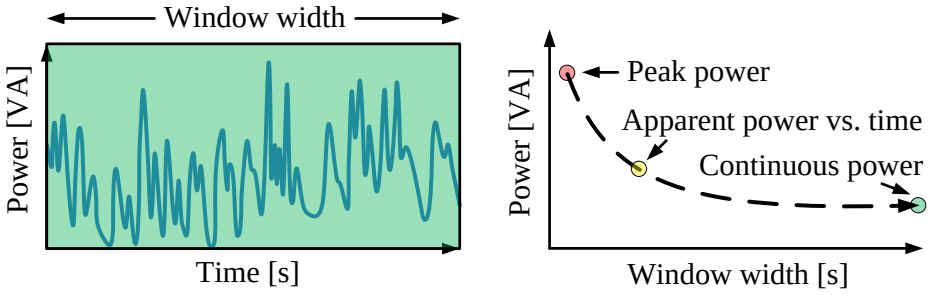

c) Long window

Figure 5.4: Power analysis

the window reaches the end of the music signal. Every time the window was moved, the apparent power of the signal within the window was calculated by (5.1) and the maximum value was stored for that particular window size. The result is the worst case power requirement scenario vs. time. The result of the analysis for a woofer can be seen in figure 5.5. As seen the worst case power is reduced from 500 VA to 40 VA in 0.1 second. In comparison the state-of-the-art power supplies and amplifiers are rated for more than 80 seconds of peak power.

$$|S| = \frac{1}{N}\sqrt{\sum_{n}^{N} v(n)^2 i(n)^2} \tag{5.1}$$

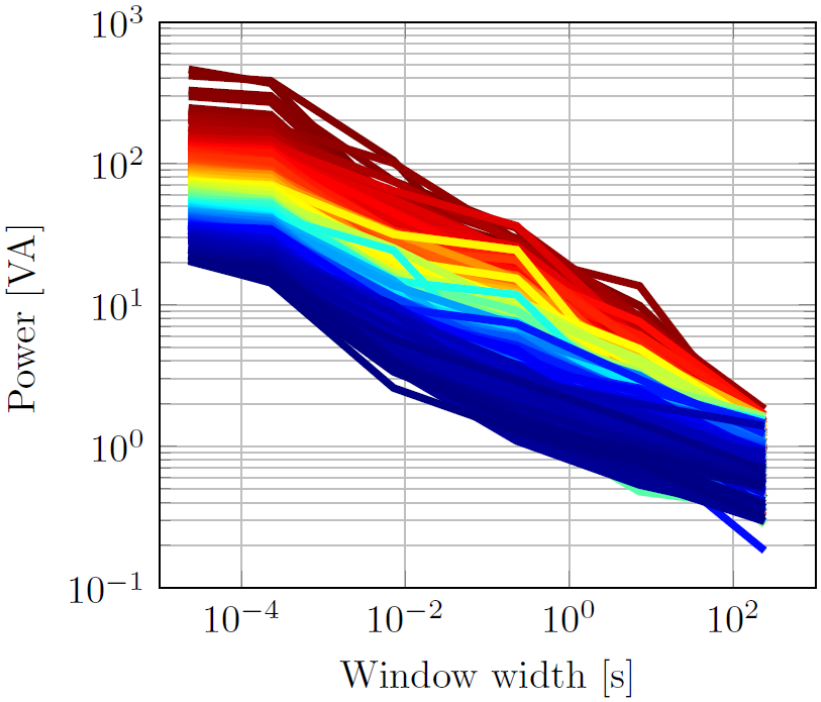

Figure 5.5: Worst case power vs. time (window width) for a woofer

5.3 Validation of requirements specification model

The previously presented power requirement model was based on a very simple linear model. Further work expanded the model to include different types of enclosures (closed and vented) and to include the most critical non-linearities $C_{ms}(x)$, $Bl(x)$ and $Le(x)$. In order to verify the models a simple measurement setup was established. A 2 way loudspeaker developed by PointSource Acoustic and suitable amplifiers were acquired. The voice coil voltage and current was preconditioned on a small circuit board before being send to a Data Acquisition Device (DAQ) from National Instruments which was controlled via Matlab. The setup is seen in figure 5.6.

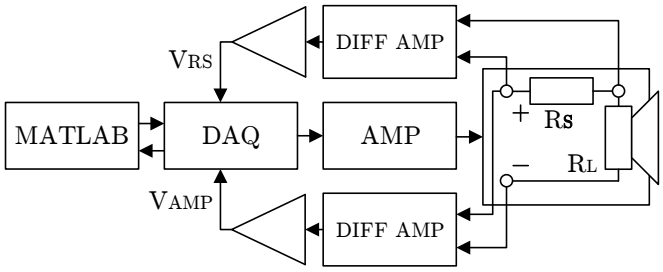

Figure 5.6: Simplified measurement setup

Figure 5.7 shows the result of the closed box woofer validation. At low voice coil voltage (4.3 V_{pk}) the coherence of the linear model is better than the non-linear

model. On the contrary the linear model overestimates the peak power at higher voice coil voltages (10.8 V_{pk}). This discrepancy could be caused by the fact that the non-linear parameters are measured at high voltage levels and not low voltage levels. Also the free air and the vented box model showed a good coherence to the measurements. All models predict the fast decay of power very accurately as function of time and thus the results from the previous research where 400 music tracks were analyzed can be trusted and is useful. Figure 5.8 shows a comparison of the measured tweeter with and without a passive cross-over filter and a linear simulation. It is clearly seen that the power requirement of the tweeter is different from that of the woofer.

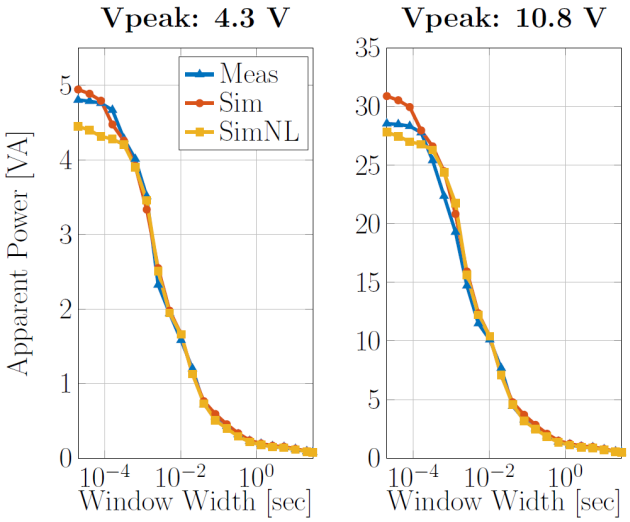

Figure 5.7: Closed box woofer validation

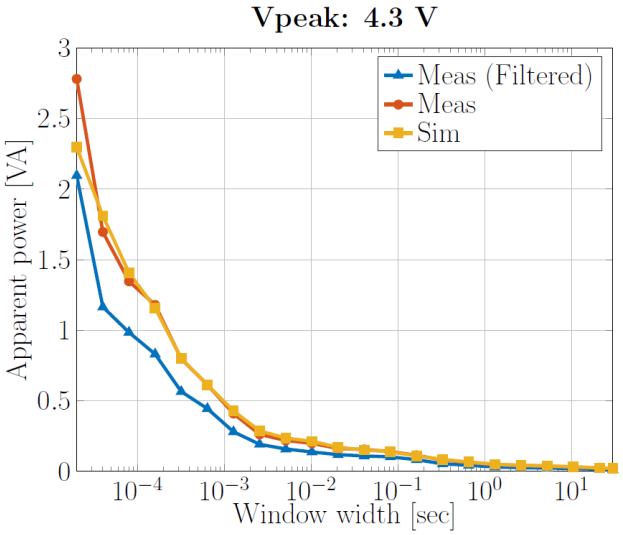

Figure 5.8: Tweeter validation

A statistical analysis of the power requirements of 128 loudspeakers with similar size (6.5") was performed in collaboration with a master student [Ausin2015Experimental]. The linear parameters was acquired from various databases on the internet and processed in Matlab. The frequency response of all the transducers were equalized to

the same target response to enable a fair comparison and then each transducer was simulated with the linear transducer model. Figure **??** shows a zoom of the power curves obtained by simulation. As seen the variance in complex power (S) is large. In future designs of general purpose power supplies and amplifiers the presented power requirement model could be used to account for such variance.

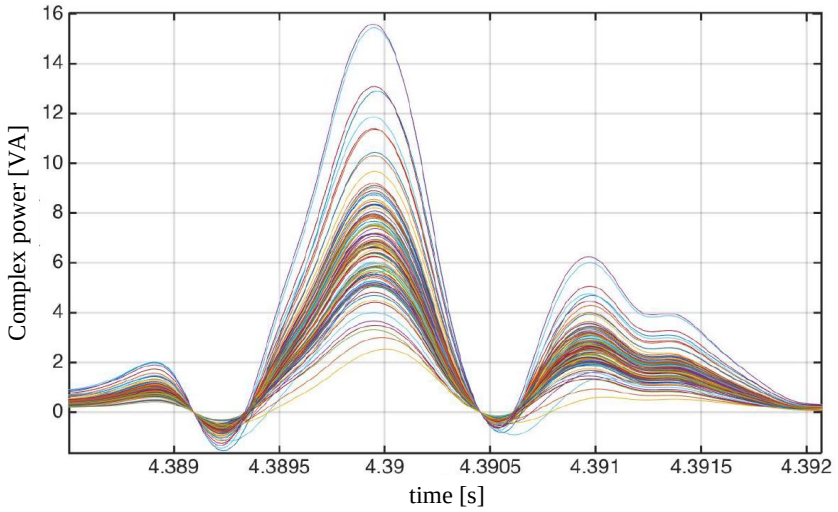

Figure 5.9: Power variance as a function different transducers

5.3.1 Discussion

Until now sound system engineers only had rough estimations of the power requirement at hand based on assumptions far from the real application. In this work a first attempt towards a realistic requirement specifications is taken considering audio material as input, loudness normalization of the audio material, crossover filters, the desired maximum loudness level as well as a non-linear model of the transducers in the most popular enclosure types. The next step is to implement this knowledge in the design of future power supplies, amplifiers and transducers.

5.4 Power supply design

[F]

5.5 Discussion

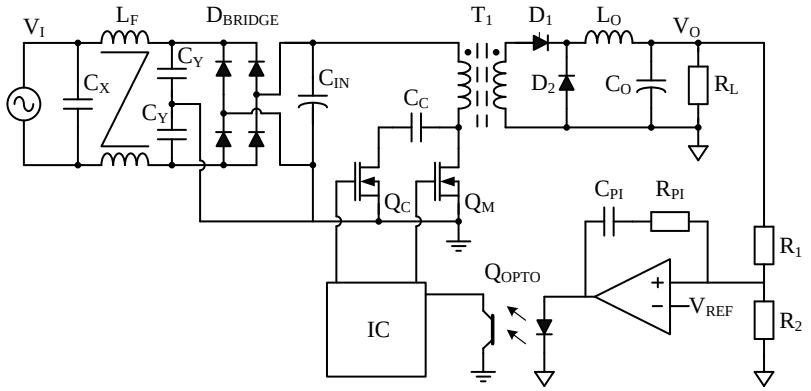

Figure 5.10: Schematic of the active clamp forward converter

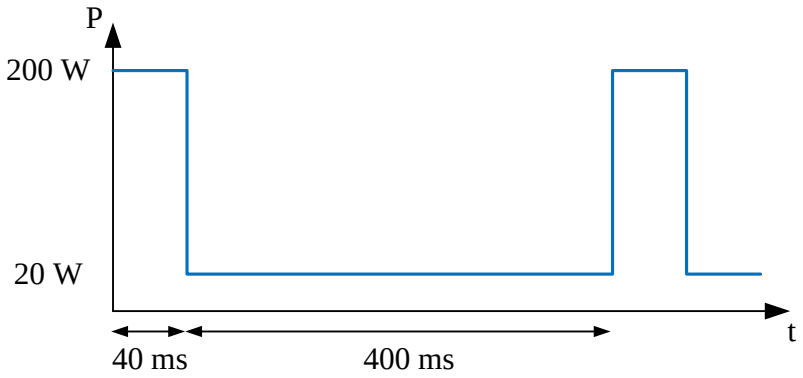

Figure 5.11: Power supply test signal simulating a deep bass rhythm with 160 beats per minute

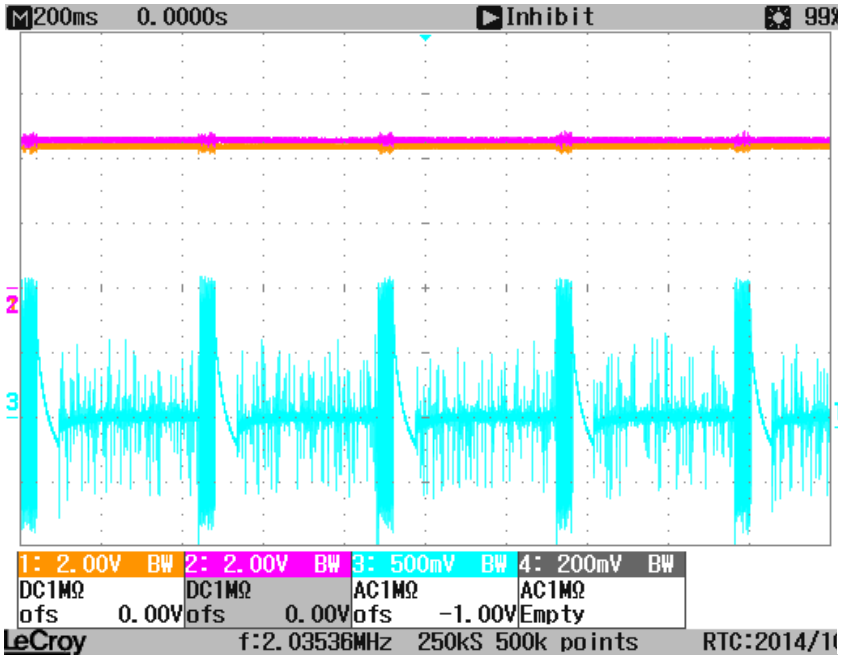

Figure 5.12: Temperature measurement during power test

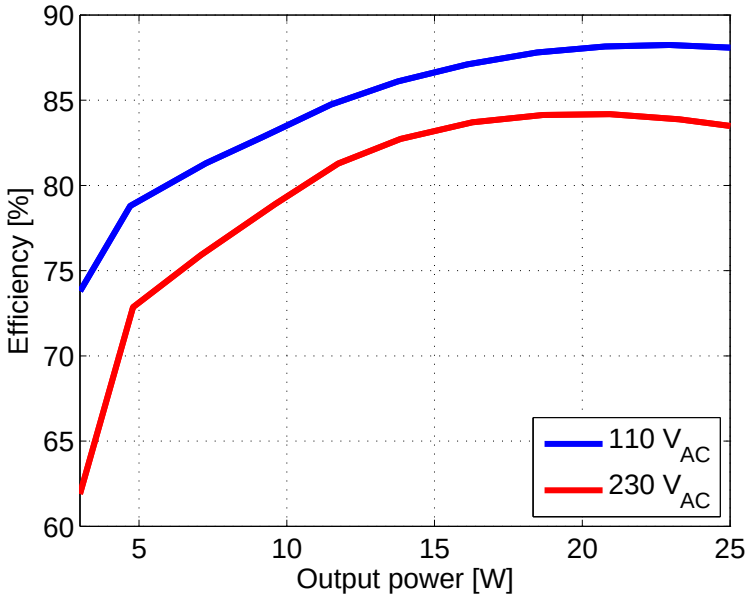

Figure 5.13: Efficiency measurement

Chapter 6

Production

6.1 Introduction

Incductors wound on toriodal cores are used in many power electronic products. An examble is shown in figure 6.1 where 6 of such inductors are used in an integrated power supply and amplifier module from Pascal Audio. As illustrated in figure 6.2 the prototyping of such inductors are fairly quick and simple to create but the step towards production require a lot of machinery and manual work which is typically performed in countries where labor expenses are low. The lead time is thus high for such inductors because it takes time to manufacture and ship the ordered inductors. If the core diameter is small and the wire diameter is large each winding must be made manually on a hook-pull type machine which is really labor extensive. Since such inductors are quite bulky they are typically placed and soldered manually. Another disadvantage of the wire wound toriodal inductor is that the copper fill factor is low because the spacing between the windings increase gradually from the inner diameter of the core to the outer diameter.

In this work a hybrid winding concept was investigated using the traces in a printed circuit board to connect a number of bended copper foils resulting in a complete winding. As usual a picture tells more than a thousand words - see figure 6.3. This concept opens up the possibility for both an automated manufacturing process and an automated production process of toroidal magnetics such as power inductors, filtering inductors, air core inductors, transformers etc. Also a faster time to market is expected since the former including the bended foils can be pre-fabricated and pre-shipped to different suppliers around the world.

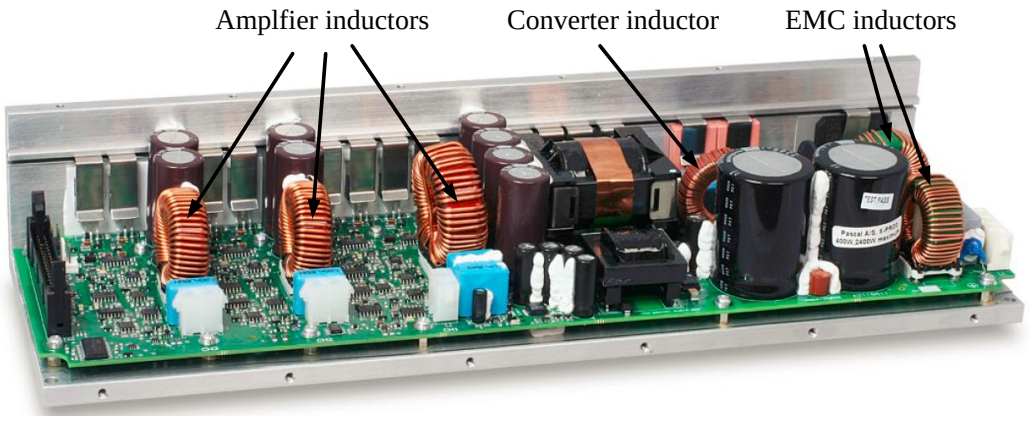

Figure 6.1: Power supply and 2.1 channel amplifier from Pascal Audio

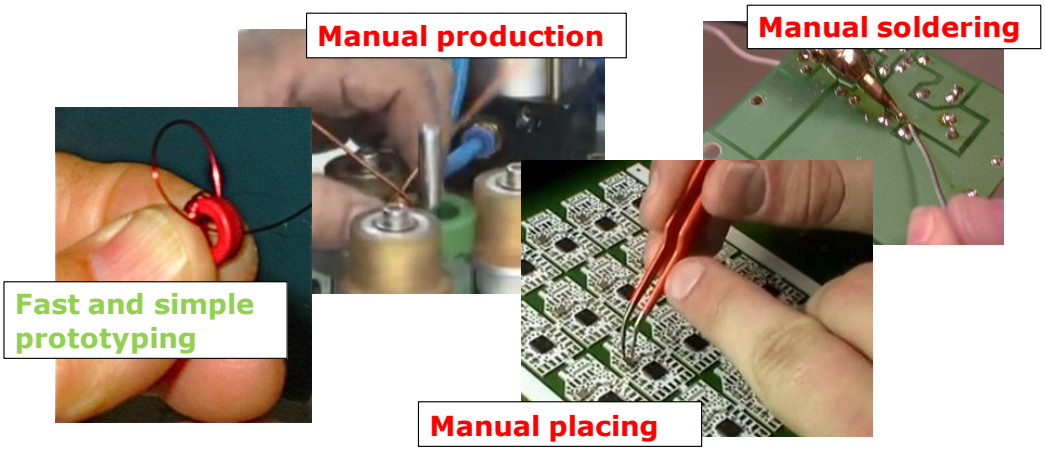

Figure 6.2: Road from prototype to finished product

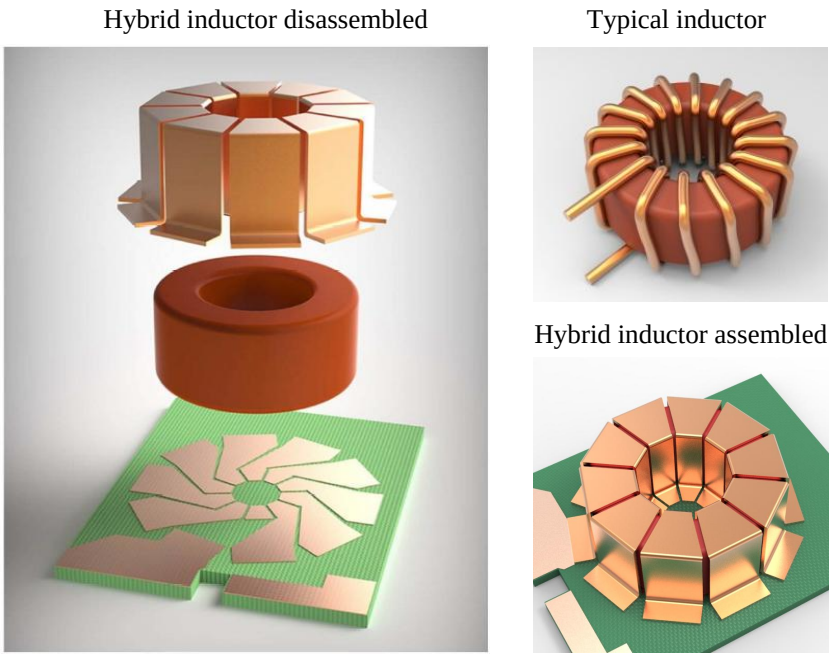

Figure 6.3: Conceptual drawings

6.2 Hybrid winding concept for toroids

In the early phase of development many thoughts about the winding implementation came up. Figure 6.4 show several ways to implement the hybrid winding. Both stamped and bend foil pieces and cast copper pieces were considered. The resistance of such winding arrangements are very complex to solve numerically and thus 3D finite element analysis (FEA) was utilized.

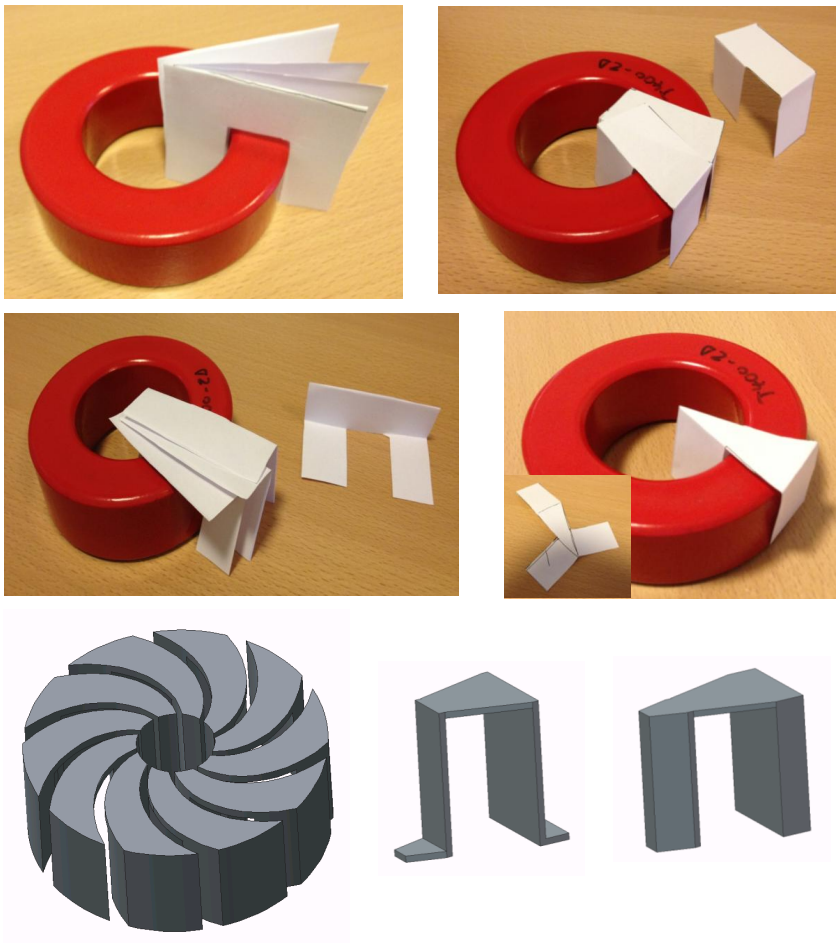

Figure 6.4: Winding concepts

It was decided to make a prototype of the typical wire wound inductor and a prototype of the hybrid wound inductor. Figure 6.5 shows the prototypes to the left and the 3d drawn versions for simulation in the right. The prototypes was only used to validate the simulation results and where never meant to be compared in terms of resistance, inductance and such. The simulations showed a good coherence up to 100 kHz where the core loss started to influence the measured resistance. Now that the simulations could be trusted the influence of the copper layer thickness of the PCB was simulated. The result shown in figure 6.6 it can be observed that the DC resistance of the hybrid inductor with bended foils of 0.5 mm thickness can be rduced by 60 % using a double sided PCB layer of 70um copper thickness. It was concluded that the bottle neck for the hybrid inductor is the connections done in the PCB. In order to reduce the conductor length in the PCB the bended

copper foils need to go in an angle over the core in order to secure that the PCB connections are as straight and short as possible.

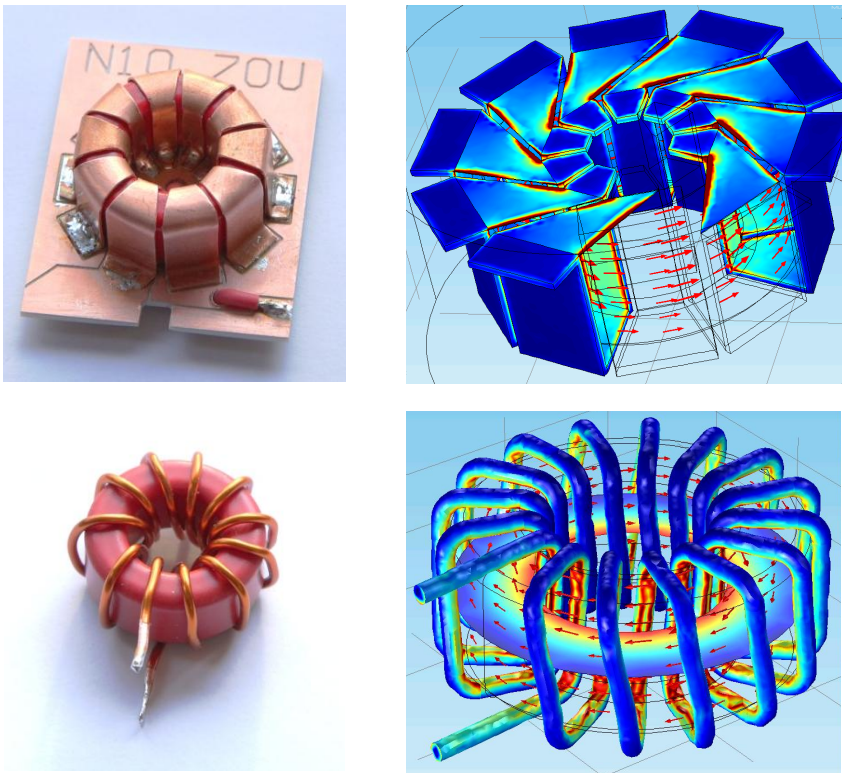

Figure 6.5: Left: Prototypes, Right: FEM simulation

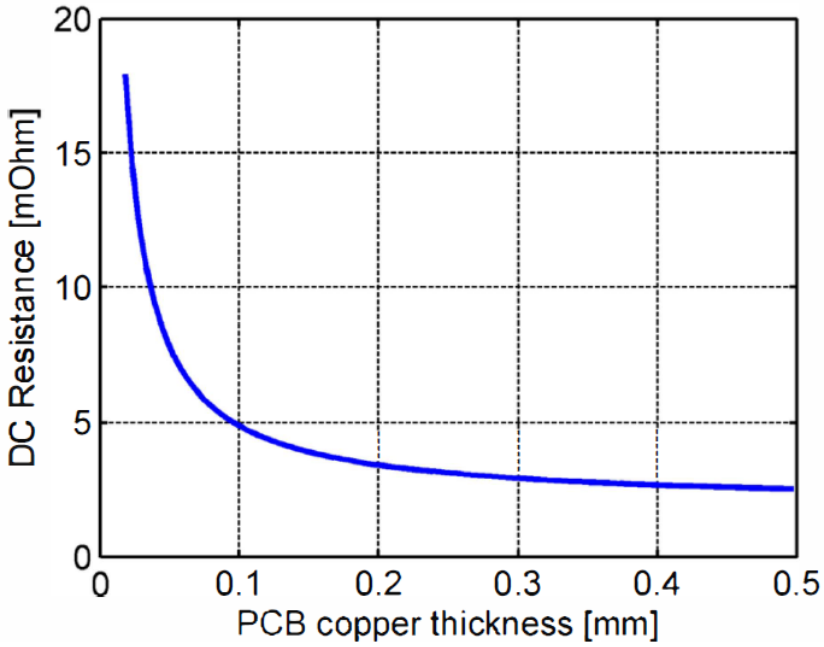

Figure 6.6: Simulated DC resistance as a function of the PCB copper thickness

6.3 DC resistance optimization of a foil wound inductor

It is very difficult and time consuming to do several 3D FEA simulations. A 2D FEA simulation was therefore chosen to attempt an optimization of the DC resistance by simulation of various winding possibilities. A Matlab program with a graphical user interface was created enabling various winding implementations to be generated and inspected visually. The program enabled the user to change the angle of each vertical or horizontal section of the winding, the number of turns and the amount of insulation between each turn. Figure 6.7 illustrate the GUI and examples of different settings and visual outputs. An optimization routine could be lunched which generated a vast range of winding configurations. Each winding configuration was automatically imported into Comsol and simulated using FEA. A 31 % improvement of the DC resistance compared to previous results where the bended copper foils went straight over the core. As mentioned earlier the thickness of the PCB traces were a bottle neck for high power inductors. Another way to cope with this problem is illustrated in figure 6.8 and 6.9.

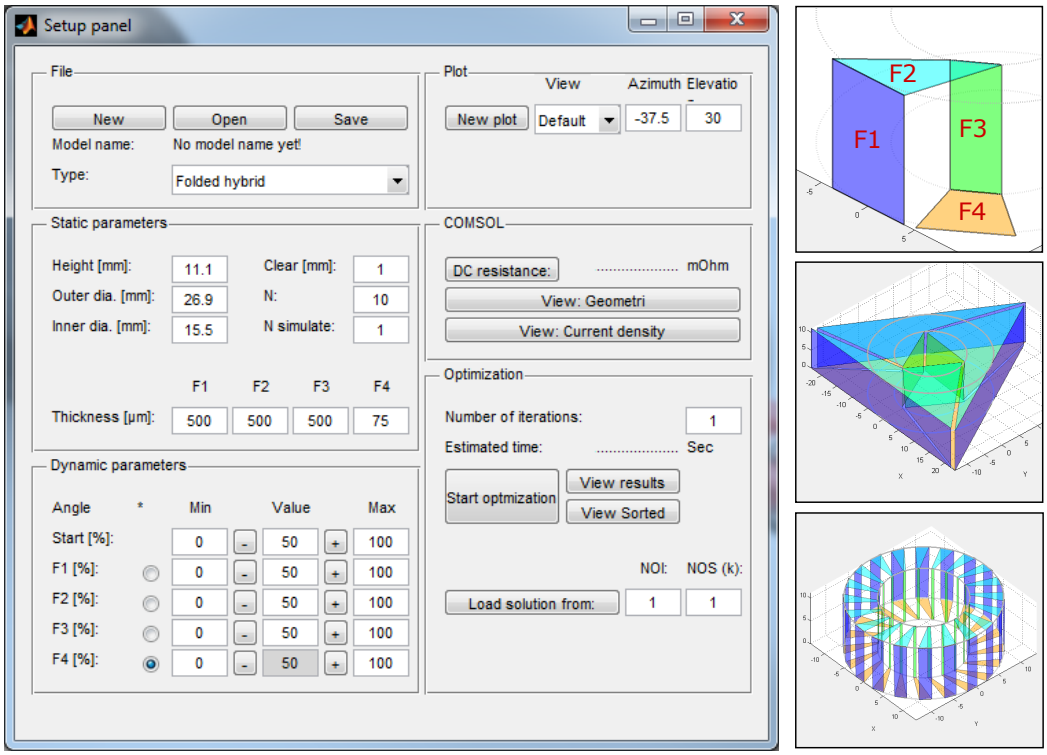

Figure 6.7: Graphical user interface and output

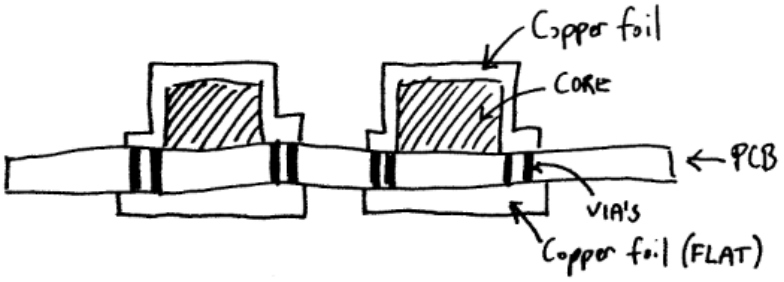

Figure 6.8: High power hybrid concept 1

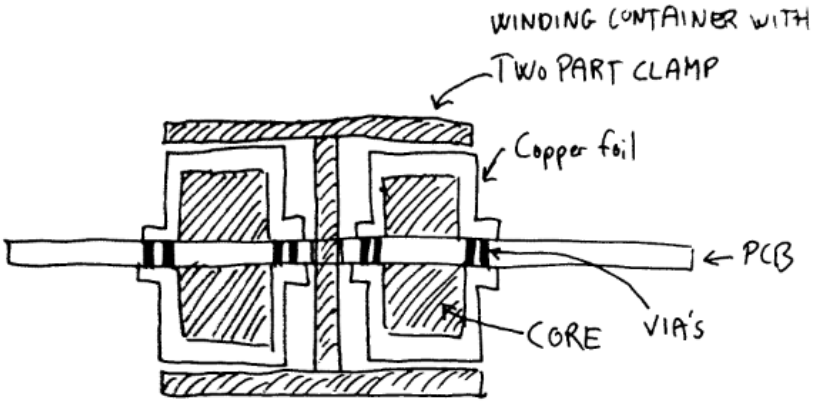

Figure 6.9: High power hybrid concept 2

6.4 Discussion

The first publication describing the hybrid winding concept won the best paper award at the ECCE Asia down under conference in 2013. The concept is still very young and the full potential is not yet exploded. The next step could be to test the hybrid inductor in a real application such as class-D amplifiers or as air inductors for very high frequency converters.

Chapter 7

Other research

A great knowledge within magnetic component design and converter optimization was acquired through a fruitful collaboration with several researchers at the electronic department at DTU. The work contributed to the development of efficient drivers for actuators based on dielectric electro active polymer which has a potential to increase the efficiency and weight of future audio transducers [62–66]. Further more a huge amount of this research is relevant for the design of power supplies used in sound systems. The flyback topology has been in focus during this work and it is also a popular topology for power supplies in sound system. It is out of scope for this thesis to present this work in further detail but the conference and journal publications related to this work are to be found in the publication list.

Chapter 8

Conclusion and Future work

This work has investigated the improvement of sound systems by electrical means. The major parts of this thesis and the associated publications correspond to the following contributions:

- Non-linear models of voltage- and current-controlled electro dynamic transducers have been derived and the accuracy have been verified using a laser measurement. Both total harmonic distortion and total intermodulation distortion as a function of frequency and displacement have been presented. The knowledge gained are crucial for the design of sounds systems with improved sound quality. Future work should focus on auralization of the non-linearities and focus on ways to determine the perceived audio quality. This will help future engineers to make meaningful design choices leading to better sound systems.
- Multi-tone distortions of voltage- and current-controlled transducers have been compared using non-linear models. It was found that current control is an alternative to the use of passive shorting rings in the pole piece that are used to linearize the voice coil inductance as a function of the displacement. Future work could focus on the combination of current control and motional feedback as sparsely presented in previous research. Listening tests would be of great future value.
- Accelerometer based motional feedback have been successfully implemented as an electrical mean to improve the sound quality. A 14 dB reduction of the total harmonic distortion was obtained in the best case. Motional feedback opens up for radical design changes such as non-linear transducer designs that has a potential to improve the very poor efficiency of linear transducers. More work is required to optimize the performance and implementation cost of motional feedback. Also the power requirement of small loudspeakers with motional feedback could be investigated in the future.
- The concept of a tracking power supply has been investigated as a mean to lower the amplifier losses at low power levels which is an environmental con-

cern. The measurements on a prototype and a commercial class-D amplifier shows a considerable efficiency improvement at low output power without significant degradation of the sound quality. Future work should implement a tracking power supply to reveal the full potential of this concept.

- A first attempt towards realistic power requirements specifications for sound systems have been taken. A new analyzing tool has been developed and experimentally validated. It is found that the full power capability of the power electronics in a sound system is only needed for a very short time in the range of milliseconds. Based on this research a huge potential in terms of size and cost of future sound systems is expected. Future work should expand this research to include a range of different sound system applications and different audio material.

- A novel hybrid winding concept for toroidal magnetic components have been proposed. The winding implementation has been optimized in terms of DC resistance with the aid of a comprehensive optimization routine incorporating finite element analysis. The proposed hybrid winding scheme should be tested in different applications such as class-D amplifiers in the future. Also very high switching frequency converters could be an interesting test application.

Bibliography

[1] A. Voishvillo, A. Terekhov, E. Czerwinski, and S. Alexandrov, "Graphing, interpretation, and comparison of results of loudspeaker nonlinear distortion measurements," *Journal of the Audio Engineering Society*, vol. 52, no. 4, pp. 332–357, 2004.

[2] D. Shmilovitz, "On the definition of total harmonic distortion and its effect on measurement interpretation," *IEEE Transactions on Power delivery*, vol. 20, no. 1, pp. 526–528, 2005.

[3] E. Czerwinski, A. Voishvillo, S. Alexandrov, and A. Terekhov, "Multitone testing of sound system components' some results and conclusions, part 1: History and theory," *Journal of the Audio Engineering Society*, vol. 49, no. 11, pp. 1011–1048, 2001.

[4] A. Voishvillo, "Measurements and perception of nonlinear distortion?comparing numbers and sound quality," in *Audio Engineering Society Convention 123*, Audio Engineering Society, 2007.

[5] E. R. Geddes and L. W. Lee, "Auditory perception of nonlinear distortion-theory," in *Audio Engineering Society Convention 115*, Audio Engineering Society, 2003.

[6] W.-S. Gan and N. Oo, "Analytical and perceptual evaluation of nonlinear devices for virtual bass system," in *Audio Engineering Society Convention 128*, Audio Engineering Society, 2010.

[7] C.-T. Tan, B. C. Moore, and N. Zacharov, "The effect of nonlinear distortion on the perceived quality of music and speech signals," *Journal of the Audio Engineering Society*, vol. 51, no. 11, pp. 1012–1031, 2003.

[8] C.-T. Tan, B. C. Moore, N. Zacharov, and V.-V. Mattila, "Predicting the perceived quality of nonlinearly distorted music and speech signals," *Journal of the Audio Engineering Society*, vol. 52, no. 7/8, pp. 699–711, 2004.

[9] I. Rec, "Bs. 1387, method for objective measurements of perceived audio quality," *International Telecommunications Union, Geneva, Switzerland*, 1998.

[10] T. Thiede, W. C. Treurniet, R. Bitto, C. Schmidmer, T. Sporer, J. G. Beerends, and C. Colomes, "Peaq-the itu standard for objective measurement of perceived

audio quality," *Journal of the Audio Engineering Society*, vol. 48, no. 1/2, pp. 3–29, 2000.

[11] S. Temme, P. Brunet, and D. Keele Jr, "Practical measurement of loudspeaker distortion using a simplified auditory perceptual model," in *Audio Engineering Society Convention 127*, Audio Engineering Society, 2009.

[12] S. Temme, P. Brunet, and P. Qarabaqi, "Measurement of harmonic distortion audibility using a simplified psychoacoustic model," in *Audio Engineering Society Convention 133*, Audio Engineering Society, 2012.

[13] H. H. Scott, "Intermodulation measurements," *Journal of the Audio Engineering Society*, vol. 1, no. 1, pp. 56–61, 1953.

[14] R. Bortoni, S. Noceti Filho, and R. Seara, "Comparative analysis of moving-coil loudspeakers driven by voltage and current sources," in *Audio Engineering Society Convention 115*, Audio Engineering Society, 2003.

[15] R. Bortoni, H. S. Silva, *et al.*, "Effects of acoustic damping on current-driven loudspeakers," in *Audio Engineering Society Convention 122*, Audio Engineering Society, 2007.

[16] R. A. Greiner and T. M. Sims Jr, "Loudspeaker distortion reduction," *Journal of the Audio Engineering Society*, vol. 32, no. 12, pp. 956–963, 1984.

[17] E. Merilainen, *Current-driving of loudspeakers: eliminating major distortion and interference effects by the physically correct operation method*. Esa Meriläinen, 2010.

[18] P. G. Mills and M. J. Hawksford, "Distortion reduction in moving-coil loudspeaker systems using current-drive technology," *Journal of the Audio Engineering Society*, vol. 37, no. 3, pp. 129–148, 1989.

[19] P. G. Mills and M. J. Hawksford, "Transconductance power amplifier systems for current-driven loudspeakers," *Journal of the Audio Engineering Society*, vol. 37, no. 10, pp. 809–822, 1989.

[20] G. Pillonnet, E. Sturtzer, T. Rossignol, P. Tournier, and G. Lemarquand, "Distortion improvement in the current coil of a loudspeaker," in *Audio Engineering Society Convention 134*, Audio Engineering Society, 2013.

[21] E. Sturtzer, G. Pillonnet, G. Lemarquand, and N. Abouchi, "Comparison between voltage and current driving methods of a micro-speaker," *Applied Acoustics*, vol. 73, no. 11, pp. 1087–1098, 2012.

[22] P. Adduci, E. Botti, E. Dallago, and G. Venchi, "Pwm power audio amplifier with voltage/current mixed feedback for high-efficiency speakers," *Industrial Electronics, IEEE Transactions on*, vol. 54, no. 2, pp. 1141–1149, 2007.

[23] J. Suykens, J. Vandewalle, and J. Van Ginderdeuren, "Feedback linearization of nonlinear distortion in electrodynamic loudspeakers," *Journal of the audio engineering society*, vol. 43, no. 9, pp. 690–694, 1995.

[24] H. Schurer, *Linearization of electroacoustic transducers*. University of Twente, 1997.

[25] W. Klippel, "Direct feedback linearization of nonlinear loudspeaker systems," *Journal of the Audio Engineering Society*, vol. 46, no. 6, pp. 499–507, 1998.

[26] A. Bright, "Tracking changes in linear loudspeaker parameters with current feedback," in *Audio Engineering Society Convention 115*, Audio Engineering Society, 2003.

[27] E. R. Hanson, "A motional feedback loudspeaker system," in *Audio Engineering Society Convention 46*, Audio Engineering Society, 1973.

[28] M. A. Beerling, C. H. Slump, and O. E. Hermann, "Reduction on nonlinear distortion in loudspeakers with digital motional feedback," in *Audio Engineering Society Convention 96*, Audio Engineering Society, 1994.

[29] R. Valk, "Control of voice coil transducers," Master's thesis, TU Delft University of Technology, The Netherlands, 2013.

[30] H. Holdaway, "Design of velocity-feedback transducer systems for stable low-frequency behavior," *Audio, IEEE Transactions on*, no. 5, pp. 155–173, 1963.

[31] C.-Y. Chen, G. T. Chiu, C. Cheng, and H. Peng, "Passive voice coil feedback control of closed-box subwoofer systems," *Proceedings of the Institution of Mechanical Engineers, Part C: Journal of Mechanical Engineering Science*, vol. 214, no. 7, pp. 995–1005, 2000.

[32] S. A. Lane and R. L. Clark, "Improving loudspeaker performance for active noise control applications," *Journal of the Audio Engineering Society*, vol. 46, no. 6, pp. 508–519, 1998.

[33] Y. Li and G. T. C. Chiu, "Control of loudspeakers using disturbance-observer-type velocity estimation," *Mechatronics, IEEE/ASME Transactions on*, vol. 10, no. 1, pp. 111–117, 2005.

[34] E. De Boer, "Theory of motional feedback," *Audio, IRE Transactions on*, no. 1, pp. 15–21, 1961.

[35] C. Peplinski and A. Miller, "Motional voltage as a distortion mechanism in loudspeakers," in *Audio Engineering Society Convention 99*, Audio Engineering Society, 1995.

[36] F. Blasizzo, P. Desii, M. Di Cola, and C. Lastrucci, "Practical applications of a closed feedback loop transducer system equipped with differential pressure control," in *Audio Engineering Society Convention 131*, Audio Engineering Society, 2011.

[37] D. Birt, "A motion transducer for low-frequency loudspeakers," in *Audio Engineering Society Convention 91*, Audio Engineering Society, 1991.

[38] W. Geiger, "Servo control of loudspeaker cone motion using an optical linear displacement sensor," *Journal of the Audio Engineering Society*, vol. 53, no. 6, pp. 518–524, 2005.

[39] F. A. Medrano, "Optical Position Sensors with Applications in Servo Feedback Subwoofer Control," Master's thesis, University of California, USA, 2009.

[40] S. Willems and G. D?Hoogh, "On the use of motion feedback as used in 4th order systems," in *Audio Engineering Society Convention 126*, Audio Engineering Society, 2009.

[41] P. Robineau and M. Rossi, "Current-controlled vented-box loudspeaker system with motional feedback," in *Audio Engineering Society Convention 108*, Audio Engineering Society, 2000.

[42] C. Bortoni, R. Bortoni, S. Noceti Filho, and R. Seara, "Real-time voice-coil temperature and cone displacement control of loudspeakers," in *Audio Engineering Society Convention 117*, Audio Engineering Society, 2004.

[43] Y.-T. Tsai and J. H. Huang, "The dynamics detection and processing method for preventing large displacement transducer damage problem," in *Audio Engineering Society Convention 137*, Audio Engineering Society, 2014.

[44] F. Nyboe, *Integrated Circuit Design of Switching Power Stages for Audio Power Amplification*. PhD thesis, Technical University of Denmark - DTU, 2006.

[45] K. Nielsen and L. M. Fenger, "The active pulse modulated transducer (at)-a novel audio power conversion system architecture," in *Audio Engineering Society Convention 115*, Audio Engineering Society, 2003.

[46] K. Nielsen, "High-fidelity pwm-based amplifier concept for active loudspeaker systems with very low energy consumption," *Journal of the Audio Engineering Society*, vol. 45, no. 7/8, pp. 554–570, 1997.

[47] S. Poulsen, *Towards Active Transducers*. PhD thesis, Technical University of Denmark - DTU, 2004.

[48] B. Putzeys, "Simple self-oscillating class d amplifier with full output filter control," in *Audio Engineering Society Convention 118*, Audio Engineering Society, 2005.

[49] A. Yamauchi, A. Knott, I. H. Jørgensen, and M. A. Andersen, "Frequency dependent loss analysis and minimization of system losses in switch-mode audio power amplifiers," in *Audio Engineering Society Convention 137*, Audio Engineering Society, 2014.

[50] M. Høyerby, *High-Performance Control in Radio Frequency Power Amplification systems*. PhD thesis, Technical University of Denmark - DTU, 2008.

[51] M. Hoyerby and M. A. E. Andersen, "Ultrafast tracking power supply with fourth-order output filter and fixed-frequency hysteretic control," *Power Electronics, IEEE Transactions on*, vol. 23, no. 5, pp. 2387–2398, 2008.

[52] P. Ljusev, *Single conversion stage amplifier - SICAM*. PhD thesis, Technical University of Denmark - DTU, 2005.

[53] W. Klippel, *Small, Loud-Speakers: Taking Physics to the Limit*, 2013. Lecture.

[54] B. R. Petersen and F. T. Agerkvist, "Efficient non linear loudspeakers," in *120th Audio Engineering Society Convention*, 2006.

[55] R. Bortoni, S. N. Filho, and R. Seara, "On the design and efficiency of class a, b, ab, g, and h audio power amplifier output stages," *J. Audio Eng. Soc*, vol. 50, no. 7/8, pp. 547–563, 2002.

[56] A. Knott and L. P. Petersen, "Comparison of power supply pumping of switch-mode audio power amplifiers with resistive loads and loudspeakers as loads," in *Audio Engineering Society Convention 134*, May 2013.

[57] N. E. Iversen and A. Knott, "Small-signal loudspeaker impedance emulator," in *Audio Engineering Society Convention 136*, Apr 2014.

[58] F. Gonzalez-Espin, E. Figueres, G. Garcera, and J. Sandia, "Design of closed loop audio power amplifiers by means of an accurate model of vented box loudspeakers," in *Power Electronics and Applications, 2007 European Conference on*, pp. 1–9, IEEE, 2007.

[59] R. Bortoni and H. Sette Silva, "Loudspeakers' electric models for study of the efforts in audio power amplifiers," in *Audio Engineering Society Convention 115*, Oct 2003.

[60] P. J. Chapman, "Programme material analysis," in *Audio Engineering Society Convention 100*, May 1996.

[61] M. Mijic, D. Masovic, D. Sumarac Pavlovic, and M. Petrovic, "Statistical properties of music signals," in *Audio Engineering Society Convention 126*, Audio Engineering Society, 2009.

[62] D. Nielsen, A. Knott, and M. A. Andersen, "Driving electrostatic transducers," in *Audio Engineering Society Convention 134*, Audio Engineering Society, 2013.

[63] D. Nielsen, A. Knott, and M. A. Andersen, "Hysteretic self-oscillating bandpass current mode control for class d audio amplifiers driving capacitive transducers," in *ECCE Asia Downunder (ECCE Asia), 2013 IEEE*, pp. 971–975, IEEE, 2013.

[64] D. Nielsen, A. Knott, and M. A. Andersen, "Comparative study of si and sic mosfet for high voltage class d audio amplifiers," in *Audio Engineering Society Convention 137*, Audio Engineering Society, 2014.

[65] D. Nielsen, A. Knott, and M. A. Andersen, "Class d audio amplifier with 4th order output filter and self-oscillating full-state hysteresis based feedback driving capacitive transducers," in *Power Electronics and Applications (EPE'14-ECCE Europe), 2014 16th European Conference on*, pp. 1–7, IEEE, 2014.

[66] D. Nielsen, A. Knott, and M. A. Andersen, "Multilevel inverter based class d audio amplifier for capacitive transducers," in *16th Conference on Power Electronics and Applications*, 2014.

List of Publications

The overview of publications accomplished during the PhD study are given below. The publications are located in Appendix A-Q.

A **Henrik Schneider**, Finn Agerkvist, Arnold Knott and Michael A. E. Andersen, "Investigation of Current Driven Loudspeakers," *AES 138th Convention*, 2015.

B **Henrik Schneider**, Emilio Pranjic, Finn Agerkvist, Arnold Knott and Michael A. E. Andersen, "Design and evaluation of accelerometer based motional feedback," *AES 138th Convention*, 2015.

C Akira Yamauchi, **Henrik Schneider**, Ivan H. H. Jorgensen, Arnold Knott and Michael A. E. Andersen, "Investigation of Energy Consumption and Sound Quality for Class-D Audio Amplifiers using Tracking Power Supplies," *AES 138th Convention*, 2015.

D **Henrik Schneider**, Anders M. Madsen, Ruben Bjerregaard, Arnold Knott and Michael A. E. Andersen, "Validation of Power Requirement Model for Active Loudspeakers," *AES 138th Convention*, 2015.

E **Henrik Schneider**, Lasse Crone Jensen, Lars Press Petersen, Arnold Knott and Michael A. E. Andersen, "Requirements Specication for Ampliers and Power Supplies in Active Loudspeakers," *AES 137th Convention*, 2014.

F **Henrik Schneider**, Lars Press Petersen, Arnold Knott and Michael A. E. Andersen, "Power Requirements of Sound Systems," *Draft ready for submission to Journal of the Audio Engineering Society (JAES) 2015.*

G **Henrik Schneider**, Finn Agerkvist, Arnold Knott and Michael A. E. Andersen, "Multitone distortion in voltage and current driven loudspeaekers," *Draft ready for submission to Journal of the Audio Engineering Society (JAES) 2015.*

H **Henrik Schneider**, Thomas Andersen, Arnold Knott and Michael A. E. Andersen, "Hybrid winding concept for toroids," in *Proc. 2013 IEEE Energy Conversion Congress and Exposition ASIA (ECCE ASIA 2013)*, Jun. 2013, pp. 936–940.
→ *Best Paper Award*

I **Henrik Schneider**, Thomas Andersen, Arnold Knott and Michael A. E. Andersen, "Optimizing dc-resistance of a foil wounded toroidal inductor combining matlab and comsol," in *Proc. 2013 IEEE AFRICON*, 'Sept. 2013, pp. 1–5.

J **Henrik Schneider**, Thomas Andersen, Jacob Døllner Mønster, Mickey Madsen, Arnold Knott and Michael A. E. Andersen, "Investigation of a Hybrid Winding Concept for Toroidal Inductors using 3D Finite Element Modeling," *Comsol Conference*, '2013.
→ *Invited paper*

K **Henrik Schneider**, Thomas Andersen, Jacob Døllner Mønster, Mickey Madsen, Arnold Knott and Michael A. E. Andersen, "Optimizing Inductor Winding Geometry for Lowest DC-Resistance using LiveLink between COMSOL and MATLAB," *Comsol Conference*, '2013.
→ *Invited paper*

L Prasanth Thummala, **Henrik Schneider**, Zhe Zhang, Ziwei Ouyang, Arnold Knott and Michael A. E. Andersen, "Efficiency Optimization by Considering the High Voltage Flyback Transformer Parasitics using an Automatic Winding Layout Technique," *IEEE Trans. Power Electronics*, DOI: 10.1109/TPEL.2014.2379439, 2014.

M Presanth Thummula, **Henrik Schneider**, Zhe Zhang, Michael A. E. Andersen and Sarban Rahimullah, "A new Incremental Actuator based on Electro Active Polymer: Conceptual, Control and Driver Design Considerations," *IEEE Transactions on Mechatronics*, 2015.

N Presanth Thummula, **Henrik Schneider**, Zhe Zhang and Michael A. E. Andersen, "Bidirectional Flyback Converter with Multiple Series Connected Outputs for High Voltage Capacitive Charge and Discharge Applications," in *Proc. 2015 IEEE Applied Power Electronics Conference and Exposition (APEC 2015)*, Mar. 2015.

O **Henrik Schneider**, Prasanth Thummala, Lina Huang, Ziwei Ouyang, Arnold Knott, Zhe Zhang and Michael A. E. Andersen, "Investigation of transformer winding architectures for high voltage capacitor charging applications," in *Proc. 2014 IEEE Applied Power Electronics Conference and Exposition (APEC 2014)*, Mar. 2014, pp. 334–341.
→ *Best Session Presentation Award*

P Prasanth Thummala, **Henrik Schneider**, Zhe Zhang, Arnold Knott and Michael A. E. Andersen, "Optimization of bi-directional flyback converter for a high voltage capacitor charging application," in *Proc. 2014 IEEE Applied Power Electronics Conference and Exposition (APEC 2014)*, Mar. 2014, pp. 2556–2563.

Q Prasanth Thummala, **Henrik Schneider**, Zhe Zhang and Michael A. E. Andersen, "Estimation of Transformer Parameters and Loss Analysis for High Voltage Capacitor Charging Application," in *Proc. 2013 IEEE Energy Conversion Congress and Exposition ASIA (ECCE ASIA 2013)*, Jun. 2013, pp. 704–710.

Appendix A

Investigation of Current Driven Loudspeakers

138th Convention of the Audio Engineering Society 2015

Audio Engineering Society

Convention Paper

Presented at the 138th Convention
2015 May 7–10 Warsaw, Poland

Investigation of Current Driven Loudspeakers

Henrik Schneider[1], Finn Agerkvist[1], Arnold Knott[1], Michael A. E. Andersen[1]

[1] *Dept. of Electrical Engineering, Technical University of Denmark, Kongens Lyngby, DK-2800, Denmark*

Correspondence should be addressed to Henrik Schneider (`hensc@elektro.dtu.dk`)

ABSTRACT

Current driven loudspeakers have previously been investigated but the literature is limited and the advantages and disadvantages are yet to be fully identified. This paper makes use of a non-linear loudspeaker model to analyse loudspeakers with distinct non-linear characteristics under voltage and current drive. A multi tone test signal is used in the evaluation of the driving schemes since it resembles audio signals to a higher degree than the signals used in total harmonic distortion and intermodulation distortion test methods. It is found that current drive is superior over voltage drive in a 5" woofer where a copper ring in the pole piece has not been implemented to compensate for eddy currents. However the drive method seems to be irrelevant for a 5" woofer where the compliance, force factor as well as the voice coil inductance has been optimized for linearity.

1. INTRODUCTION

Traditionally loudspeakers are driven by voltage controlled amplifiers exhibiting low output impedance. The electromagnetic driving force acting on the diaphragm is however proportional to the coil current which is inversely proportional to the non-linear loudspeaker impedance in the case of voltage drive. Current controlled amplifiers exhibit a much higher output impedance than the loudspeaker impedance and thus changes in the voice coil resistance due to heating, changes in voice coil inductance as a function of the displacement and the contribution from the loudspeakers electro motive force (EMF) dos not have any effect on the electromagnetic driving force. Even though these are great benefits current drive was probably turned down since an individual filter is needed to dampen the mechanical resonance of the loudspeaker unit adding complexity and cost to the electronic implementation as indicated in this paper from 1943 [1]. A static filter is unfortunately not sufficient since the mechanical resonance of a loudspeaker can drift due to ageing of the suspensions components, due to production variance, temperature change and so on. Other research has dealt with mechanical damping and electrical damping by advanced amplifier control to alleviate this problem [2, 3]. Another disadvantage of

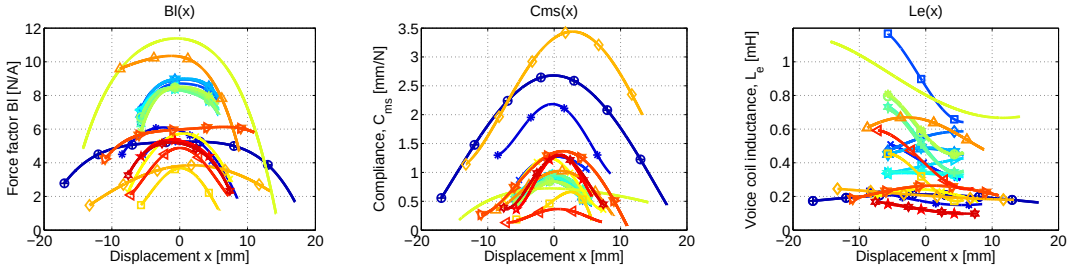

Fig. 1: Example of non-linearites as a function of displacement for 25 different 5" woofers

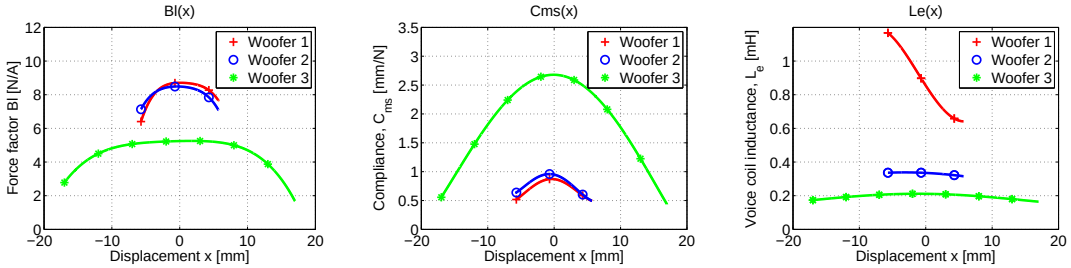

Fig. 2: Example of non-linearites as a function of displacement for 25 different 5" woofers

current drive is the requirement of an extra circuity to deal with a no-load situation and while this isn't a problem in many present audio applications where the amplifier and loudspeaker is integrated in a single unit, historically this was a disadvantage due to interchangeable demands of the amplifier and loudspeakers. Current controlled amplifiers are simple to implement in existing amplifier topologies controlling the voltage and in fact some voltage controlled amplifiers already have an inner current feedback loop [2]. As indicated by Klippel [4], other critical non-linearities such as the displacement dependent compliance and force factor dominate at lower frequencies where current control dos not have a strong impact. In [5–7], motional feedback was combined with current drive to deal with the non-linearities and at the same time deal with the previously mentioned damping issue inflicted by current drive. Recent publications questions the voltage drive principle and compare it to current drive [8–11]. Only in [8,9] a comparison related to distortion of different types of loudspeaker units from woofers to microspeakers is found. In this work the limited evaluation of current drive is expanded by analysis of three 5" woofers with distinct non-linear characteristics. A model of voltage and current drive of the woofers is implemented and a static filter is utilized to enable comparison of the drive methods. Even though a static filter can not be used in a real application because of the drifting issue mentioned previously this is not the case for the model. The model can be used to examine the potential of current drive before a great effort is put into the actual implementation.

2. LOUDSPEAKER MODELLING

Large signal measurements performed with the Klippel analyzer [12] of 25 individual 5" loudspekaer drivers was collected for this work. As seen in figure 2 the measured force factor Bl, compliance C_{ms} and voice coil inductance L_e as a function of displacement x show a huge deviation in both level and form. The benefit of each driving scheme will also deviate and . Eleven of the woofers originates from a study of eddy current compensation (with different implementations of copper and aluminium rings in the pole piece) and thus exhibit nearly the same force factor and compliance characteristics.

In this work two of the eleven woofers from this study is chosen to represent a woofer with and without eddy current compensation. A third driver is chosen because of a flat force factor, a soft and symmetric compliance and a low and flat voice coil inductance which are characteristics that are expected to result in very low distortion. The chosen woofers will be referred to as woofer 1, 2 and 3 respectively in the rest of this paper. Their non-linear characteristics are shown in figure **??**. The displacement was limited to the maximum displacement x_{MAX} of woofer 1 and 2 during the examination. In this displacement span it is noted that the voice coil inductance of woofer 1 is very displacement sensitive and that the characteristics of woofer 3 are less sensitive to displacement and are more symmetric in comparison to woofer 1 and 2.

The loudspeaker models used in this work are based on the fundamental loudspeaker equations

$$u(t) = R_e i(s) + sL_e i(s) + \frac{R_2 sL_2}{R_2 + sL_2} i(s) + sBlx(s)$$

$$F(s) = Bl \cdot i(s) \tag{1}$$

$$F(s) = M_{ms} s^2 x(s) + R_{ms} s x(s) + \frac{1}{C_{ms}} x(s)$$

2.1. Impedance

The electromagnetic driving force is inversely proportional to the impedance in voltage drive. An investigation of the impedance variance as a function of displacement is therefore relevant and has been performed in this work. In (2) the impedance is derived based on (1). Bl, C_{ms} and L_e are made dependent on the displacement x and the impedance for the 3 chosen woofers are illustrated in figure 3 by varying x from -5.7 mm to +5.7 mm in incremental steps. This is equivalent to a small signal analysis at various displacement offsets. From this analysis it is expected that woofer 3 will be less effected by the driving scheme.

$$Z_{load}(s) = \frac{u(s)}{i(s)} = R_e + sL_e(x) + \frac{R_e sL_2}{R_e + sL_2} + \frac{Bl(x)^2}{sM_{ms} + R_{ms} + \frac{1}{sC_{ms}(x)}} \tag{2}$$

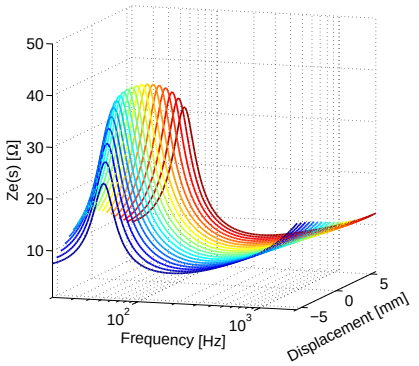

(a) Woofer 1: Without copper ring

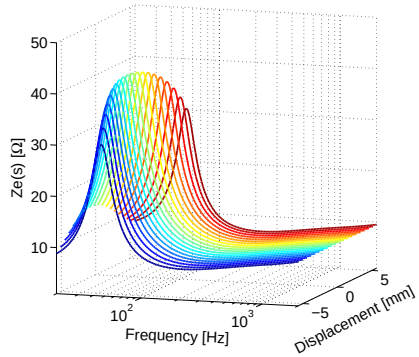

(b) Woofer 2: With copper ring

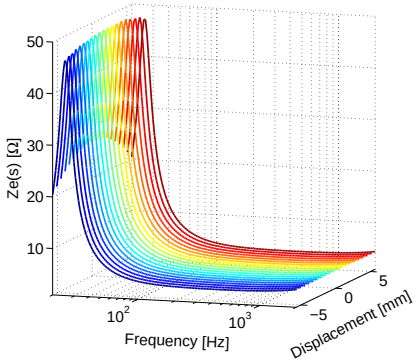

(c) Woofer 3: With very linear characteristics

Fig. 3: Non-linear impedance variation as a function of displacement

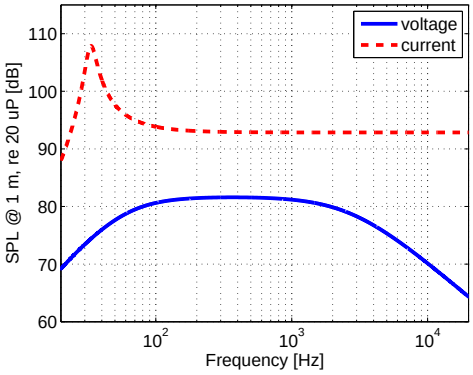

Fig. 4: SPL's with voltage and current drive

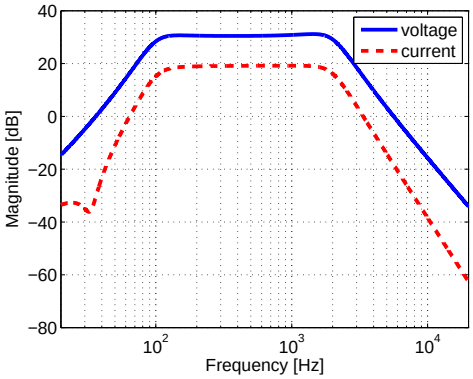

Fig. 5: Applied filter

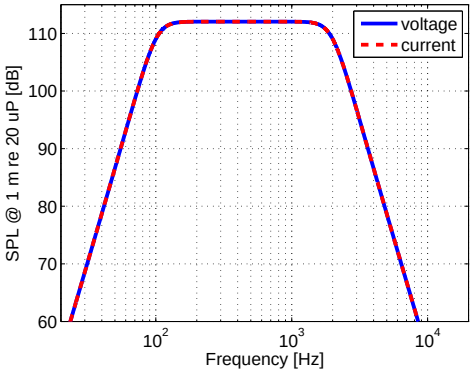

Fig. 6: Resulting 4th order bandpass response

2.2. Sound pressure level

The fundamental equations in (1) can be used to derive the transfer functions from voltage to acceleration and from current to acceleration respectively

$$Z_{(a/v)} = \frac{Bls^2}{Bl^2 s + (sL_e + R_e)(s^2 M_{ms} + sR_{ms} + \frac{1}{C_{ms}})}$$

$$Z_{(a/i)} = \frac{Bls^2}{(s^2 M_{ms} + sR_{ms} + \frac{1}{C_{ms}})} \quad (3)$$

It is noted that the acceleration due to current drive is independent of L_e, R_e and less independent of Bl. The acceleration is proportional to the sound pressure level (SPL) and the resulting SPL of voltage and current drive is shown in figure 4. The characteristic peak in the frequency response around the resonant frequency of the loudspeaker using current drive is evident. The amplitude of the sinusoidal signal used to calculate the SPL's were 1 for both voltage and current drive which explains the difference in SPL's. In order to compare voltage and current drive the power applied to the woofer in both driving schemes have to be equalized, thus the SPL's have to match. This is achieved using the filter shown in figure 5 and by applying the filter the resulting SPL's optain the form of a 4th order bandpass filter as shown in figure 6. The chosen bandpass characteristic resembles a typical crossover design for a woofer in a 2 way loudspeaker. Implementation of the filters makes it possible to use a signal with the same amplitude as input for both voltage and current drive and it enables comparison of the two driving schemes. The filters are designed to obtain a maximum displacements just bellow x_{MAX} (determined by the Klippel measurement).

3. DISTORTION ANALYSIS

The models used to predict the distortion due to the woofer non-linearities are implemented in matlab simulink. The models are inspired by [8, 9]. The input stimuli consists of 10 sinusoidal signals with equal amplitude spread over a frequency range of 20 Hz to 2 kHz. In figure 9 the output spectrum

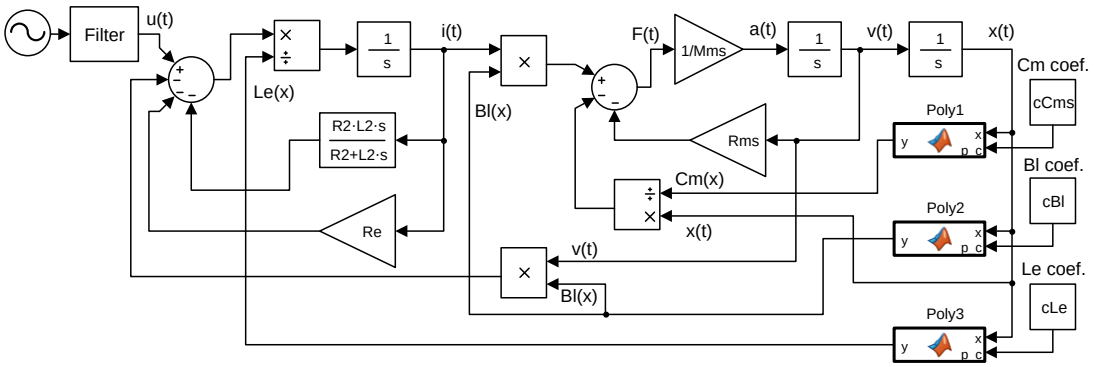

Fig. 7: Simulink model of voltage driven transducer

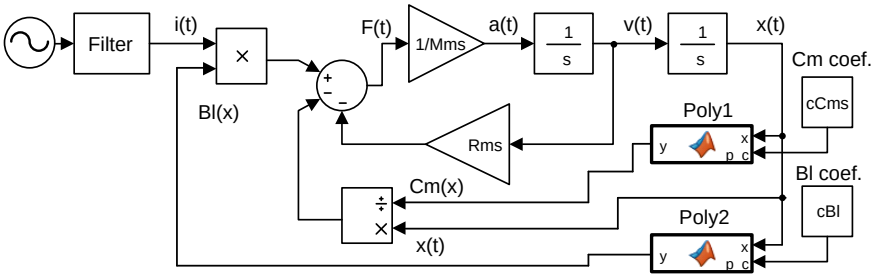

Fig. 8: Simulink model of current driven transducer

caused by low displacements (around ± 2.7 mm) and high displacements (around ± 5.7 mm) are shown for Woofer 1, 2 and 3.

In figure 9.a and figure 9.d, the advantage of current drive is clearly seen at both displacement levels for Woofer 1 since the distortion is significantly reduced. At high displacement level even Woofer 2 with low variance in voice coil inductance has an advantage of current drive as seen in figure 9.e but at lower displacements only a small difference is observed as seen in figure 9.b. In the case of woofer 3 the driving scheme seems irrelevant as seen in figure 9.c and 9.f. These results support the predicted performance based on plots of the impedance as a function of displacement.

4. FUTURE WORK

Future works should investigate the advantages of current drive for loudspeaker drivers used in a higher frequency range above the resonant frequency such as fulltone units and tweeters. The model of the tweeter should be expanded to include the nonlinear viscous damping Rms. Furthermore electronic damping at the resonance frequency could be considered using amplifier control techniques. And finally the real cost-benefit should be experimentally verified.

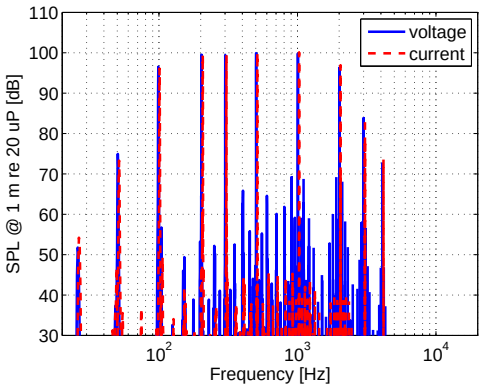

(a) Woofer 1 ($x_{MAX} = \pm$ 2.7 mm)

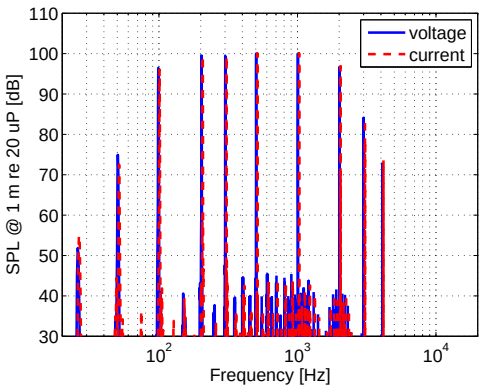

(b) Woofer 2 ($x_{MAX} = \pm$ 2.7 mm)

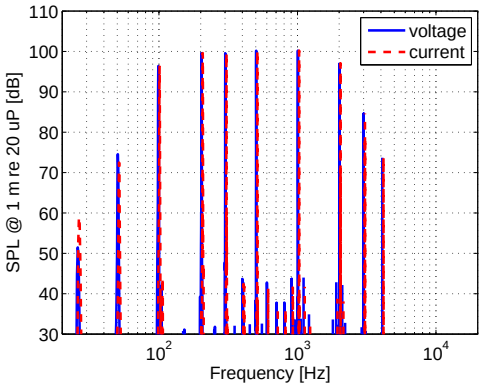

(c) Woofer 3 ($x_{MAX} = \pm$ 2.7 mm)

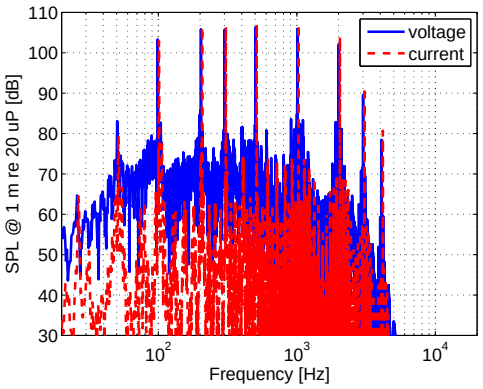

(d) Woofer 1 ($x_{MAX} = \pm$ 5.7 mm)

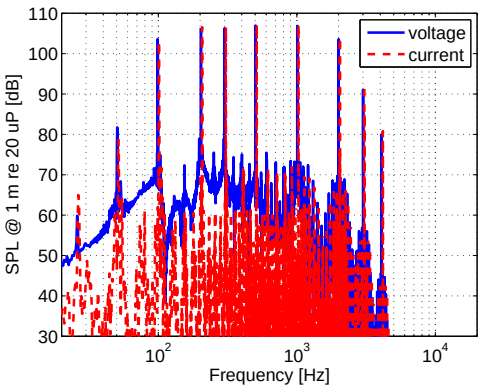

(e) Woofer 2 ($x_{MAX} = \pm$ 5.7 mm)

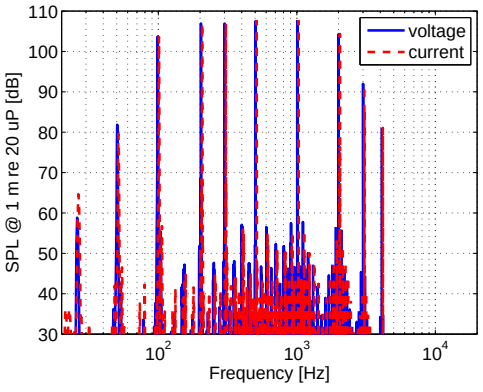

(f) Woofer 3 ($x_{MAX} = \pm$ 5.7 mm)

Fig. 9: Distortion analysis

5. CONCLUSION

This paper present a comparison of voltage and current drive for 3 distinct 5 inch woofers. A non-linear Matlab Simulink model including the major displacement related non-linear distortions is implemented including a loudspeaker specific filter to obtain a target response. It is found that current drive is superior to voltage drive in the case where the voice coil inductance is non-linear due to eddy currents. It seems that voltage drive is sufficient for loudspeakers where a shorting ring is implemented to reduce the eddy current effect and even more so if the compliance and the force factor has been optimized for linearity. Current drive is a welcome low cost alternative to shorting rings, since the cost of current controlled amplifiers is not expected to increase.

6. ACKNOWLEDGEMENT

The authors wish to thank PointSource Acoustics A/S who contributed with their loudspeaker expertise and helped with the non-linear characterisation of the loudspeaker drivers.

7. REFERENCES

[1] E. Schulz, "Comparison of voltage-and current-feedback amplifiers," *Proceedings of the IRE*, vol. 31, no. 1, pp. 25–28, 1943.

[2] P. Adduci, E. Botti, E. Dallago, and G. Venchi, "Pwm power audio amplifier with voltage/current mixed feedback for high-efficiency speakers," *Industrial Electronics, IEEE Transactions on*, vol. 54, no. 2, pp. 1141–1149, 2007.

[3] R. Bortoni, H. S. Silva, *et al.*, "Effects of acoustic damping on current-driven loudspeakers," in *Audio Engineering Society Convention 122*, Audio Engineering Society, 2007.

[4] W. Klippel, "Active compensation of transducer nonlinearities," in *Audio Engineering Society Conference: 23rd International Conference: Signal Processing in Audio Recording and Reproduction*, Audio Engineering Society, 2003.

[5] R. A. Greiner and T. M. Sims Jr, "Loudspeaker distortion reduction," *Journal of the Audio Engineering Society*, vol. 32, no. 12, pp. 956–963, 1984.

[6] P. G. Mills and M. J. Hawksford, "Transconductance power amplifier systems for current-driven loudspeakers," *Journal of the Audio Engineering Society*, vol. 37, no. 10, pp. 809–822, 1989.

[7] P. G. Mills and M. J. Hawksford, "Distortion reduction in moving-coil loudspeaker systems using current-drive technology," *Journal of the Audio Engineering Society*, vol. 37, no. 3, pp. 129–148, 1989.

[8] E. Sturtzer, G. Pillonnet, G. Lemarquand, and N. Abouchi, "Comparison between voltage and current driving methods of a micro-speaker," *Applied Acoustics*, vol. 73, no. 11, pp. 1087–1098, 2012.

[9] G. Pillonnet, E. Sturtzer, T. Rossignol, P. Tournier, and G. Lemarquand, "Distortion improvement in the current coil of a loudspeaker," in *Audio Engineering Society Convention 134*, Audio Engineering Society, 2013.

[10] R. Bortoni, S. Noceti Filho, and R. Seara, "Comparative analysis of moving-coil loudspeakers driven by voltage and current sources," in *Audio Engineering Society Convention 115*, Audio Engineering Society, 2003.

[11] E. Merilainen, *Current-driving of loudspeakers: eliminating major distortion and interference effects by the physically correct operation method*. Esa Meriläinen, 2010.

[12] W. Klippel, "Direct feedback linearization of nonlinear loudspeaker systems," *Journal of the Audio Engineering Society*, vol. 46, no. 6, pp. 499–507, 1998.

Appendix B

Design and evaluation of accelerometer based motional feedback

138th Convention of the Audio Engineering Society 2015

Audio Engineering Society

Convention Paper

Presented at the 138th Convention
2015 May 7–10 Warsaw, Poland

Design and Evaluation of Accelerometer based Motional Feedback

Henrik Schneider[1], Emilio Pranjic[1], Finn Agerkvist[1], Arnold Knott[1], Michael A. E. Andersen[1]

[1] *Dept. of Electrical Engineering, Technical University of Denmark, Kongens Lyngby, DK-2800, Denmark*

Correspondence should be addressed to Henrik Schneider (hensc@elektro.dtu.dk)

ABSTRACT

The electro dynamic loudspeaker is often referred to as the weakest link in the audio chain due to low efficiency and high distortion levels at low frequencies and high diaphragm excursion. Compensating for loudspeaker non-linearities using feedback or feedforward methods can improve the distortion and enable radical design changes in the loudspeaker which can lead to efficiency improvements. In combination this has motivated a revisit of the accelerometer based motional feedback technique. Experimental results on a 8 inch subwoofer show that the total harmonic distortion can be significantly reduced at low frequencies and large displacements.

1. INTRODUCTION

In 1973 Edward R. Hanson from Phillips [1] stated the most important loudspeaker conditions to comply with being

- Size as small as possible
- Frequency response as wide as possible
- Frequency response as flat as possible
- Distortion as little as possible
- Efficiency and power handling capability must be considered

Back then the size condition was stressed by the advent of 4 channel sound and today this condition is still actual with the advent of 3D sound which require 12 loudspeakers in a 7.1.4 set up. A small transducer will have to move the diaphragm further to provide the same sound pressure level compared to a larger transduceer and this tends to increase the distortion due to displacement dependent non-linearities of the compliance, the force factor and the self inductance [2]. Further more a small loudspeaker enclosure will have a high impedance which will limit the low frequency range resulting in a narrow and non flat frequency response if no action is taken. It was noted that the efficiency and power-handling capability must be considered

in any attempt to correct these problems. Today, efficient and powerful class-D amplifiers and switch mode power supplies are up for this task.

The distortion and frequency response can be corrected by equalization combined with motional feedback (MFB) or model based feedforward methods. Feedforward methods have received a lot of focus in recent years due to advances in digital processors, loudspeaker characterization methods and loudspeaker modelling [3–5]. Feedforward compensation avoids a motional sensor but requires an accurate model of the loudspeaker that is able to adapt to time drifting loudspeaker parameters, and non-linearities [6]. Even though feedforward compensation has come a long way and seems very promising the alternative MFB technique is revisited in this work. The output or motion of the loudspeaker can either be captured as acceleration [1, 7, 8], velocity [9–14], pressure [15] or position [16–18]. MFB is normally implemented on closed box systems because only a single sensor is necessary to sense the output. Attempts with higher order systems including passive radiators has also been successfully implemented [19]. In [20–22] MFB was alternatively used to control the undamped mechanical resonance of a current driven loudspeakers. Loudspeaker protection using feedforward or feedback has also been proposed [23, 24].

2. CONTROL THEORY

A block diagram of the control scheme used in this work is shown in figure 1. The design of the controller is based on the transfer function of the Plant which consist of an amplifier, a loudspeaker and an accelerometer. The Feedback applies a gain to control the level of feedback compared to the input level.

2.1. Class-d amplifier

The class-D amplifier can be modeled as a 2nd order butterworth filter given by

$$G_{amp} = \frac{G_0 \omega_c^2}{s^2 + \sqrt{2}\omega_c s + \omega_c^2} \tag{1}$$

where

$$\omega_c = 2\pi f_c = \frac{1}{\sqrt{L_f C_f}} \tag{2}$$

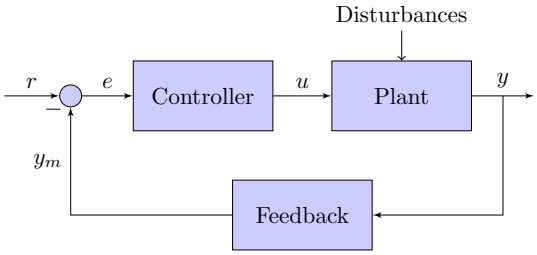

Figure 1: Block diagram of negative feedback

2.2. Loudspeaker

The transfer function from voltage to acceleration given in equation (3) is derived from the well known equations (4) of the lumped loudspeaker model [5].

$$G_{(a/v)} = \frac{Bls^2}{Bl^2 s + (sL_e + R_e)(s^2 M_{ms} + sR_{ms} + \frac{1}{C_{ms}})} \tag{3}$$

$$\begin{aligned} u(s) &= R_e i(s) + sL_e i(s) + sBlx(s) \\ F(s) &= Bl \cdot i(s) \\ F(s) &= M_{ms} s^2 x(s) + R_{ms} s x(s) + \frac{1}{C_{ms}} x(s) \end{aligned} \tag{4}$$

R_e and L_e are electrical resistance and inductance, Bl is the force factor, M_{ms}, Rms and C_{ms} are respectively the mechanical mass, resistance and compliance.

2.3. Sensor

The accelerometer has a bandwidth of 10 kHz and a sensitivity of 6.7 mV/G with a supply voltage of 5 V. The accelerometer can be modelled as a 2nd order peaking low-pass filter with a peak located around 21 kHz, and a peaking magnitude of 7 dB.

2.4. Control

A bode plot of the Plant which consist of $G_{amp} \cdot G_{v/a} \cdot G_{sens}$ is shown in figure 3. As seen the magnitude of the Plant needs to be raised at low frequencies in order to obtain a higher loop gain at lower frequencies. The controller consists of two

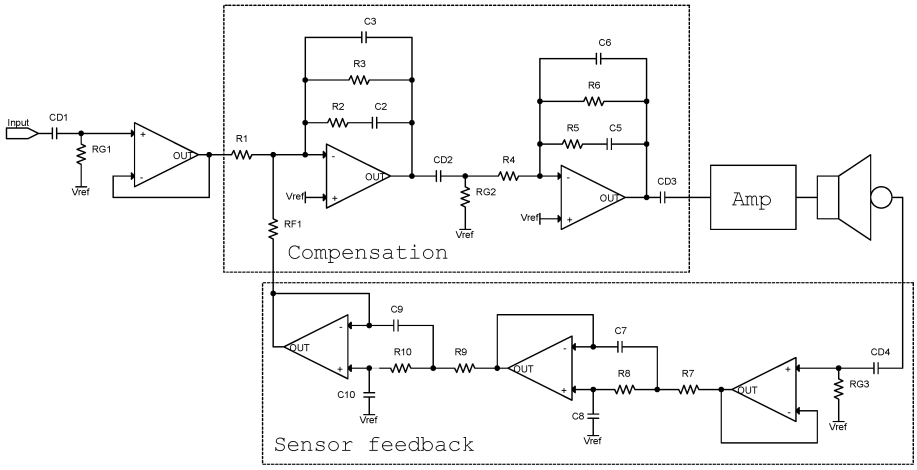

Figure 2: Simplified schematic.

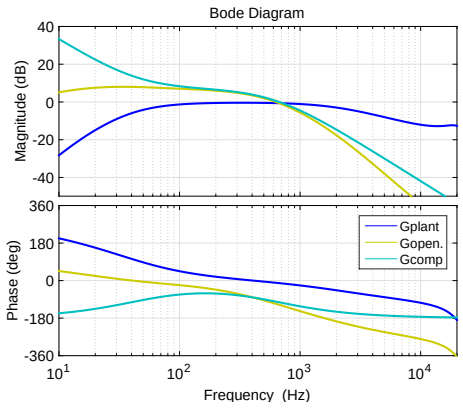

Figure 3: System transfer functions

poles at DC, 2 zeroes at the lower cut-off frequency of the Plant and 2 poles at 600 Hz. This is done to attenuate noise and high frequency break up modes of the cone as seen in the sound pressure level measurement in figure 5a.

The compensation transfer function is given by

$$G_{comp} = K_c \frac{(\tau_{z1}s+1)(\tau_{z2}s+1)}{(\tau_{p1}s)(\tau_{p2}s)}, \tau_{z,p} = \frac{1}{2\pi f_{z,p}} \quad (5)$$

The resulting open loop transfer function G_{open} is plotted in figure 3. It resembles a low-pass characteristic with an open loop phase margin of around 70 degrees at 630 Hz.

3. EXPERIMENTAL WORK

The transducer used during this work is an 8" woofer, HiVi-M8N. The cone of the transducer is an aluminium/magnesium blend, which gives a light weight and stiff cone. Severe breakup modes appear from 1 kHz and up as seen in figure 5a. The sensor is implemented with an of the shelf one-axis accelerometer from Analog Devices (ADXL001-250BEZ) that can handle up to 250 G and provides a 10 kHz bandwidth. The accelerometer is glued to the center of the transducer, figure 4a. Small wires run from the accelerometer to the printed circuit board (PCB) connecting supply voltage, ground, and the output signal of the accelerometer. The wires goes in a soft arc from the accelerometer to the loudspeaker frame to avoid bending stress on the wires.

3.1. Implementation

It is out of scope to fully describe the analogue design and implementation of the MFB scheme. However figure 2 can be used to get a rough idea of the implementation. V_{ref} is a bias voltage, equal

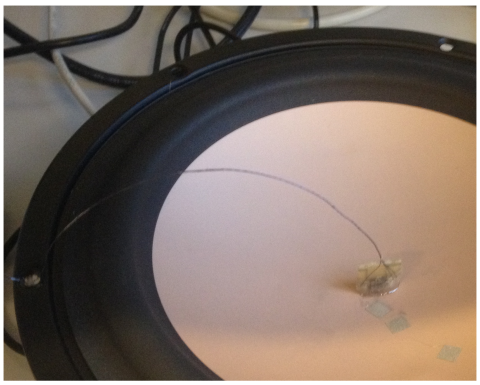

(a) Loudspeaker with attached accelerometer.

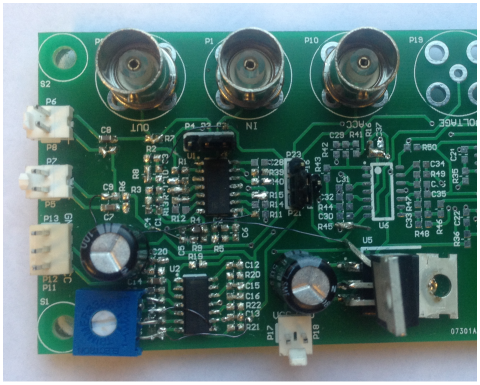

(b) Control PCB prototype.

Figure 4: Hardware

to half of the supply voltage of the operational amplifiers. The operational amplifiers use a single supply voltage of +12 V. Figure 4b shows a picture of the prototype. Three BNC connecters are mounted on the PCB to be able to measure the input signal, the output signal (signal to amplifier) and the output of the accelerometer. A set of jumpers makes it possible to enable/disable the controller and the MFB.

The gain G_0, as described in equation 1, of the used amplifier is 20 and the cut-off frequency is $61kHz$. It is noted that the accelerometer has a relatively high noise floor at low accelerations. Two series connected 2nd order butterworth low-pass filters are therefore utilized and they are modelled with (1). The gain is set to 1.5 and the cut-off frequency is set to 600 Hz.

3.2. Sensor verification

A Polytec Doppler laser is used to investigate the influence of the accelerometer mounted to the cone. The sound pressure response is measured with and without the accelerometer mounted on the speaker cone, figure 5a. It is found that the response is not affected particularly until around 1 kHz. Since the design is intended for a subwoofer, this is beyond the required frequency range.

Laser measurements were also used to verify the

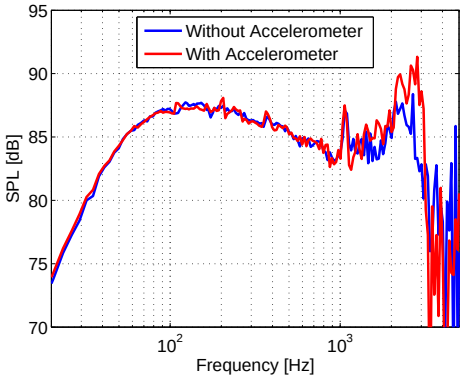

(a) Loudspeaker SPL response.

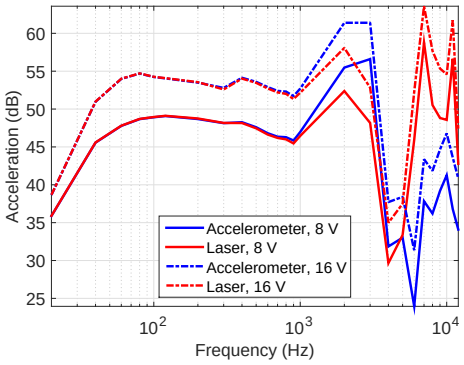

(b) Comparison of accelerometer and laser measurements.

Figure 5: Validation of accelerometer

output of the accelerometer. A comparison of laser and accelerometer measurements at different voltage levels is shown in figure 5b. The measurements show a very good coherence up to around 900 Hz. The bandwidth of the controller was chosen to be lower than 900 Hz based on this observation.

3.3. Results

A comparison of a 20 Hz measurement with and without MFB can be seen in figure 6a and 6b. As seen in figure 6a the harmonics are lowered and the THD is improved by more than 2 times from 54.9 % to 20.6 %. Figure 6b illustrates the time domain signals where it is clearly seen that the distortion has been improved greatly with MFB.

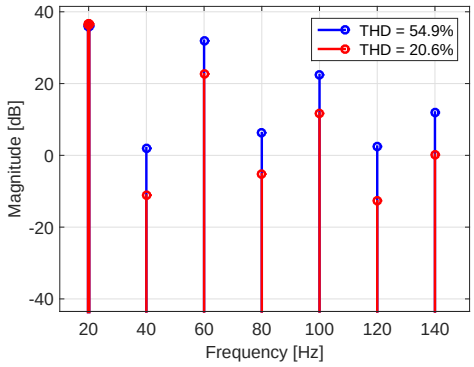

(a) Spectrum comparison of acceleration with (RED) and without (BLUE) MFB measured with laser.

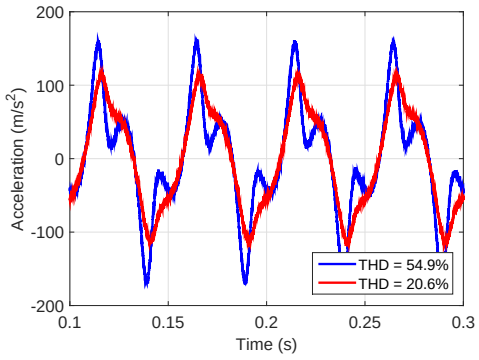

(b) Time comparison of acceleration with (RED) and without (BLUE) MFB measured with laser.

Figure 6: 20 Hz and 8 V_{RMS} comparison

Frequency (Hz)	THD w/o. / w. (%)		
	$2\,V_{rms}$	$4\,V_{rms}$	$8\,V_{rms}$
20	5.3 / 1.2	15.0 / 3.7	54.9 / 20.6
30	2.4 / 0.8	5.6 / 1.8	22.0 / 6.7
40	1.3 / 0.7	2.5 / 1.2	7.0 / 2.8
50	0.9 / 0.7	1.5 / 1	3.2 / 1.7

Table 1: Laser THD Measurements Without and With Compensation

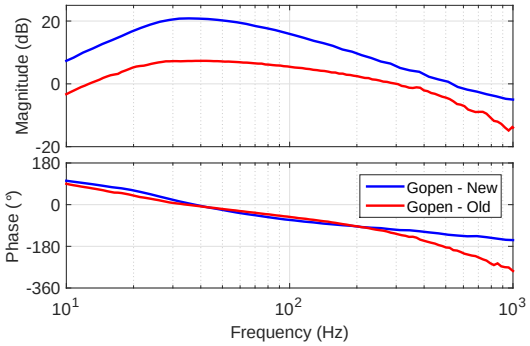

Figure 7: Measured original (RED) and improved (BLUE) open loop response

Frequency (Hz)	THD w/o. / w. (%)		
	$2\,V_{rms}$	$4\,V_{rms}$	$8\,V_{rms}$
20	5.3 / 1.1	15.0 / 1.3	54.9 / 9.1
30	2.4 / 0.4	5.6 / 0.5	22.0 / 2.1
40	1.3 / 0.3	2.5 / 0.5	7.0 / 1.6
50	0.9 / 0.5	1.5 / 0.8	3.2 / 0.5

Table 2: Improved Laser THD Measurements Without and With Compensation

In table 1 the THD at low frequencies with and without MFB are shown at different voltage levels. The magnitude of the open loop response will drop at low frequencies and high excursions due to the non-linear behaviour of the loudspeaker which

was not accounted for in the small signal analysis. In order to improve the open loop gain at lower frequencies an integrator was added to the control circuit. A comparison of the old and new open loop response is shown in figure 7. New laser measurements where performed and the improved results are listed in table 2. The THD is improved over the whole measuring range and at 20 Hz and 8 V_{RMS} the THD is lowered by more than 5 times.

4. FUTURE WORK

In future work the MFB could be limited as a function of displacement in order to improve the signal to noise ratio. Listening tests and transient response should also be performed in order to reveal the full acoustical potential of MFB. As mentioned previously the power requirement will increase when the transducer is forced to deliver a certain frequency response which is the case with MFB. The power requirement and protection must thus also be investigated. The sound quality and power requirements vs. enclosure size is another interesting topic to explore. A digital implementation would probably be advantageous in terms of added functionality. The added cost of the MFB implementation may be compensated for by cost savings on the transducer, since the linear requirements of the transducer is lowered.

5. CONCLUSION

Accelerometer based MFB of an 8 inch woofer is designed and validated. Experimental results show that the accelerometer is useful as a sensor and the feedback loop was successfully implemented. The worst case THD was substantially reduced by more than 5 times. The full potential of motional feedback in terms of transient response, perceived sound quality, cost and power requirements is still to be revealed.

6. REFERENCES

[1] E. R. Hanson, "A motional feedback loudspeaker system," in *Audio Engineering Society Convention 46*, Audio Engineering Society, 1973.

[2] W. Klippel, "Prediction of speaker performance at high amplitudes," in *Audio Engineering Society Convention 111*, Audio Engineering Society, 2001.

[3] J. Suykens, J. Vandewalle, and J. Van Ginderdeuren, "Feedback linearization of nonlinear distortion in electrodynamic loudspeakers," *Journal of the audio engineering society*, vol. 43, no. 9, pp. 690–694, 1995.

[4] H. Schurer, *Linearization of electroacoustic transducers*. University of Twente, 1997.

[5] W. Klippel, "Direct feedback linearization of nonlinear loudspeaker systems," *Journal of the Audio Engineering Society*, vol. 46, no. 6, pp. 499–507, 1998.

[6] A. Bright, "Tracking changes in linear loudspeaker parameters with current feedback," in *Audio Engineering Society Convention 115*, Audio Engineering Society, 2003.

[7] M. A. Beerling, C. H. Slump, and O. E. Hermann, "Reduction on nonlinear distortion in loudspeakers with digital motional feedback," in *Audio Engineering Society Convention 96*, Audio Engineering Society, 1994.

[8] R. Valk, "Control of voice coil transducers," Master's thesis, TU Delft University of Technology, The Netherlands, 2013.

[9] H. Holdaway, "Design of velocity-feedback transducer systems for stable low-frequency behavior," *Audio, IEEE Transactions on*, no. 5, pp. 155–173, 1963.

[10] C.-Y. Chen, G. T. Chiu, C. Cheng, and H. Peng, "Passive voice coil feedback control of closed-box subwoofer systems," *Proceedings of the Institution of Mechanical Engineers, Part C: Journal of Mechanical Engineering Science*, vol. 214, no. 7, pp. 995–1005, 2000.

[11] S. A. Lane and R. L. Clark, "Improving loudspeaker performance for active noise control applications," *Journal of the Audio Engineering Society*, vol. 46, no. 6, pp. 508–519, 1998.

[12] Y. Li and G.-C. Chiu, "Control of loudspeakers using disturbance-observer-type velocity estimation," *Mechatronics, IEEE/ASME Transactions on*, vol. 10, no. 1, pp. 111–117, 2005.

[13] E. De Boer, "Theory of motional feedback," *Audio, IRE Transactions on*, no. 1, pp. 15–21, 1961.

[14] C. Peplinski and A. Miller, "Motional voltage as a distortion mechanism in loudspeakers," in *Audio Engineering Society Convention 99*, Audio Engineering Society, 1995.

[15] F. Blasizzo, P. Desii, M. Di Cola, and C. Lastrucci, "Practical applications of a closed feedback loop transducer system equipped with differential pressure control," in *Audio Engineering Society Convention 131*, Audio Engineering Society, 2011.

[16] D. Birt, "A motion transducer for low-frequency loudspeakers," in *Audio Engineering Society Convention 91*, Audio Engineering Society, 1991.

[17] W. Geiger, "Servo control of loudspeaker cone motion using an optical linear displacement sensor," *Journal of the Audio Engineering Society*, vol. 53, no. 6, pp. 518–524, 2005.

[18] F. A. Medrano, "Optical Position Sensors with Applications in Servo Feedback Subwoofer Control," Master's thesis, University of California, USA, 2009.

[19] S. Willems and G. D?Hoogh, "On the use of motion feedback as used in 4th order systems," in *Audio Engineering Society Convention 126*, Audio Engineering Society, 2009.

[20] R. A. Greiner and T. M. Sims Jr, "Loudspeaker distortion reduction," *Journal of the Audio Engineering Society*, vol. 32, no. 12, pp. 956–963, 1984.

[21] P. G. Mills and M. J. Hawksford, "Transconductance power amplifier systems for current-driven loudspeakers," *Journal of the Audio Engineering Society*, vol. 37, no. 10, pp. 809–822, 1989.

[22] P. Robineau and M. Rossi, "Current-controlled vented-box loudspeaker system with motional feedback," in *Audio Engineering Society Convention 108*, Audio Engineering Society, 2000.

[23] C. Bortoni, R. Bortoni, S. Noceti Filho, and R. Seara, "Real-time voice-coil temperature and cone displacement control of loudspeakers," in *Audio Engineering Society Convention 117*, Audio Engineering Society, 2004.

[24] Y.-T. Tsai and J. H. Huang, "The dynamics detection and processing method for preventing large displacement transducer damage problem," in *Audio Engineering Society Convention 137*, Audio Engineering Society, 2014.

Appendix C

Investigation of Energy Consumption and Sound Quality for Class-D Audio Amplifiers using Tracking Power Supplies

---

138th Convention of the Audio Engineering Society 2015

Audio Engineering Society
Convention Paper

Presented at the 138th Convention
2015 May 7–10 Warsaw, Poland

Investigation of Energy Consumption and Sound Quality for Class-D Audio Amplifiers using Tracking Power Supplies

Akira Yamauchi[1], Henrik Schneider[1], Arnold Knott[1], Ivan H.H. Jørgensen[1] and Michael A.E. Andersen[1]

[1] Technical University Denmark 2800 Kgs. Lyngby, Denmark

Correspondence should be addressed to Akira Yamauchi (afuno1@gmail.com)

ABSTRACT

The main advantage of Class-D audio amplifiers is high efficiency which is often stated to be more than 90 % but at idle or low power levels the efficiency is much lower. The waste energy is an environmental concern, a concern in mobile applications where long battery operation is required and a concern in other applications where multiple amplifier channels are generating heat problems. It is found that power losses at low power levels account for close to 78 % of the energy consumption based on typical consumer behavior investigations. This paper investigates the theoretical limits of stepless power supply tracking and its influence on power losses, audio performance and environmental impact for a 130 W class-D amplifier prototype as well as a commercialized class-D amplifier. Both modeled and experimental results verify that a large improvement of efficiency can be achieved. The total harmonic is found to be unaffected by stepless power supply tracking due the high supply rejection ratio of the used amplifiers under test.

1. INTRODUCTION

Class-D audio amplifiers have a great advantage in high power efficiency over traditional linear amplifier designs [2, 3, 4, 5, 6]. With the major trends in power electronics towards decreasing energy consumption, this technology is promising since the maximum efficiency improves along with advances in the power semiconductor technology towards its inherent theoretical efficiency of 100 %. On the other hand, the efficiency advantage is relatively poor at idle and low power levels as confirmed in a measurement (Fig. 1), which is not usually emphasized on published data where a linear scale is commonly used [17]. The energy consumption in a specific case is therefore considered to shed light on the environmental impact of this efficiency characteristic.

The amplifier energy consumption in a given period of time is an important parameter because it affects requirements specification for a preceding power supply, or system cost. However, there is only little correlation between the power efficiency (Fig. 1) and

the energy consumption. The power efficiency is typically specified at a certain constant output power, while the energy consumption depends on consumer behavior, that is, a distribution of volume positions and music contents over a given period of time.

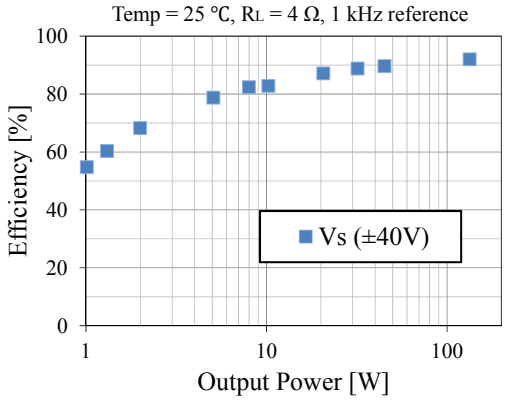

Fig. 1: Measured power efficiency of a 130W class-D amplifier vs output power (4 Ω) with 1 kHz reference signal under the supply voltage, Vs = ±40 V.

From previous research [4, 7], generalized distribution of volume control positions in time and corresponding output power which is categorized by four subjective listening levels is recalled. In order to make it more specific in this paper, the case of a 130 W class-D power amplifier is considered based on the measurement (Fig. 1). Accordingly, the energy consumptions are calculated and summarized (Table 1).

Due to the fact that the amplifier operates at the subjective "background" level most of the time, it is obvious that the power efficiency at low power (at 1.3 W peak power) leads to the main cause of the energy consumption which accounts for close to 78 %. On the other hand, music is dynamic and full power ("clipping") is only reached for a very short time during the peaks in the music. Therefore, the efficiency at full power may arguably not be the most critical factor when optimizing the losses in an amplifier or power supply intended for audio applications. In order to make a rough estimation of the CO2 emission generated per year, it is assumed that around 5 % of the world population (about 0.36 billion) listen to music in stereo (2 amplifiers). Using a CO2 emission factor 0.537 kg/kWh [9], it is found that a ½ million tons of CO2 is generated per year.

In this paper, the power losses at low power levels are analyzed based on the author's previous work [1]. Accordingly, a concept of Class-D audio amplifiers using tracking power supply is investigated. The experimental results with an ideal stepless supply voltage demonstrate that a great efficiency improvement can be achieved at low power and that 72 % of energy consumption can be. Finally, the effect on the audio performance is also studied.

Table 1: Average distribution of volume control positions and corresponding amplifier energy consumption based on the measurement [1, 4, 7, 8, 9].

				Optimized Class-D Amplifier (Vs = ±40 V)		
Subjective level	Distribution	Hour/day	Peak Power	Peak Loss	Efficiency	Energy Consumption (person & day)
Clipping	0 .001 %	0.00 h	130 W	11.6 W	92 %	0.0 Wh
Party	0.999 %	0.04 h	45 W	5.2 W	90 %	0.2 Wh
Listening	10 %	0.36 h	8 W	1.7 W	82 %	0.6 Wh
Background	89 %	3.20 h	1.3 W	0.9 W	60 %	2.8 Wh

Energy Consumption per year	3.6 Wh
CO2 Emission per year	510,585 ton

2. INVESTIGATION OF ENERGY CONSUMPTION AT LOW POWER

2.1. POWER LOSS MODELING

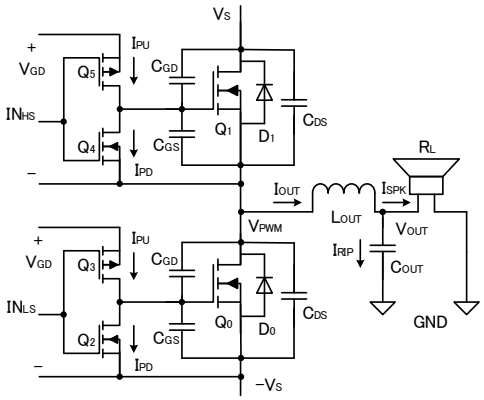

Fig. 2: A half-bridge with N-type MOSFETs and a second order LC low pass output filter

Power loss modeling was done with an analytical model of class-D audio amplifiers, which consist of a half-bridge with N-type MOSFETs (the power stage) and a second order LC low pass output filter (Fig. 2) [1]. The model is briefly summarized in this section.

2.1.1. MOSFET conduction loss

Conduction loss of MOSFETs is modeled as the energy loss dissipated in the on-resistance of the MOSFETs R_{ON} by its conducting current I_{OUT} during each on-period.

2.1.2. MOSFET switching loss

At every switching transition of the PWM, the stored energy in the parasitic capacitances of the MOSFETs C_{GD} and C_{DS} is dissipated. This is called switching loss. The four switching scenarios are defined depending on the relation between the output current I_{OUT} and the drive current for the MOSFETs I_{PU} and I_{PD} at the transition. Since the non-linear characteristics of the parasitic capacitance need to be taken into account for the accurate loss estimation [1], they are characterized from the published manufacture data by curve fitting.

2.1.3. Inductor core switching loss

Core loss in the inductor L_{OUT} in the output filter is estimated by Steinmetz equation [10], where most of the parameters are determined from the manufacture's published data.

2.1.4. Inductor conduction loss

Conduction loss of the inductor L_{OUT} (copper loss) is given by the sum of the DC loss and the AC loss in the winding of the inductor L_{OUT}. The AC loss is affected by the skin effect and the proximity effect [11].

Loss in the capacitor C_{OUT} in the filter typically contributes to less than 50 mW [2]. Compared with the power losses in the Table 1 (in the row "Peak Loss"), this contribution is quite small. Therefore, it is ignored from the analysis.

2.2. LOSS ANALYSIS

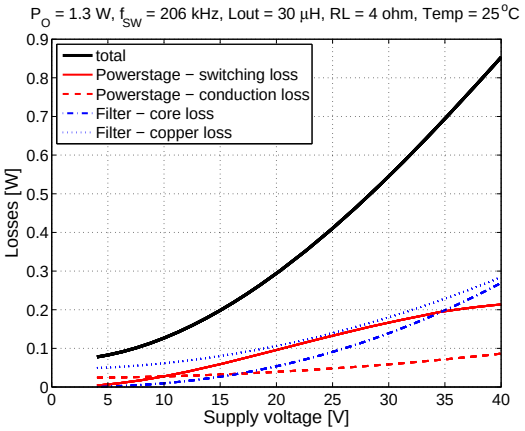

Fig. 3: Power losses analysis vs supply voltage at 1.3 W constant output power (4 Ω)

The introduced model allows us to separate each contribution to the total power loss. The loss analysis for the case of 1.3 W constant output power ("background") is conducted by changing the supply voltage from the original value (40 V) down to a minimum supply voltage (Fig. 3). By applying the approach in [1], each power loss contribution at 40 V is compromised to minimize the total loss. The minimum supply voltage is determined from the minimum required voltage to reproduce 1.3 W output power in a 4

Ω resistive load without clipping. Provided the maximum modulation index is 0.8, it becomes around 3.6 V as shown in the Fig. 3.

The findings about the power losses in such low modulation index are :

- In the power stage
  - The conduction loss of MOSFETs is less dependent on the power supply because it is mainly dissipated by the on-resistance of the MOSFETs R_{ON} and DC current (constant regardless of supply voltage).
  - When a supply voltage is fixed at 40 V, the switching loss dominates about one third of the total losses and strongly relates to the supply voltage as a well-known simplified expression $1/2CV^2 f_{SW}$ expects.
- In the output filter
  - The core loss strongly depends on the supply voltage because pulse amplitude which equals the supply rails changes the peak flux.
  - The conduction loss of the inductor L_{OUT} is more dependent on the supply voltage than the conduction loss of the MOSFETs because the former is affected by the AC loss. The AC loss in the inductor L_{OUT} is dependent on the supply voltage because the ripple current I_{RIP} varies with the supply voltage.

Although these finding are based on a certain design, more or less the similar voltage dependency can be generally assumed for any Class-D amplifier. The main difference is that each loss contribution may differ in different designs.

2.3. CLASS-D AUDIO AMPLIFIERS USING TRACKING POWER SUPPLY

Since dominant power loss sources highly depend on the supply voltage, using a stepless power supply tracking audio reference for a class-D amplifier allows a considerable amount of power savings (Fig. 4).

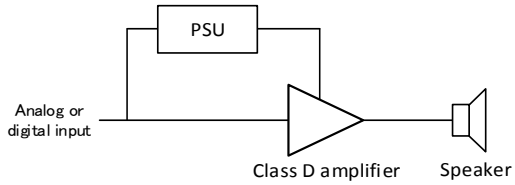

Fig. 4: Class-D audio amplifiers using tracking power supply.

Such power supply rails can vary depending on the content of the music (Analog or digital input). In this work, the power supply was related to the peak amplitude plus given headroom. The minimum required power supply voltage V_S is found by :

$$V_S = A \cdot \max(|v_i|) + \Delta \qquad (1)$$

,where A is a gain which includes the power stage gain and the additional gain. Δ is an optional headroom, and v_i is a input reference signal.

Similar ideas are introduced in [3, 11], even though further study or real implementation haven't been reported yet. The envelope tracking power supply is often used in RF application [12]. In mobile applications, a two-level supply voltage approach instead of stepless has been adopted to improve the efficiency at low power levels. A boost converter is switched on if the amplitude of the music signal exceeds a certain threshold and more power is needed. The combined solutions of tracking power supplies with audio amplifiers for audio application are studied in [13].

3. EXPERIMENTAL RESULT

The experimental measurements are conducted with a 130 W hysteretic self-oscillating class-D amplifier [5], which is originally designed to operate with a fixed 40 V power supply voltage and the switching frequency is optimized in terms of the power efficiency at idle in the author's previous work [1]. The prototype is shown in Fig. 5.

As for the equation (1), it is worth mentioning that the parameters A, Δ need to be chosen carefully to ensure some headroom between the reproduced signal and the supply voltage to have enough open loop gain for the self-oscillating class-D amplifier. For this measurement,

$A \approx 32$ and $\Delta = 0$ are selected. An external power supply was supplying the control circuit.

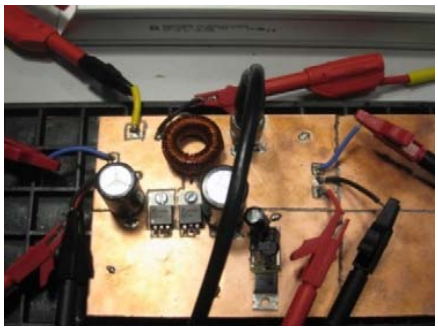

Fig. 5: The power stage and the output filter for the prototype.

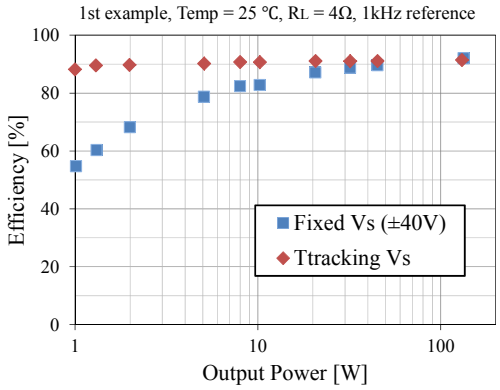

Fig. 6: The comparison of measured power efficiency between a traditional system (Fig. 1) and the system with a tracking power supply, 4 Ω load, 1 kHz reference signal.

3.1. POWER EFFICIENCY

The efficiency of the power stage and the output filter is measured with varying power supply rails for the amplifier (Fig. 6). The considerable amounts of losses are reduced at low output power as predicted by the loss analysis. Again, the energy consumptions of both cases are calculated and compared in Table 2. It is concluded that 72 % of energy consumption is deducted (From 3.6 Wh to 1 Wh) by varying the power supply voltage depending on the required output power. This may account for 373 thousand tons of CO2 reduction per year.

3.2. TOTAL HARMONIC DISTORTION (THD)

Measurement of THD vs output power and THD vs frequency are conducted as shown in Fig. 7 and Fig. 8. Each power supply rail where adjusted to ±5V, ±13 V, ±30 V, and ±40 V targeting for the 1.3 W, 8 W, 45 W, and 130 W power levels, respectively in the same way as done in the efficiency measurement.

Table 2: The comparison of energy consumption between a traditional system and the system with a tracking power supply based on the measurement.

	Optimized Class-D Amplifier (Vs = ±40 V)			The system with a tracking power supply		
Subjective level	Peak Loss	Efficiency	Energy consumption per (person & day)	Peak Loss	Efficiency	Energy consumption per (person & day)
Clipping	11.6 W	92 %	0.0 Wh	11.6 W	92 %	0.0 Wh
Party	5.2 W	90 %	0.2 Wh	4.4 W	91 %	0.2 Wh
Listening	1.7 W	82 %	0.6 Wh	0.8 W	91 %	0.3 Wh
Background	0.9 W	60 %	2.8 Wh	0.2 W	90 %	0.5 Wh

Energy Consumption per year	3.6 Wh	1.0 Wh
CO2 Emission per year	510,585 ton	136,770 ton

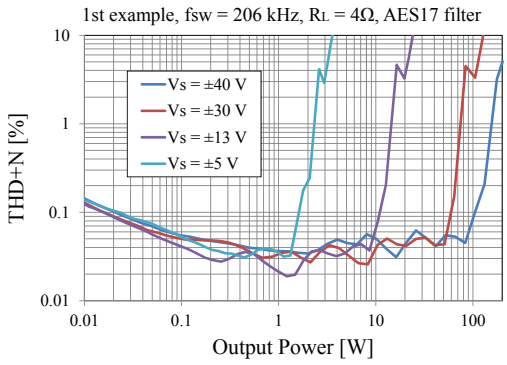

Fig. 7: Measured THD vs output power (4 Ω), 1 kHz reference signal.

In the Fig. 7, only minor changes in the THD vs power measurements are observed up to the point where clipping is reached due to varying power supply voltages.

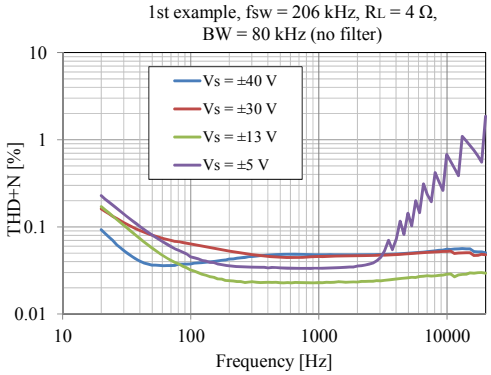

Fig. 8: Measured THD vs frequency, 1.3 W output power (4 Ω).

On the contrary, there is a certain difference in frequency dependency of THD (Fig. 8). This is especially apparent when the supply voltage is ±5 V. The reason is that the open loop bandwidth of the comparator in a hysteretic self-oscillating class-D amplifier decreases due to the significant drop of the switching frequency at higher duty cycles [14, 15]. Thus, the open loop gain is not enough to suppress the error sources at high frequencies. To avoid this, a higher open loop bandwidth for the controller by increasing the switching frequency (Fig. 9), a lower limit of the tracking power supply voltage (Fig. 10), or constant switching frequency technique might be helpful [14, 16].

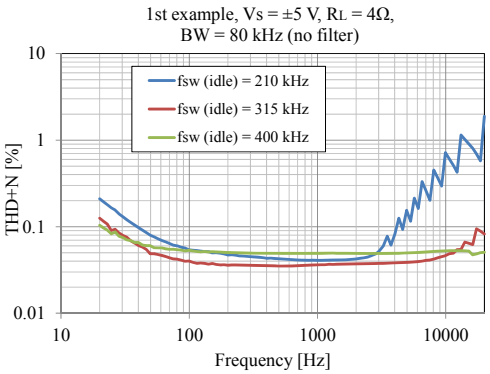

Fig. 9: Measured THD vs frequency, 1.3 W output power (4 Ω), increasing the switching frequency.

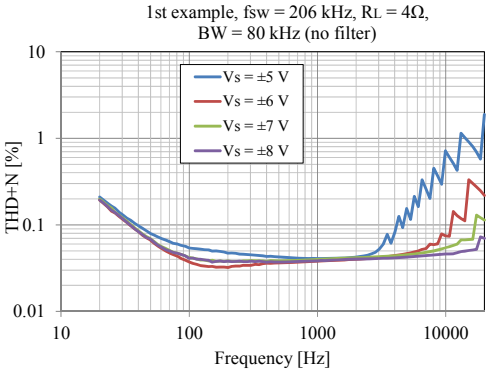

Fig. 10: Measured THD vs frequency, 1.3 W output power (4 Ω), increasing headroom for the supply voltage.

3.3. A COMMERCIALIZED CLASS-D AMPLIFIER

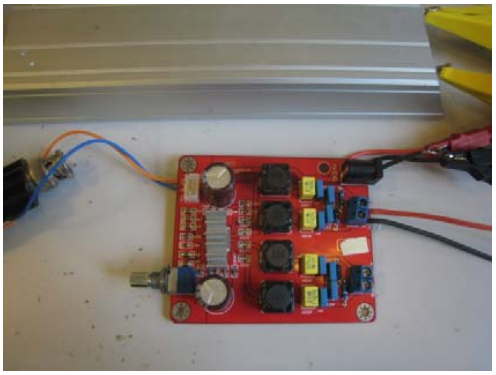

Fig. 11: The PCB board with a commercialized class-D amplifier.

The investigation is extended to a commercialized clocked class-D amplifier (Fig. 11) in terms of the power efficiency and the THD performance [17].

The amplifier gain of the commercial amplifier is 26 dB. Since the supply voltage is supplied through the common terminal (PV_{CC}), the minimum voltage $(PV_{CC\min})$ needs to be secured to keep the controller operational. Therefore, a small modification is applied to determine the required supply voltage.

$$PV_{CC} = \max(A \cdot \max(|v_i|) + \Delta, PV_{CC\min}) \qquad (2)$$

,where the parameters are the same as in (1).

The efficiency measurement is conducted by varying the power supply rails of the amplifier (Fig. 12). $A \approx 24$ and $\Delta = 0$ are selected to find the required supply voltage.

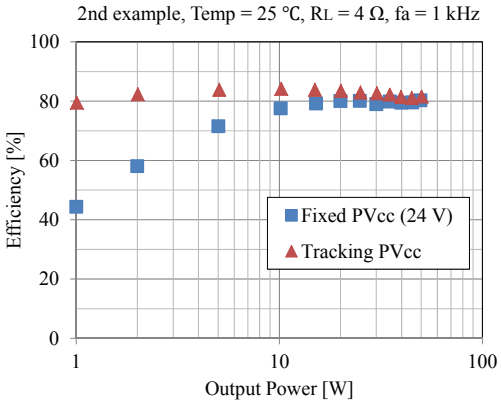

Fig. 12: The comparison of measured power efficiency between a traditional system and the 2nd example with 1 kHz reference signal.

As confirmed in the previous prototype, the considerable amounts of losses are reduced at the low power as well.

THD performance is measured in respect to the output power dependency (Fig. 13) and the frequency dependency (Fig. 14). Every plot shows the same performance until clipping occurs. It is observed that the THD is less affected by a decreased supply voltage compared to the self-oscillating amplifier previously investigated. It is however noticed in both cases that a lower supply voltage limit must be utilized in order to avoid THD degradation. Based on this study the THD vs. frequency measurement is an efficient tool to find the actual limit.

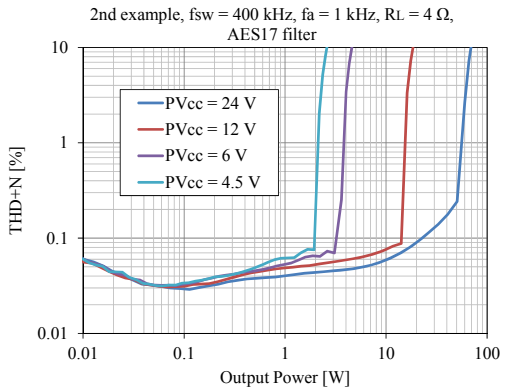

Fig. 13: Measured THD vs output power of the 2nd example with 1 kHz reference signal.

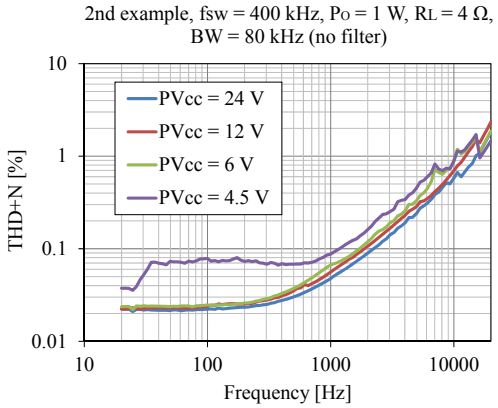

Fig. 14: Measured THD vs output power of the 2nd example with 1 kHz reference signal.

4. CONCLUSION AND FUTURE WORK

In this paper, one of main concerns about Class-D audio amplifiers, significant amount of power losses at low power levels is emphasized based on the consumer behavior. The power losses at such condition are analyzed in detail and the theoretical limits of ideal stepless power supply tracking are studied in terms of the power efficiency and the audio performance. The experimental results show that the energy consumption can be reduced by 72 % and that the environmental impact can be drastically decreased. Another demonstration with a commercialized Class-D amplifier is found to verify the same benefit. As for the audio performance, with a self-oscillating controller, the designer needs to notice the switching frequency starts to drop at lower power levels by decreasing supply voltage. This leads to the performance degradation due to the decreased open loop gain of the controller. To avoid this, some applicable solutions are suggested. Apart from that, no significant performance difference is found from the amplifier with the fixed supply voltage.

The remaining work is to implement a whole system with a class-D amplifier and a tracking power supply.

5. ACKNOWLEDGEMENTS

The author would like to thank colleagues in the DTU electronics group for supporting this work.

6. REFERENCES

[1] Akira Yamauchi, Arnold Knott, Ivan H.H. Jørgensen, and M.A.E. Andersen, “Frequency dependent loss analysis and minimization of system losses in switch-mode audio power amplifiers”, AES 137th Convention, California, USA, Oct 9-12, 2014.

[2] Flemming Nyboe, PhD thesis, “Integrated Circuit Design of Switching Power Stages for Audio Power Amplification”, Ørsted DTU, Kgs. Lyngby, 2006.

[3] Karsten Nielsen, and Lars Michael Fenger, “The Active pulse modulated Transducer (AT) A novel audio power conversion system architecture”, AES 115th New York, USA, Oct 10-13, 2003.

[4] Karsten Nielsen, “High-Fidelity PWM Based Amplifier Concept for Active Speaker Systems with a Very Low-Energy Consumption”, AES 100th Convention, Copenhagen, Denmark, May 11-14, 1996.

[5] Søren Poulsen, PhD thesis, “Towards Active Transducers”, Ørsted DTU, Kgs. Lyngby, 2004.

[6] Bruno Putzeys, “Simple Self-Oscillating Class-D Amplifier with Full Output Filter Control”, AES 118th Convention, Barcelona, Spain, May 28-31, 2005.

[7] Rowena Mosher, “Music Survey Data Analysis” (Created: Oct. 16, 2012).

[8] International Energy Agency, "Key World Energy Statistics 2013".

[9] DEFRA (June 2007) Act on CO2 Calculator: Public Trial Version Data, Methodology and Assumptions Paper.

[10] R.W. Erickson, D. Maksimović, "Fundamental of Power Electronics", 2nd edition, Springer, 2001.

[11] Karsten Nielsen, Lars Michael Fenger, "POWER CONVERSION SYSTEM", US patent application US7321262 B2, 2008.

[12] M.C.W. Høyerby, PhD thesis, "High-Performance Control in Radio Frequency Power Amplification Systems", Ørsted DTU, Kgs. Lyngby, 2008.

[13] Petar Ljušev, PhD thsis, "SIngle Conversion stage Amplifier - SICAM", Ørsted DTU, Kgs. Lyngby, 2005.

[14] Søren Poulsen, M.A.E. Andersen, "Hysteresis controller with constant switching frequency", IEEE Trans. on Consumer Electronics, vol. 51, no. 2, pp.688-693, May 2005.

[15] M.C.W. Høyerby, M.A.E. Andersen, "small-signal model of the hysteretic comparator in linear-carrier self-oscillating switch-mode controllers", proc. of NORPIE 2006, Lund, Sweden, June 2006.

[16] M.C.W. Høyerby, M.A.E. Andersen, "Ultrafast Tracking Power Supply With Fourth-Order Output Filter and Fixed-Frequency Hysteretic Control", IEEE Trans. on Power Electronics, vol. 23, no. 5, pp.2387-2398, September 2008.

[17] TPA3116D2, SLOS708C Datasheet [online]. Available: http://www.ti.com/ (Accessed: Nov. 13, 2014)

Appendix D

Validation of Power Requirement Model for Active Loudspeakers

---

138th Convention of the Audio Engineering Society 2015

Audio Engineering Society

Convention Paper

Presented at the 138th Convention
2015 May 7–10 Warsaw, Poland

Validation of Power Requirement Model for Active Loudspeakers

Henrik Schneider[1], Anders N. Madsen[1], Ruben Bjerregaard[1], Arnold Knott[1], Michael A. E. Andersen[1]

[1] *Dept. of Electrical Engineering, Technical University of Denmark, Kongens Lyngby, DK-2800, Denmark*

Correspondence should be addressed to Henrik Schneider (`hensc@elektro.dtu.dk`)

ABSTRACT

The actual power requirement of an active loudspeaker during playback of music has not received much attention in the literature. This is probably because no single and simple solution exists and because a complete system knowledge from input voltage to output sound pressure level is required. There are however many advantages that could be harvested from such knowledge like size, cost and efficiency improvements. In this paper a recently proposed power requirement model for active loudspeakers is experimentally validated and the model is expanded to include the closed and vented type enclosures in addition to the main loudspeaker non-linearities.

1. INTRODUCTION

Recent analysis of the actual power requirements of an active loudspeaker during playback of music predicts that full power capability is only needed for a very short time in the range of a few milliseconds [1]. However, the main parts of an active loudspeaker, the power supply (PSU), the amplifier and the loudspeaker are normally designed for significantly higher continuous power in the range of seconds to minutes [2–4]. One reason is that the design and test process, due to simplicity, are based on an amplifier with a sinusoidal input and a resistive load. A second reason is that general purpose PSU and amplifier modules are produced and sold due to mass production benefits etc.

This work is a step towards a method for proper characterization of required voltage, current and thus power for playback of music in an active loudspeaker in order to facilitate a quantum leap in performance relative to size, cost and efficiency. In this work a commercial 2-way loudspeaker is targeted and used to validate and expand the work done in [1]. A future goal is to develop a testing framework for active loudspeaker components for evaluation of system performance (acoustic, thermal, magnetic and electrical), making

it possible to optimize individual components with respect to overall system performance in realistic conditions.

The importance of considering reactive loads has been verified in [5–8] instead of just resistive loads. In [9] passive crossover filters were also considered. In previous work the dynamic range or crest factor (CF) as well as the statistical loudness of different music genres have been analysed [10, 11].

2. POWER REQUIREMENT FUNDAMENTALS

The end user has final control of the level at which a sound system is operating. Power consumption is thus influenced by parameters in the path from power mains to the perceived sound level. Since active loudspeakers are designed for music playback, the power requirements should match a highly dynamic signal with a relatively low continuous power consumption. On the contrary, a sinusoidal input has the same continuous apparent power independent of signal length. The influence of a music signal on a woofer and tweeter is evident in Figure 2.

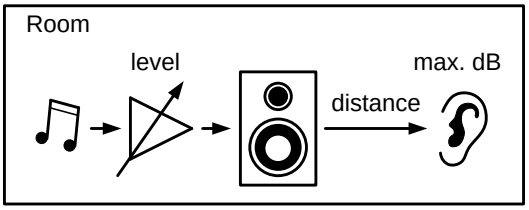

Figure 1: Simple illustration of main parts that influence the power requirements.

Music genres are dynamically different. In addition, the perceived loudness of the human ear is not a flat gain and is dependent on the room acoustics and the distance to the loudspeaker, which may exhibit non-linear behaviour. These parameters, together with subjective evaluation of sound level, set the power requirements for the PSU, amplifier and loudspeaker. However, this work focuses on the influence from the loudspeaker non-linearities and enclosure type.

3. LOUDSPEAKER MODELLING

Modelling of a loudspeaker driver in free air, in a closed box and in a vented box was done in Simulink. A model of the loudspeaker in free air is shown in Figure 4. In this model the three main non-linearities $L_E(x)$, $Bl(x)$ and $C_{MS}(x)$ have been included. A linear model for a loudspeaker in free air can be found in [1].

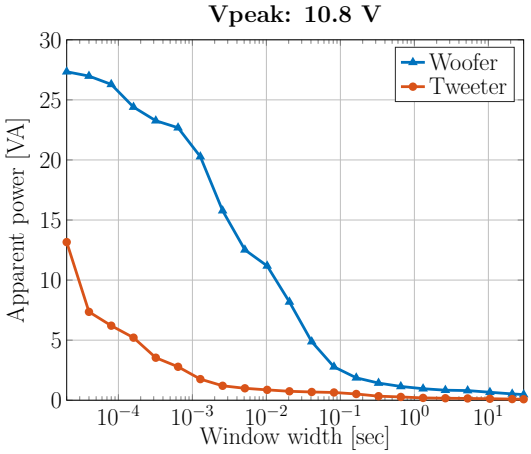

Figure 2: Comparison of measured power requirements of a 5.5” woofer and a 1” tweeter including amplifier, crossover and vented box enclosure.

The voice coil is modelled with a lossy inductance R_2 in parallel with L_2, which is then in series with L_E. The Klippel analyzer used to measure the values of these components uses the same model for a lossy inductor.

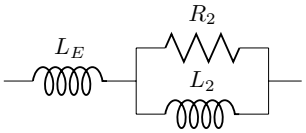

Figure 3: Model of lossy inductor [12].

3.1. Including the enclosure

An enclosure adds additional impedance to the system seen from the input terminals. Modelling the enclosure is done using the impedance analog method described in [12]. For this work, the closed and vented box enclosures were investigated. When

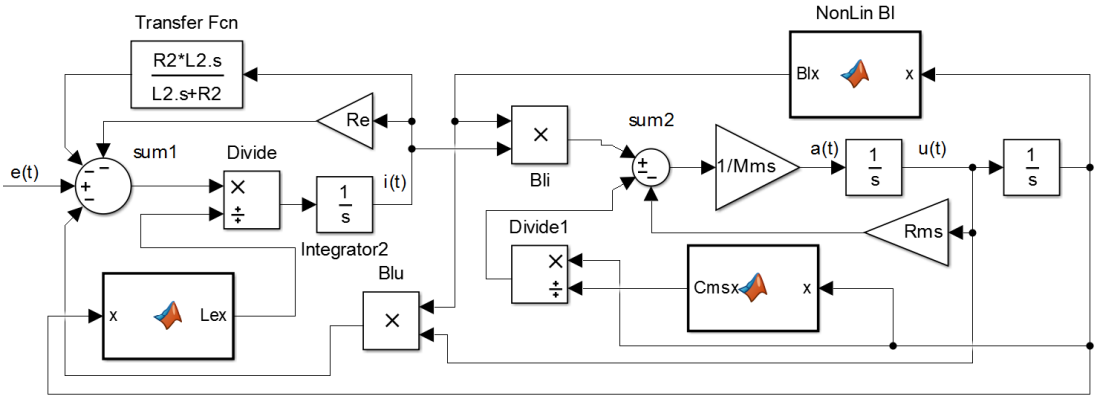

Figure 4: Model of the non-linear loudspeaker in free air.

a loudspeaker is mounted in a closed box, acoustical mass M_{AB}, compliance C_{AB} and losses R_{AB} of the back volume are added. R_{AB} was in this case negligible because the box is not filled with damping material. By referring acoustical parameters to the mechanical domain, the mechanical parameters in Figure 4 can be changed to

$$C_{tot} = C_{MS} + S_D^2 C_{AB} \tag{1}$$

$$M_{tot} = M_{MS} + S_D^2 M_{AB} \tag{2}$$

where S_D is the effective area of the diaphragm and C_{MS}, M_{MS} and R_{MS} are the mechanical compliance, mass and resistance of the diaphragm, respectively. The air load on the diaphragm is included in M_{MS}.

Compared to the closed box, the vented box introduces additional acoustical impedance with the mass of air in the vent M_{AP} and acoustical resistance R_{AL} that models air leaks. A transfer function was added to the feedback loop in the model (Fig. 4) as depicted in Figure 5, where $u(t)$ is the velocity of the diaphragm and $i(t)$ is the current.

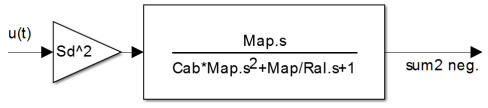

Figure 5: Vented box transfer function feedback.

3.2. Including the non-linearities

The non-linear behaviour of the loudspeaker introduces compression and distortion in the signal waveform and is due to a displacement dependent force factor $Bl(x)$, suspension compliance $C_{MS}(x)$ and voice coil inductance $L_E(x)$. Using the Klippel analyzer, the displacement dependent parameters were estimated by a 6th order polynomial. The coefficients for the polynomials are shown in Table 2. MATLAB functions containing these polynomials were introduced as shown in Figure 4, effectively including the non-linearities in the model.

4. VALIDATION OF LOUDSPEAKER MODELS

To validate the loudspeaker models a commercial loudspeaker developed by PointSource Acoustics, the *Medium* model, was used which utilizes a 5.5" woofer and a 1" tweeter. The small and large signal parameters of the drivers were measured with a Klippel analyzer and are listed in Table 1 and 2.

4.1. Measurement setup

MATLAB is used to generate and capture the signal data using a Data Acquisition Device (DAQ) from National Instruments (USB-6356). The DAQ sampling rate was set to 50 kHz (dividable with the maximum sampling frequency of the specific DAQ, which is 1.25 MHz). The signal was amplified and sent through a 0.1 Ω sense resistor, R_S, in series with the load, R_L. The current was measured by capturing the voltage across R_S. A digital lowpass

Parameter	Woofer	Tweeter	Units
f_s	40	978.5	Hz
V_{AS}	35.26	3.5	l
Q_{TS}	0.42	0.954	
Q_{ES}	0.49	2.105	
Q_{MS}	3.14	1.738	
S_D	153.94	6.16	cm^2
R_E	3.47	3.18	Ω
L_E	0.216	0.008	mH
R_2	5.52	0.67	Ω
L_2	0.421	0.015	mH
C_{MS}	1.05	0.124	mm/N
R_{MS}	1.20	0.757	kg/s
M_{MS}	15.05	0.214	g
Bl	5.2	1.410	N/A

Table 1: Loudspeaker parameters of the 5.5" woofer.

n	Bl_n	C_{MS_n}	L_{E_n}
0	5.14	1.78	381.08e-6
1	-63.30e-3	2.33e-3	-43.03e-6
2	-21.75e-3	-18.19e-3	17.08e-6
3	320.09e-6	712.57e-6	610.27e-9
4	-840.06e-6	-3.55e-6	-15.18e-9
5	6.29e-6	-8.70e-6	-4.94e-9
6	8.39e-6	662.45e-9	0.40e-12

Table 2: Polynomial coefficients of non-linear woofer parameters.

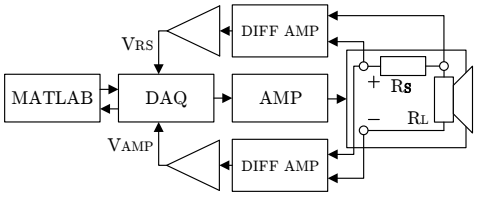

Figure 6: Simplified measurement setup.

filter was applied in MATLAB to simulate the passive crossover from the commercial loudspeaker.

An ICEpower 50ASX2 amplifier was used to amplify the signal as this has an outer control loop ensuring a constant gain in the audible frequency range independent of the load. A comparison with a Texas Instruments evaluation board amplifier is shown in Figure 7. Compensation of the input-to-output transfer function of the amplifier must be considered if the gain is not flat.

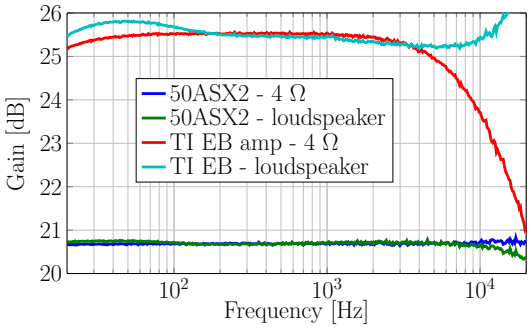

Figure 7: Measured amplifier gain of an ICEpower ASX2 and a Texas Instrument evaluation board.

4.2. Power requirement analysis

The power requirement analysis method was used according to [1]. The music signal was multiplied in the time domain with a square window with stepwise logarithmically increasing window width. For each window width the window was moved forward with 10 % of the window width until the end of the music signal met the end of the window. Every time the window was moved, the apparent power of the signal within the window is calculated and the maximum value is stored for that particular window size.

$$P_{RMS} = \frac{1}{N}\sqrt{\sum_{n}^{N} v(n)^2 i(n)^2} \qquad (3)$$

N is the number of samples in the window. The results of this algorithm can be analysed visually to grant information about the power requirement with a specific signal at a specific level.

The commercial loudspeaker was mounted in different enclosures to measure the power requirement, i.e. free air, closed box and vented box. Since the commercial loudspeaker is designed as a vented box, the same enclosure was used for the closed box measurements with the vent sealed. For the main part of the measurements, 30 seconds

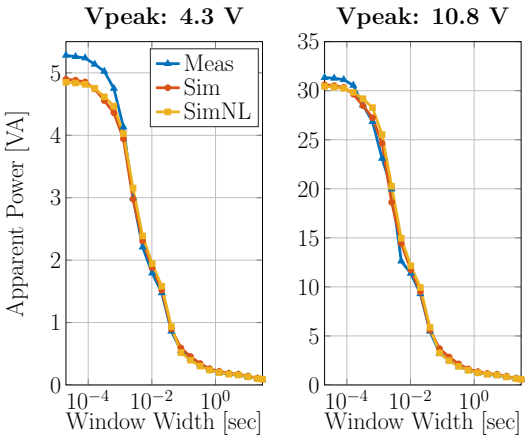

Figure 8: Free air (infinite baffle) power comparison.

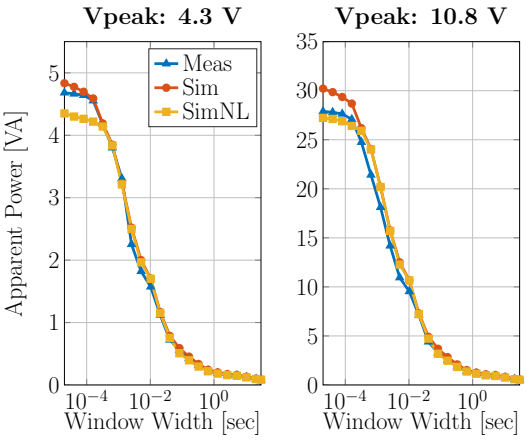

Figure 10: Vented box power comparison.

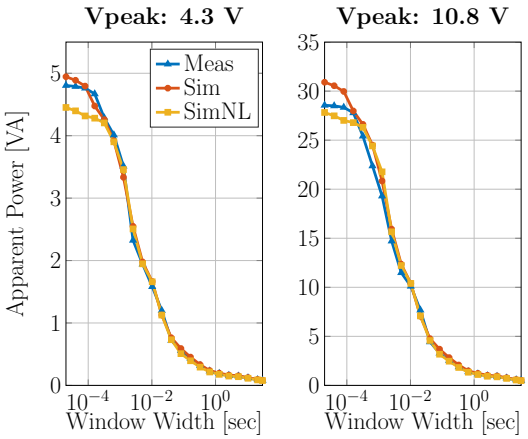

Figure 9: Closed box power comparison.

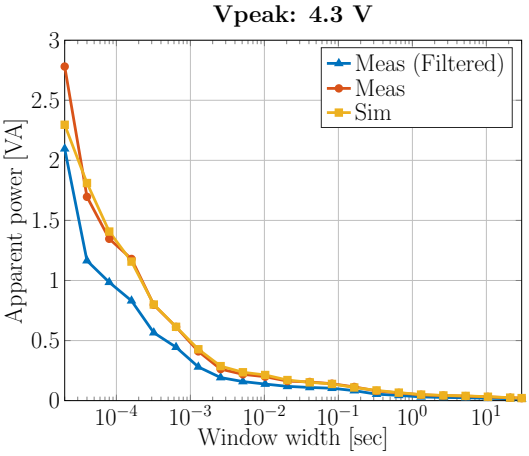

Figure 11: Ttweeter power comparison.

of a rock music track was used as the test signal to ensure wide frequency range content and a broad dynamic range. The measurement results were compared with simulations to verify coherence.

Mounting a loudspeaker in an enclosure adds acoustic impedance to the system based on the order of the enclosure. Measurements show that power is slightly reduced as expected when a closed box (2nd order enclosure) is used in comparison with the driver in free air. In addition, power is further reduced for a vented box (4th order enclosure). Measured results and linearly and non-linearly simulated results are shown in Figures 8, 9, 10 and 11.

For high input levels, measurements begin to resemble simulations where the non-linearities of the loudspeaker have been included. It is apparent that the power requirements, especially at peak levels, are higher for the woofer than for the tweeter. This is expected as low frequencies have peak levels that are present for longer periods of time and because the

Title	Artist	Genre	ReplayGain
What She Came For	Franz Ferdinand	Rock	-14.2 dB
Nardis	Bill Evans Trio	Jazz	-4.5 dB
Kill Everybody (Bare Noize remix)	Skrillex	Dubstep	-16.2 dB

Table 3: Measured music tracks.

efficiency of a woofer is comparatively lower. The woofer is thus of most importance when looking at the power requirement for a 2 way loudspeaker.

The linear model overestimates the peak power compared to the non-linear model thus providing a small design headroom. To the authors opinion the linear model is sufficient in most cases. The additional precision that the non-linear model provides comes at the cost of much longer simulation time and require the non-linear parameters of the loudspeaker drivers to be known.

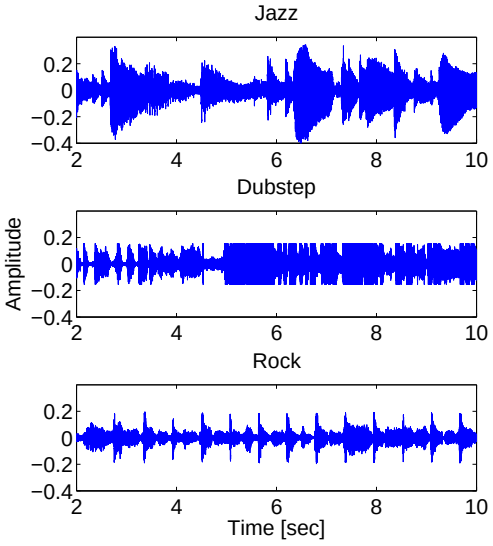

Figure 12: Time signals for three different music tracks normalized with ReplayGain.

The choice of music has shown to have a great influence on the measured apparent power due to the dynamics of the signal. Prior to comparison of music tracks a ReplayGain [13] normalization was added.

Figure 13 shows the apparent power comparison of the tracks in Table 3.

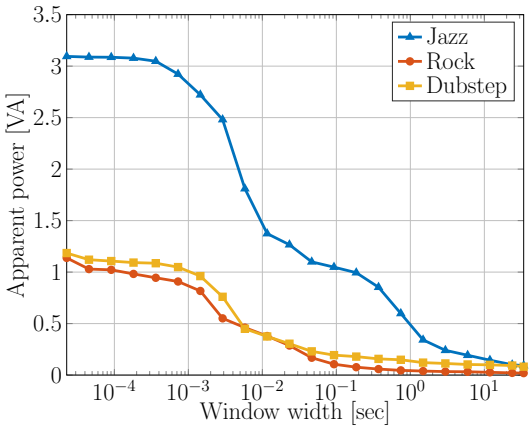

Figure 13: Different music tracks perceived equally loud (normalized) measured for the complete active speaker.

5. FUTURE WORK

For future work it could be interesting to compare the power requirements of different loudspeaker enclosures having the same volume and frequency response. Furher more there is an increasing demand for smaller loudspeakers in consumer electronics. The effect on the power requirements of these loudspeakers is therefore an obvious choice for further investigations. In addition, passive crossovers vs. active crossovers could be examined in terms of power requirements. A simplified worst-case apparent power model could be derived based on analysing a large music library. The model used to predict the power requirements can also be used to get worst case current and voltage

information. This is very valuable in the design phase of the power components in a sound system.

6. CONCLUSION

In this paper the fundamentals behind the power requirements of active loudspeakers have been discussed and models including the influence of the enclosure and the main non-linearities of the loudspeaker drivers have been presented and validated experimentally. The non-linearities were found to have influence on the accuracy at higher sound pressure levels where the peak power requirements are defined. However, the linear model was found to overestimate the peak power requirements providing a small design headroom and is expected to be sufficient in most design cases. In addition, the selected music content for playback was confirmed to have a great influence of the power requirements. This work is a step towards improved design of power components like the amplifier, the power supply and the loudspeaker in an active loudspeaker. The models and methods presented in this work is applicable in other sound system applications.

7. REFERENCES

[1] H. Schneider, L. C. Jensen, L. P. Petersen, A. Knott, and M. A. Andersen, "Requirements specification for amplifiers and power supplies in active loudspeakers," in *Audio Engineering Society Convention 137*, Audio Engineering Society, 2014.

[2] ICEpower, *ICEpower50ASX2 - 2x50W or 1x170W ICEpower Amplifier with integrated ICEpower Supply*. Datasheet: Rev. 1.3.

[3] Texas Instruments, *SLOU293C - A 600-W, Isolated PFC Power Supply for AVR Amplifiers Based on the TAS5630 and TAS5631*. Application note: Rev. 2012.

[4] Hypex, *SMPS400 - High Efficiency Audio SMPS*. Datasheet.

[5] R. Bortoni, S. N. Filho, and R. Seara, "On the design and efficiency of class a, b, ab, g, and h audio power amplifier output stages," *J. Audio Eng. Soc*, vol. 50, no. 7/8, pp. 547–563, 2002.

[6] A. Knott and L. P. Petersen, "Comparison of power supply pumping of switch-mode audio power amplifiers with resistive loads and loudspeakers as loads," in *Audio Engineering Society Convention 134*, May 2013.

[7] N. E. Iversen and A. Knott, "Small-signal loudspeaker impedance emulator," in *Audio Engineering Society Convention 136*, Apr 2014.

[8] F. Gonzalez-Espin, E. Figueres, G. Garcera, and J. Sandia, "Design of closed loop audio power amplifiers by means of an accurate model of vented box loudspeakers," in *Power Electronics and Applications, 2007 European Conference on*, pp. 1–9, IEEE, 2007.

[9] R. Bortoni and H. Sette Silva, "Loudspeakers' electric models for study of the efforts in audio power amplifiers," in *Audio Engineering Society Convention 115*, Oct 2003.

[10] P. J. Chapman, "Programme material analysis," in *Audio Engineering Society Convention 100*, May 1996.

[11] M. Mijic, D. Masovic, D. Sumarac Pavlovic, and M. Petrovic, "Statistical properties of music signals," in *Audio Engineering Society Convention 126*, May 2009.

[12] W. M. Leach, *Introduction to electroacoustics and audio amplifier design*. Kendall/Hunt Publishing Company, 2003.

[13] "Replay Gain - A Proposed Standard", "http://replaygain.hydrogenaud.io/proposal/contents.html".

Appendix E

Requirements Specication for Ampliers and Power Supplies in Active Loudspeakers

---

137th Convention of the Audio Engineering Society 2014

Audio Engineering Society

Convention Paper

Presented at the 137th Convention
2014 October 9–12 Los Angeles, USA

Requirements Specification for Amplifiers and Power Supplies in Active Loudspeakers

Henrik Schneider[1], Lasse C. Jensen[1], Lars P. Petersen[1], Arnold Knott[1], Michael A. E. Andersen[1]

[1] *Dept. of Electrical Engineering, Technical University of Denmark, Kongens Lyngby, DK-2800, Denmark*

Correspondence should be addressed to Henrik Schneider (`hensc@elektro.dtu.dk`)

ABSTRACT

This work aims to provide designers with a method to develop a requirements specification for power supplies and amplifiers in active loudspeakers. The motivation is to avoid over-sizing and unnecessary cost. A realistic estimation of the power supplied during playback of audio in a given loudspeaker is obtained by considering a wide range of audio source material, loudness normalization of the source material, crossover filtering, driver characteristics as well as a perceived maximum loudness/volume level. The results from analysing a sub-woofer and a woofer reveals the peak power, peak voltage, peak current and apparent power - thus providing a solid foundation for a requirement specification.

1. INTRODUCTION

Imagine that a loudspeaker has been designed, tested and approved. Now it is time to match it with amplifiers and a power supply unit (AMPs+PSU) to create an active loudspeaker. A requirements specification is in demand for the AMPs+PSU since it influence the cost, size and weight of the final product. The task is thus to estimate the maximum power supplied to the loudspeaker during playback. The supplied power is mainly a function of the input (music), the desired perceived loudness level (volume) at a given distance and the load (loudspeaker).

The power rating of current commercial audio AMPs and PSUs are however based on sinusoidal input excitation into a resistive load [1–3] and their power capabilities are stated for a limited time period at a given frequency (typically at 1 kHz) resulting in a given Total Harmonic Distortion (typically 1% THD). The limited time period was found to vary from 20 ms. to 5 min. and it is typically determined by thermal shut down. The importance of considering reactive loads has been verified in [4–7] instead of just resistive loads. In [8] passive crossover filters were also considered. In previous work the dynamic range or crest factor (CF) as well as the statistical loudness of different music

genres have been analysed [9, 10]. However these studies are not suitable for this work since the music has been peak normalized which doesn't correlate with perceived loudness. Further more the signal amplitude isn't proportional to the supplied power to a non-linear load such as a loudspeaker.

The importance of considering loudness normalized audio material instead of sinusoidal input stimuli is investigated in this work. The proposed scheme for a realistic estimation of the supplied power is illustrated in Fig. 1. As seen it interoperates audio material as input, loudness normalization for fair comparison, crossover filtering, a maximum volume setting based on listening tests and measurements of sound pressure level (SPL) as well as a model of the drivers and enclosure forming the loudspeaker. In this work the enclosure was however not taken into account.

2. LOUDSPEAKER POWER REQUIREMENTS

In this section the concepts behind the proposed scheme for estimation of the loudspeaker power requirements is explained.

2.1. Audio material

The audio material should ideally resemble the audio material played by the end user. Since this is very difficult to predict a wide range of audio material of different music genres could be studied. In this work more than 400 music tracks in lossless format were collected based on the most popular music of different genres using various music charts. A dynamic range database including 58900 albums at present time [11] was also used to select music with high, medium and low dynamic range values.

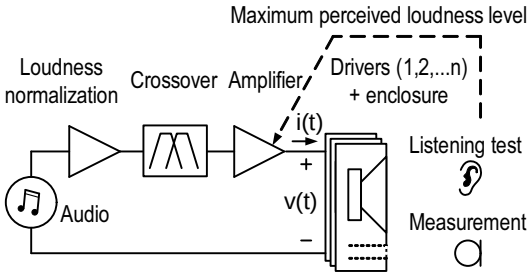

Figure 1: Scheme for estimation of loudspeaker power requirements

Considering music as input stimuli comes with the price of increased computation complexity. Conversely more than 400 songs were analysed in this work which corresponds to more than 24 hours of music with an average song length of 4 minutes. With a sampling frequency of 44100 samples per second more than 3.8 billion samples are to be processed.

2.2. Loudness normalization

In order to compare the power consumption during playback of two or more audio tracks, all tracks needs to sound equally loud.

Algorithms for objectively determining the perceived loudness of various broadcast content were investigated using extensive listening tests in [12]. Based on this work the European Broadcasting Union (EBU) published a recommendation about loudness normalisation [13] with a goal of preventing loudness difference between programs and channels. The algorithms which are published in [14] can be used to normalize the loudness of mono, stereo and multichannel signals with a minor discrepancy due to listeners, audio material and listening conditions. The numerical result of the loudness is given in LKFS (Loudness K-weighted Full Scale) or LUFS (Loudness Units Full Scale) which are identical scales. One unit of LKFS or LUFS is equivalent to one dB, thus a gain of 1 dB of the audio signal will cause a 1 dB gain in LKFS. In order to normalize the loudness of a track with loudness of L_{KG} to a reference loudness of L_{ref} (Typically -23 dB), a gain of $G = L_{\mathrm{ref}} - L_{\mathrm{KG}}$ is applied to the track.

Fig. 2 shows the composition of the ITU-R BS.1770 algorithm. The K-filter consists of two stages used to do a frequency based weighting of the audio signal. The first stage takes into account the acoustic effect of the human head by modelling it as a rigid sphere.

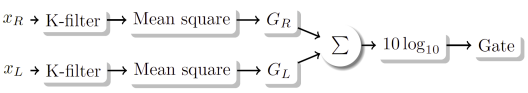

Figure 2: Block diagram of stereo loudness determination algorithm

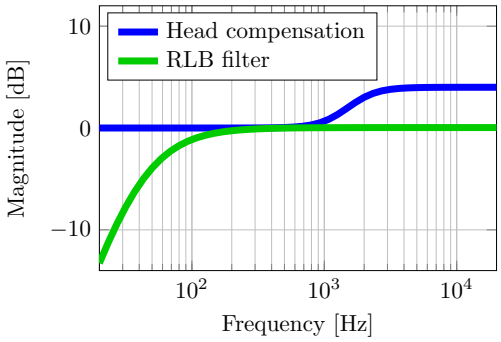

Figure 3: Frequency response of the two filters constituting the K-filter

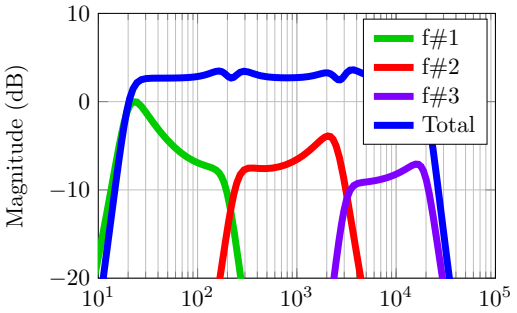

Figure 4: Frequency response of crossover filters (f#1 to f#3) and total frequency response

The second stage of the filter is a simple high pass filter referred to as the revised low-frequency b-curve (RLB) used to mimic the frequency sensitivity of the human ear. Fig. 3 shows the frequency response of the two filters.

The signal is split into 400 ms blocks, each overlapping the previous block by 75 %. The mean square calculation is employed to give a signal which is proportional to the energy content of the signal. The weighting factors G_R and G_L are used to compensate for the fact that the sound from the rear speakers in a 5.1 setup is perceived to be louder than sound from the front and center speakers. When dealing with stereo signals, only the front speakers is used and thus the gain factor is simply set to unity.

Gating is used to remove quiet periods which should not be taken into account when determining the loudness. Both an absolute and a relative gate threshold is employed. An absolute gate threshold is used to remove very low sounds and a relative gate threshold is used to remove any intervals with a loudness lower than -10 LKFS compared to the mean loudness. In essence the gating makes it possible to loudness align a 2 hour movie with a 20 seconds commercial.

A full description of the objective loudness perception algorithm as well as filter coefficients and weightings for the individual audio channels is available in [14].

2.3. Crossover filters

The crossover filter design has a huge impact on the power supplied to each individual driver in a loudspeaker. Due to the difference in driver efficiency high frequency drivers are often attenuated to the level of the lower frequency drivers in order to achieve some targeted frequency response. In this work a 4th order crossover filter was crudely designed with a flat target response to investigate the proposed scheme. The frequency response is shown in Fig. 4. The cut-off frequencies of the 1st filter $f\#1$ is 20 Hz and 200 Hz, the cut-off frequencies of the 2nd filter $f\#2$ is 240 Hz and 2.5 kHz and the cut-off frequencies of the 3rd filter $f\#3$ is 3.3 kHz and 20 kHz.

2.4. Desired loudness level

The desired maximum loudness level (volume max. setting) is determined by the application. As an example a 60 dB a-weighted SPL was found to be the average preferred listening level for public domain television in [15]. In this work a listening level of 85 dB a-weighted SPL was experimentally found to be the desired maximum listening level. This level was also found to be the preferred level in portable audio players [16]. The maximum volume level should be limited by the tolerable distortion level of the amplifier and the loudspeaker rather than the maximum power ratings. A listening test on a new loudspeaker design is therefore a must. A distortion vs. power plot is often found in amplifier data sheets. The same doesn't apply for loudspeakers but sometimes the linear excursion is specified. These factors is considered as out of scope tor this work.

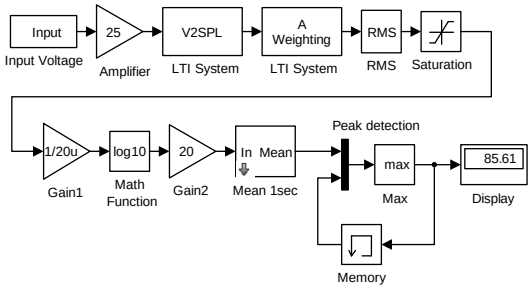

Figure 5: Model for finding the maximum volume gain

The normalized audio material needs to be gained to obtain a SPL equal to the reference of 85 dBa found experimentally. This gain was manually found by tuning a gain in a model of the loudspeaker and by the use of a SPL meter model similar to the SPL meter used in the experimental test as shown in Fig. 5. The input is any audio track and the V2SPL block is the transfer function from voltage to SPL for a given driver.

2.5. Linear driver model

A linear MATLAB Simulink model is used to model the loudspeaker as done in [17]. The inputs to the model is typical parameters found in driver datasheets. The model which is based on (1)-(3) is shown in Fig. 6. The output of the model is the recorded input voltage and input current which can be used to calculate the power supplied to the loudspeaker. In future work a non-linear model could be investigated for improved accuracy.

$$u(t) = R_e i(t) + L_e \frac{\mathrm{d}i(t)}{\mathrm{d}t} + Blv(t) \quad (1)$$

$$F(t) = i(t)Bl \quad (2)$$

$$F(t) = m_m a(t) + r_m v(t) + \frac{1}{cm} x(t) \quad (3)$$

3. ANALYSIS

It is time to analyse the data from the model and create the requirements specification when the audio material has been gathered, normalized, filtered and passed through the model of the speaker. The most

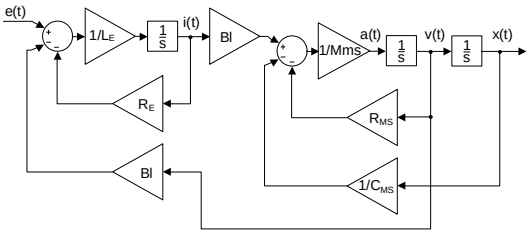

Figure 6: Linear model of the driver

obvious is to inspect the peak voltage, the peak current, the peak power and the average apparent power which is plotted in fig. 10-13. The average apparent power of a track is given by

$$P_{avg} = \sqrt{\sum_n^N v(n)^2 \sum_n^N i(n)^2} \quad (4)$$

where N is the total number of samples.

The knowledge of worst case average apparent power

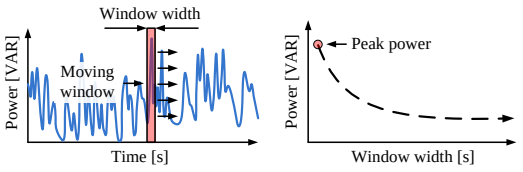

Figure 7: Power sweep with short window width

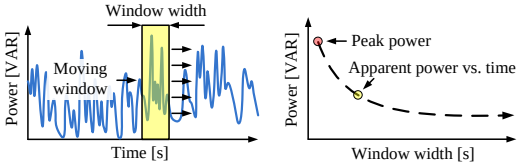

Figure 8: Power sweep with increased window width

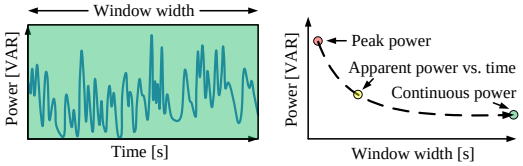

Figure 9: Power sweep with full window width

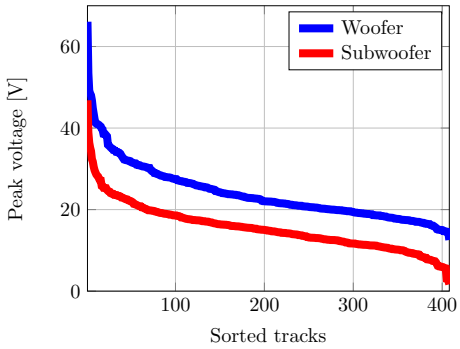

Figure 10: Tracks sorted per peak voltage for woofer and subwoofer

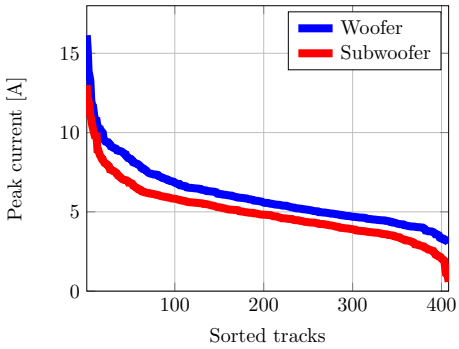

Figure 11: Tracks sorted per peak current for woofer and subwoofer

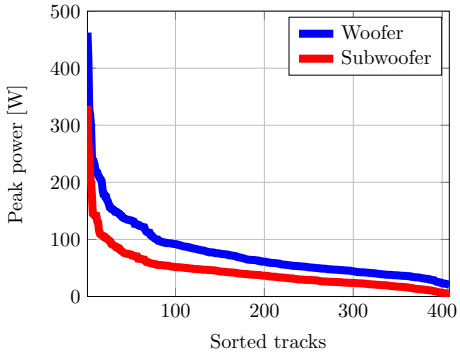

Figure 12: Tracks sorted per peak power for woofer and subwoofer

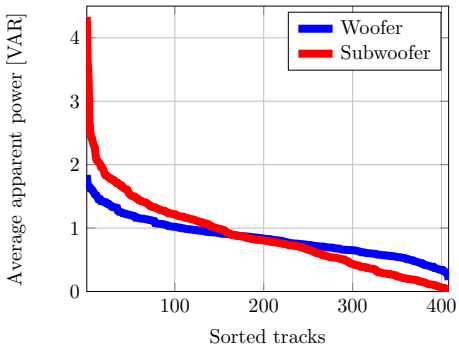

Figure 13: Tracks sorted per average apparent power for woofer and subwoofer

is very valuable if the design goal is to design the smallest possible AMP and PSU. The size may be limited to the maximum allowed temperature of the AMP + PSU which shouldn't be exceeded under continuous use. The maximum ratings of the components could be decided based on the peak power. The thermal design is however limited by the worst case supplied power as a function of time. Unfortunately there is no easy way to acquire such data. Each audio track considered needs to be analysed and for each track the worst case supplied power during a given time period needs to be found. Since no existing solutions was found a new technique was developed to resolve this issue. The concept is illustrated in fig. 7 - 9. The instantaneous power stored during simulation of an audio track is sweept by a short time window. The window is only moved one sample instant at a time and every time the window moves the average apparent power of that time frame is stored. When the window reaches the end of the audio track the worst case average apparent power can be found by the maximum value of the stored data. As the window width is increased the maximum average apparent power will decrease as seen in fig. 8. The final plot will reveal the maximal power supplied as a function of time for a given audio track. Fig. 14 and 15 shows the result of this special ankalysis for more than 400 audio tracks. The resulting knowledge could be used as a new power test methods for AMP's and

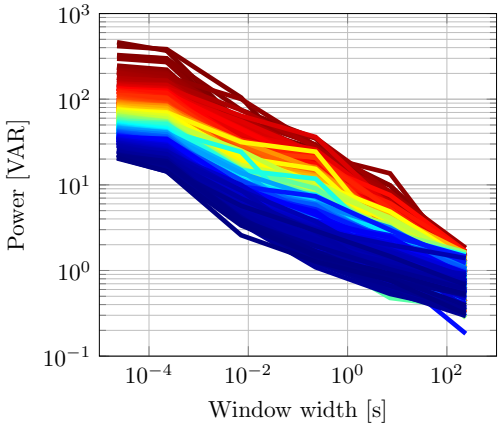

Figure 14: Power vs. window width of woofer

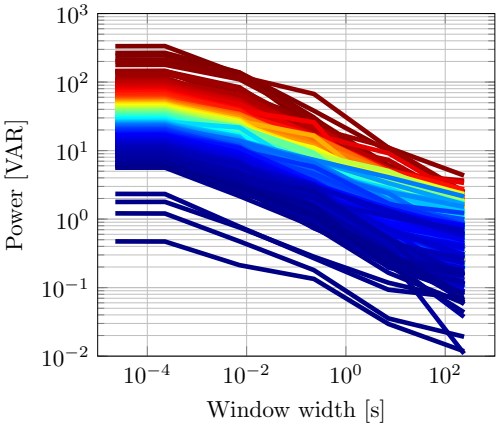

Figure 15: Power vs. window width of subwoofer

Artist	**Title**	P_{peak}	P_{avg}	CF
The Oscar Peterson Trio	Things Ain't What They Used to Be	231	0.75	15.8
Wolfgang Amadeus Mozart	Symphony No.41 in C, K.551 - 'Jupiter'	208	0.75	14.9
Ludwig Van Beethoven	Symphony No.6 - Andante molto mosso	159	0.49	11.4
Art Tatum	Hallelujah	115	0.17	13.7
Louis Armstrong	Makin' Whoopee ft. Oscar Peterson	105	0.47	11.1
Wolfgang Amadeus Mozart	Concerto per Clarinetto K622	106	0.91	11.3
The Beatles	Love You To	30	0.81	4.8
Art Tatum	A Foggy Day	25	0.76	6.6
Skrillex	With Your Friends (Long Drive)	18	0.72	2.9
Bill Evans Trio	Autumn Leaves	43	0.71	6.8
Metallica	Orion	10	0.15	4.7
D-A-D	True Believer	10	0.26	5.5
Beastie Boys	Beastie Boys	11	0.26	4.8
Skrillex	Rock N' Roll	11	0.30	2.3
Slayer	Reborn	12	0.35	6.1
Green Day	F.O.D./All By Myself	30	0.14	8.4
Metallica	The Thing That Should Not Be	11	0.15	4.8
Beastie Boys	Sabrosa	50	0.16	6.4
Bill Evans Trio	Nardis	115	0.17	8.6
Vivaldi	Autumn - Adagio	84	0.21	18.5

Table 1: Woofer: 5 worst case peak power tracks, 5 worst case average power tracks, 5 best case peak power tracks and 5 best case average power tracks

PSU's in integrated sound systems such as mobile phones, audio docks and active loudspeakers. It must however be mentioned that the results are the first results obtained using this new method. These results will be evaluated further in future work. One known error source is that the high peak values in a minority of the audio material analysed was caused by clicks and noise in the tracks that properly shouldn't be reproducible. Further more a more accurate result can be obtained by the use

Artist	**Title**	P_{peak}	P_{avg}	CF
The Oscar Peterson Trio	Things Ain't What They Used to Be	166	0.86	15.8
Bill Evans Trio	Nardis	100	2.16	8.6
Vivaldi	Summer - Adagio	71	0.19	14.9
Art Tatum	Hallelujah	57	0.14	13.7
Beastie Boys	Slow And Low	54	1.02	5.4
Bill Evans Trio	Nardis	100	2.1	6.0
Beastie Boys	Twenty Questions	50	1.8	5.1
Common:	I Used To Love H.E.R [Explicit]	37	1.6	3.7
Skrillex	Kill Everybody (Bare Noize remix)	21	1.15	2.6
Metallica	Suicide & Redemption J.H.	33	1.01	6.9
Vivaldi	Spring - Largo	0.2	0.01	7.4
R. Wagner	Die Walkure-Solti	0.9	0.03	5.8
Louis Armstrong	Nobody Knows the Trouble I've Seen	2.8	0.03	10.1
Wolfgang Amadeus Mozart	Sinfonia Concertante K364	2.8	0.03	10.5
Verdi	Giuseppe: O patria mia (Aida)	3.3	0.01	6.1

Table 2: Subwoofer: 5 worst case peak power tracks, 5 worst case average power tracks and 5 best case peak power tracks

of a non-linear driver model and by adding the loudspeaker box to the model. Despite the above mentioned issues it is still interesting to point out the most power demanding tracks found in this work and a list is provided in table 1 - 2.

4. CONCLUSION

Until now designers of active loudspeakers only had rough estimations of the power requirements at hand based on sinusoidal input excitation and a resistive load. In this work a first attempt towards a realistic requirements specification is taken considering audio material as input, loudness normalization of the audio material, crossover filters, the desired maximum loudness level as well as a model of the drivers of the loudspeaker. The proposed method has the potential to decrease the size and cost of the AMP's + PSU because it enables a customized design. In this work more than 400 audio tracks were analysed which is a minuscule sample compared to existing audio material. The search for worst case audio tracks should therefore be continued and the accuracy of the method should be improved and validated experimentally. Finally the designers of AMP's and PSU should start to take advantage of the fact that a minimal design instead of a conservative and over sized design is durable for audio applications.

5. REFERENCES

[1] ICEpower, *ICEpower50ASX2 - 2x50W or 1x170W ICEpower Amplifier with integrated ICEpower Supply.* Rev. 1.3.

[2] Hypex, *SMPS400 - High Efficiency Audio SMPS.*

[3] Texas Instruments, *SLOU293C - A 600-W, Isolated PFC Power Supply for AVR Amplifiers Based on the TAS5630 and TAS5631.* Rev. 2012.

[4] R. Bortoni, S. N. Filho, and R. Seara, "On the design and efficiency of class a, b, ab, g, and h audio power amplifier output stages," *J. Audio Eng. Soc*, vol. 50, no. 7/8, pp. 547–563, 2002.

[5] A. Knott and L. P. Petersen, "Comparison of power supply pumping of switch-mode audio power amplifiers with resistive loads and loudspeakers as loads," in *Audio Engineering Society Convention 134*, May 2013.

[6] N. E. Iversen and A. Knott, "Small-signal loudspeaker impedance emulator," in *Audio Engineering Society Convention 136*, Apr 2014.

[7] F. Gonzalez-Espin, E. Figueres, G. Garcera, and J. Sandia, "Design of closed loop audio

power amplifiers by means of an accurate model of vented box loudspeakers," in *Power Electronics and Applications, 2007 European Conference on*, pp. 1–9, IEEE, 2007.

[8] R. Bortoni and H. Sette Silva, "Loudspeakers' electric models for study of the efforts in audio power amplifiers," in *Audio Engineering Society Convention 115*, Oct 2003.

[9] P. J. Chapman, "Programme material analysis," in *Audio Engineering Society Convention 100*, May 1996.

[10] M. Mijic, D. Masovic, D. Sumarac Pavlovic, and M. Petrovic, "Statistical properties of music signals," in *Audio Engineering Society Convention 126*, May 2009.

[11] "Dynamic range database." www.dr.loudness-war.info.

[12] G. A. Soulodre, "Evaluation of objective loudness meters," in *Audio Engineering Society Convention 116*, May 2004.

[13] EBU, "Loudness normalisation and permitted maximum level of audio signals," Tech. Rep. EBU R 128-2011, European Broadcasting Union, Le Grand-Saconnex, 1218 Geneva Switzerland, August 2011.

[14] ITU, "Algorithms to measure audio programme loudness and true-peak audio level," Tech. Rep. ITU-R BS.1770-3, International Telecommunication Union, Place des Nations, 1211 Geneva 20 Switzerland, August 2012.

[15] E. Benjamin, "Preferred listening levels and acceptance windows for dialog reproduction in the domestic environment," in *Audio Engineering Society Convention 117*, Oct 2004.

[16] H. A. Breinbauer, J. L. Anabalón, D. Gutierrez, R. Cárcamo, C. Olivares, and J. Caro, "Output capabilities of personal music players and assessment of preferred listening levels of test subjects: Outlining recommendations for preventing music-induced hearing loss," *The Laryngoscope*, vol. 122, no. 11, pp. 2549–2556, 2012.

[17] E. Sturtzer, G. Pillonnet, N. Abouchi, and F. Goutti, "System approach to avoid audio amplifier oversizing in mobile phone application," in *Audio Engineering Society Conference: 43rd International Conference: Audio for Wirelessly Networked Personal Devices*, Sep 2011.

Appendix F

Power Requirements of Sound Systems

Draft ready for submission to Journal of the Audio Engineering Society (JAES) 2015.

Power Requirements of Sound Systems

Henrik Schneider, AES Member
Lars Press Petersen, AES Member
Arnold Knott, AES Member
and Michael A. E. Andersen, AES Member

Dept. of Electrical Engineering, Technical University of Denmark, Kongens Lyngby, DK-2800, Denmark

Abstract

The actual power requirements of a given sound system during playback of music has not received much attention in the literature. This is probably because no single and simple solution exists and because a complete system knowledge from input voltage to output sound pressure level is required. There are however many advantages that could be harvested from such knowledge like size, cost and efficiency improvements. In this paper a model for sound system power requirements is presented and experimentally validated. The model is used to analyze a huge collection of different music genres and different transducers with varying characteristics. Finally the knowledge obtained from these studies is applied in a radical low cost and low size power supply design customized for sound system applications.

Introduction

For many years it seemed like the saying "more is better" applied for amplifier power in a sound system. In recent years the game has changed since many new sound systems integrate the power supply, the amplifiers and the transducers in a single unit. New design possibilities arise as a consequence of the integration but at the same time size and cost of the main components is a major challenge. Present design practices relying on sinusoidal test signals and resistive amplifier loads which are far from the actual audio signals and amplifier loads are hindering improvements in this area [1–7]. Previous work presented a power requirements model and provided an experimental validation [8,9]. This paper presents this research in a condensed form and expand the analysis to cover the power requirements of 128 different 6.5" transducers enabling a one-fit-all design approach for the power supply and amplifier design. The combined knowledge is applied in a radical low cost and low size power supply design customized for sound system applications.

Power Requirements Model

The power required during audio reconstruction is mainly a function of the audio material being reproduced, the desired loudness level and the efficiency of the loudspeaker as illustrated in figure 1. In order to ensure a fair power requirements comparison of different audio tracks a loudness normalization can be performed. A gain that is equivalent to the maximum desired loudness level can be applied after the normalization each audio track. A listening test revealed that a measured value of 85 dB a-weighted performed with a SPL-meter from a distance of 3 meters was very loud. In the end it is up to the designer to specify the desired maximum sound pressure level for a given application.

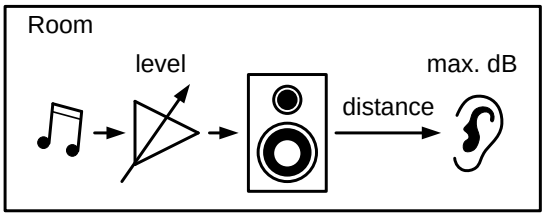

Figure 1: Simple illustration of the main parts that influence the power requirements of a sound system

At model of the loudspeaker was implemented in Matlab/Simulink (figure 2) based on the following fundamental loudspeaker equations.

$$u(s) = R_e i(s) + sL_e i(s) + \frac{R_2 s L_2}{R_2 + sL_2} i(s) + sBlx(s) \tag{1}$$

$$f(s) = Bl \cdot i(s) \tag{2}$$

$$f(s) = M_{ms} s^2 x(s) + R_{ms} s x(s) + \frac{1}{C_{ms}} x(s) \tag{3}$$

where $u(t)$ is the voice coil voltage, R_e is the voice coil resistance, L_e is the voice coil inductance, R_2 and $L2$ models the eddy current effect, $i(t)$ is the voice coil current, u_{emf} is the voltage induced by the back electromotive force, Bl is the force factor (flux in the gap times the length of the wire in the gap), $v(t)$ is the velocity of the cone, R_{ms} is the suspension related loss due to friction, M_{ms} is the mass of the moving assembly, C_{ms} is the compliance of the suspension and $f(t)$ is the Lorentz force applied to the moving assembly. The model was inspired by [10–12]

The major non-linearities such as the suspension compliance $C_{ms}(x)$, the force factor $Bl(x)$ and the voice coil inductance $L_e(x)$ is also included in the model. Measurements of the non-linear parameters as a function of the displacement can be fitted to polynomials by

$$L_e(x) = \sum_{n=0}^{N-1} a_n x^n \quad Bl(x) = \sum_{n=0}^{N-1} a_n x^n \quad C_{ms}(x) = \sum_{n=0}^{N-1} a_n x^n \tag{4}$$

where N is the order of the polynomial and a_n is the n^{th} coefficient of the polynomial.

The filter block in the Matlab/Simulink model can be used to implement a crossover filter and equalization wich will also influence the power requirements of the individual transducer in a given sound system. As the voice coil voltage and current are stored during a simulation of a given audio track the instantaneous power can be calculated and the power requirements can be analyzed.

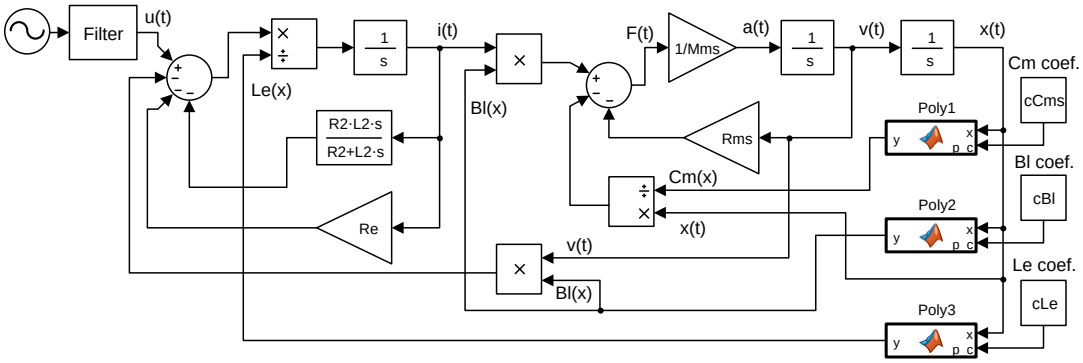

Figure 2: Simulink model of voltage driven transducer

Proposed Power Analyzes

The peak and average power can easily be calculated based on a simulation but the worst case power requirements scenario during playback of an audio track is harder to predict. Figure 3 illustrate the recommended scheme for analysis of the power requirements as a function of time (window width). The stored data of the voltage and current from the simulation were multiplied to form the power signal. Then the power signal is multiplied in the time domain with a square window with stepwise logarithmically increasing window width. For each window width the window is moved forward with 1 sample until the window reaches the end of the music signal. Every time the window is moved, the apparent power of the signal within the window is calculated by (5) and the maximum value is stored for that particular window size. The result should be the worst case power requirement scenario vs. time.

$$|S| = \frac{1}{N}\sqrt{\sum_{n}^{N} v(n)^2 i(n)^2} \tag{5}$$

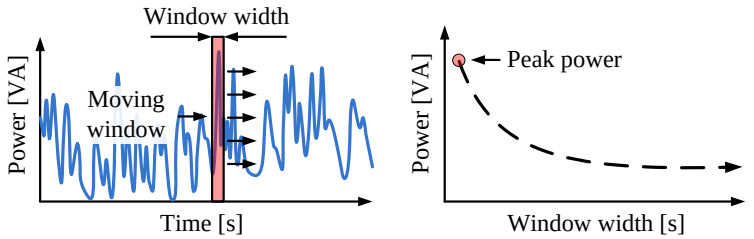

a) Short window

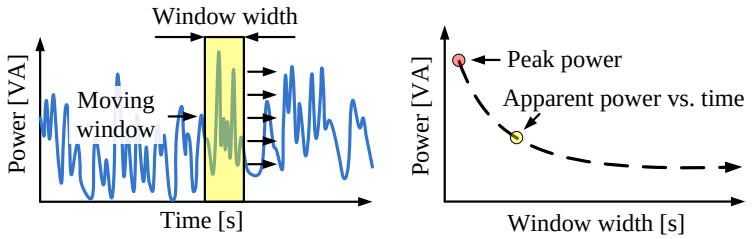

b) Medium window

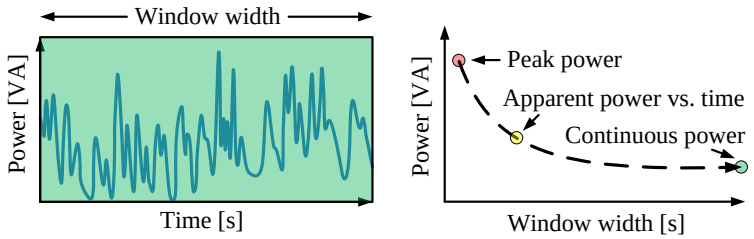

c) Long window

Figure 3: Power analysis

Validation of Power Requirements Model

In order to verify the model a simple measurement setup was established. A 2 way loudspeaker developed by PointSource Acoustic and suitable amplifiers were acquired. The voice coil voltage and current was preconditioned on a small circuit board before being send to a Data Acquisition Device (DAQ) from National Instruments which was controlled via Matlab. The setup is seen in figure 4.

Figure 5 shows the result of the closed box woofer validation. At low voice coil voltage (4.3 V_{pk}) the coherence of the linear model is better than the non-linear model. On the contrary the linear model overestimates the peak power at higher voice coil voltages (10.8 V_{pk}). This discrepancy could be caused by the fact that the non-linear parameters are measured at high voltage levels and not low voltage levels. Based on these results the linear model is considered to be sufficient for the purpose of analyzing the power requirements of sound systems. It will provide a small overhead in terms of the peak power requirement and the simulation complexity and simulation time will be drastically reduced which is a

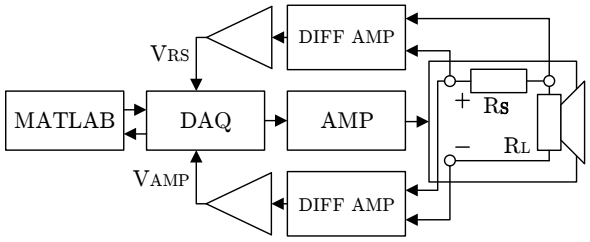

Figure 4: Simplified measurement setup

huge advantage.

Figure 6 shows a comparison of the measured tweeter with and without a passive cross-over filter and a linear simulation. It is clearly seen that the power requirement of the tweeter is different from that of the woofer. It is commonly seen that two identical amplifiers are used to drive the woofer and the tweeter. It is also commonly seen that several hundreds of watt are allocated for the tweeter. Knowledge like this could prevent such over dimensioned designs and be used to optimize both the transducers, the amplifiers and the power supplies in sound systems.

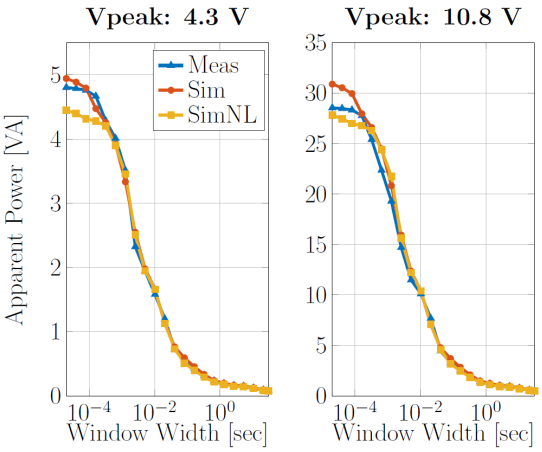

Figure 5: Closed box woofer power analyzis

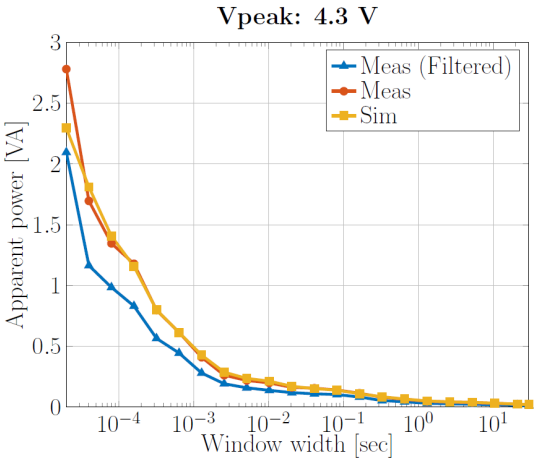

Figure 6: tweeter power analyzis

Power Analysis of 400 Music Tracks

Since the worst case power requrements are depending on the dynamics of a given audio track the search for the worst case tracks were initiated. 400 music tracks of various genres were gathered and analyzed using the linear loudspeaker model. The result of the analysis for a woofer can be seen in figure 7. As seen the required peak power of the 400 audio tracks varies from 20 W to 500 W indicating the importance of a continuous search for the worst case audio tracks. The worst case power requirements of this analysis is reduced from 500 VA to 40 VA in 0.1 second. In comparison the state-of-the-art power supplies and amplifiers are rated for more than 80 seconds of peak power [13–15]. It can also be observed that the power peaks can be expected to be 250 times higher than the average power. This is a true inspiration to radical design changes.

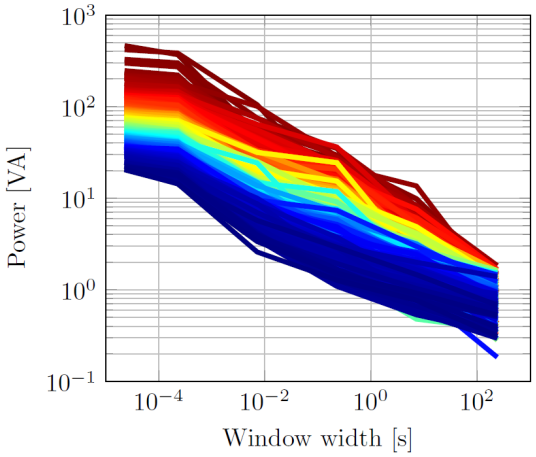

Figure 7: Simplified measurement setup

Power Analysis of 128 different 6.5” Woofers

As mentioned earlier the characteristics of each transducer in a loudspeaker is influencing the power requirements. A statistical analysis of the power requirements of 128 loudspeakers with similar size (6.5”) was therefore conducted. The linear parameters was acquired from various databases on the internet and processed in Matlab. The frequency response of all the transducers were equalized to the same target response to enable a fair comparison and then each transducer was simulated with the linear transducer model and the same audio material. Figure 8 shows a zoom of the power curves obtained by simulation. As seen the variance in complex power (VA) is large. Results like this could be important for future designs of general purpose (one-fit-all) power supplies and amplifiers modules.

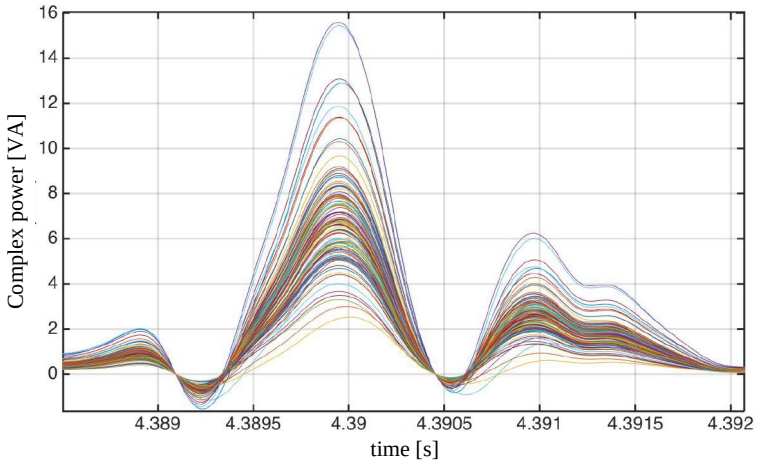

Figure 8: Power variance as a function different transducers

Examble of a radical power supply design

This chapter briefly presents an universal mains (90 V_{RMS} - 264 V_{RMS}) active clamp forward converter designed to deliver 25 V out and 200 W peak power for a short period of time. A schematic is shown in figure 9. The active clamp circuit (Q_C and C_C) enables zero voltage switching which enable a high switching frequency without severe switching loss as a penalty. The operational switching frequency is set to 500 kHz which is about 5 times higher than typical audio power supplies. Future work will aim to increase the switching frequency up to 1 Mhz in order to futher decrease the size of the magnetic components. A prototype of the converter is seen in the left of figure 10 and a commercial power supply with similar specifications is shown in the right of figure 10. The big difference between the two power supplies is the operating switching frequency and the amount of time that they can drive 200 W peak power. As a consequence the magnetic components are much smaller and no heatsinks are required which

result in more than 5 times smaller prototype compared to the commercial power supply. The cost are expected to decrease in a similar manner.

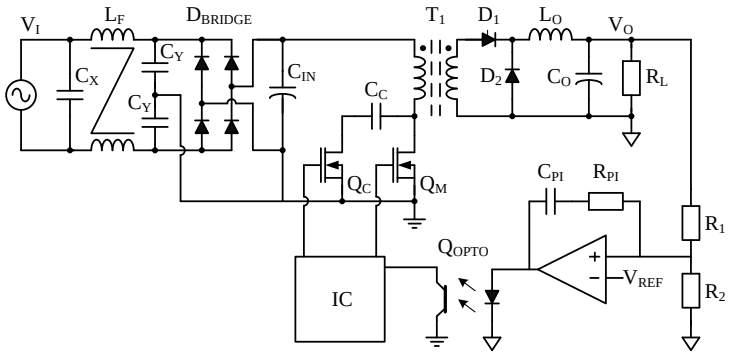

Figure 9: Schematic of the active clamp forward converter

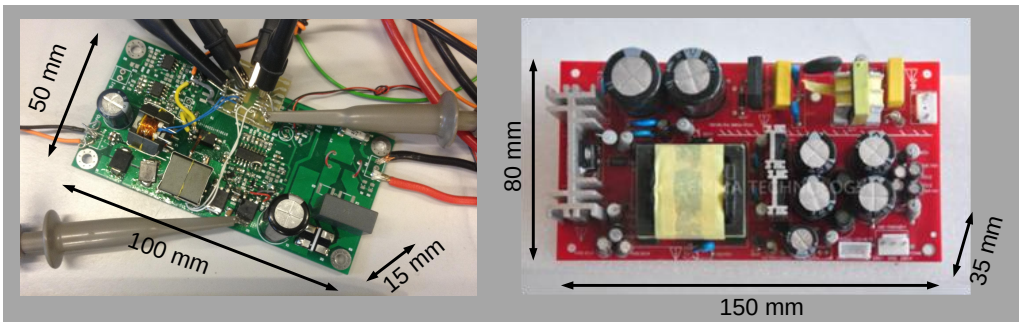

Figure 10: Power supplies: prototype (left) and commercial (right)

The prototype was initially tested with an electrical load that was programmed to simulate a deep bass rhythm with 160 beats per minute. The power test is illustrated in figure 11. Thermal sensors were placed near the semiconductors and inside the magnetic components between the windings and the core. The temperature measurements confirmed that no severe temperature hot spots occurred during the tests. The hottest measured temperature with the sensors and an infrared temperature camera was 89 °C. Later on the prototype was setup to drive a 2.1 stereo where an extreme bass boost was utilized. Even when this sound system was pushed to its limits the maximum measured temperature of the power supply was 69 °C. This work indicate the importance of considering audio signals instead of rough simplifications of audio signals in both the design phase and test phase.

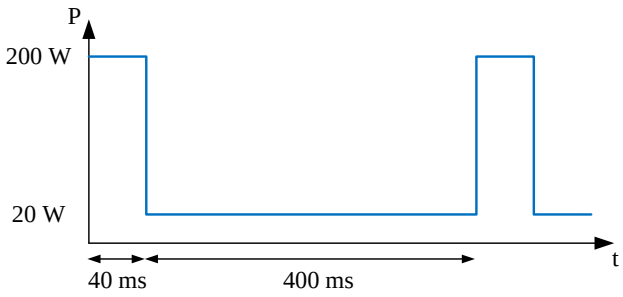

Figure 11: Power supply test signal simulating a deep bass rhythm with 160 beats per minute

Conclusion

Until now sound system engineers only had rough estimations of the power requirement at hand based on assumptions far from the real application. In this paper a method for realistic requirement specifications are presented and used to investigate the influence of different music and different transducers of similar size. It was found that full power capability is only needed for a few milliseconds which inspire radical design changes and large reduction of size and cost for power supplies, amplifiers and transducers. A radical design of a power supply prototype was investigated and despite a size reduction of more than 5 times compared to a commercial power supply the prototype was able to drive a 2.1 stereo setup with a huge bass boost without thermal issues. Future work should expand this power requirements analysis to a range of different sound system applications and investigate a broader range of audio material. The common design practice of power supplies, amplifiers and transducers should be reconsidered in regards to the acquired knowledge.

References

[1] R. Bortoni, S. N. Filho, and R. Seara, "On the design and efficiency of class a, b, ab, g, and h audio power amplifier output stages," *J. Audio Eng. Soc*, vol. 50, no. 7/8, pp. 547–563, 2002.

[2] A. Knott and L. P. Petersen, "Comparison of power supply pumping of switch-mode audio power amplifiers with resistive loads and loudspeakers as loads," in *Audio Engineering Society Convention 134*, May 2013.

[3] N. E. Iversen and A. Knott, "Small-signal loudspeaker impedance emulator," in *Audio Engineering Society Convention 136*, Apr 2014.

[4] F. Gonzalez-Espin, E. Figueres, G. Garcera, and J. Sandia, "Design of closed loop audio power amplifiers by means of an accurate model of vented box loudspeakers," in *Power Electronics and Applications, 2007 European Conference on*, pp. 1–9, IEEE, 2007.

[5] R. Bortoni and H. Sette Silva, "Loudspeakers' electric models for study of the efforts in audio power amplifiers," in *Audio Engineering Society Convention 115*, Oct 2003.

[6] P. J. Chapman, "Programme material analysis," in *Audio Engineering Society Convention 100*, May 1996.

[7] M. Mijic, D. Masovic, D. Sumarac Pavlovic, and M. Petrovic, "Statistical properties of music signals," in *Audio Engineering Society Convention 126*, Audio Engineering Society, 2009.

[8] H. Schneider, L. C. Jensen, L. P. Petersen, A. Knott, and M. A. Andersen, "Requirements specication for ampliers and power supplies in active loudspeakers," in *AES 137th Convention*.

[9] H. Schneider, A. M. Madsen, R. Bjerregaard, A. Knott, and M. A. Andersen, "Validation of power requirement model for active loudspeakers," in *AES 138th Convention*.

[10] W. M. Leach, *Introduction to electroacoustics and audio amplifier design*. Kendall/Hunt Publishing Company, 2003.

[11] G. Pillonnet, E. Sturtzer, T. Rossignol, P. Tournier, and G. Lemarquand, "Distortion improvement in the current coil of a loudspeaker," in *Audio Engineering Society Convention 134*, Audio Engineering Society, 2013.

[12] E. Sturtzer, G. Pillonnet, G. Lemarquand, and N. Abouchi, "Comparison between voltage and current driving methods of a micro-speaker," *Applied Acoustics*, vol. 73, no. 11, pp. 1087–1098, 2012.

[13] ICEpower, *ICEpower50ASX2 - 2x50W or 1x170W ICEpower Amplifier with integrated ICEpower Supply*. Rev. 1.3.

[14] Hypex, *SMPS400 - High Efficiency Audio SMPS*.

[15] Texas Instruments, *SLOU293C - A 600-W, Isolated PFC Power Supply for AVR Amplifiers Based on the TAS5630 and TAS5631*. Rev. 2012.

Appendix G

Multitone distortion in voltage and current driven loudspeaekers

---

Draft ready for submission to Journal of the Audio Engineering Society (JAES) 2015.

Appendix H

Hybrid winding concept for toroids

IEEE Energy Conversion Congress and Exposition Asia 2013 (ECCE Asia)

Hybrid winding concept for toroids

Henrik Schneider, Thomas Andersen, Arnold Knott, Michael A. E. Andersen
Technical University of Denmark - DTU
Kongens Lyngby, Denmark

***Abstract* - This paper proposes a hybrid winding concept for toroids using the traces in a printed circuit board to make connection to bended copper foil cutouts. In a final product a number of strips with a certain thickness would be held by a former and the whole assembly could be placed by pick and placement machinery. This opens up the possibility for both an automated manufacturing process and an automated production process of toroidal magnetics such as power inductors, filtering inductors, air core inductors, transformers etc. Both the proposed hybrid and the common wire wound winding implementation is simulated using finite element modeling and the DC and AC resistance of the inductors are verified with experimental measurements on prototypes. It is found that commercial available layer thickness of printed circuit boards is a bottleneck for high power applications. Furthermore, the winding configuration is crucial for performance.**

Keywords—inductor; toroid; toroidal; FEM, winding resistance

I. INTRODUCTION

The spacing between the windings in a single layer wire wound toroidal inductor increases gradually from the inner diameter towards the outer diameter of the core. This limits the utilization of the available winding space for a single layer winding – see Fig. 1a. Furthermore, in the manufacturing process of a toroidal inductor with a large diameter wire and a small core a hook/pull type winding machine is utilized. Under manufacturing a tool must pass through the center of the toroidalcore to grab and pull the wire which is manually feed to the hook for each turn. Utilizing more of the windings space by customization of the winding leads to either a constant resistance with increased number of turns or constant number of turns with decreased resistance for the same core size [1-6]. In Fig. 1b a manufacturing process that alters the width of the wire periodical along the length of the wire was used to take advantage of winding customization. However the altering of the wire requires special machinery and must also use the manual operated hook/pull machine for thick wires. The PCB integrated toroid shown in Fig. 1c has the potential to utilize the full winding space and simplify the manufacturing. However the DC resistance of the winding is limited by the PCB layer thickness and a core is difficult to embed. The foil wound toroid shown in Fig. 1d eliminates the disadvantages of the PCB integrated toroid except the manufacturing process which is even more difficult than the wire wound process and completely manual.

In this work a hybrid winding solution is proposed – see Fig. 1e. The winding consist of bended copper foil cutouts which are connected through the PCB. The obvious advantages compared to the other single layer toroids is great utilization of the winding space together with a potential of a fully automatic process from manufacturing to assembly with pick and place machinery.

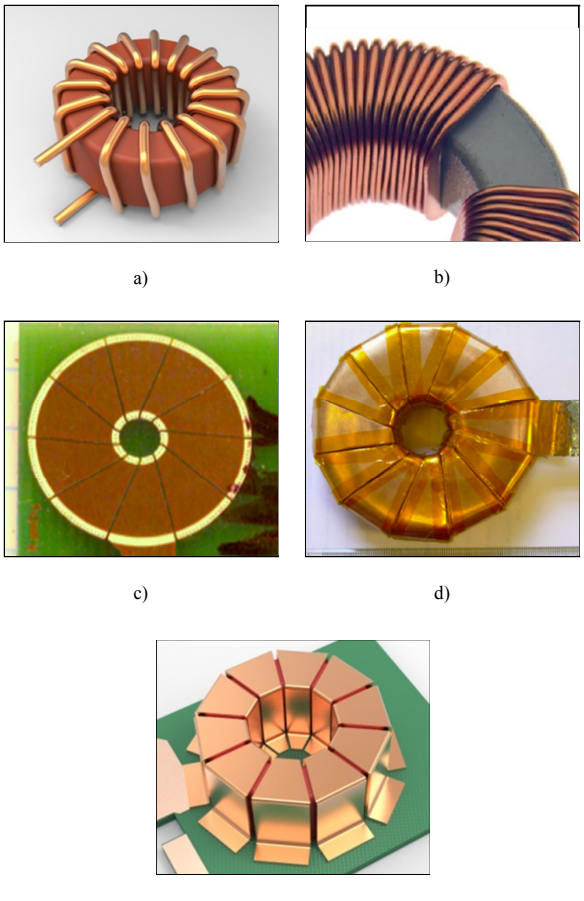

a) b) c) d) e)

Fig. 1 Single layer toroidals a) Conventional wire wound. b) Squized wire wound [1] . c) PCB integrated [2] d) Foil wound [3] e) Foil based hybrid.

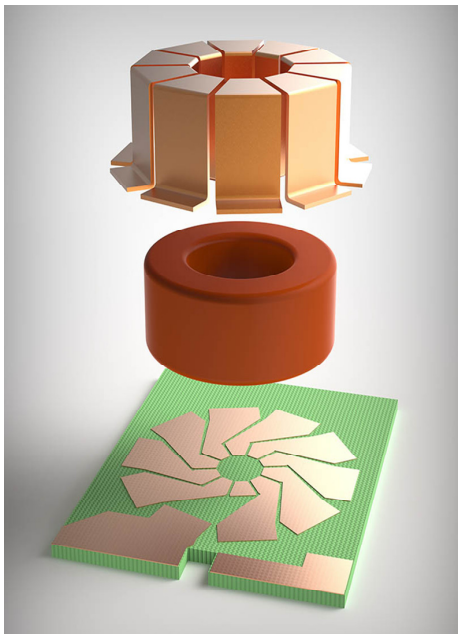

Fig. 2 Exploded view of the hybrid toroidal principle

The outline of this work is split into sections describing the pros and cons of the hybrid winding concept in section II, deriving the geometry and dimension of the winding in section III, Validating FEM with experimental results for the winding resistance and exploring the opportunities of the solution in section IV.

II. HYBRID WINDING CONCEPT

The basic idea is to cut and bend copper foils into "U" shaped foil cutouts that fits the core as shown in Fig. 2. To complete the winding the foil pieces needs to be connected through the PCB traces. The number of foil cutouts determines the maximum number of turns, thus the designer has the flexibility to customize the connections in the PCB as suited. In a final product the foil pieces would be pre-attached to a former for easy handling and alignment on the PCB. The hybrid winding concept may have the following benefits compared to the conventional single layer wire wound inductor:

- Large scale production and distributed stock of foil assemblies reduce cost and delivery time.
- Fully automated manufacturing process. Foil pieces are stamped, bended and attached to a plastic former. The core and the foil assembly can be placed by a pick and place machine.
- Better utilization of winding space. Constant resistance with increased number of turns or constant number of turns with decreased resistance for the same core size
- Low AC resistance due to increased surface area using foil.
- Configurable winding structure. The connections of the foil pieces through the PCB can be freely defined by the design engineer. The number of turns can be decreased by paralleling the foils pieces. It enables the same foil assembly to be used for inductors, common mode EMC chokes, transformers etc.
- Different core materials can be used with the same foil assembly.

The disadvantages may be as followed:

- Commercial available PCB layer thickness and interconnections between the foil cutouts and the PCB tracks is a bottle neck for high power applications.
- The assembly of the foil cutouts is limited to a specific core size.

III. DERIVING THE DIMENSIONS OF THE FOIL CUTOUT

Fig. 3a shows a cross section view of the core and the foil cutout through the symmetry axis of a winding space. The foil is divided into five segments S1-S5. Fig. 3b shows a top view of a half winding space used for calculating the dimensions of the foil cutout. The angle W_{SA} that determines the full winding space is determined by the number of turns N and thus

$$W_{SA} = 2\pi/N \tag{1}$$

In this section the details of each segment of the foil cutout is explained and formulas governing the dimensions are derived using simple geometry. The parameters known in advance is the number of turns N, the inner radius of the core C_{IR}, the outer radius of the core C_{OR}, the height of the core C_H, the clearance between the windings W_C and the foil thickness F_T.

A. Segment S1

The length of the inner solder tap F_{IT} depends on the inner radius of the toroid, the foil thickness, the clearance and the number of turns.

$$F_{IT} = C_{OR} - F_W - F_T - W_{CT} \tag{2}$$

where F_W is given in equation (9) and

$$W_{CT} = W_C/\left(2sin(\pi/N)\right) \tag{3}$$

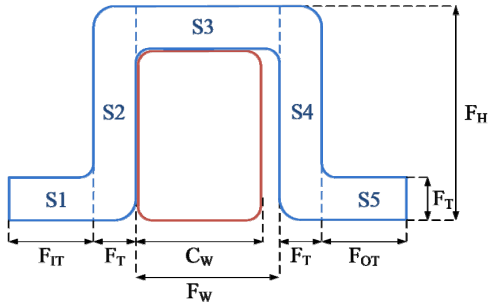

a)

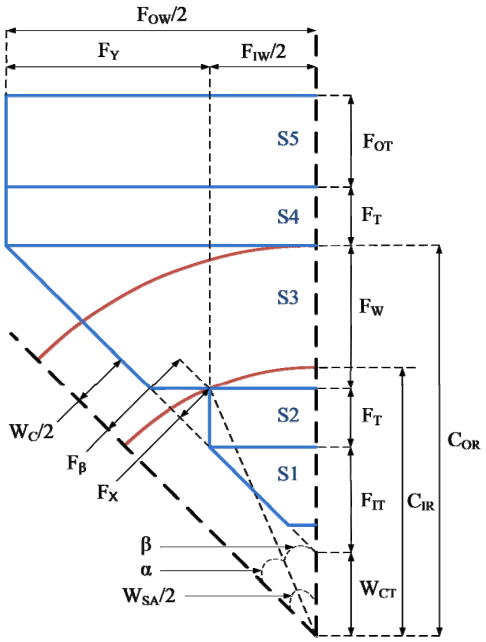

b)

Fig. 3 a) Cross sectional view of assembly. b) Top view of a halve winding space.

In this design the tip of the tap is shortened to avoid sharp angles. The maximum width of the tap depends on the width of the inner foil bend F_{IW}.

B. Segment S2

The width of the inner foil bend F_{IW} depends on the clearance between the windings W_C, the inner radius of the toroid C_{IR} and the thickness of the foil F_T. F_{IW} is given by

$$F_{IW} = 2C_{IR}sin(\beta) \tag{4}$$

where

$$\beta = W_{SA}/2 - \alpha \tag{5}$$

$$\alpha = sin^{-1}(F_\beta/C_{IR}) \tag{6}$$

$$F_\beta = W_C/2 + F_X \tag{7}$$

$$F_X = F_T sin(W_{SA}/2) \tag{8}$$

C. Segment S3

The section covering the top of the toroid F_W is given by

$$F_W = C_{OR} - C_{IR}cos(\beta) \tag{9}$$

D. Segment S4

The width of the outer bend F_{OW} is limited by the clearance.

$$F_{OW} = F_{IW} + 2F_Y \tag{10}$$

where

$$F_Y = (F_T + F_W)tan(W_{SA}/2) \tag{11}$$

E. Segment S5

The outer foil tap must be as small as possible to reduce the footprint area of the inductor but long enough to secure the foil.

IV. Results

The resistance of the winding is hard to predict analytically due to changes in the cross sectional area of the foil and PCB tracks and therefore FEM analysis is used. A 3D model as well as a prototype of both the wire wound and the hybrid toroidal inductor is created in order to validate the FEM models with measurements.

In order to simplify the cut and bending of the foil cutouts for the hybrid prototype a total of 10 turns is implemented as shown in Fig. 4a. The thickness of the foil is 0.5 mm and the PCB is CNC milled on a single layer board with 70um copper. The wire wound inductor shown in Fig. 4b. have 11 turns and the diameter of the wire is 1.5mm. It is important to note that the prototypes were not created for a specific application or for direct comparison of the winding technology but for validating the FEM model. The validated model is later used to explore the properties of the hybrid inductor.

Fig. 5 illustrates two of the FEM simulations to calculate the AC resistance of the inductors as a function of frequency. The colors of the winding illustrate the current distribution. As expected the current is running close to the core.

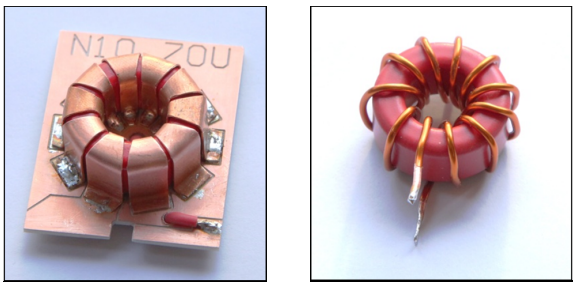

a) b)

Fig. 4 a) Hybrid prototype. b) wire wound prototype

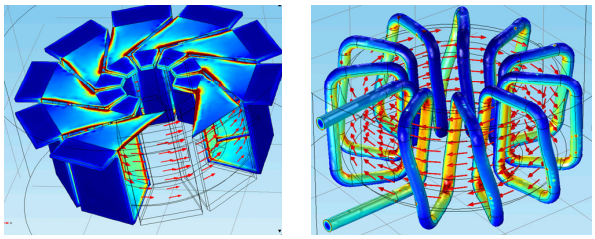

a) b)

Fig. 5 FEM simulation illustrating current density and the magnetic flux density. a) Bottom view of the hybrid inductor. b) Wire wounded inductor

The result of the resistance for the hybrid inductor is shown in Fig. 6 for both the measured and simulated values. A low frequency the resistance is simulated to a lower value than the measured. The source of deviation might be caused by soldering material, imprecise cuts and clearance of the bended foils, all of which are not included in the FEM simulation. Therefore, an offset of 2.5 mΩ is added to the result from the FEM simulation to compensate for any static sources of resistance. This additional line with an offset of 2.5 mΩ is added in Fig. 6. The simulation with offset fits the measured results close 10 Hz to 100 kHz.

The result of the resistance as function of frequency for the wire wounded inductor is shown in Fig. 7. The FEM simulation fits the measurement from 10 Hz to 100 kHz.

For both the hybrid and the wire wounded FEM model the resistance starts to deviate above 100 kHz. As the same core material is used for both prototypes the deviation above 100 kHz might be caused by an improper loss model for the magnetic core material - which is out of the scope in this work.

From the FEM simulation of the hybrid inductor in Fig. 5a it can be observed from the colors that the highest current density is in the PCB that connects all the bended copper foils. This is reasonable as the PCB thickness is only 70 µm compared to the foil which is 500 µm thick. A simulation of the PCB thickness impact on the total DC resistance of the hybrid inductor is plotted in Fig. 8. The DC resistance of the hybrid prototype with foil thickness of 0.5 mm is reduced by 60 % using a double sided PCB layer of 70 µm copper

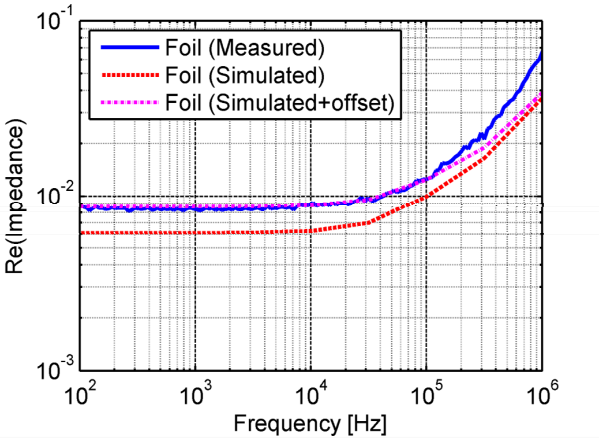

Fig. 6. Plot of resistance as a function of frequency for the hybrid inductor

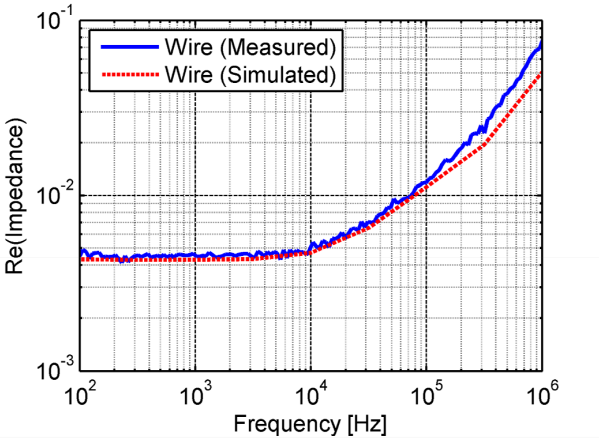

Fig. 7. Plot of resistance as a fuction of frequency for the wire wounded inductor.

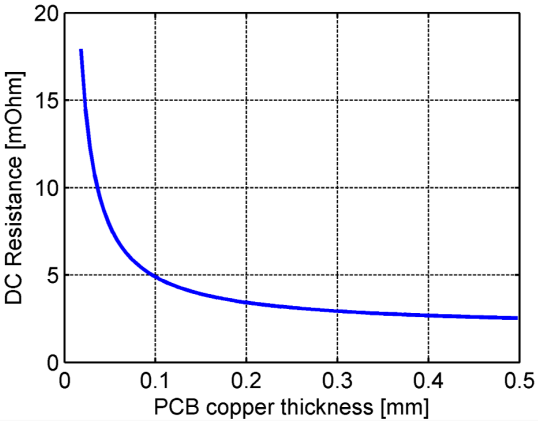

Fig. 8. Simulated DC resistance of the hybrid inductor as a function of PCB copper thickness. Foil thickness is fixed at 500 µm.

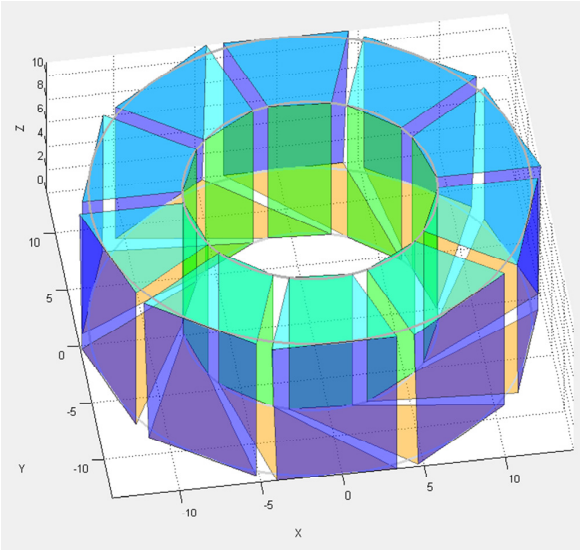

a)

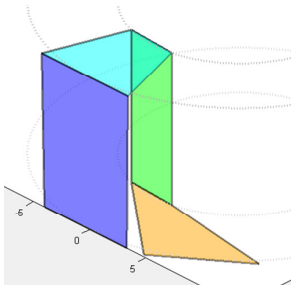

b) Bottom

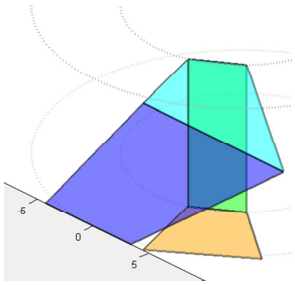

c) Outer

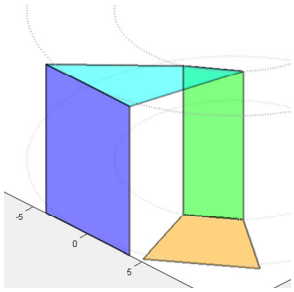

d) Top

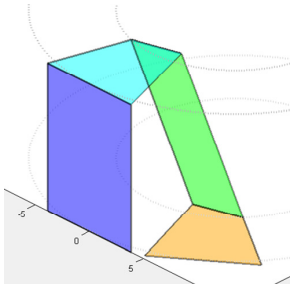

e) Inner

Fig. 9 a) Winding configuration of the 10 turn hybrid prototype with bottom angled. b) Bottom angled. c) Outer angled. d) Top angled. e) Inner angled.

compared to a single layer of 35 µm copper. Thus the bottle neck for the hybrid inductor is the commercial available PCB copper thickness. One way to decrease the resistance is to straighten the path of the PCB trace to make it shorter by angling the copper foil cutouts. A plot of the winding configuration for the hybrid prototype is illustrated in Fig. 8a. The same winding configuration is repeated in Fig. 9b but only a single turn is shown for a clear visual understanding. For this particular winding configuration only the bottom segment of the turns are angled to complete the turns. In Fig. 9c.d.e only the outer, top and inner segment of the turns are angled respectively in order to complete the turn. These simplified 3D models are used by FEM to simulate the DC winding resistance. The DC winding resistance and the improvement compared to the prototype is shown in Table 1. A reduction in DC resistance of 30 % is achieved in this case by choosing a top angled winding configuration. Further investigation is needed to explore combinations of top, bottom, outer and inner angled winding segments to take fully advantage of the hybrid winding concept.

TABLE I.

Foil thickness: 500 µm, PCB thickness: 70 µm				
Winding configuration	***Bottom***	***Outer***	***Top***	***Inner***
DC resistance [mΩ]	6.46	4.75	4.52	4.85
Improvement [%]	Ref.	27	30	25

CONCLUSION

A hybrid winding concept for toroids using the traces in a printed circuit board to make connection to bended copper foil cutouts has been proposed which inherit most of the advantages from the foil wound toroid while offering the potential of a fully automated process from manufacturing to production. The technical principles of the solution have been described and equations governing the dimensions of the foil cutouts needed for an assembly have been derived. Several FEM analyses have been carried out and the models have been experimentally validated. Results shows that the ratio between thickness of copper foil cutouts and PCB traces together with the winding configuration are critical in terms of DC resistance. Future work requires research in optimal winding configurations.

REFERENCES

[1] M. Seitz and M. Roeber, "Squeeze more performance out of toroidal inductors," *Power Electronics Technology,* vol. 31, p. 30, 2005.

[2] P. Kamby, *et al.*, "Printed circuit board integrated toroidal radio frequency inductors," in *IECON 2012-38th Annual Conference on IEEE Industrial Electronics Society*, 2012, pp. 680-684.

[3] M. Nigam and C. R. Sullivan, "Multi-layer folded high-frequency toroidal inductor windings," in *Applied Power Electronics Conference and Exposition, 2008. APEC 2008. Twenty-Third Annual IEEE*, 2008, pp. 682-688.

[4] C. Marxgut, *et al.*, "Multi-objective optimization of ultra-flat magnetic components with a PCB-integrated core," in *Power Electronics and ECCE Asia (ICPE & ECCE), 2011 IEEE 8th International Conference on*, 2011, pp. 460-467.

[5] S. Orlandi, *et al.*, "Optimization of Shielded PCB Air-Core Toroids for High-Efficiency DC–DC Converters," *Power Electronics, IEEE Transactions on,* vol. 26, pp. 1837-1846, 2011.

[6] J. Biela, *et al.*, "Passive and active hybrid integrated EMI filters," *Power Electronics, IEEE Transactions on,* vol. 24, pp. 1340-1349, 2009.

Appendix I

Optimizing dc-resistance of a foil wounded toroidal inductor combining matlab and comsol

IEEE AFRICON 2013

Optimizing DC-Resistance of a Foil Wounded Toroidal Inductor Combining Matlab and Comsol

Henrik Schneider, Thomas Andersen, Arnold Knott and Michael A. E. Andersen

Department of Electrical Engineering,
Technical University of Denmark,
Kgs. Lyngby, 2800, Denmark

***Abstract*—an optimization routine is presented to optimize the shape of a foil winding of a toroid inductor in terms of the DC resistance. MATLAB was used to define the geometry of the foil winding and COMSOL was used to import the geometry and create a 3D finite element model. The initial parameters, the execution and the results of the optimization routine were all managed from a graphical user interface and the feedback from COMSOL in terms of DC resistance was used to find and plot the optimal shape of the foil. The DC resistance was improvement by 31 % compared with previous work for a 10 turn toroidal inductor.**

Keywords—Inductor;Toroid;FEM;Foil;Optimization;GUI

I. INTRODUCTION

The conventional wire wound toroid is used in many power electronic applications such as EMC filters, power inductors, transformers and so on. However it has the following disadvantages regarding the winding scheme and the manufacturing/production process [1, 2]:

- The spacing between the windings increases gradually from the inner diameter towards the outer diameter of the core limiting the utilization of the winding area.
- For large wire diameters a hook/pull type manufacturing machine is used. The space required for the hook and the wire being pulled through the center of the core further decrease the utilized winding area.
- For large wire diameters manual work is required for feeding the hook with the wire leading to increased cost.
- Complex manufacturing machines are needed for winding due to non-separable core.
- Manufacturer lead time and price strongly depends on the purchase history and number of ordered magnetic components.
- The leaded toroid may be placed and soldered manually in a production increasing time to market and cost.

By using thinner wires in parallel the disadvantages regarding the winding space can be improved [1]. However this work focus on a different approach using a hybrid foil + printed circuit board (PCB) based winding scheme in an attempt to improve both the utilized winding space and improve the time to market by creating more freedom in the manufacturing and production process.

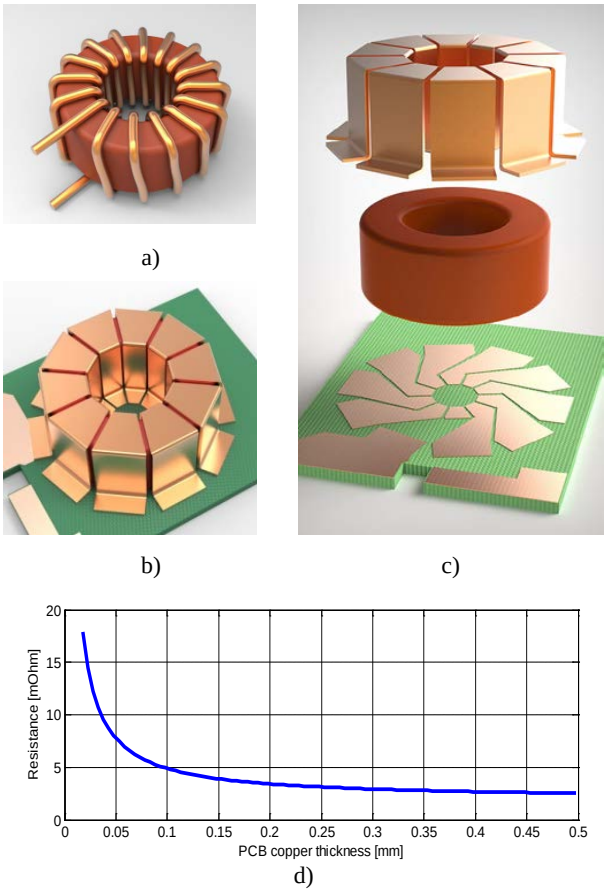

Figure 1. a) Conventional toroidal wire wound inductor. b) Surface mounted hybrid inductor. c) Exploded view of a hybrid inductor. d) Example of a DC resistance vs. PCB layer thickness plot for a hybrid inductor.

The basic idea is to cut and bend copper foils into "U" shaped pieces that fit around the toroidal core as shown in Figure 1.b and Figure 1.c. The number of bended foil pieces determines the number of turns and in a final product all the foil pieces would be pre-attached to a plastic former for easy

handling and alignment on the PCB. This assembly is referred to as the winding assembly. The foil pieces needs to be connected through the PCB traces to complete the winding. In the case of an inductor the completed inductor (winding assembly + connecting PCB tracks) is referred to as the hybrid inductor. A single patent [3] was found late in this work describing the same idea. However no commercial product or relevant publications have been found on the subject.

Different arrangements of the winding assembly with different foil thicknesses, number of turns and core dimensions for various purposes could be sold via component distributors all over the world. Due to large scale production and distributed stock of winding assemblies this could reduce cost and time to market. In addition a fully automatic production process could be utilized where the core and winding assembly were placed by pick and place machinery and soldered along with other surface mount devices (SMD's).

In previous work [4] a hybrid inductor with 15 turns, a foil thickness of 500um and a single layer PCB with a layer thickness of 70um was implemented as a prototype. The measurements were used to evaluate a 3D Finite element model (FEM) created in COMSOL with good agreement. The DC resistance of a 15 turn hybrid inductor with a foil thickness of 500um was simulated and plotted vs. varying PCB layer thicknesses as shown in fig. 1.d. The results showed that typical available PCB layer thicknesses (18um – 210um) are a bottle neck for the DC resistance in a hybrid inductor.

In the implemented model the bended copper pieces went straight over the core and the traces in the PCB was angled to complete the winding as shown in Figure 1.a. and Figure 1.b. It is easy to imagine how the DC resistance would be improved if the thin traces in the PCB were straight and short and the thicker copper pieces were angled over the core connecting the winding. It is however hard to predict the optimum angles of each segment in a turn and to predict the impact on the DC resistance. It is necessary to find an answer to these questions in order to take full advantage of the hybrid inductor.

II. GEOMETRY

In order to find the optimum shape of the foil winding a set of equations governing the geometry of a bendable foil around a toroid was setup in MATLAB. The initial parameters used to define and draw the foil shape was the core dimension, number of turns, clearance between the turns, starting position of the winding following the tangent of the core, angle of each segment in a turn and the thickness of each segment in a turn.

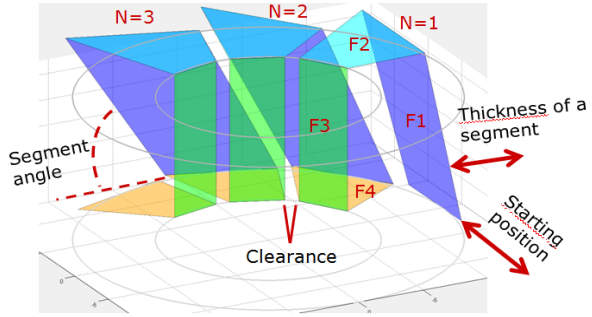

Figure 2. Geometry of the winding and the related parameters

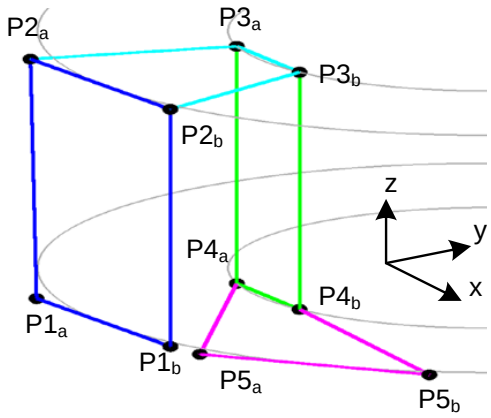

Figure 3. Geometry of the winding and the related parameters

A graphical representation of these parameters is shown in Figure 2. The four segments of a turn are labeled F1, F2, F3 and F4.

A. *Procedure of geometry*

The bendable turn is based on 10 points, connecting the point by straight lines forms four faces as shown in Figure 3. For a winding to be continuous point P5a and P5b must equal point P1a and P1b rotated the angle of a wingding space. The winding space angle is given by (1) where N is the number of turns.

$$A_{ws} = \frac{2\pi}{N} \tag{1}$$

The position of point P1a is defined on the tangent line ($M_{tangent}$) by a starting position angle (A_{sp}). This is illustrated on Figure 4. P2a is based on the location of P1a and rotated according to its predefined segment angle. Likewise is P3a defined by the position of P2a. For the turn to be bendable P4a is based on the interception with the line formed between P3a and P4b in the x-y plan. The remaining "b"-points are calculated from there respected "a"-points by rotating a winding space angle subtracted the distance of clearance.

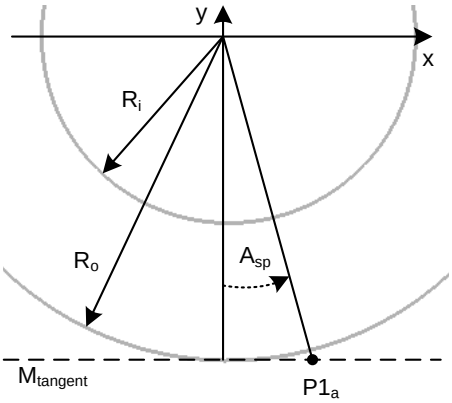

Figure 4: Definition of starting position for point $P1_a$

B. *Illustation*

In Figure 5.a the starting position is offset to the left of the core center line. In Figure 5.b-e the angle of the individual segments of a single turn is varied with a non offset starting position. At first the bottom layer (F4) is angled 100% which indicates that all the other segments in the turn are not angled. Then the remaining segments are angled 100% one at a time. In Figure 5.f the number of turns is very low to verify the geometry of only 3 turns. In Figure 5.g a larger number of turns are selected and finally the clearance is increased in Figure 5.e. The thickness of each segment in a turn can also be set individually even though the final simulation is made in 2D. This was accomplished by multiplying the resistance by a thickness factor.

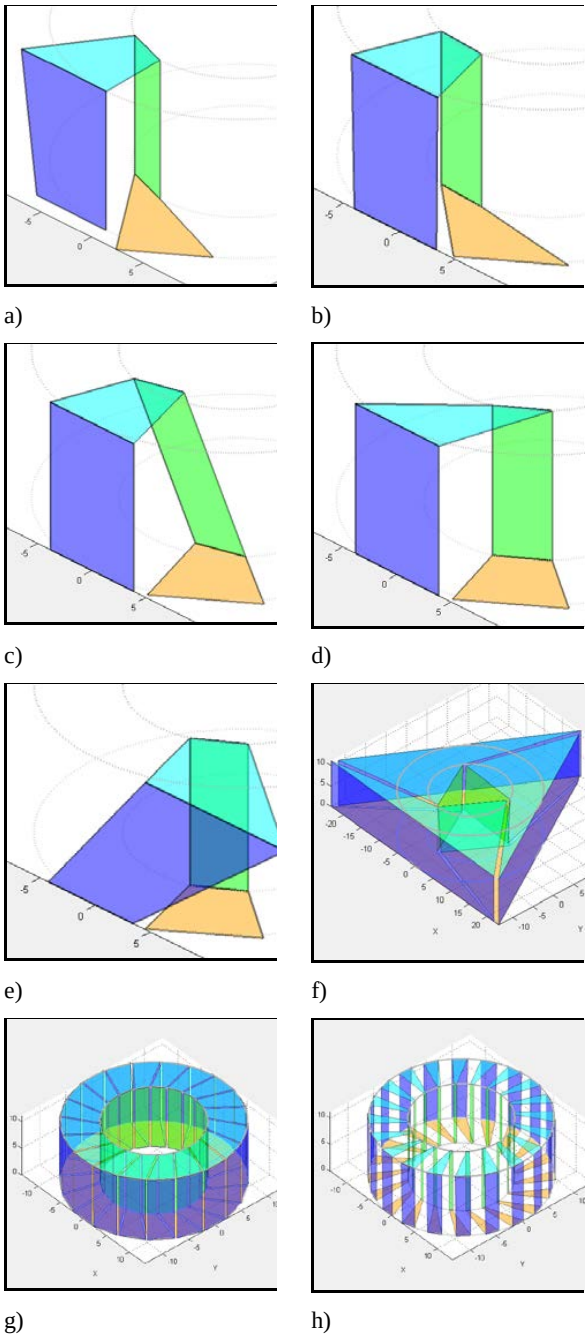

Figure 5. 3D plots generated using the GUI. a) Full bottom (F4) twist and left shifted start position. b) Full bottom (F4) twist and centered start position. c) Full inner (F3) twist. d) Full top (F2) twist. e) Full outer (F1) twist. f) A few number of turns. g) Many number of turns. h) Increased clearance.

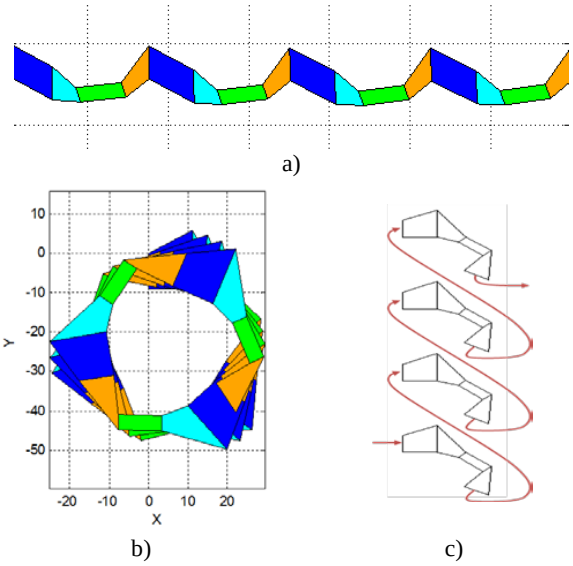

Figure 6 a) Foil folded out b) Foil folded out with overlapping c) 2D continuity

A graphical user interface (GUI) was created in order to verify the geometry in terms of the dynamic parameters of the inductor. Optimizing visualization and user friendliness paid off quickly and the GUI soon became an invaluable tool. As an example the GUI was used to plot the different winding geometries in Figure 5.a – 4.h. showing each parameter varied at a time.

III. COMSOL

In COMSOL the AC/DC module and the LiveLink to MATLAB was used to implement the optimization routine [5, 6]. COMSOL uses FEM to calculate the DC resistance of any 2D shape. The resistivity for each segment in a turn is utilized to model the thickness of the individual sections.

A. *2D mapping*

2D FEM simulations, as opposed to 3D FEM simulations, speeds up the simulation time and lower the computer resources needed.

The turns shown in Figure 7 are on purpose bendable shapes in the sense that the whole winding can be unfolded in one piece to a flat 2D structure by a 2D mapping. An example of an unfolded winding is shown in Figure 6.a. The plain 2D structure is imported to COMSOL through Matlab live-link. Unfortunately, bendable structures when unfolded can overlap them self as seen in Figure 6.b. importing an overlapping structure to COMSOL will lead to non-real result. To avoid the issue of overlap each single 2D mapped turn is taken apart and placed above each other and then imported to COMSOL. Within COMSOL each turns are mathematical linked together again by a boundary condition pair of continuity. This approach is illustrated in Figure 6.c. with 4 2D mapped turns

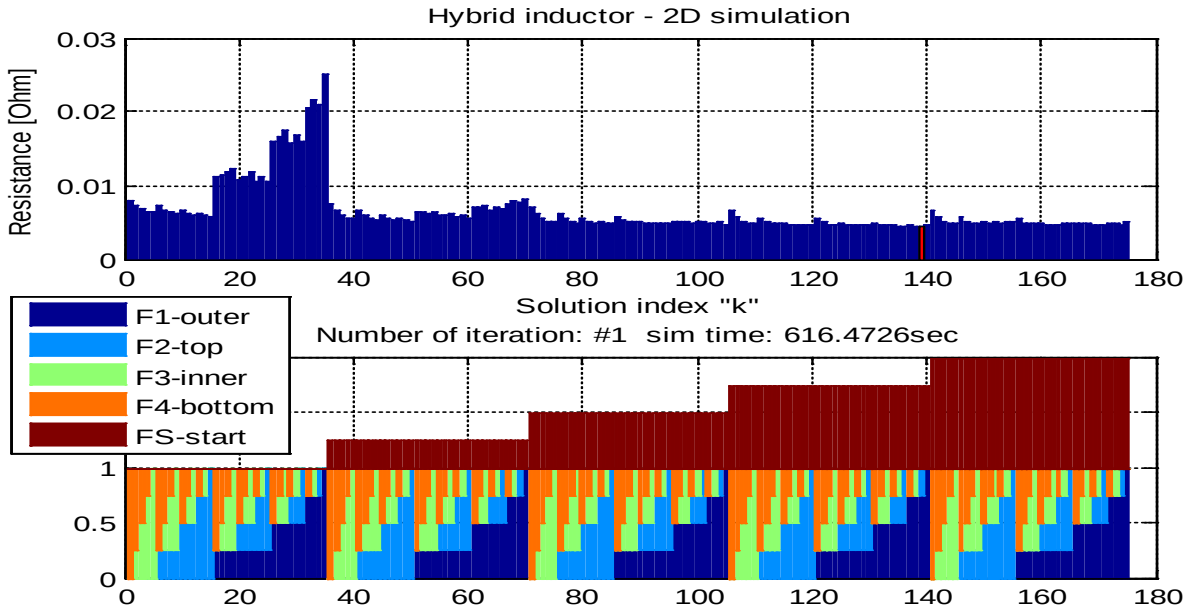

Figure 7. Illustration of optimizing routine for a single integration. The x-axis is the combination number for the given angle span. Angle combinations are shown in the lower plot and the corresponded DC resistance is shown in the top plot.

placed above each other, the arrows indicates how the 4 shapes are linked together with boundary condition pairs of continuity.

IV. Optimization

Based on the FEM simulation of the DC resistance the segment angle parameters of a turn are optimized. The optimization targets the lowest DC resistance by an iterative process of narrowing down the angle span for each segment based on the parameters for previous solution. A predefined minimum and maximum value for the angle span of each segment limits the span of solution. The angle span is divided into five values. The DC resistance for the combinations of segment angels is simulated. The combination resulting in the lowest DC resistance is used to derive the set of angle spans for the next iteration. The optimization routine is ended when the preset number of iterations is reached. The lower plot in Figure 7 illustrates how the optimization routine works by stepping through the combination of angels for each segment. The resulting DC resistance is shown in the top plot of Figure 7.

V. Results

The optimization routine was tested with a 106-2 core from Micrometals given the following parameters.

- Core height: 11.1 mm
- Core outer radius: 26.9 mm
- Core inner radius: 15.5 mm

In the first test case the following winding setup was used:

- Segment thicknesses: F1,F2,F3 = 500 µm and F4 = 70 µm
- Number of turns: 10
- Clearence: 1 mm

Resulst for three different setups are shown in TABLE I. In the “PCB 100%” the angle is 100% in the PCB trace. Since the PCB layer thickness is much thinner than the bended foil pieces it is obvious that this setup result in a high DC-resistance. The “Optimal shape” is found using the optimization routine. The resistance is reduced by 32% compared to the “PCB 100%”. Only the angles in the outer and the top segment has been angled and the starting position is 20%. Due to the offset of the starting position and the angle on outer segment the overall footprint of the hybrid inductor is increased. A much simpler implementation that dos not take up more space is the “Top 100%” where only the top segment is angled 100%. Here an improvement off 31% is reached compared to the “PCB 100%”.

In the next test case only the number of turns was increased with a factor of 10 and the clearence was decreased with a factor of 10. The same three setups as in case 1 was simulated. The results shown in TABLE II. indicates that the “PCB connection” is sufficient because the degree of fredom in terms of starting position and segment angles is decreased as a function of number of turns. In the second test case the

TABLE I. Case 1

	PCB 100%	**Optimal shape**	**Top 100%**
SP	0	20%	0
F1	0	63%	0
F2	0	37%	100%
F3	0	0	0
F4	100%	0	0
DC resistance	6.78 mΩ	4.64mΩ	4.71mΩ
Improvement	Ref.	≈32%	≈31%

TABLE II. CASE 2

	PCB 100%	Optimal shape	Top 100%
SP	0	0	0
F1	0	75%	0
F2	0	25%	100%
F3	0	0	0
F4	100%	0	0
DC resistance	435 mΩ	432 mΩ	432 mΩ
Improvement	Ref.	≈0.8%	≈0.8%

TABLE III. CASE 3

	PCB 100%	Optimal shape	Top 100%
SP	0	100%	0
F1	0	38%	0
F2	0	21%	100%
F3	0	0.5%	0
F4	100%	40.5%	0
DC resistance	2.60 mΩ	2.31 mΩ	2.46 mΩ
Improvement	Ref.	≈11%	≈6%

following setup was used:

- Segment thickness: F1,F2,F3 = 500 µm and F4 = 70 µm
- Number of turns: 100
- Clearence: 0.1 mm

In the last test case the thickness of each segment in a turn was kept constant. The result of this case could also be used in the design of a foil wounded toroidal inductor. In the third case the following setup was used:

- Segment thickness: F1,F2,F3,F4 = 500 µm
- Number of turns: 10
- Clearence: 1 mm

The results shown in TABLE III. indicates that the “Optimal shape” is superior to both the “PCB 100%” and the “Top 100%” in this case. The Optimal shape is 11% better than the “PCB 100%” and 5% better than the “Top 100%”.

VI. CONCLUSION

The shape of a bendable foil piece for a hybrid inductor has been optimized regarding the DC-resistance. It has been found that a complex optimization isnt nessesary because the added advantage is small compared to a simpler implementation using a 100% top angled segment. It is also shown that as the number of turns increases an angle of 100% in the PCB is sufficient as the number of turns increases. This leads to a simplified winding assembly of the hybrid inductor.

It is observed that the optimization routine has an advantage when the thickness of each segment in a turn is constant. The conclusions in this work is only based on the DC-resistance. In future work the influence of other factors like the AC-resistance and parasitic capacitance will be taken into account. This may enable a fair comparison between the hybrid inductor vs. a conventional wire wound toroidal inductor.

VII. REFERENCES

[1] B. Carsten, "Calculating the high frequency resistance of single and double layer toroidal windings", Micrometals,

[2] Datasheet, "WH 200 Toroid Hook winding machine", Available: www.coilwindingmachines.eu.

[3] P. Mignano, A. Mark, Huang, and C. Young, "Surface munt magnetic core winding structure", US 2004/0130428 A1, 2004.

[4] H. Schneider, T. Andersen, A. Knott, and M. A. E. Andersen. "Foil based single layer hybrid toroidal inductor", ECCE Asia Downunder, in press.

[5] "Introduction to AC/DC Module", COMSOL, Application note, 2012.

[6] "Introduction to LiveLink for MATLAB", COMSOL, Application note, 2012.

Appendix J

Investigation of a Hybrid Winding Concept for Toroidal Inductors using 3D Finite Element Modeling

---

Comsol Conference 2013

Investigation of a Hybrid Winding Concept for Toroidal Inductors using 3D Finite Element Modeling

H. Schneider*, T. Andersen, J. D. Mønster, M. P. Madsen, A. Knott and M. A. E. Andersen
Department of Electrical Engineering, Technical University of Denmark - DTU
*Corresponding author: Oersteds Plads 349, Kgs. Lyngby, 2800, Denmark, hensc@elektro.dtu.dk

Abstract: This paper investigates a hybrid winding concept for a toroidal inductor by simulating the winding resistance as a function of frequency. The problem of predicting the resistance of a non-uniform and complex winding shape is solved using 3D Finite Element Modeling. A prototype is built and tested experimentally to verify the simulation results. Finally COMSOL LiveLink to CAD is utilized to highlight a bottleneck for this kind of winding scheme.

Keywords: Inductor, Resistance, Mesh, Boundary layers, LiveLink.

1. Introduction

The conventional wire wound toroid shown in Figure 1 is used extensively in switch mode power supplies in EMC filters and as inductors and transformers. However the space between the windings increases gradually from the inner diameter towards the outer diameter of the core which limits the utilization of the available winding space. This effect can increases the resistance and thus the conduction loss of the component [1,2].

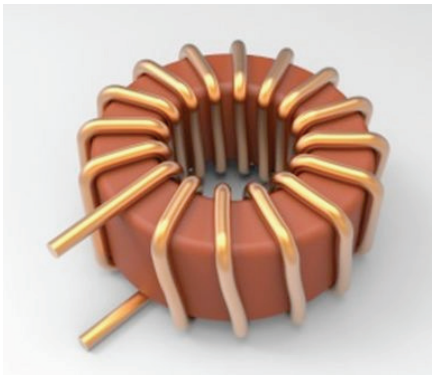

Figure 1. Conventional toroidal inductor

Furthermore, in the manufacturing process of a toroidal inductor with a large diameter wire and a small core a hook/pull type winding machine must be utilized. Under manufacturing a tool pass through the center of the toroidal core to grab and pull the wire which is manually feed to the hook for each turn.

To overcome these disadvantages a hybrid winding scheme may be used [3]. The basic idea of the hybrid winding scheme is to cut and bend copper foils into "U" shaped pieces that fit around the toroidal core as shown in Figure 2. To complete the winding the foil pieces are connected through the traces in a printed circuit board (PCB). In a final product the foil pieces would be pre-attached to a former for easy handling and alignment on the PCB.

Figure 2. Exploded view of the hybrid winding concept for a toroidal inductor.

The hybrid winding concept has the following benefits compared to the conventional single layer wire wound inductor:

- Large scale production and distributed stock of foil assemblies reduce cost and delivery time.
- Fully automated manufacturing process. Foil pieces are stamped, bended and attached to a plastic former. The core and the foil assembly can be placed by a pick and place machine.
- Better utilization of winding space. Constant resistance with increased number of turns or constant number of turns with decreased resistance for the same core size
- Low AC resistance due to increased surface area using foil.
- Configurable winding structure. The connections of the foil pieces through the PCB can be freely defined by the design engineer. The number of turns can be decreased by paralleling the foil pieces. It enables the same foil assembly to be used for inductors, common mode EMC chokes, transformers etc.
- Different core materials can be used with the same foil assembly.

The disadvantages may be as follows:

- Commercial available PCB layer thickness and interconnections between the foil cutouts and the PCB tracks is a bottleneck for high power applications.
- The assembly of the foil cutouts is limited to a specific core size.

2. Use of COMSOL Multiphysics

The challenge of predicting the resistance as a function of the frequency of such a complex 3D winding geometry is solved using the COMSOL AC/DC module[4]. The greatest challenge was to create the mesh since eddy currents need to be considered and the thickness of the foil to the PCB traces in this work vary from 0.5mm to 70µm. A boundary layer mesh with 4 layers and a stretch factor of 2.5 was used. The first layer fitness was set manually to 5µm. A free tetrahedral mesh was used for the DC resistance simulation.

3. Results

In Figure 3 the current density at 100kHz in the foil cutouts and the PCB traces are shown. The 3D model of the hybrid inductor is shown from beneath in order to inspect the PCB traces. Some of the windings and the core are hidden in order to look at the inner part of the winding. From the colors it is easy to see that the current density is highest closest to the core where the current path is shortest and in the places where the width of the foil cutout is lowest. This suggests that the foil cutouts should be angled instead of the PCB traces in order to reduce the resistance.

The implemented prototype is shown in figure 4. The PCB were milled with a router and the foil pieces were cut with a scissor and soldered manually. It is clear that the prototype has rounded corners and unequal spacing compared to the 3D drawing shown in figure 3.

In Figure 5 the simulated and measured resistance as a function of the frequency is shown. An offset is added to the simulation result to compensate for any static error sources such as imprecise cuts and clearance of the bent foils, all of which is not included in the 3D model. The simulation with offset fits the measured results from 10 Hz to 100 kHz which is the common operating frequency range. It is eddy currents in the core that causes the increase in the measured AC-resistance beyond the 100 kHz which is not accounted for in the simulation model.

A LiveLink to a computer aided design (CAD) program [5] was also implemented and several simulations were performed in order to investigate the DC-resistance versus the PCB Thickness. The result shown in figure 6 indicates that the DC-resistance could be halfed by using 220 um thick PCB traces compared to the common 70 um PCB trace thickness. The simulation prove that the PCB trace thickness is a bottleneck for high power applications.

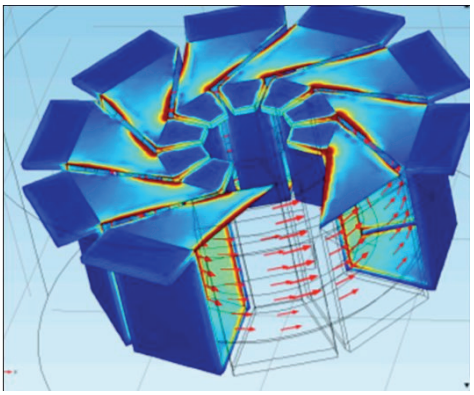

Figure 3. Simulated current density and magnetic flux density

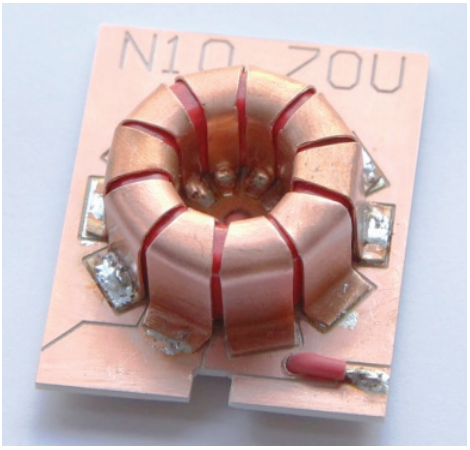

Figure 4. Prototype used for validation of the simulation results

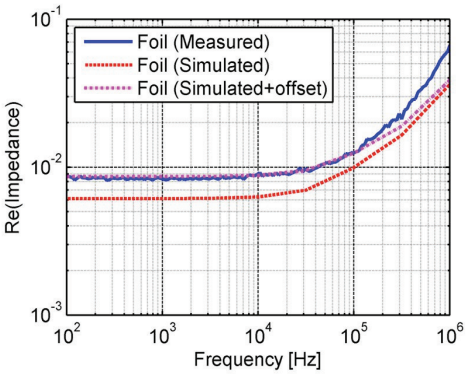

Figure 5. Resistance as a function of the frequency

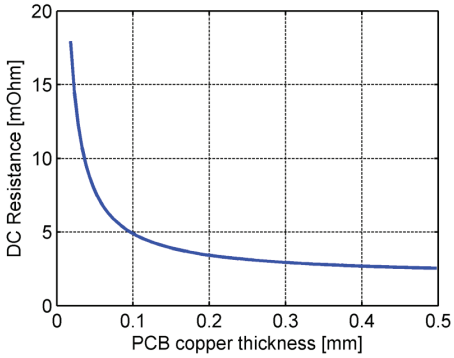

Figure 6. Simulated DC-resistance as a function of PCB copper thickness. Foil thickness is fixed at 500 µm.

4. Conclusion

A hybrid winding concept for toroids using the traces in a printed circuit board to make connection to bent copper foil cutouts has been evaluated in terms of AC-resistance and the DC-resistance as a function of PCB trace thickness.

A FEM analyses have been carried out and the model have been experimentally validated.

It is found that the commercially available layer thickness in a PCB is a bottleneck for high power applications. Finally a plot of the simulated current density in the winding reveals that the winding configuration can be optimized which is crucial for performance.

5. References

1. M. Seitz and M. Roeber, Squeeze more performance out of toroidal inductors, *Power Electronics Technology*, vol. 31, p. 30 (2005)

2. M. Nigam and C. R. Sullivan, Multi-layer folded high-frequency toroidal inductor windings, *Applied Power Electronics Conference and Exposition – APEC,* Twenty-Third Annual IEEE,, pp. 682-688 (2008)

3. H. Schneider, T. Andersen, A. Knott and M. A. E. Andersen, "Hybrid winding concept for toroids", ECCE Asia (2013)

4. Introduction to AC/DC Module, COMSOL, Application note, www.comsol.com.

5. CAD Import Module and LiveLink™ for CAD V4.3b, COMSOL, Presentation, www.comsol.com.

Appendix K

Optimizing Inductor Winding Geometry for Lowest DC-Resistance using LiveLink between COMSOL and MATLAB

Comsol Conference 2013

Optimizing Inductor Winding Geometry for Lowest DC-Resistance using LiveLink between COMSOL and MATLAB

H. Schneider*, T. Andersen, J. D. Mønster, M. P. Madsen, A. Knott and M. A. E. Andersen
Department of Electrical Engineering, Technical University of Denmark - DTU
*Corresponding author: Oersteds Plads 349, Kgs. Lyngby, 2800, Denmark, hensc@elektro.dtu.dk

Abstract: An optimization routine is presented to optimize a hybrid winding geometry for a toroid inductor in terms of the DC resistance. The hybrid winding geometry consist of bended foil pieces connected through traces in a printed circuit board. MATLAB is used to create a graphical user interface that visually plots the winding using input parameters such as core dimensions, number of turns, clearance between windings, and the winding angle of each segment of the winding. COMSOL LiveLink is used to import the winding geometry from MATLAB and create a 2D finite element model to simulate the DC reisistance. Finally the winding configuration with the lowest DC resistance is found by sweeping the parameters of the winding geometry and simulate and save the result in each step. An improvement of more than 30% compared to previous work where achieved in this way

Keywords: Inductor, Resistance, Mesh, Boundary layers, LiveLink.

1. Introduction

The conventional wire wound toroid is used in many power electronic applications such as EMC filters, power inductors, transformers and so on. However it has the following disadvantages regarding the winding scheme and the manufacturing/production process [1, 2]:

- The spacing between the windings increases gradually from the inner diameter towards the outer diameter of the core limiting the utilization of the winding area.
- For large wire diameters a hook/pull type manufacturing machine is used. The space required for the hook and the wire being pulled through the center of the core further decrease the utilized winding area.
- For large wire diameters manual work is required for feeding the hook with the wire leading to increased cost.
- Complex manufacturing machines are needed for winding due to non-separable core.
- Manufacturer lead time and price strongly depends on the purchase history and number of ordered magnetic components.
- The leaded toroid may be placed and soldered manually in a production increasing time to market and cost.

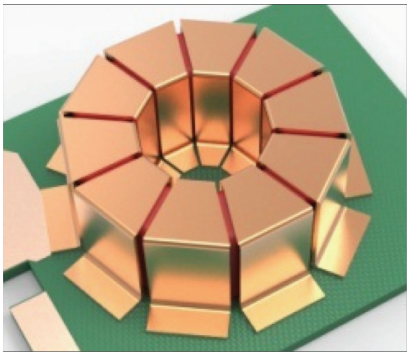

Figure 1. Surface mounted hybrid toroidal inductor.

This work focus on a hybrid foil combined with printed circuit board (PCB) trace winding scheme in an attempt to improve both the utilized winding space and improve the time to market by creating more freedom in the manufacturing and production process.

The basic idea is to cut and bend copper foils into “U” shaped pieces that fit around the toroidal core. The number of bended foil pieces determines the number of turns and in a final product all the foil pieces would be pre-attached to a plastic former for easy handling and alignment on the PCB.

In previous work [4] a hybrid inductor with 15 turns, a foil thickness of 500um and a single layer PCB with a layer thickness of 70um was implemented as a prototype. The measurements were used to evaluate a 3D Finite element model (FEM) created in COMSOL with good agreement. The results showed that typical available PCB layer thicknesses (18um – 210um)

are a bottle neck for the DC resistance in a hybrid inductor.

In the implemented model the bended copper pieces went straight over the core and the traces in the PCB was angled to complete the winding. It is easy to imagine how the DC resistance would be improved if the thin traces in the PCB were straight and short and the thicker copper pieces were angled over the core connecting the winding. It is however hard to predict the optimum angles of each segment in a turn and to predict the impact on the DC resistance. It is necessary to find an answer to these questions in order to take full advantage of the hybrid inductor.

2. Use of COMSOL Multiphysics

COMSOL is used to simulate and find the DC resitance of the windings in the inductor. The system is set up as a 2D simulation to improve simulation time, which is needed for the optimization algortihm solution time not to get extremely long.

The 3D model is based on four segments per turn, labeled F1-F4 as shown in Figure 2. The optimization algortihms input parameters is the coil dimensions, number of turns, minimum clearance between turns, the starting position of the winding following the tangent of the core, the angle of each segment and the thickness of each segment.

.

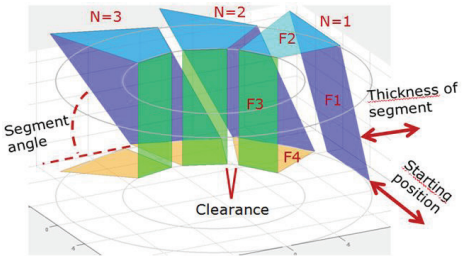

Figure 2. Geometry of the winding and the related parameters.

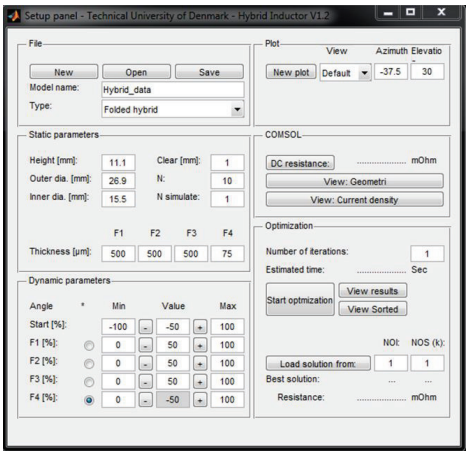

Figure 3. The designed MATLAB GUI with LiveLink to COMSOL.

To control the optimization rutine a MATLAB program was developed, that can take all the inputs, and set the different constraints, and in general control the optimization. For setting up the 2D structure in COMSOL the LiveLink for MATLAB [5] was used. The following steps were implemented in the MATLAB code in order to automate the calculation of the DC resistance with changing winding geometry:

- Creating a MATLAB GUI – See Figure 3
- Creating the winding geometry
  - The geometry of a single turn is created based on the parameters set by the GUI for the winding such as size of the core, clearance, thickness of the foil and the angle of each segment in a turn. The coordinates positions are translated from 3D to 2D by unfolding the each turn.
  - A for loop creates the desired turns by copying the coordinates of the single turn by rotating them in a polar coordinate system. Every section of a turn is created as a polygon and the coordinates is saved for later selection of domains and boundaries. Each segmet is shifted so they lay in layers. This is done to ensure that the windings will not

cross each other, as shown in Figure 4.

- Selecting the boundaries. As the specific boundaries are not number as the are generated, it is nessary to find them in order to set up the rest of the simulation. This is done by using the LiveLink method "mphselectbox". The saved positions used to generate the turns are used and the boundary are stored for later use.

- The material setup is defined for each segment in the simulation, instead of using the standard Copper material, this is done since the different segments can (and usaully have) different thickness of the copper. The differrence is used to define an electrical conductivity for each segment modelling the thickness.

- The physics is set up as an "Electrical Currents" model, with a stationary study, and the discretixation of the electric potential to (the standard) quadratic. To enforce a voltage over the entire structure a Terminal is added on the first structure (bottom structure, red boundary). Here a voltage of 1V is set. On the last (top) structure a Ground node is added. To ensure the connection betweeen each turns structure the Periodic Condition is used, between the boundaries of the end of one structure and the input of the next, as indicated by the arrows in Figure 4.

- The geometry is meshed using the standard mesh Free Triangular, with the seize set to "Normal". This gives an simple, yet accurate enough approximation.

- The study is set as a stationary standard study, with direct solving.

- The results are taken in two parts

  - A global variable is used to calculate the DC resistance seen from the terminals. The conductance G is available directly from the solution and the DC resistance is then calculated as The current density was evaluated in the

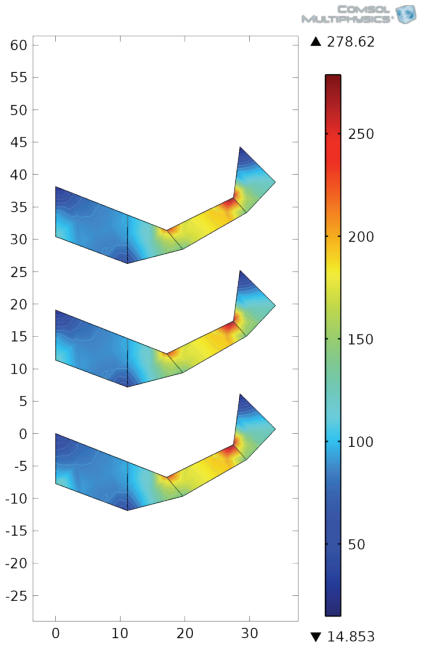

Figure 1 Current density plot of each of the turns structures.

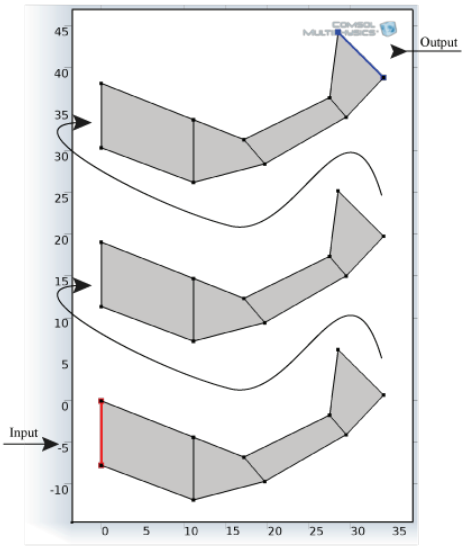

Figure 2 Ilustration of an unfold winding which is copied and connected in series via "Periodic Condition"

$$R_{DC} = \frac{1}{G}$$

same way but as a surface maximum and minimum, as well as plotted using in COMSO, see Figure and shown in a MATLAB figure using the function "mphplot".

3. Results

The result of the optimization routine is shown in Figure 5. The plot shows the simulated resistance for a given number of solutions where the previously mentioned parameters of the winding were altered. In this specific case the resistance don't change much as a function of the winding parameters as in other cases. In this work the following 3 cases were examined:

- **Case 1**: Few turns,
  PCB layer thickness << Foil thickness
- **Case 2**: Many turns,
  PCB layer thickness << Foil thickness
- **Case 3**: Few turns,
  PCB layer thickness = Foil thickness

In table 1-3 the parameters and result for each of the 3 cases are summarized. In each case 3 winding configurations are compared. One where only the PCB trace is angled called "Bottom", one where the lowest DC-resistance were found called "Opt." for optimized and one where only the top segment of the bended foil was angled called "Top".

In Case 1 the optimized solution resulted in an improvement of 32 % compared with only angling the PCB trace. However an 31 % improvement was achieved by only angling the top segment of the bonded foil piece. If few turns and a big difference in foil and PCB trace is utilized the "Top" solution may be sufficient since it will result in a low DC-resistance and may be easier to fabricate.

In Case 2 a very small improvement of 0.8 % for both the "Opt." and the "Top" compared to the "Bottom" is achieved. The limited space due to many turns reduce the influence of angling the segments in the winding and obviate the optimization.

In Case 3 the "Opt." and "Top" configuration resulted in 11 % and 6 % improvement respectively. For few turns and equal winding thickness the optimized solution is therefore attractive. This could be an important conclusion since this configuration is highly suitable for high frequency operation which is in high demand. However this must be confirmed in a 3D simulation of the AC-resistance which is out of the scope in this work.

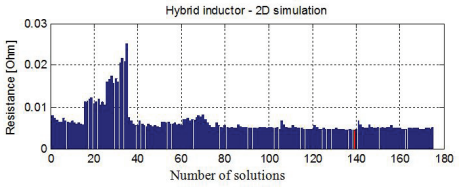

Figure 5. Illustration of optimizing routine for a single integration. The x-axis is the combination number for the given angle span and the y-axis is corresponded DC resistance.

Table 1: Case 1 (Few turns, PCB layer thickness << Foil thickness)

Number of turns: 10, Segment thickness: F1, F2, F3 = 500 µm, F4 = 70um, Clearance = 1mm			
Winding angle configuration	***Bottom***	***Opt.***	***Top***
Starting point SP [%]	0	20	0
Outer Foil Segment F1 [%]	0	63	0
Top Foil Segment F2 [%]	0	37	100
Inner Segment F3 [%]	0	0	0
Bottom Segment F4 [%]	100	0	0
DC resistance [mΩ]	6.78	4.64	4.71
Improvement [%]	Ref.	32	31

Table 2: Case 2 (Many turns, PCB layer thickness << Foil thickness)

Number of turns: 100, Segment thickness: F1, F2, F3 = 500 µm, F4 = 70um, Clearance = 1mm			
Winding angle configuration	***Bottom***	***Opt.***	***Top***
Starting point SP [%]	0	0	0
Outer Foil Segment F1 [%]	0	75	0
Top Foil Segment F2 [%]	0	25	100
Inner Segment F3 [%]	0	0	0
Bottom Segment F4 [%]	100	0	0
DC resistance [mΩ]	435	432	432
Improvement [%]	Ref.	0.8	0.8

Table 3: Case 3 (Few turns, PCB layer thickness = Foil thickness)

Number of turns: 10, Segment thickness: F1, F2, F3, F4 = 500 µm, Clearance = 1mm			
Winding angle configuration	***Bottom***	***Opt.***	***Top***
Starting point SP [%]	0	100	0
Outer Foil Segment F1 [%]	0	38	0
Top Foil Segment F2 [%]	0	21	100
Inner Segment F3 [%]	0	0.5	0
Bottom Segment F4 [%]	100	40.5	0
DC resistance [mΩ]	2.6	2.3	2.5
Improvement [%]	Ref.	11	6

4. Conclusion

A MATLAB program for optimizing the structure of an inductor in order to minimize the DC resistance have been created. The program sets up the 2D simulation of the structure dividide into turns, again dividede into 4 segments, each with different thickness. The system is simlated and the numerical as well as grapical results are extracted. The program shows that it is capacble of finding the optimum winding geometry, leading to an improved DC-resistance. The findings are in general:

- Few turns and large difference in foil and PCB trace thickness
  - Angeling the top segment (F2) is a suitable solution
- Many turns
  - Less degree of freedom to alter the shape of the winding
- Same thickness of all the segments in a turn
  - An optimized solution is preferred

5. References

1. M. Seitz and M. Roeber, Squeeze more performance out of toroidal inductors, *Power Electronics Technology*, vol. 31, p. 30 (2005)

2. M. Nigam and C. R. Sullivan, Multi-layer folded high-frequency toroidal inductor windings, *Applied Power Electronics Conference and Exposition – APEC,* Twenty-Third Annual IEEE,, pp. 682-688 (2008)

3. H. Schneider, T. Andersen, A. Knott and M. A. E. Andersen, "Hybrid winding concept for toroids", ECCE Asia (2013)

4. Introduction to AC/DC Module, COMSOL, Application note, www.comsol.com.

5. CAD Import Module and LiveLink™ for CAD V4.3b, COMSOL, Presentation, www.comsol.com.

Appendix L

Efficiency Optimization by Considering the High Voltage Flyback Transformer Parasitics using an Automatic Winding Layout Technique

---

IEEE Transactions on Power Electronics 2014

Efficiency Optimization by Considering the High Voltage Flyback Transformer Parasitics using an Automatic Winding Layout Technique

Prasanth Thummala, *Student Member*, *IEEE*, Henrik Schneider, *Student Member*, *IEEE*, Zhe Zhang, *Member*, *IEEE*, Ziwei Ouyang, *Member*, *IEEE*, Arnold Knott, *Member*, *IEEE*, and Michael A. E. Andersen, *Member*, *IEEE*

Electronics group, Department of Electrical Engineering, Technical University of Denmark, 2800 Kongens Lyngby, Denmark.

Email: pthu@elektro.dtu.dk

***Abstract* — This paper presents an efficiency optimization approach for a high voltage bidirectional flyback dc-dc converter. The main goal is to optimize the converter for driving a capacitive actuator, which must be charged and discharged from 0 V to 2.5 kV dc and vice versa, supplied from a 24 V dc supply. The energy efficiency is optimized using a proposed new automatic winding layout (AWL) technique and a comprehensive loss model. The AWL technique generates a large number of transformer winding layouts. The transformer parasitics such as dc resistance, leakage inductance and self-capacitance are calculated for each winding layout. An optimization technique is formulated to minimize the sum of energy losses during charge and discharge operations. The efficiency and energy loss distribution results from the optimization routine provide a deep insight into the high voltage transformer design and its impact on the total converter efficiency. The proposed efficiency optimization approach is experimentally verified on a 25 W (average charging power) with 100 W (peak power) flyback dc-dc prototype.**

***Index Terms* — switched-mode power supply, high voltage dc-dc power converter, transformer design, optimization, energy efficiency, actuators, dielectric films**

Statement: *A part of this manuscript was presented at the IEEE APEC 2014 conference [24]. It is not currently under review for publication in any other journal. Compared with the conference papers, the proposed automatic winding layout technique is explained in detail, the detailed information about the proposed efficiency optimization technique is provided, and the loss modeling has been improved and updated. Furthermore, the calculated and experimental results are updated.*

NOMENCLATURE

a_{uC}, b_{uC}	Coefficients of Fourier series of the magneto motive force (MMF) during charge process (AT: Ampere-turns)
B_{mC} / B_{mD}	Maximum flux density during charge / discharge process (T)
B_{nC}	Magnitude of negative flux density at the beginning of a switching cycle during charge process (T)
ΔB	Peak-to-peak flux density of the current excitation (T)
C_{in} / C_{load}	Input capacitance / Capacitance of the load or actuator (F)
C_s	Self-capacitance of secondary winding (F)
C_{ossp} / C_{osss}	Output capacitance of low voltage MOSFET M_p / high voltage MOSFET M_s (F)
C_{Db}	Junction capacitance of high voltage diode D_b (F)
d_p / d_s	Diameter of primary / secondary winding of transformer (mm)
D_2 / D_b	High voltage (5 kV) freewheeling diode / blocking diode
$d_{insulation}$	Uniform spacing or thickness of the insulating tape, between secondary layers (mm)
D_{onC} / D_{offC}	On-time / Off-time duty cycle of low voltage MOSFET M_p during charge process
D_{onD} / D_{offD}	On-time / Off-time duty cycle of high voltage MOSFET M_s during discharge process
$E_{load}(V_{out})$	Stored energy in the load at an output voltage V_{out} (J)
f_{swC} / f_{swD}	Switching frequency during charge / discharge process (kHz)
FF_{LL}	Fill factor of the last layer in the high voltage winding
$F_{uC}(0)$ / $F_{uC}(h)$	MMF amplitude of u^{th} harmonic at x=0 / x=h, h is the thickness of layer (AT)
G_1, G_2	Constants used in the power loss expressions and are functions of ε_u
H_W	Window height of transformer bobbin (mm)
i_{in} / i_p / i_s	Input current / Primary current / Secondary or load current (A)
i_{mp} / i_{ms}	Primary / Secondary magnetizing current (A)
I_{ppkC} / I_{ppkD}	Primary peak current during charge process / discharge process (A)
I_{spkC} / I_{spkD}	Secondary peak current during charge process / discharge process (A)
i_{min}	Magnitude of the negative primary current at the beginning of charge process (A)
I_{pavgC} / I_{savgC}	Primary / Secondary average current during charge process (A)
k_z	Core loss constant in the improved generalized Steinmetz equation (iGSE)
L_{mp} / L_{ms}	Primary / Secondary magnetizing inductance of transformer (H)

L_{lkp} / L_{lks}	Leakage inductance referred to primary / secondary side of transformer (H)
M_p / M_s	Low voltage MOSFET / High voltage (4 kV) MOSFET
N_p / N_s / n	Number of primary / secondary turns / Turns ratio of transformer from secondary to primary
n_{lp} / n_{ls}	Number of layers in primary / secondary winding of transformer
n_{parp} / n_{pars}	Number of parallel wires in primary / secondary winding of transformer
N_h / N_c	Total number of harmonics considered / Total number of switching cycles during charge process
P_{layerC}^{k}	Power loss in k^{th} layer during charge process (W)
P_{windC} / P_{TwindC}	Winding loss at each switching cycle / Total winding loss during charge process (W)
P_{swC} / P_{swD}	Capacitive switching loss due the self-capacitance during charge / discharge process (W)
P_{snC} / P_{snD}	Snubber loss due leakage inductance during charge / discharge process (W)
R_p / R_s	dc resistance of primary / secondary winding of transformer (Ω)
R_{psense} / R_{ssense}	Primary / Secondary current sense resistance (Ω)
R_{layer}	dc resistance of a given layer (Ω)
t_{onC} / t_{offC}	On-time / Off-time of low voltage MOSFET M_p during charge process (s)
t_{onD} / t_{offD}	On-time / Off-time of high voltage MOSFET M_s during discharge process (s)
T_{sC} / T_{sD}	Switching period during charge / discharge process (s)
T_{ch}	Charging time to reach the target output voltage from 0 V (s)
T_{layer}	Number of turns in a given layer (primary or secondary) of transformer
V_{leakD}	Increase in the steady state drain-to-source voltage of M_s due to leakage inductance L_{lks} (V)
V_{in} / V_{out}	Input voltage / Output or load or actuator voltage (V)
W_W	Window width of bobbin (mm)
W_{sqp} / W_{sqs}	Width of square for primary / secondary in the automatic winding layout generator routine (mm)
γ_s / γ_p	Height allocation factor for secondary / primary winding with γ_p=(1-γ_s)
δ_u / δ	Skin depth of the conductor at u^{th} harmonic frequency / fundamental (u=0) frequency (mm)
ε_u	Ratio of conductor diameter to the effective skin depth of u^{th} harmonic
$\varphi_{uC}(0)$ / $\varphi_{uC}(h)$	Phase of u^{th} harmonic of the MMF during charge process at x=0 / x=h (h is thickness of layer)
ρ / μ_0	Resistivity of copper (Ω-m) / Magnetic permeability of vacuum (H/m)
α, β, k	The constants related to core material which are provided by the core manufacturer
δ_C	Capacitance ratio factor on the high voltage side

I. INTRODUCTION

Dielectric electro active polymer (DEAP) [1]-[3] is an evolving smart material that can be used in actuation, sensing and energy harvesting applications [4]. DEAPs, when used as linear actuators, have the potential to be an effective replacement for many conventional linear actuators because of their unique properties, including light weight, low noise operation, high flexibility, large strain, and autonomous capability. The axial DEAP actuator as shown in Fig. 1(a) is ideally equivalent to a capacitive load. When a DEAP actuator is driven with high voltage (2-2.5 kV), it converts a portion of the electrical energy into mechanical displacement, which is of the order of mm (~1-1.5 mm) [5]-[7]. Three of such axial DEAP actuators are used to create a DEAP incremental actuator [8] as shown in Fig. 1(b). The DEAP incremental actuator technology has the potential to be used in various industries, e.g. automotive, aeronautics, and medicine. For using the DEAP actuators in such applications, the high voltage drivers should have low volume to fit inside or above the actuators. The overall energy efficiency of battery powered high voltage driver influences, the distance travelled by the incremental actuator. Hence, for DEAP actuator applications, both volume and energy efficiency of high voltage drivers are extremely important and need to be optimized.

The flyback converter is suitable for high voltage and low power applications due to its simple structure and a low component count [9]. High voltage switch-mode power supplies for charging the capacitive loads are implemented in [10]-[12]. Bidirectional dc-dc power converters are needed for the DEAP based capacitive actuators [13], to increase the lifetime of the battery, also to discharge the high voltage across them. Bidirectional flyback converter [14]-[17], and a forward-flyback bidirectional converter [18] are implemented for various applications. Due to high reverse recovery time (~2.6 μs) of high voltage MOSFET, a modified high voltage bidirectional flyback converter topology [19] as shown in Fig. 2, is proposed and implemented for driving a DEAP actuator. The loss analysis of the same converter is performed in [20].

Transformer design plays a very important role in high voltage dc-dc power converters employed in low, medium and high power applications. The design methodologies for transformers used in conventional switch-mode power supplies are well documented [9], [21]-[23]. Often, a transformer for a given application is designed based on some assumptions such as,

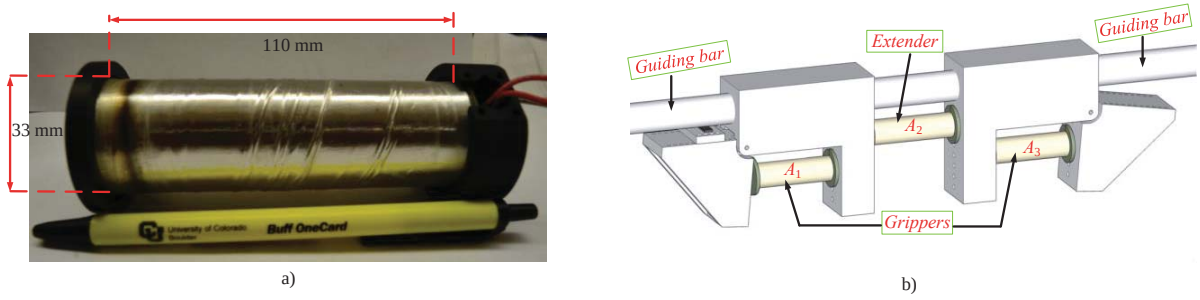

a) b)

Fig. 1. a) DEAP actuator; b) DEAP incremental actuator.

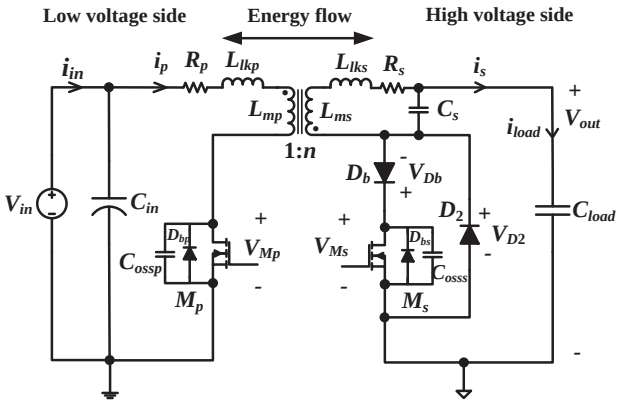

Fig. 2. Circuit configuration of the high voltage bidirectional flyback converter for driving a capacitive load.

constant switching frequency, maximum temperature rise, estimated converter efficiency, winding fill factor, and winding current density. However, those assumptions are not valid or suitable for some applications. Hence, more customized procedures are needed to design efficient transformers, for specific applications. In a high voltage capacitor charge and discharge application, the high voltage transformer will have a large amount of (> 200) secondary turns. For such application, it is very difficult to select an optimum winding diameter and number of winding layers beforehand, which decide the values of the transformer parasitics. To avoid this difficulty, an automatic winding layout (AWL) technique is introduced in [24], for the winding design of a high voltage transformer. The high voltage flyback converter operation is very sensitive to the transformer parasitics. The proposed AWL technique, utilizes the entire available space in a given transformer bobbin and provides an optimum winding diameter that minimizes the total loss due to the transformer parasitics.

In the initial design phase, it is difficult to predict which core type is optimal for a given application. In a flyback converter, a long transformer window width is often preferred, in order to minimize the leakage inductance and ac resistance by providing a close coupling between windings, and to decrease the number of winding layers. For high output or input voltage flyback converters, this could be different, since the self-capacitance of the high voltage winding has significant impact on the performance of the converter. In this paper, an efficiency optimization algorithm is proposed, which provides an optimum solution for a given transformer core, by using the proposed AWL technique and the comprehensive loss model. Different transformer winding architectures (TWAs) for the high voltage capacitor charge and discharge application are investigated in [25]. In [26], a digital control technique is proposed for improving the energy efficiency and charge/discharge speed. Control algorithms for optimal-flyback charging of a capacitive load are proposed in [27]. A number of switch-mode power supply design optimization methods have been described in the literature [28]-[34].

The proposed efficiency optimization technique has the following features:

1. an automatic winding layout (AWL) technique, which produces the information about winding diameters, number of layers, and number of parallel windings, for both primary and secondary windings;
2. an accurate calculation of transformer parasitics using the outputs of AWL technique;
3. calculation of energy losses during charge and discharge modes using a comprehensive loss model;
4. an objective function that minimizes the sum of energy losses during charge and discharge modes, over a range of operating points.

This paper is organized as follows: Section II describes the proposed automated winding layout (AWL) technique. Section III provides the loss modeling of the bidirectional flyback converter. Section IV discusses the proposed optimization routine. Section V provides the optimization and experimental results, followed by the conclusions in Section VI.

II. Automatic Winding Layout (AWL) Technique

The bidirectional flyback converter design specifications are provided in Table I. The magnetic transformer is the most critical component in the high voltage bidirectional flyback converter. The leakage inductance causes voltage spikes across drain-to-source of the MOSFET, and this can be avoided by a dissipative snubber circuit or by using an over rated MOSFET. The self-capacitance of secondary winding creates large resonating current spikes in the leading edge of the MOSFET current waveform [19]. Additional switching losses will be created due to those two parasitics, respectively [30]. The remaining losses in the transformer are core loss, and the winding loss due to dc and ac resistances. The losses due to the high voltage transformer need to be minimized to improve the bidirectional flyback converter efficiency and reliability.

The transformer design decisions considered for the proposed AWL technique are given in Table II. The core types are limited to ETD, EFD, E, RM and PQ. The N87 core material is chosen for most of the cores, due to its lower core losses at high frequency up to 500 kHz. For those cores for which N87 material is not available, other core materials which are suitable for operation up to 500 kHz are considered. A simple non-interleaved winding structure (P/S; P: Primary, S: Secondary), is considered in this paper to limit the complexity of the proposed AWL technique. Nevertheless, the proposed AWL technique

TABLE I. Converter Design Specifications

Parameter	**Value**
Input voltage V_{in}	24 V
Output voltage V_{out}	0-2500 V
Capacitance of load C_{load}	400 nF
Stored energy in the load E_{load} at 2.5 kV	1.25 J
Target charging time T_{ch}	50 ms
Turns ratio of the transformer n	25
Primary magnetizing inductance L_{mp}	44 μH
Primary peak current during charge process I_{ppkC}	4.2 A
Primary peak current during discharge process I_{ppkD}	5.3 A

TABLE II. TRANSFORMER DESIGN DECISIONS

Description	Design decision	Comments
Ferrite core and bobbin type	ETD, EFD, E, RM and PQ	Typically used in switch-mode power supplies.
Core material	N87	Suitable for switching frequencies up to 500 kHz.
Winding structure	P/S	Simple implementation and decreases analytical complexity.
Primary winding type	Solid wire	Flexible winding type in terms of design and prototyping.
Primary winding insulation	Triple insulation (TEX-E)	Edge tape can be avoided. No need for interlayer insulation tape between the primary and secondary windings.
Secondary winding type	Solid wire	Suitable winding type, for a large number of turns. Flexible winding type in terms of design, prototyping and different winding structures.
Secondary winding insulation	Single insulation	Provides minimum insulation thickness for a large number of turns.
Air gap	All legs	Simplifies the prototyping.
Maximum transformer temperature	130 °C	With a predicted ambient temperature of 35 °C, this enables transformer temperature rise of 95 °C.

can be easily extended for the interleaved transformer structures (P/S/P or S/P/S). The proper insulation between the low voltage (primary) and high voltage (secondary) windings is achieved by using a triple insulated (TEX-E) solid wire for primary winding. To avoid the high insulation thickness (0.2 mm) of TEX-E wire, single insulated solid wire is used for a large number of secondary turns. A maximum transformer temperature limit of 130 °C is chosen. These limitation values can be altered based on the experience of the user or the initial design specifications. The AWL technique is described below:

A. AWL technique:

The space allocated for the primary and secondary windings for a given transformer bobbin with winding width W_W and window height H_W are shown in Fig. 3(a). Different steps associated with the proposed AWL technique for an example of N_p=6 primary turns and N_s=18 secondary turns, are explained below:

1. The first step is, to split the available winding space for primary (see Figs. 3(a)) and secondary (Figs. 3(f)) into a number of squares, with a square width equal to height allocated for that winding. As shown in Figs. 3(d) and 3(g), it results into 4 squares and a crossed non-square, which is considered as an unusable space for both primary and secondary windings. In each square, a solid round wire could be placed with a diameter equal to the width of square or a bundle of round wires with an outside bundle diameter equal to the width of square.
2. Since the number of available squares is 4 in Figs. 3(d) or 3(g), which is less than the required 6 primary and 18 secondary turns, more squares are required to fill the needed turns. Hence, the width of square for primary or secondary is decreased from its maximum value of $\gamma_p H_W$ or $\gamma_s H_W$, respectively.
3. The fill factor of the last layer FF_{LL} for a given winding is defined as the ratio of number of squares used in the final layer to the number of squares available in it. For example, in Fig. 3(i), 9 squares are available and 9 squares are occupied in the final layer, hence FF_{LL}=1. Similarly, in Fig. 3(j), 16 squares are available and 13 squares are occupied in the final layer,

hence FF_{LL}=0.81. In the proposed AWL technique a maximum limit of 0.85 is set for FF_{LL}, since the calculation of transformer parasitics are based on fully occupied layers.

4. When the square width is reduced as shown in Figs. 3(e) and 3(h), the new square size limits the use of a shaded space above the squares. For primary winding since only 6 turns are needed, this will be a valid solution. However, for secondary winding, since 18 turns are needed, the shaded space can be occupied by the other windings, by reducing the square width further.
5. When the square width is reduced further as shown in Fig. 3(i), the winding space contains 18 squares in 2 layers, and a shaded space. The non-square horizontal space is utilized to provide an insulation tape (with thickness $d_{insulation}$) between the secondary layers. This is the final step of AWL technique for 6 primary and 18 secondary turns.
6. If 45 turns are required for secondary winding, the square width is decreased again, as shown in Fig. 3(j), the solution contains 3 layers and 16 squares in each layer. The last layer fill factor FF_{LL} in this case is 0.81, which is less than 0.85. Hence, this is not a valid solution and the square width needs to be decreased further.
7. In Fig. 3(b), a solution from the AWL technique is shown. The primary and secondary squares are filled with triple isolated and single isolated solid wires, respectively. The same steps described above apply for the real high voltage transformer design which will have more than 200 secondary turns.
8. Finally, the outputs of AWL technique are various winding implementations, including specific winding details such as, diameters of primary and secondary windings, number of primary and secondary winding layers, and insulation thicknesses for placing between secondary windings, for which FF_{LL}>0.85, respectively.

B. Calculation of transformer parasitics using the results of AWL technique:

The outputs of the AWL technique are used to calulate the transformer parasitics [20], [24], [35]-[37] such as dc resistance, leakage inductance and self-capacitance. In Fig. 4, one output of AWL technique such as the insulation thickness ($d_{insulation}$) for a PQ 20/20 core, and calculated transformer parasitics are shown with respect to square width (W_{sqs}) of secondary winding. As the width of the secondary square (or secondary winding) decreases, the insulation spacing $d_{insulation}$ between secondary winding layers increases, dc resistance R_s increases, leakage inductance L_{lkp} slightly decreases, and the self-capacitance C_s decreases.

III. LOSS MODELLING

In order to investigate the bidirectional flyback converter efficiency, it is necessary to calculate the losses associated with each circuit component in the converter. The loss model is a function of transformer parasitics. Different losses in the bidirectional flyback converter are given below:

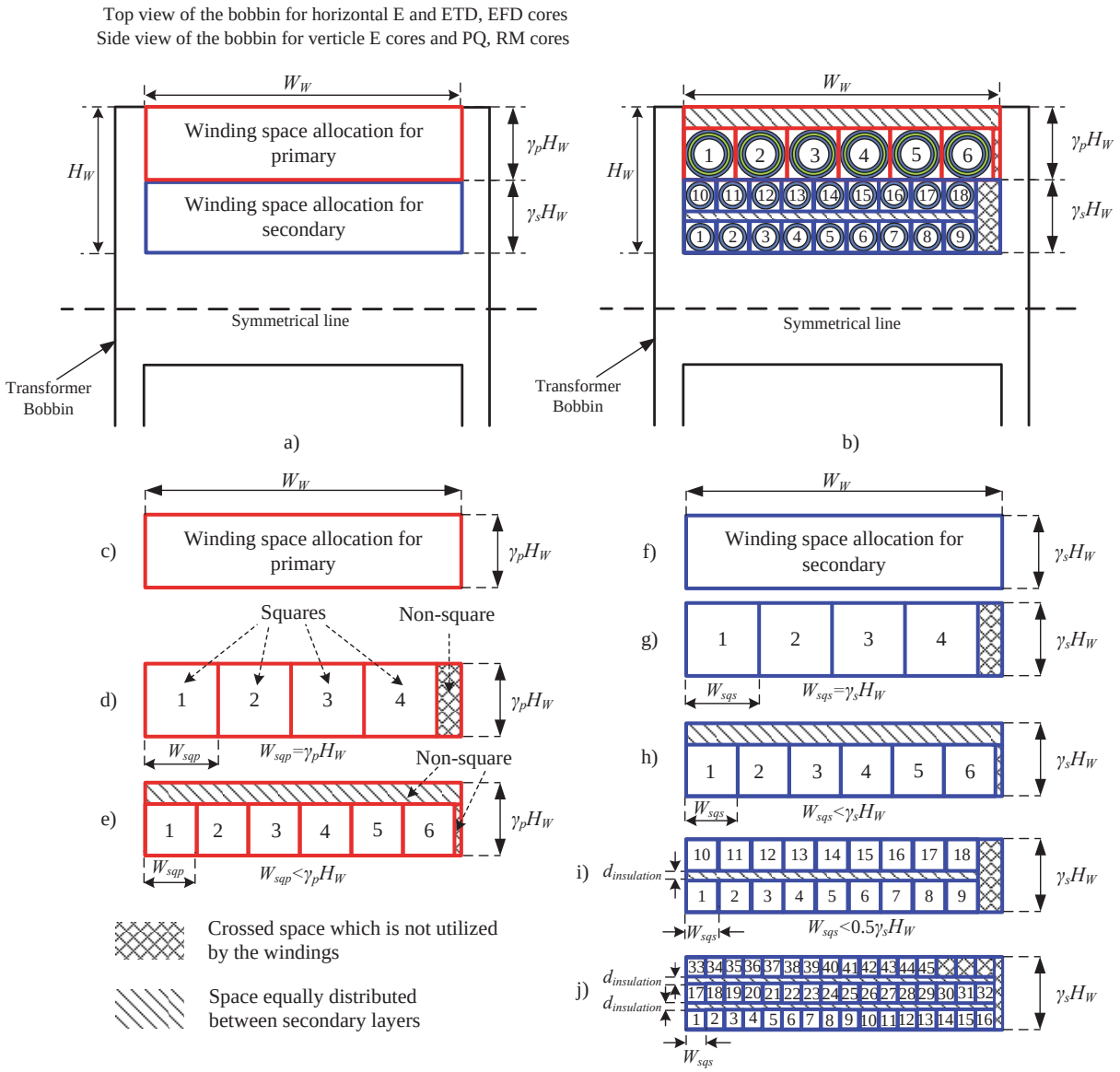

Fig. 3. a) Allocated winding space a) before applying AWL technique; b) after applying AWL technique; c) - e) Different steps involved in AWL technique for primary winding; f) - j) Different steps involved in AWL technique for secondary winding;

A. Transformer winding loss

In a flyback converter the primary and secondary currents are 180° out of phase, hence the conventional equations cannot be used to calculate the ac resistance [38], [39]. The calculation of the total winding loss in a flyback converter using the magneto motive force (MMF) analysis [40], [41] is described below.

1) Winding loss in a flyback transformer during charge process:

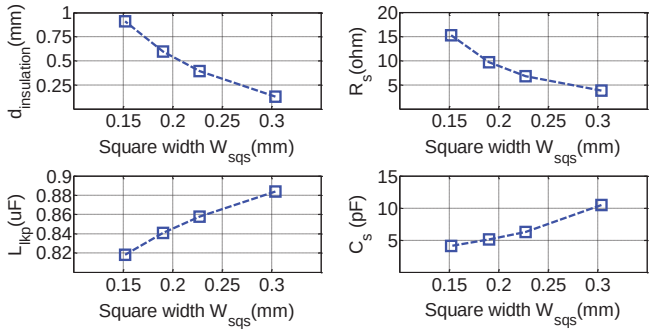

Fig. 4. Variation of transformer parasitics with the diameter of secondary winding, for PQ 20/20 core (when γ_s=0.8).

For the winding loss modeling, a non-interleaved transformer with 2 layers on the primary side (P_1 and P_2) and 5 layers on the secondary side (S_1, S_2, S_3, S_4 and S_5), is considered as an example. The MMF distribution in a flyback transformer is different from that of a normal transformer [40]. Figure 5 shows different MMF distributions during both turn-on ($0<t<t_{onC}$) and turn-off ($t_{onC}<t<t_{onC}+t_{offC}$) periods in a non-interleaved flyback transformer. In Fig. 5, N_{p1} and N_p, are the number of turns in the primary layer 1 and the total primary turns, respectively, and H_0, H_1,….H_7 are the magnetic field intensities between the layers. The terms N_1, N_2, N_3, N_4, N_5 are defined as follows: $N_1=N_{s1}$, $N_2=N_{s1}+N_{s2}$, $N_3=N_{s1}+N_{s2}+N_{s3}$, $N_4=N_{s1}+N_{s2}+N_{s3}+N_{s4}$, and $N_5=N_{s1}+N_{s2}+N_{s3}+N_{s4}+N_{s5}=N_s$ where N_{s1}, N_{s2}, N_{s3}, N_{s4}, N_{s5} and N_s are the number of turns in the secondary layers 1, 2, 3, 4, 5, and the total number of secondary turns, respectively. The primary $i_{mp}(t)$ and secondary $i_{ms}(t)$ magnetizing current waveforms in a

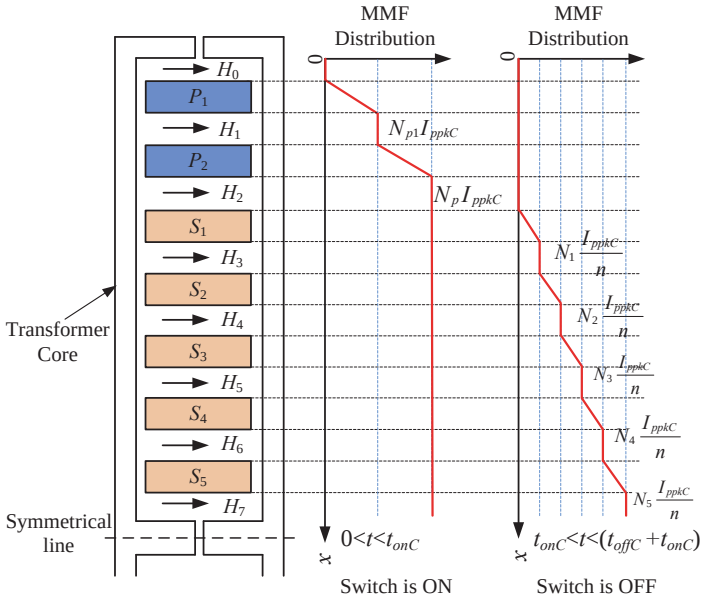

Fig. 5. MMF distribution of the non-interleaved (P-P-S-S-S-S-S) flyback transformer with respect to space.

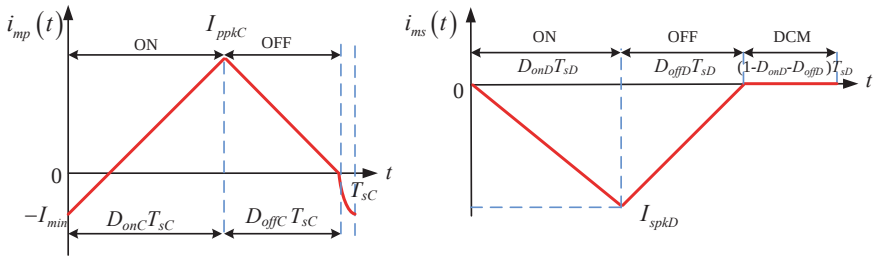

a) b)

Fig. 6. a) Primary magnetizing current in a given swithcing cycle during charge process, and b) Secondary magnetizing current discharge process.

given switching cycle, during charge and discharge processes are shown in Figs. 6(a) and 6(b), respectively. The MMF distribution in each transformer winding layer in the time domain is decomposed into sinusoidal harmonics by Fourier series analysis [24]. The power loss is then computed for each harmonic, and the power loss densities over all harmonics are summed to find the power dissipated in each layer.

The power loss expression in k^{th} layer P_{layerC}^{k} is given by [24], [40], [41]

$$P_{layerC}^{k}=\frac{R_{layer}}{2T_{layer}^{2}}\sum_{u=1}^{N_h}\varepsilon_u\left[\left(\left|F_{uC}(h)\right|^2+\left|F_{uC}(0)\right|^2\right)G_1(\varepsilon_u)-4\left|F_{uC}(h)\right|\left|F_{uC}(0)\right|\cos(\Delta\varphi)G_2(\varepsilon_u)\right] \tag{1}$$

$$\delta_u=\sqrt{\frac{\rho}{\pi\mu_0 u f_{swC}}} \tag{2}$$

$$\varepsilon_u=\left(\frac{\pi}{4}\right)^{0.75}\sqrt{\frac{T_{layer}}{W_W}}\left(\frac{d^{1.5}}{\delta_u}\right) \tag{3}$$

where $F_{uC}(0)$ and $F_{uC}(h)$ are the MMF amplitudes of the u^{th} harmonic at the beginning (x=0) and end (x=h) of a layer, respectively, d is the diameter of the given winding, h is the thickness of a given layer, with the suffix u being the harmonic number [24].

The magnitude $\left|F_{uC}\right|$ and phase φ_{uC} of u^{th} harmonic of the MMF during charge process are given by

$$\left|F_{uC}\right|=\sqrt{a_{uC}^2+b_{uC}^2} \tag{4}$$

$$\varphi_{uC}=\begin{cases}\tan^{-1}\left(-\dfrac{b_{uC}}{a_{uC}}\right), & \text{if } a_{uC}\geq 0\\ \pi+\tan^{-1}\left(-\dfrac{b_{uC}}{a_{uC}}\right), & \text{if } a_{uC}<0\end{cases} \tag{5}$$

$$\Delta\varphi=\varphi_{uC}(0)-\varphi_{uC}(h) \tag{6}$$

where a_{uC} and b_{uC} are the coefficients of Fourier series of the MMF during charge process and are provided in [24], and $\Delta\varphi$ is the difference between the phase angles of the u^{th} harmonic at the beginning (x=0) and end (x=h) of a layer, respectively.

The expression for the winding loss in a flyback transformer at each switching frequency (each switching cycle) index j during charge process is

$$P_{windC}(j) = I^2_{pavgC}(j) R_p + I^2_{savgC}(j) R_s + \sum_{k=1}^{n_{ls}+n_{lp}} P^k_{layerC}(j) \tag{7}$$

The total winding loss during charge process having N_c switching cycles is

$$P_{TwindC} = \sum_{j=1}^{N_c} P_{windC}(j) \tag{8}$$

2) Discussion

The winding loss during discharge process is calculated similar to that during charge process. The AC loss due to air-gap fringing field [28] has not been considered because of difficulties in interfacing the 2-D/3-D finite element analysis (FEA) simulation results with the optimization process. The negative current at the beginning of the turn-on process during charge process in Fig. 6(a) is due to the high voltage winding self-capacitance. When the secondary winding current becomes zero, the drain to source voltage V_{Mp} tends to decrease. Since the control IC, LT3751 [42] operates under boundary mode control, the next switching cycle starts before the high voltage winding capacitance completely discharges. Hence, the current flows in the reverse direction to discharge the high voltage winding capacitance.

B. Transformer core loss

The time-average core loss per unit volume P_v due to non-sinusoidal excitation is calculated using the improved generalized Steinmetz equation (*i*GSE) [43] which is given by

$$P_v = \frac{1}{T_s}\left[\int_0^{T_s} k_z \left|\frac{dB(t)}{dt}\right|^{\alpha} (\Delta B)^{\beta-\alpha}\, dt\right] \tag{9}$$

where $\left|\frac{dB(t)}{dt}\right|$ is the absolute value of the change rate of the flux density, ΔB is the peak-to-peak flux density, T_s is the switching period, and k, α and β are the constants provided by the core manufacturer. The core loss coefficient k_z in (9) is calculated using the following expression

$$k_z = \frac{k}{(2\pi)^{\alpha-1} 2^{\beta-\alpha}\left[\int_0^{2\pi} |\cos\theta|^{\alpha}\, \mathrm{d}\theta\right]} \tag{10}$$

The angle θ in (10) represents the phase angle of the sinusoidal excitation. For a given values of k, α and β, the value of coefficient k_z in (10) is fixed, irrespective of shape of flux density waveform.

The core loss per unit volume using iGSE during charge operation (where $\Delta B = B_{mC} + B_{nC}$ during the turn-on period and $\Delta B = B_{mC}$ during the turn-off period), in each switching cycle is given by

$$P_{vC} = \frac{k_z}{T_{sC}} \left[\left(B_{mC} + B_{nC} \right)^{\beta} \cdot {t_{onC}}^{1-\alpha} + {B_{mC}}^{\beta} \cdot {t_{offC}}^{1-\alpha} \right] \tag{11}$$

Similarly, the core loss per unit volume during discharge operation (where $\Delta B = B_{mD}$), in each switching cycle is given by

$$P_{vD} = \frac{k_z}{T_{sD}} {B_{mD}}^{\beta} \left[{t_{onD}}^{1-\alpha} + {t_{offD}}^{1-\alpha} \right] \tag{12}$$

C. Switching loss due to transformer self-capacitance

The capacitive turn-on or switching loss due the self-capacitance when the converter employs valley switching/boundary conduction mode (BCM) control during charge process is given by [26], [44], [45]

$$P_{swC} = \frac{1}{2} \left(n^2 C_s \right) \left(V_{in} - \frac{V_{out}}{n} \right)^2 f_{swC} \tag{13}$$

When the output voltage V_{out} is greater than nV_{in}, the capacitive switching loss P_{swC} is 0 W, since the converter operates with zero voltage switching (ZVS). The capacitive switching loss due the self-capacitance when the converter employs DCM control during discharge process is [26]

$$P_{swD} = \frac{1}{2} C_s \left(V_{Ms} \right)^2 f_{swD} \tag{14}$$

In DCM, the drain-to-source voltage V_{Ms} at the beginning of next switching cycle can be anywhere between $V_{out} + \delta_C n V_{in} + \delta_C V_{leakD}$ and $V_{out} + \left(2\delta_C - 1 \right) n V_{in} + \delta_C V_{leakD}$. The expression for δ_c is given by [26]

$$\delta_c = \frac{C_{osss}}{C_{osss} + C_{Db}} \tag{15}$$

The output capacitance C_{osss} of M_s and junction capacitance C_{Db} of diode D_b are approximately 15 pF and 1 pF, respectively.

D. Switching loss due to transformer leakage inductance

The loss due to the dissipative RCD snubber during charge process is given by

$$P_{snC} = \frac{1}{2} L_{lkp} I_{ppkC}^2 \frac{V_{snC}}{V_{snC} - \frac{V_{out}}{n}} f_{swC} \tag{16}$$

The loss due to the dissipative RCD snubber during discharge process is given by

$$P_{snD} = \frac{1}{2} L_{lks} I_{spkD}^2 \frac{V_{snD}}{V_{snD} - nV_{in}} f_{swD} \tag{17}$$

where V_{snC} and V_{snD} are the snubber clamp voltages for low and high voltage MOSFETs, respectively.

E. Remaining losses in the bidirectional flyback converter

The remaining losses in the converter during charge process are: switching loss of M_p, conduction losses of M_p, D_2 and R_{psense}, gate drive loss of M_p, and power consumption of charge control IC. Similarly, the remaining losses in the converter during discharge process are: switching loss of M_s, conduction losses of M_s, D_b and R_{ssense}, gate drive loss of M_s, and power consumption of discharge control IC. Since during both charge and discharge operations the converter employs BCM and DCM control, respectively, there are no diode reverse recovery losses in both modes.

IV. Efficiency Optimization for a DC-DC Converter Driving Capacitive Load

Efficient design of a high voltage bidirectional flyback converter, necessitates many trade-offs and iterations with a large number of design variables. The first step of the optimization routine is to determine the design specifications of the converter. The low voltage and high voltage MOSFETs, high voltage diode, turns ratio and magnetizing inductance are used as the constraints in the optimization, and are kept constant throughout the optimization routine. The flow chart of the proposed optimization routine is shown in Fig. 7. The converter specifications are used to calculate the number of primary and secondary turns, for a given ferrite core. The outputs of AWL technique are used to calculate the transformer parasitics. The energy losses during both charge E_{lossC} and discharge E_{lossD} modes are calculated and added to represent the total energy loss for that specific core. Finally, the energy efficiencies during charge η_C and discharge η_D modes are calculated as a function of output voltage.

The design decisions presented in Table II are used, to limit the solution space of the optimization routine. The ranges for the cores and parameters to be optimized are shown in Table III. The optimization routine iterates through all design possibilities, and finally presents an optimized (most efficient) solution for each core. The outputs of the AWL technique are represented as O_{AWL}.

TABLE III. Ranges of the design parameters

Parameters	**Ranges for optimization**
Transformer cores	EFD12, EFD 15, EFD 20, EFD 25, E 16, E 20, E 25, E 30, ETD 29, ETD 34, ETD 39, RM 8, RM 10, RM 12, PQ 20/20 and PQ 26/20
Height allocation factors for secondary winding (γ_s)	[0.5, 0.6, 0.7, 0.8]
Outputs from AWL technique O_{AWL}	see Section II and Figure 7

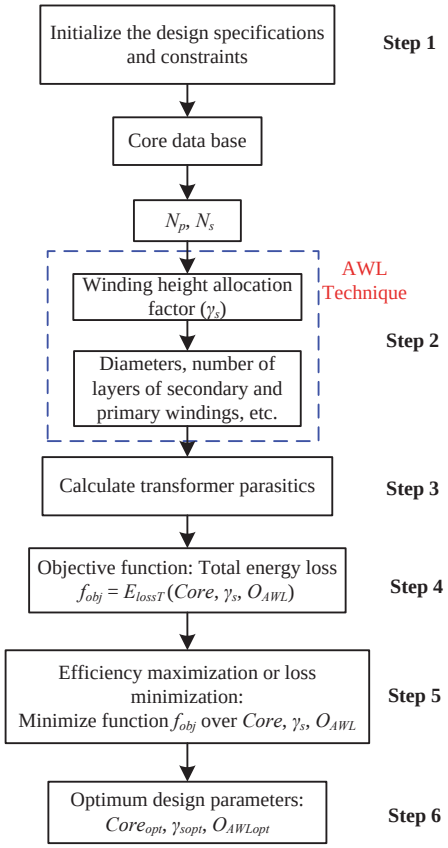

Fig. 7. Flow chart of the proposed efficiency optimization procedure.

The proposed optimization routine is described in the following steps:

1. Transformer turns ratio, peak currents (for charge and discharge operations), magnetizing inductance are selected from the design specifications and constraints. Number of primary and secondary turns are calculated for a given transformer core.
2. The proposed AWL technique is applied to calculate an array of the outputs (diameter, number of layers, turns per layer, number of parallel wires, for both primary and secondary windings). The condition for the last layer fill factor is FF_{LL}>0.85, this is to approximately make, equal number of turns per layer in final secondary layer and remaining secondary layers).
3. The transformer parasitics are calculated for each set of outputs resulted from AWL technique.
4. The objective function f_{obj} is defined as sum of the total energy losses in the bidirectional flyback converter over a set of operating points, and is given by

$$f_{obj} = E_{lossT}\left(Core,\ \gamma_s,\ O_{AWL}\right) \tag{18}$$

5. The efficiency optimization or loss minimization of function f_{obj} is

$$\min_{Core,\ \gamma_s,\ O_{AWL}} \left[f_{obj} \right] = \min_{Core,\ \gamma_s,\ O_{AWL}} \left[E_{lossT} \right] = \min_{Core,\ \gamma_s,\ O_{AWL}} \left[E_{lossC} + E_{lossD} \right] \tag{19}$$

6. The end results of the optimization routine are the set of parameters which contributes to the minimum total energy loss. Finally, the optimum charge and discharge energy efficiencies are calculated as a function of output voltage

$$\eta_C \left(V_{out} \right) = \frac{E_{load} \left(V_{out} \right)}{E_{load} \left(V_{out} \right) + E_{lossC}} = \frac{0.5 C_{load} V_{out}^2}{0.5 C_{load} V_{out}^2 + E_{lossC}} \tag{20}$$

$$\eta_D \left(V_{out} \right) = \frac{E_{load} \left(V_{out} \right) - E_{lossD}}{E_{load} \left(V_{out} \right)} = \frac{0.5 C_{load} V_{out}^2 - E_{lossD}}{0.5 C_{load} V_{out}^2} \tag{21}$$

V. Efficiency Optimization Results and Experimental Validation

A. Details of the optimizaton results

The components used in the bidirectional flyback converter except the transformer are shown in Table IV. All losses in the bidirectional flyback converter are calculated in MATLAB using the proposed comprehensive loss model. The winding loss is calculated during both charge and discharge processes, up to 100th order harmonics (N_h=100). The optimum secondary height allocation factor γ_s, for each core is provided in Fig. 8. Figure 9 provides the results of the optimum charge, discharge and overall (product of charge and discharge) energy efficiencies, and an overall energy efficiency of a typical design where 50 % space is allocated for primary and secondary windings, at an output voltage of 2.5 kV, with respect to different core volumes.

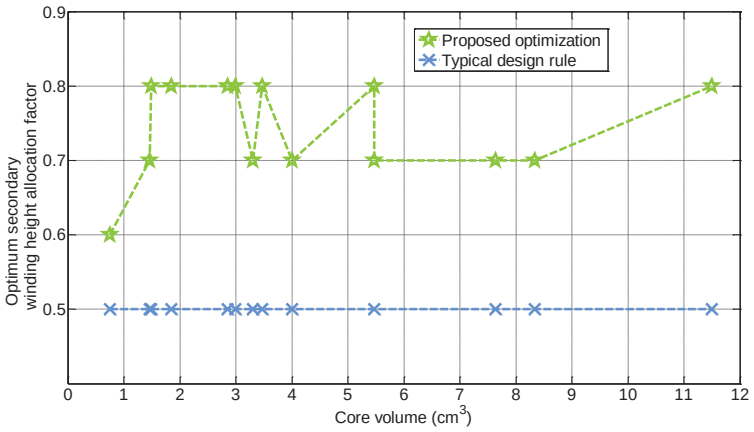

Fig. 8. Optimum secondary winding height allocation factor γ_s vs. core volume.

The total energy loss E_{lossC} at an output voltage of 2.5 kV is the loss occurred in all components of the converter, for charging the capacitive load from 0 V to 2.5 kV. Similarly, the total energy loss E_{lossD} at an output voltage of 2.5 kV is the loss occurred in all components of the converter, for discharging the capacitive load from 2.5 kV to 0 V. The most efficient and smallest transformer (or core) designs are two important outcomes of the proposed efficiency optimization routine. Table V shows a comparison of smallest core (SCD) and optimized core (OCD) designs.

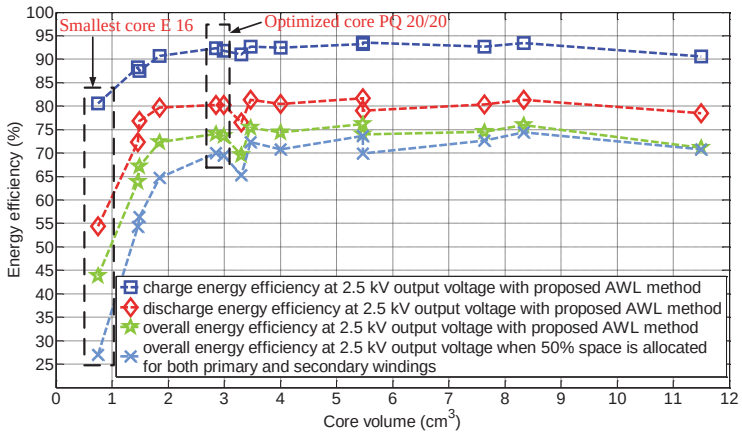

Fig. 9. Calculated optimized energy efficiencies at an output voltage of 2.5 kV vs. core volume. The sequence of the 14 cores is: [E 16, EFD 20, E 20, RM 8, PQ 20/20, E 25, EFD 25, RM 10, E 30, PQ 26/20, ETD 29, ETD 34, RM 12, ETD 39].

The smallest and optimized core designs are described below:

1) Smallest core design (SCD)

The smallest core is selected as the core whose temperature rise is less than the maximum temperature limit (130 °C). Several small cores such as, EFD 12, EFD 15, E 16 have been used in the optimization routine, out of those E 16 is the smallest

TABLE IV. COMPONENTS USED IN THE BIDIRECTIONAL FLYBACK CONVERTER

Component	Name / Manufacturer
Low voltage MOSFET M_p	IPB600N25N3 G [250 V, 25 A, 60 mΩ]
High voltage MOSFET M_s	IXTV03N400S [4 kV, 300 mA, 290 Ω]
High voltage diode D_2 or D_b	SP5LFG [5 kV, 400 mA, 50 ns (t_{rr})]
Film capacitive load C_{load}	WIMA [400 nF, 3 kV]
Analog control IC	LT3751

TABLE V. RESULTS OF THE OPTIMIZATION FOR SMALLEST CORE DESIGN (SCD) AND OPTIMIZED CORE DESIGN (OCD)

Parameter	SCD	OCD
Core name	E 16	PQ 20/20
Core volume	0.75 cm^3	2.85 cm^3
Maximum flux density B_{mC}	0.33 T	0.26 T
Total number of turns of primary N_p / secondary N_s winding	29 / 720	12 / 300
Number of layers of primary n_{lp} / secondary n_{ls}	2 / 8	1 / 4
Number of parallel wires (or squares) of primary n_{parp} / secondary n_{pars}	1 / 1	1 / 1
Number of turns (or squares) per layer of primary / secondary	15 / 90	12 / 75
Diameter of primary d_p / secondary winding d_s	0.4 mm / 0.1 mm	(0.5+0.2) mm / 0.143 mm
Primary magnetizing inductance L_{mp}	40 μH	44 μH
Height allocation for secondary winding γ_s	0.6	0.8
Spacing (or insulation) between secondary layers $d_{insulation}$	66 μm	0.9 mm
Transformer maximum temperature rise in a single bidirectional charge and discharge cycle	94 °C	30 °C

core with a maximum temperature rise of 94 °C (in a single bidirectional charge and discharge cycle). In the optimization routine, for all small cores (EFD 12, EFD 15, E 16), a maximum flux density of 0.33 T is chosen, hence for E 16, N_p becomes 29. As shown in Fig. 8, the optimum secondary height allocation factor for E 16 core is 0.6, this is for accommodating the 29 primary turns on the small core. The spacing between the secondary winding layers for SCD is 66 μm.

2) Optimized core design (OCD)

The core which has a lower volume and a better overall energy efficiency compared to other cores, is selected as an optimized core. In Fig. 9, most of the cores whose volume is above 2.85 cm^3 have overall energy efficiency between 74 % and 76 %. The EFD 25 core with volume 3.3 cm^3 has lower discharge efficiency (hence lower overall efficiency), since its window height H_W is less compared with the neighboring cores, such as EF 25 and RM 10 (see Fig. 9). For a better trade-off between the core volume and overall efficiency, the cores whose volume is between 2.85 and 4 cm^3 could be more suitable for the high voltage driver (with specifications shown in Table I). The cores with volumes 4 cm^3 (E 30) and 2.85 cm^3 (PQ 20/20) have overall efficiencies of 75 % and 74 %, respectively. However, PQ 20/20 core is selected as an optimized core, as 40 % increase in the core volume provides only 1 % increase in the overall energy efficiency. In the optimization routine, a maximum flux density of 0.26 T is chosen for all cores whose volumes are greater than equal to 1.46 cm^3 (EFD 20). As shown in Fig. 8, for all cores except the smallest core, the optimum secondary winding height allocation factor varies between 0.7 and 0.8. For PQ 20/20 core, the secondary height allocation factor is 0.8. The spacing between the secondary winding layers for OCD is 0.9 mm.

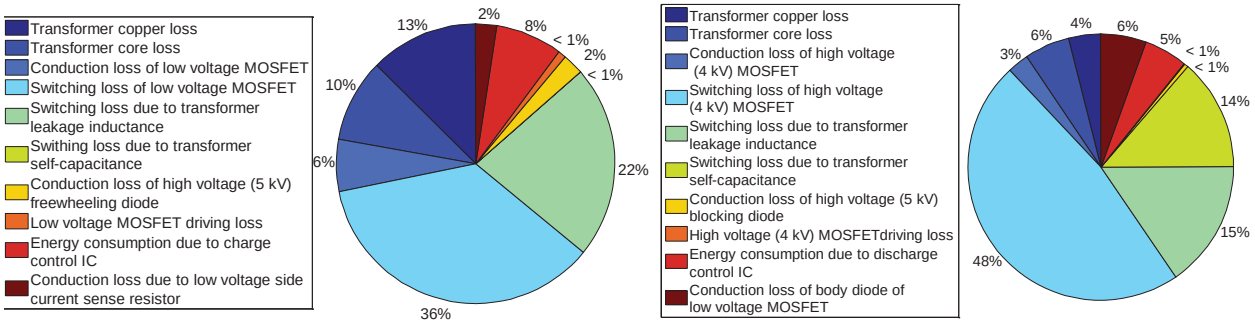

Fig. 10. Energy loss distribution of the optimized core (PQ 20/20), a) during charge and b) during discharge process.

The energy loss distributions for PQ 20/20 core during charge and discharge processes are shown in Figs. 10(a) and 10(b), respectively. During charge process, the converter operates with boundary conduction mode (BCM) control; hence the capacitive switching loss due to the self-capacitance is very low compared with other losses. The significant losses during charge process are: switching loss of low voltage MOSFET M_p, switching loss/snubber loss due to the transformer leakage inductance and transformer winding loss. During discharge process, the converter operates with discontinuous conduction

mode (DCM) control; hence the capacitive switching loss due to the self-capacitance cannot be neglected. The significant losses during discharge process are: switching loss of high voltage MOSFET M_s, switching loss due to the transformer leakage inductance, and capacitive switching loss due to the transformer self-capacitance.

B. Experimental Results

The experimental prototype of the bidirectional flyback converter is shown in Fig. 11 a). The comparison of measured [19] and calculated charge and discharge energy efficiencies for the smallest and optimized cores is provided in Figs. 12(a) and 12(b), respectively. In Figs. 12(a) and 12(b), the maximum difference between the calculated and measured energy efficiencies during charge and discharge modes is less than ±5%, except for the smallest core design at very high output voltage (>2.2 kV). The total loss due to the transformer parasitics for SCD is higher than that of OCD by 5 times, and the remaining losses in the converter, are the same for both designs.

In the bidirectional flyback converter an input capacitance C_{in} of 1800 μF (100 V) is used. The primary R_{psense} and secondary R_{ssense} sense resistors used in the converter are 25 mΩ and 0.5 Ω, respectively. The Z-type winding scheme [25] is implemented for the secondary winding of the flyback transformer, to reduce the self-capacitance. To remove the interlayer insulation tape between primary and secondary windings, triple insulated wire (TEX-E) from Furukawa [46] is used for the primary winding, and it has an insulation thickness of 0.2 mm. As shown in Table VI, 0.7 mm overall diameter wire (0.5 mm TEX-E wire) is used in the primary winding of PQ 20/20 core, and 0.4 mm overall diameter normal single insulated wire is used in the primary winding of E 16 core, due to non-availability of 0.2 mm TEX-E wire during practical implementation.

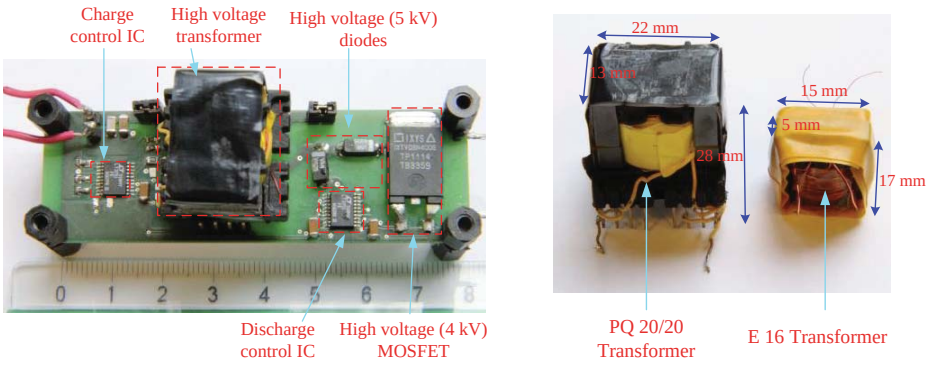

a) b)

Fig. 11. a) Experimental prototype of the bidirectional flyback converter with PQ 20/20 core; b) Optimized (PQ 20/20) and smallest (E 16) transformers.

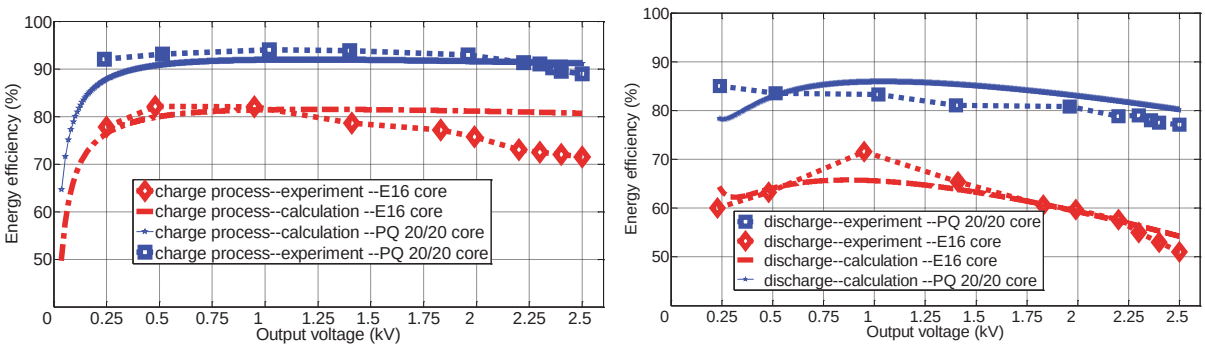

a) b)

Fig. 12. Comparison of calculated and measured a) charge and b) discharge energy efficiencies for the optimized (PQ 20/20) and smallest (E 16) cores.

For PQ 20/20 core, no snubber is used on either low voltage or high voltage side. Since the leakage inductance of E 16 core is very high, RCD snubbers are used on both primary and secondary sides and the loss model is updated accordingly. The loss model automatically considers RCD snubbers, when the leakage inductance L_{lkp} in the optimization is higher than 1.2 μH. The low voltage V_{snC} and high voltage V_{snD} RCD snubber clamp voltages are chosen as $\frac{2V_{out,max}}{n}$ and $2nV_{in}$, respectively, with a maximum output voltage $V_{out,max}$ of 2.5 kV. The insulation between the secondary layers of transformer is provided by the kapton tape which has a single layer thickness of 66 μm. The calculated and measured transformer parasitics for both SCD and OCD are provided in Table VI. The comparison shows that the model used for calculating the parasitics, for multiple solutions in the optimization routine is accurate enough.

TABLE VI. COMPARISON OF CALCULATED AND MEASURED TRANSFORMER PARAMETERS FOR SMALLEST AND OPTIMIZED CORE DESIGNS

Parameter of Transformer	**SCD**		**OCD**	
	Calculation	**Measurement**	**Calculation**	**Measurement**
Leakage inductance referred to primary L_{lkp}	3.22 μH	3.3 μH	818 nH	857 nH
Self-capacitance of secondary (high voltage) winding C_s	18.1 pF	21.62 pF	4.5 pF	6.23 pF
DC resistance of secondary (high voltage) winding R_s	46.54 Ω	44 Ω	15.3 Ω	18.2 Ω

VI. CONCLUSIONS

This paper presents an efficiency optimization approach for a high voltage bidirectional flyback dc–dc converter. The energy efficiency is optimized using a proposed new automatic winding layout generator technique and a comprehensive loss model. The proposed optimization technique is experimentally validated on a 25 W (charging power) high voltage bidirectional flyback converter. The measured charge and discharge energy efficiencies of the converter, with PQ 20/20 core at an output voltage of

2.5 kV are 89 % and 77.1 %, respectively. For both optimized and smallest core designs, energy efficiency during discharge process is less compared to that during charge process, mostly due to the switching loss of output capacitance of high voltage MOSFET.

The important conclusions of this paper are as follows:

1. The proposed AWL technique is highly recommended for high input or high output voltage applications which need a transformer with many turns (primary or secondary). It automatically calculates and provides the necessary winding design data such as wire sizes, number of winding layers, number of turns per layer, and number of parallel wires.
2. The AWL technique can be easily extended to interleaved and/or sectioned transformer structures.
3. Transformer parasitics are calculated for each set of outputs from AWL technique, which are needed to estimate the energy efficiency. By iteratively changing the spacing between secondary winding layers, the loss due to self-capacitance, leakage inductance and dc resistance of transformer are balanced.
4. Providing a very thick insulating tape between the secondary winding layers reduces the self-capacitance. The self-capacitance can be reduced significantly by allocating more space (or height) for the secondary winding.
5. Non-sectioned bobbins with larger window height are suitable for minimizing the self-capacitance, hence are recommended for high voltage capacitor charge and discharge application.
6. The output of the proposed efficiency optimization (overall energy efficiency vs. core volume curve) gives the flexibility for the designer to choose the necessary core and winding configurations.

REFERENCES

[1] Y. Bar-Cohen, *Electroactive Polymer [EAP] Actuators as Artificial Muscles: Reality, Potential, and Challenges*, 2nd Ed. Washington, DC: SPIE, 2004.

[2] R. E. Pelrine, R. D. Kornbluh, Q. Pei, J. P. Joseph, "High-speed electrically actuated elastomers with strain greater than 100%," *Science*, vol. 287, pp. 836–839, 2000.

[3] F. Carpi, D. DE Rossi, R. Kornbluh, R. Pelrine, P. Sommer-Larsen, Eds, "Dielectric Elastomer As Electromechanical Transducers," Amsterdam, The Netherlands: Elsevier, 2008.

[4] Danfoss PolyPower, Denmark, Online avilable: http://www.polypower.com/ [accessed 16 Oct. 2014].

[5] M. Tryson, H. E. Kiil, M. Benslimane, "Powerful tubular core free dielectric electro active polymer (DEAP) push actuator," in *Proc. SPIE*, vol. 7287, 2009.

[6] R. Sarban, B. Lassen, M. Willatzen, "Dynamic Electromechanical Modeling of Dielectric Elastomer Actuators With Metallic Electrodes," *IEEE/ASME Tran. Mechatronics*, vol. 17, no. 5, pp. 960-967, Oct. 2012.

[7] P. Thummala, H. Schneider, Z. Zhang, M. A. E. Andersen, R. Sarban, "A new Incremental Actuator based on Electro Active Polymer: Conceptual, Control and Driver Design Considerations," *IEEE/ASME Trans. Mechatronics* (under review process).

[8] P. Thummala, Z. Zhang, M. A. E. Andersen, S. Rahimullah, "Dielectric electro active polymer incremental actuator driven by multiple high-voltage bi-directional DC-DC converters," in *Proc. IEEE ECCE USA*, pp. 3837-3844, 2013.

[9] R. W. Erickson, D. Maksimovic, *Fundamentals of Power Electronics*, 2nd Ed., New York: Springer, 2001.

[10] J. Elmes, C. Jourdan, O. Abdel-Rahman, I. Batarseh, "High-Voltage, High-Power-Density DC-DC Converter for Capacitor Charging Applications," in *Proc. IEEE APEC*, pp. 433-439, 2009.

[11] T. Andersen, M. S. Rødgaard, O. C. Thomsen, M. A. E. Andersen, "Low voltage driven dielectric electro active polymer actuator with integrated piezoelectric transformer based driver," in *Proc.* SPIE, vol. 7976, p. 79762N, 2011.

[12] S. K. Chung, H. B. Shin, "High-voltage power supply for semi-active suspension system with ER-fluid damper," *IEEE Trans. on Vehicular Technology*, vol. 53, no. 1, pp. 206- 214, Jan. 2004.

[13] L. Eitzen, T Hoffstadt, J. Maas, "Power electronics concepts for driving EAP actuators," in *Proc. SPIE*, *Electroactive Polymer Actuators and Devices (EAPAD)*, pp. 86870D, 2013.

[14] K. Venkatesan, "Current Mode Controlled Bidirectional Flyback Converter," in *Proc. IEEE PESC*, pp. 835-842, 1989.

[15] G. Chen, Y.-S. Lee, S.Y.R. Hui, D. Xu, Y. Wang, "Actively clamped bidirectional flyback converter," *IEEE Trans. on Industrial Electronics*, vol. 47, no. 4, pp. 770-779, Aug. 2000.

[16] T. Bhattacharya, V. S. Giri, K. Mathew, L. Umanand, "Multiphase Bidirectional Flyback Converter Topology for Hybrid Electric Vehicles," *IEEE Trans. Industrial Electronics*, vol. 56, no. 1, pp. 78-84, Jan. 2009.

[17] M. Karpelson, G. Y. Wei, R. J. Wood, "Driving high voltage piezoelectric actuators in microrobotic applications," *Sensors and Actuators A*, vol. 176, pp. 78– 89, 2012.

[18] F. Zhang, Y. Yan, "Novel Forward–Flyback Hybrid Bidirectional DC–DC Converter," *IEEE Trans. Industrial Electronics*, vol. 56, no. 5, pp. 1578-1584, May 2009.

[19] P. Thummala, Z. Zhang, M. A. E. Andersen, "High Voltage Bi-directional Flyback Converter for Capacitive Actuator", in *Proc. IEEE EPE*, pp. 1-10, 2013.

[20] P. Thummala, H. Schneider, Z. Ouyang, Z. Zhang, M. A. E. Andersen, "Estimation of transformer parameters and loss analysis for high voltage capacitor charging application," in *Proc. IEEE ECCE Asia*, pp. 704-710, 2013.

[21] C. W. T. McLyman, *Transformer and Inductor Design Handbook*, 3rd Ed., New York: Marcel Dekker, 2004.

[22] W. G. Hurley, W. H. Wolfle, *Transformers and Inductors for Power Electronics: Theory, Design and Applications*, 1st Ed., John Wiley and Sons Ltd., 2013.

[23] M. Kazimierczuk, *High-frequency magnetic components*, 2nd Ed., John Wiley and Sons Ltd., 2014.

[24] P. Thummala, H. Schneider, Z. Zhang, A. Knott, M. A. E. Andersen, "Optimization of a bi-directional flyback converter for a high voltage capacitor charging application," in *Proc. IEEE APEC*, pp. 2556-2563, 2014.

[25] H. Schneider, P. Thummala, L. Huang, A. Knott, Z. Zhang, M. A. E. Andersen, "Investigation of Transformer Winding Architectures for High Voltage Capacitor Charging Applications," in *Proc. IEEE APEC*, pp. 334-341, 2014.

[26] P. Thummala, D. Maksimovic, Z. Zhang, M. A. E. Andersen, "Digital control of a high-voltage (2.5 kV) bidirectional DC-DC converter for driving a dielectric electro active polymer (DEAP) based capacitive actuator," in *Proc. IEEE ECCE USA*, 14-18th Sept. 2014.

[27] N. O. Sokal, R. Redl, "Control algorithms and circuit designs for optimal flyback-charging of an energy storage capacitor (e.g., for flash lamp or defibrillator)," *IEEE Trans. Power Electronics*, vol. 12, no. 5, pp. 885-894, Sep. 1997.

[28] R. Prieto, J.A. Cobos, O. Garcia, R. Asensi, J. Uceda, "Optimizing the winding strategy of the transformer in a flyback converter," in *Proc. IEEE PESC*, pp. 1456-1462, 1996.

[29] C. R. Sullivan, T. Abdallah, T. Fujiwara, "Optimization of a flyback transformer winding considering two-dimensional field effects, cost and loss," in *Proc. IEEE APEC*, pp.116-122, 2001.

[30] H. K. Sang, D. Maksimovic, I. Cohen, "Efficiency Optimization in Digitally Controlled Flyback DC–DC Converters Over Wide Ranges of Operating Conditions," *IEEE Trans. Power Electronics*, vol. 27, no. 8, pp. 3734-3748, Aug. 2012.

[31] A. C. Nanakos, E.C. Tatakis, N. P Papanikolaou, "A Weighted-Efficiency-Oriented Design Methodology of Flyback Inverter for AC Photovoltaic Modules," *IEEE Trans. Power Electronics*, vol. 27, no. 7, pp. 3221-3233, July 2012.

[32] X. Zhou, T. G. Wang, F. C. Lee, "Optimizing Design for Low Voltage DC-DC Converters," in *Proc. IEEE APEC*, pp. 612-616, 2007.

[33] U. Badstuebner, J. Biela, J. W. Kolar, "An optimized, 99% efficient, 5 kW, phase-shift PWM DC-DC converter for data centers and telecom applications," in *Proc. IEEE IPEC,* pp.626,634, 21-24 June 2010.

[34] J. Biela, U. Badstuebner, J. W. Kolar, "Impact of Power Density Maximization on Efficiency of DC-DC Converter Systems," *IEEE Trans. Power Electronics*, vol. 24, no. 1, pp. 288-300, Jan 2009.

[35] E. C. Snelling, *Soft Ferrites-Properties and applications,* 2nd Ed. London, UK, Butterworth, 1988.

[36] L. Dalessandro, F. da Silveira Cavalcante, J. W. Kolar, "Self-Capacitance of High-Voltage Transformers," *IEEE Trans. Power Electronics,* vol. 22, no.5, pp. 2081-2092, Sept. 2007.

[37] J. Biela, J. W. Kolar, "Using Transformer Parasitics for Resonant Converters—A Review of the Calculation of the Stray Capacitance of Transformers," *IEEE Trans. Industry Applications,* vol. 44, no.1, pp. 223-233, 2008.

[38] W.G. Hurley, E. Gath, J. G. Breslin, "Optimizing the AC resistance of multilayer transformer windings with arbitrary current waveforms," *IEEE Trans. Power Electronics*, vol. 15, no. 2, pp. 369-376, Mar 2000.

[39] J. A. Ferreira, "Improved analytical modeling of conductive losses in magnetic components," *IEEE Trans. Power Electronics*, vol. 9, no. 1, pp. 127,131, Jan 1994.

[40] J. Vandelac, P. D. Ziogas, "A Novel Approach for Minimizing High-Frequency Transformer Copper Losses," *IEEE Trans. Power Electronics,* vol. 3, no. 3, pp. 266-277, Jul. 1988.

[41] S. H. Kang, “Efficiency Optimization in Digitally Controlled Flyback DC-DC Converters Over Wide Ranges of Operating Conditions,” Ph.D. Thesis, Dept. Electrical, Computer and Energy Engineering, University of Colorado Boulder, USA 2011.

[42] LT3751 datasheet, “High voltage capacitor charger controller with regulation,” Linear Technology Corporation, USA, Online available: http://cds.linear.com/docs/en/datasheet/3751fc.pdf [accessed 16 Oct. 2014].

[43] K. Venkatachalam, C. R. Sullivan, T. Abdallah, H. Tacca, “Accurate prediction of ferrite cores loss with nonsinusoidal waveforms using only Steinmetz parameters,” in *Proc. IEEE Workshop Comput. Power Electron.*, pp. 36–41, 2002.

[44] M. T. Zhang, M. M. Jovanovic, F. C. Lee, “Design considerations and performance evaluations of synchronous rectification in flyback converters,” in *Proc. IEEE APEC*, pp. 623-630, Feb 1997.

[45] C. P. Basso, *Switch-mode power supplies-spice simulations and practical designs*, 2nd Ed., McGraw Hill, 2008.

[46] Furukawa webpage, “Triple Insulated Wire: Standard Type TEX-E,” Furukawa Electric, Japan, Online avilable: http://www.furukawa.co.jp/makisen/eng/product/texe_series.htm [accessed 16 Oct. 2014].

Appendix M

A new Incremental Actuator based on Electro Active Polymer: Conceptual, Control and Driver Design Considerations

---

IEEE Transactions on Mechatronics 2015

A new Incremental Actuator based on Electro Active Polymer: Conceptual, Control and Driver Design Considerations

Prasanth Thummala[*], *Student Member*, *IEEE*, Henrik Schneider[*], *Student Member*, *IEEE*, Zhe Zhang[*], *Member*, *IEEE*, Michael A. E. Andersen[*], *Member*, *IEEE*, Sarban Rahimullah[#], *Member*, *IEEE*,

***Abstract*— This paper presents an overview of the widely used conventional linear actuator technologies, and already existing electro active polymer based linear and rotary actuators. It also provides conceptual, control and driver design considerations for a new dielectric electro active polymer (DEAP) based incremental actuator. The DEAP incremental actuator consists of three electrically-isolated and mechanically-connected capacitive actuators. To accomplish the incremental motion, each actuator needs to be independently charged and discharged by a high voltage bidirectional dc-dc converter. The topology used for the high voltage driver is a peak-current controlled bidirectional flyback converter. The high voltage drivers are experimentally tested with both film capacitive loads and DEAP incremental actuator. The proposed DEAP incremental actuator moves with a maximum velocity of 1.5 mm/s, at 2.78 Hz incremental actuation frequency, when all actuators are driven with 1.8 kV.**

***Index Terms*—linear actuators, switch-mode power supplies, dc-dc power converters, actuators, energy efficiency, dielectric electro active polymer (DEAP)**

I. INTRODUCTION

ACTUATORS providing linear motion are used in a vast variety of applications ranging from large size machineries (e.g., cranes) to small scale micro-electro-mechanical system (MEMS) devices used for micro positioning. Linear actuators are typically characterized by their maximum stroke length, force, speed, and precision (or resolution). The typical linear actuators include mechanical, electro-mechanical, hydraulic, pneumatic, and piezo, etc.

Mechanical linear actuator as shown in Fig. 1 operates by converting the rotary motion into linear motion. The advantages of mechanical actuators are low price, precision positioning, and no need of a power source. The disadvantage

This work was supported by the Danish National Advanced Technology Foundation under the "Highly efficient low cost energy generation and actuation using disruptive DEAP technology" project, managed by Danfoss PolyPower A/S, Denmark.

Part of this paper was presented and selected as a best student paper award at IEEE Energy Conversion Congress and Exposition (ECCE) USA'13 (Sept. 15-19th, 2013, Denver, CO, USA).

[*]All authors are with the Department of Electrical Engineering, Technical University of Denmark, DK-2800 Kongens Lyngby, Denmark (e-mail: pthu@elektro.dtu.dk, hensc@elektro.dtu.dk, zz@elektro.dtu.dk, ma@elektro.dtu.dk).

[#]The author is with LEAP Technology, Science and Technology Park, DK-2800 Kongens Lyngby, Denmark (e-mail: Rahim@leaptechnology.com).

Fig. 1. A mechanical linear actuator [1].

is that they have to be operated manually. An electromechanical linear actuator use DC motor and stepper motor to control as shown in Fig. 2, a linear-action shaft output. Rotary motion of the motor is converted to linear displacement. These actuators are heavier than their motor counterparts due to the addition of the actuator assembly. Piezoelectric actuators can achieve extremely fine positioning resolution, but have a very short range of motion. The piezo actuator as shown in Fig. 3 is expensive and fragile. Pneumatic linear actuators as shown in Fig. 4 operate with an external source of compressed air. They are efficient, but

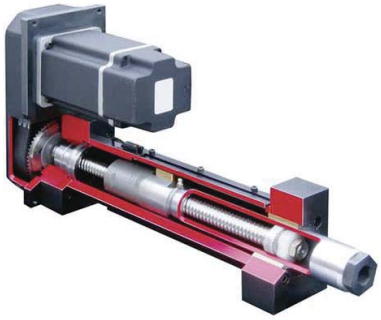

Fig. 2. An electro-mechanical linear actuator [2].

relatively complex to control via pressure valves and compressor manipulation. Hydraulic linear actuators are used in many industrial applications requiring higher levels of force than provided through equivalently sized electromechanical systems. Hydraulic linear actuator as shown in Fig. 5 requires an external source for fluid pressurization. Unlike pneumatic actuators, a leak from hydraulic equivalents can foul

Fig. 3. A piezo linear actuator [3].

equipment and require additional clean up procedures depending on the type of fluid used. Control is complex, involving compressor control and hydraulic valves.

Fig. 4. A piezo linear actuator [4].

Dielectric electro active polymer (DEAP) is an emerging smart material that has experienced substantial development and has gained increasing attention by the researchers from academia and industry [6]-[8]. The DEAP material is a very thin (35-55 μm) incompressible silicone elastomer film with a compliant electrode layer on both sides [9]-[12]. DEAP can be used in actuation, sensing and energy harvesting applications. The basic operation of the DEAP is the reduction in the polymer's thickness and increase in its area, due to an applied electric field. The unique properties of DEAP are large strain (5-100%), light weight (7 times lighter than steel), high flexibility (100,000 times less stiff than steel), low noise operation, and low power consumption. DEAP, when used as actuators, have the potential to be an effective replacement for many conventional actuators viz. electro-mechanical, piezo, pneumatic, hydraulic, etc. The linear DEAP actuator shown in

Fig. 5. A hydraulic linear actuator [5].

Fig. 6 is ideally equivalent to a pure capacitive load [12], [13].

Fig. 6. A prototype of linear DEAP actuator.

Several researchers have investigated and implemented electro active polymer based linear and rotary type actuators. Numerous applications of dielectric elastomers including inchworm robot and rotary motors have been described in [14]. The robotic inchworm as shown in Fig. 7 uses electrostatic clamps which enable it to travel over both vertical and horizontal surfaces, for tasks such as inspection in narrow pipes [14]. The walking robot using a multifunctional electro elastomer (MER) spring roll as each of the robot's six legs is shown in Fig. 8 [15]. Each spring roll leg was a linear actuator, with 3-6 mm stroke at 1-10 Hz frequency. The speed was as high as 2.7 in/s. A rotary motor made with a pair of bow tie elastomer actuators as shown in Fig. 9, with an output power of 4 W at 100 RPM has been demonstrated in [14]. The emerging DE technology has been thoroughly reviewed presents exciting possibilities across a wide range of applications including soft robotics [16]. An earthworm robot

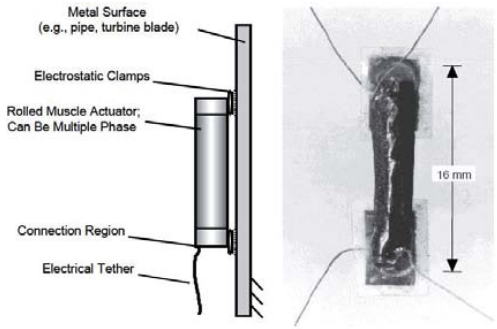

Fig. 7. An inchworm robot with a dielectric elastomer body [14].

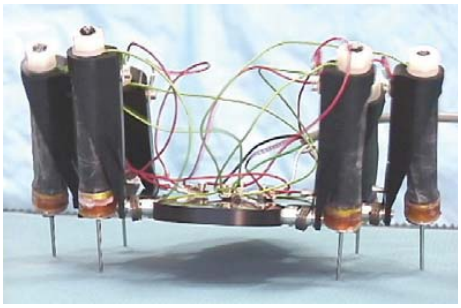

Fig. 8. A walking robot with MER spring rolls as legs [15].

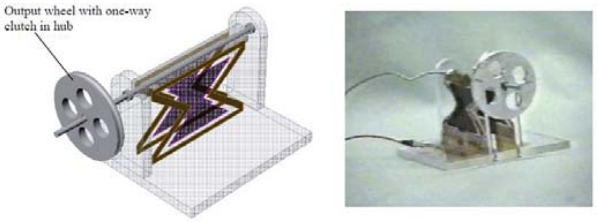

Fig. 9. A simple rotary motor based on dielectric elastomers [14].

as shown in Fig. 10 has been made using a novel soft actuator based on a dielectric elastomer. It has been demonstrated that the actuator moved with 1 mm/s at 5 Hz [17]. A simple rotary motor based on dielectric elastomers as shown in Fig. 11, has been proposed in [18]. A new way to achieve the rotary motion using the DEAP actuators has been reported in [19]. Furthermore, several researchers have investigated piezo, pneumatic and hydraulic based actuators. The gain scheduling control of a walking piezo actuator is proposed in [20]. Bipolar piezo electric actuators are proposed in [21]. High-accuracy tracking control of hydraulic actuators is discussed in [22].

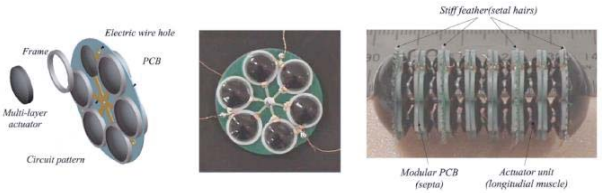

Fig. 10. Earthworm robot with the actuator module [17], [16].

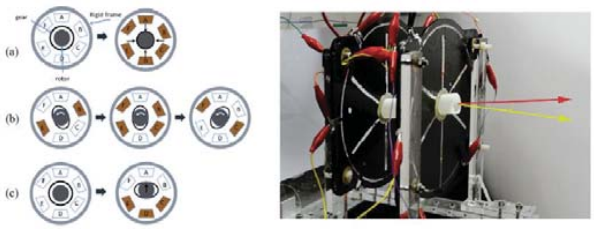

Fig. 11. A simple rotary motor based on dielectric elastomers [18].

The DEAP incremental actuator concept, recently proposed in [23], consists of two grippers at both ends (to enable gripping operation) and an extender (to move the grippers), as shown in Fig. 12. These grippers connect with the extender mechanically. The grippers A_1 and A_3 and the extender A_2 are similar to the DEAP actuator shown in Fig. 6. For moving the DEAP incremental actuator, the three DEAP actuators (which behave as electrically isolated capacitive loads) need to be controlled. Details of the DEAP incremental actuator operation can be found in [23]. The DEAP_incremental actuator technology has the potential to be used in various

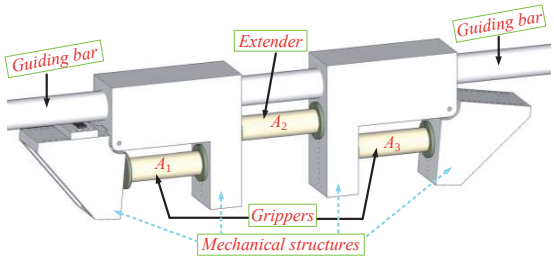

Fig. 12. Conceptual diagram of the proposed DEAP incremental actuator.

industries, e.g., automotive, space and medicine. Table I, provides a short comparison of the DEAP and piezo incremental actuator technologies. To summarize, the DEAP incremental actuator technology has a coarser resolution and a lower force density, but has the potential for higher velocity, higher structural flexibility and robustness compared to piezo technology. The DEAP technology is still a new technology and future performance improvements are expected.

Driving the DEAP incremental actuator has three main challenges from a power electronics standpoint. Firstly, it

TABLE I
COMPARISON BETWEEN DEAP AND PIEZO INCREMENTAL ACTUATOR TECHNOLOGIES

Parameter	Piezo Technology	DEAP Technology
Strain (Resolution)	Small (~ 0.02-0.1 %)	Large (~ 1-100 %)
Force density	High (~ 20 N/mm^2)	Medium (~ 0.5 N/mm^2)
Structural flexibility	Low (Young's Modulus Y= ~ 40-60 GPa)	High (Young's Modulus Y= ~ 1.1-1.8 MPa)
Incremental actuation frequency	~ 100-5000 Hz	~ 1-15 Hz
Linear velocity per unit length = Strain×incremental actuation frequency	Medium (~ 20-500 Hz)	High (~ 1-1500 Hz)

requires high voltages (2-2.5 kV), to generate sufficient force and stroke from each DEAP actuator. Suitable energy sources for this application are lithium batteries with a voltage range: 9-24 V DC. This necessitates the need of high voltage step-up circuits as a driving mechanism for the DEAP actuator. Secondly, DEAP actuators convert only a small fraction of the input electrical energy into mechanical work, while they store the remainder in the capacitive structure of the actuator, and must be recovered to maximize the system efficiency. This necessitates the need of bidirectional converters [24]-[26]. Finally, to move the incremental actuator with the required speed and direction, the three DEAP actuators needs to be driven by a specific sequence of high voltage signals.

The flyback converter is suitable for high voltage and low power applications due to its simple structure and low component count [27]. Control algorithms for optimal-flyback charging of a capacitive load have been proposed in [28]. High

voltage switch-mode power supplies for charging the capacitive loads have been implemented in [29], [30]. The bidirectional flyback converters are proposed in [31]-[33] to transfer the power in both directions. Prior work on the high voltage drivers for the DEAP actuators demonstrated a low voltage piezoelectric transformer based DEAP solution, and it was incorporated into a coreless DEAP actuator [34], and a bidirectional flyback converter topology to drive the PolyPower Push Inlastor DEAP actuator [35]. In [36] an efficiency optimization technique is proposed for a bidirectional flyback converter in a high voltage capacitor charging application. Several transformer winding architectures have been investigated in [37] for the high voltage capacitor charge and discharge application. Experimental study of DEAP actuator energy conversion efficiency is performed in [38]. Intelligent control of electro active polymer actuators based on fuzzy and neuro fuzzy methodologies is proposed in [39]. Digital control of the bidirectional flyback converter is proposed in [40] for driving capacitive actuators. The objectives of this paper are, to provide the conceptual design of the DEAP actuator, and the necessary control and driving circuits for the newly proposed DEAP incremental actuator.

The paper is organized as follows: Section III provides different concepts for the DEAP incremental actuators proposed by Danfoss Poly Power A/S. Section IV discuss the conceptual design of an axial DEAP actuator. Section V describes the basic idea and operational diagrams of the DEAP incremental actuator concept. Section VI presents high voltage driving circuits for the incremental actuator. Section VII discusses the experimental results, and the implementation issues. Section VIII provides the system integration, followed by the conclusion in Section IX.

II. Different Concepts of DEAP Incremental Actuators

Two different concepts (1 and 2) of DEAP incremental actuators are provided in this section. Each concept has its unique characteristics which can demonstrate various unique properties of DEAP as described in earlier sections.

A. Concept 1

Figures 13 (a) shows the Concept 1 of DEAP incremental actuator. It is designed to operate outside a cylindrical bar and consists of three sub components, namely one extender and two grippers at either end. The corrugation profile of the extender and the grippers are 90° shifted. When in operation, one gripper holds the bar while the other gripper is in the released position. The extender either pushes or pulls the released gripper.

The grippers are rolled on a core with radial tension. Rigid mechanical connections of type M_2 are subsequently applied. The extender sub component can be realized by simply using platforms Axial 1 component. The grippers and extender are joined by gluing or screwing their mechanical connections together (green plates in Fig. 13 (a)). Mechanical constrainers can be applied to the grippers in order to avoid the axial extension of the grippers when in operation. Such constrainers enable the gripper to exhibit only radial movements. Soft encapsulation for protection and/or aesthetics can be applied as shown in Fig. 13 (b).

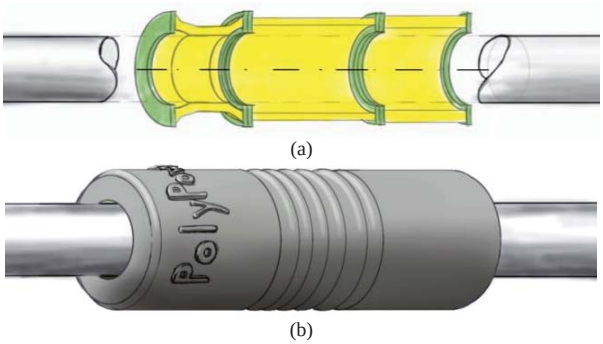

Fig. 13. Concept 1 of DEAP incremental actuator. (a) Cross section view of the actuator, (b) incremental actuator with protective and/or aesthetic encapsulation.

B. Concept 2

Concept 2 is designed to operate inside a cylindrical tube as opposed to Concept 1. Concept 2 consists of one extender and two grippers on either end. Both the grippers and the extender of Concept 2 are platforms Axial 1 standard components. Additional gripping mechanisms are applied to the grippers (red structures in Fig. 14). The gripping mechanism extends or contracts radially when the grippers are, respectively, contracting or extending axially as illustrated by the arrows in Fig. 14. The three Axial 1 actuators are joined together, at their mechanical connections, by gluing or screws.

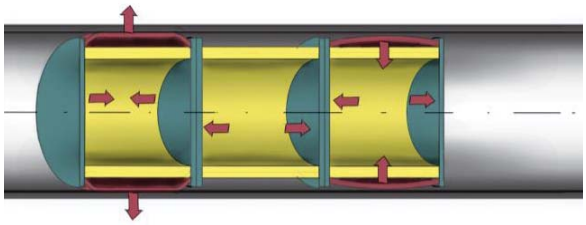

Fig. 14. Concept 2 of DEAP incremental actuator: Cross section view of the actuator with operation arrows.

Fast and precise adjustment, low noise operation, and high energy efficiency are the key advantages of the proposed DEAP incremental actuators compared to other linear incremental actuators or other sliding dielectric elastomer actuators.

III. Conceptual Design of an Axial DEAP Actuator

The conceptual design of an axial DEAP actuator is a tubular structure being formed by rolling a DEAP sheet as shown in Fig. 15. The generic dimension of such structure is its height h_0, the inner diameter R_i, and the wall thickness (R_o-R_i). All these dimensions have to be calculated based on the material's electric field strength E, blocking force F_{block}, and the required stroke Δh.

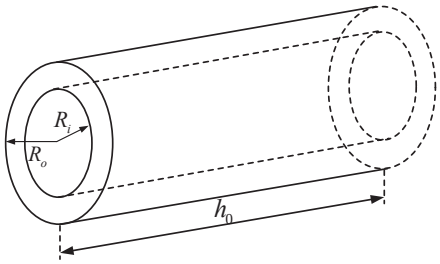

Fig. 15. Conceptual drawing of an axial DEAP actuator.

A. Functional characteristics during the static operation

The equation governing the electrostatic, elastic and blocking forces in a DEAP actuator system during static operation is given by

$$F_{electrostatic} - F_{elastic} = F_{load} \tag{1}$$

Assuming low strain (S<10 %) operation, (1) can be simplified as [6]

$$\frac{\varepsilon_0 \varepsilon_r A_{act} V_{DEAP}^2}{d^2} - \frac{Y A_{act} \Delta h}{h_0} = F_{load} \tag{2}$$

The cross sectional area of the DEAP actuator is given by

$$A_{act} = \frac{F_{block,max}\big|_{\Delta h=0}}{\varepsilon_0 \varepsilon_r E^2} \tag{3}$$

For an electric field strength of E=40 V/μm, with a permittivity of vacuum ε_0= 8.854×10^{-12} F/m, relative permittivity of the dielectric material ε_r=3.1, and maximum blocking force of $F_{block,max}$=40 N, the calculated area of cross section of the actuator from (3) is A_{act}=910 mm^2.

If R_o and R_i are the outer and inner diameters of the actuator then,

$$A_{act} = \pi\left(R_o^2 - R_i^2\right) \tag{4}$$

By choosing one of the inner or outer diameters of the actuator, the other diameter can be calculated from (4). The height of the actuator h_0 is calculated from (2), based on the following specifications: blocking force of F_{block}=10 N, stroke of Δh=1 mm, applied voltage to the actuator V_{DEAP}=2400 V, thickness of the polymer film d=40 μm. The calculated height is h_0=25 mm.

The maximum stroke that can be achieved for a given DEAP actuator height h_0 is given by

$$\Delta h_{max}\big|_{F_{block}=0} = \frac{\varepsilon_0 \varepsilon_r E^2 h_0}{Y} = 1.3 \text{ mm} \tag{5}$$

where Y is the modulus of elasticity, its value is 1.8 MPa, at the limited strain range. The strain S of the DEAP actuator is given by

$$S = \frac{\Delta h}{h_0} \times 100 = 4\ \% \tag{6}$$

The length of DEAP sheet to be rolled L_{act} is given by

$$L_{act} = \frac{A_{act}}{d} = 10.12 \text{ m} \tag{7}$$

The operating region of a DEAP actuator can be represented by the relationship between its force, stroke and applied voltage. The force-stroke, stroke-voltage and force-voltage characteristics of a DEAP actuator are shown in Figs. 16, 17 and 18, respectively. In Fig. 16, for an applied voltage of V_{DEAP}=2.4 kV, the blocking force becomes F_{block}=10 N at a stroke Δh of 1 mm. As shown in Fig. 4, to achieve a certain stroke, the blocking force decreases with the applied voltage. As shown in Fig. 17, at a given applied voltage, the stroke decreases as the load on the DEAP actuator increases. Similarly, as shown in Fig. 18, at a given applied voltage, the blocking force decreases as the stroke increases.

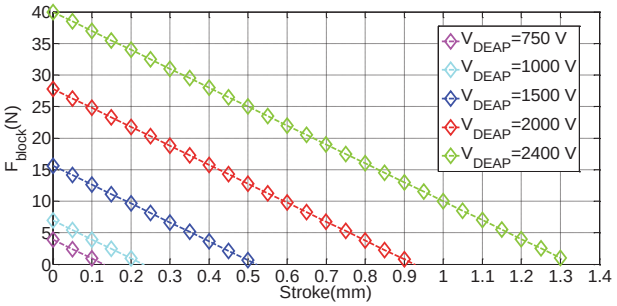

Fig. 16. Stroke vs. blocking force curve at different applied voltages.

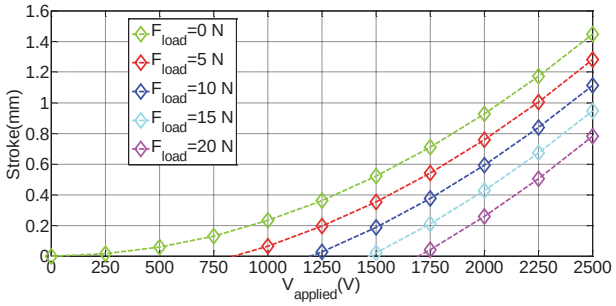

Fig. 17. Applied voltage vs. stroke curves at different load forces.

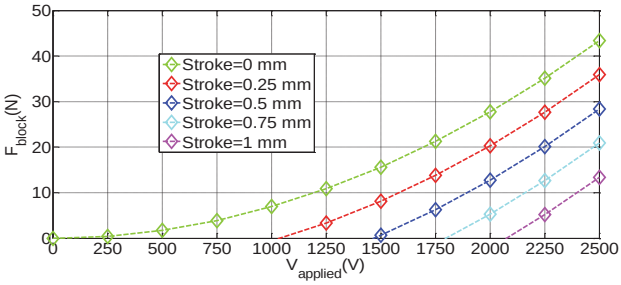

Fig. 18. Applied voltage vs. blocking force curves at different strokes.

B. Discussion

The calculated height h_0 (25 mm) of the DEAP actuator described in the above section differs from the real value (110 mm) due to the following reasons:

1. Real DEAP actuators will have 20-30 mm extra height because of the stabilizing passive areas at each end.
2. Real DEAP actuators are not driven with electric field strength of 60 V/μm, but much lower to avoid breakdown which would need larger height to achieve the same stroke.
3. Real DEAP actuators don't have 40 μm uniform film thicknesses. There is always ±5 μm tolerance on the film thickness (35-45 μm), but mechanically the actuator will have a higher thickness which again reduces the stroke. Hence, a larger height is needed for the DEAP actuator to achieve a certain stroke.
4. Real DEAP actuators are made of corrugated films which reduce the stroke, hence require longer actuator height for a certain stroke.
5. Real DEAP actuators become stiffer by 2 to 4 times when rolled i.e. the stiffness or Young's modulus Y of the DEAP actuator is 2 to 4 times higher than the stiffness of the DEAP film.

IV. Control of Incremental Motor

The DEAP incremental actuator consists of three axial DEAP actuators (one extender and two grippers). The incremental actuation sequence and the driving voltage waveforms for the grippers and the extender are shown in Figs. 19 and 20, respectively. Each gripper is connected to mechanical supports on either side. It expands and clamps to the guiding bar (e.g., a rod) surface when charged (with high voltage), and unclamps from it, when discharged. The extender expands axially along the guiding bar. During the operation, one gripper holds the guiding bar while the other gripper is in a released position. The extender either pushes or pulls the released gripper. The incremental actuator performs 6 different steps, to achieve a single incremental actuation stroke Δx as shown in Fig. 19.

A. Moving sequence of the linear incremental motion towards the positive x-axis direction

1. *Start:* All actuators are in the discharged state.
2. *Step* 0 (S_0): A_1 is charged and clamps to the guiding bar. A_2 and A_3 are in the discharged state.
3. *Step* 1 (S_1): A_1 remains in the charged state. A_2 is charged and pushes the mechanical structure towards right, and A_3 remains in the discharged state.
4. *Step* 2 (S_2): A_1 and A_2 still remain in the charged state. A_3 is charged.
5. *Step* 3 (S_3): A_1 is discharged and is in the released position. A_2 and A_3 still remain in the charged state.
6. *Step* 4 (S_4): A_1 remains in the discharged state. A_2 is discharged, and A_3 remains in the charged state.
7. *Step* 5 (S_5): A_1 is charged. A_2 remains in the discharged state, and A_3 remains in the charged state.
8. *Step* 6 (S_6): A_1 remains in the charged state. A_2 remains in the discharged state, and A_3 is discharged.
9. End: All actuators are discharged at the end.

The Step 0 is only used for charging the actuator A_1. The Steps 1-6 (S_1-S_6) repeat for achieving continuous incremental actuation cycles. The End step is used to discharge all actuators. The moving sequence for the reverse linear incremental motion towards the negative x-axis direction can be easily drawn similar to Fig. 19. For moving towards the negative x-axis (reverse) direction, the driving voltages of actuators A_1 and A_3 need to be reversed, without changing the

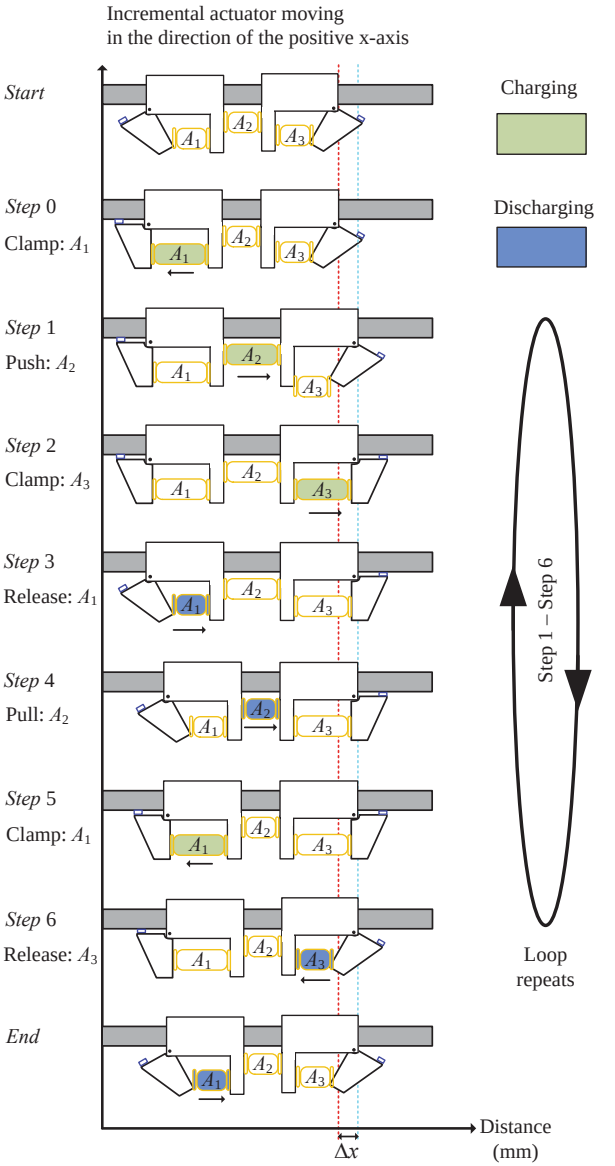

Fig. 19. Moving sequence of the DEAP incremental actuator for incremental motion towards the positive x-axis direction.

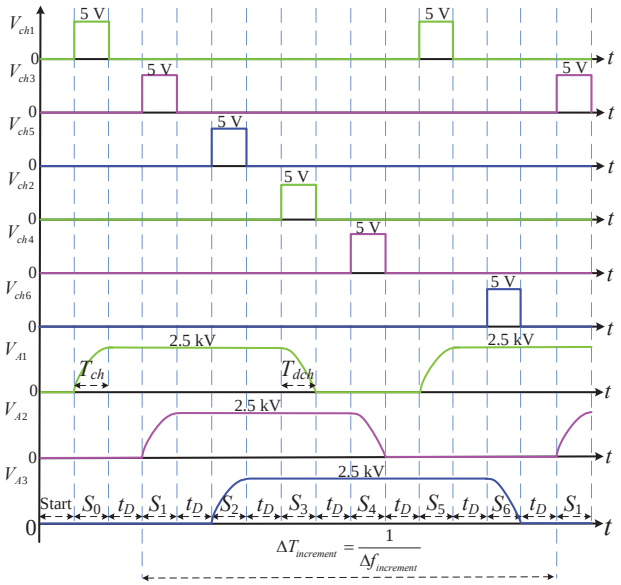

Fig. 20. Enable signals and driving voltages of all DEAP actuators, to achieve the incremental motion with variable speed, towards the positive x-axis direction.

driving voltage of actuator A_2. The driving voltages for moving with the certain incremental frequency are shown in Fig. 20. To move the actuator with maximum incremental frequency, zero delay (t_D=0) is needs to be provided between the charge and discharge cycles of actuators A_1, A_2 and A_3.

B. Incremental actuation frequency

Assuming the same charge T_{ch} and discharge T_{dch} times for all DEAP actuators, the maximum incremental actuation frequency $\Delta f_{increment\_max}$ or minimum incremental period $\Delta T_{increment\_min}$ is given by

$$\Delta f_{increment\_max} = \frac{1}{6\left(T_{ch} + T_{dch}\right)} = \frac{1}{\Delta T_{increment\_min}} \tag{8}$$

The incremental actuator speed can be changed, by proving a delay t_D between the charge and discharge cycles of actuators A_1, A_2 and A_3. The expression for the variable incremental actuation frequency $\Delta f_{increment}$ or variable incremental period $\Delta T_{increment}$ is given by

$$\Delta f_{increment} = \frac{1}{6\left(T_{ch} + T_{dch}\right) + 6t_D} = \frac{1}{\Delta T_{increment}} \tag{9}$$

When the DEAP incremental actuator is loaded during the operation, the delay between the steps S_1 and S_2 can be skipped. This can prevent the pulling of the incremental actuator by the load when actuator A_2 is charged.

V. Power Electronics: HV Drivers

. The complete circuit schematic of the DEAP incremental actuator driven by multiple bidirectional high voltage dc-dc converters is shown in Fig. 21. The topology is a peak current controlled bidirectional flyback converter. Three bidirectional flyback converters are powered by the same source. Each converter independently controls the charge and discharge operations of the three axial DEAP actuators (two grippers and an extender) in the incremental actuator.

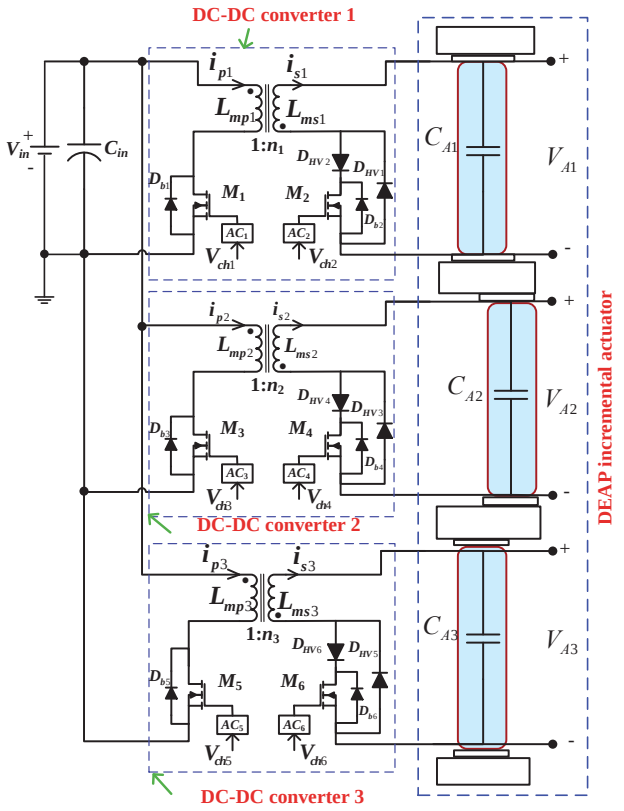

Fig. 21. Circuit schematic of the DEAP incremental actuator driven by multiple high voltage bidirectional dc-dc converters.

Three high voltage bidirectional flyback converters are experimentally tested with both film capacitor loads and the DEAP incremental actuator. The picture of the experimental prototype with film capacitor loads is shown in Fig. 22. The setup of the DEAP incremental actuator is shown in Fig. 23. The converter specifications are provided in Table II. During the experimental work 3 different implementations of the flyback transformer are investigated. The parameters of the

TABLE II
Converter Design Specifications

Parameter	Value
Input voltage	24 V
Output voltage	0-2500 V
Capacitance of each DEAP acator in the DEAP incremental actuator setup	400 nF
Capacitance of film capacitor load	200 nF
Incremental actuation frequency	~ 1-5 Hz
Primary peak current during charging/discharging process	4.2 A / 5.3 A

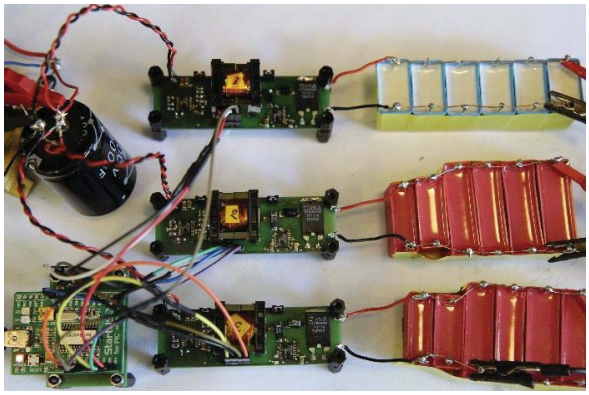

Fig. 22. Experimental setup picture with film capacitive loads.

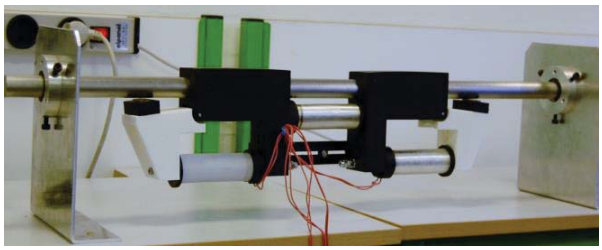

Fig. 23. Setup of the DEAP incremental actuator driven by three high voltage drivers.

flyback transformer 1 are given in Tables III. The capacitance of each film capacitor load is 200 nF. The capacitance of each axial DEAP actuator in the setup shown in Fig. 23 is 400 nF.

The experimental test results with the film capacitor loads are provided in Figs. 24-20. During the charging process the converter operates in boundary conduction mode (BCM), and during discharge process it operates in discontinuous conduction mode (DCM). In Fig. 24, the output voltages of all converters are shown when the film capacitor loads are driven with a single incremental cycle (similar to Fig. 20, with t_D=0) with a maximum driving voltage of 2.5 kV. The maximum incremental actuation frequency is $\Delta f_{increment\_max}$=4.34 Hz. Since the real DEAP actuator has a capacitance of 400 nF, the maximum incremental frequency is less than 4.34 Hz, and it is

TABLE III

FLYBACK TRANSFORMER 1 PARAMETERS

Parameter	Value
Flyback transformer core type / Material	EF20 / N87
Primary / Secondary magnetizing inductance	29.5 μH / 16 mH
Number of primary turns / secondary turns	16 / 375
Leakage inductance of transformer primary / secondary	1.11 μH / 633 μH
Secondary winding self / Interwinding capacitance	17 pF / 41 pF
DC resistance of primary / secondary winding	62 mΩ / 28.5 Ω
Number of primary / secondary layers	1 / 5
Diameter of primary / secondary winding	0.5 mm / 0.1 mm

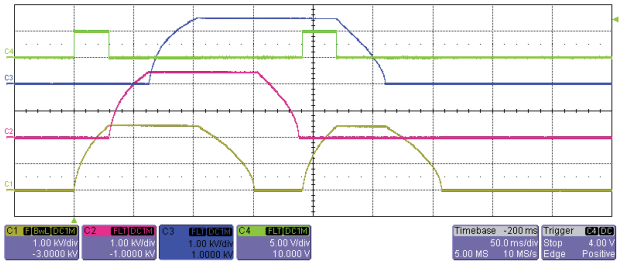

Fig. 24. Experimental results for demonstrating a single incremental actuation cycle, when the 3 HV dc-dc converters are driving the film capacitor loads; CH1: V_{A1} ; CH2: V_{A2} ; CH3: V_{A3} ; CH4: V_{ch1} ; $\Delta f_{increment\_max}$ = 4.34 Hz.

explained in the following sections.

In Fig. 25, the output voltages of all converters are shown when the film capacitor loads are driven with multiple incremental actuation cycles with a maximum driving voltage of 2.5 kV. In Fig. 25, the film capacitor loads are driven with multiple incremental actuation cycles with a maximum driving voltage of 2.5 kV, and with a delay time t_D=100 ms. The incremental actuation frequency in this case is $\Delta f_{increment}$=1.4 Hz.

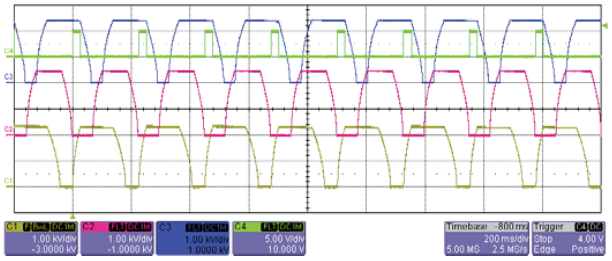

Fig. 25. Experimental results for demonstrating multiple incremental actuation cycles,when the 3 dc-dc converters are driving the film capacitor loads; CH1: V_{A1} ; CH2: V_{A2} ; CH3: V_{A3} ; CH4: V_{ch1} ; $\Delta f_{increment\_max}$ = 4.34 Hz.

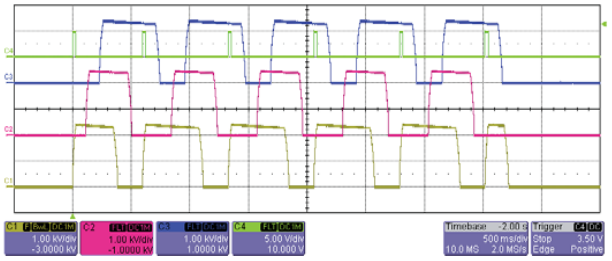

Fig. 26. Experimental results for demonstrating multiple incremental actuation cycles,when the 3 dc-dc converters are driving the film capacitor loads with a delay time t_D=100 ms; CH1: V_{A1} ; CH2: V_{A2} ; CH3: V_{A3} ; CH4: V_{ch1} ; $\Delta f_{increment}$ = 1.4 Hz.

The energy efficiency [35] is measured for all converters with film capacitors as loads. The charging and discharging energy efficiency measurement results with film capacitor loads are provided in Figs. 27 and 28, respectively. The maximum energy efficiency of the converters during charging operation (transferring the input energy to the actuator) was 87%, and during discharging operation (transferring the

actuator energy back to the source) it was 79%. As shown in Figs. 21 and 22, the energy efficiency of all converters is not identical, because 3 different transformer designs are utilized. For any dc-dc converter, the discharge energy efficiency is less than the charge energy efficiency, due to very high conduction losses, switching loss due to leakage inductance and capacitive switching losses of the HV MOSFET.

Practical experience reveals that careful design of the flyback transformer with low leakage inductance and low self-capacitance is required for achieving high energy efficiency in high voltage bidirectional operation. The HV MOSFET used for this research is IXTV03N400S (4 kV, 300 mA, 290 Ω). The available high voltage MOSFETs for this application, in the current market is IXTA02N450HV (4.5 kV, 200 mA, 750 Ω). Improper flyback transformer designs may lead to failure of the HV MOSFET during the discharging operation.

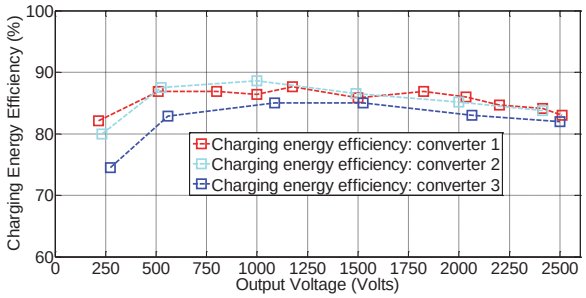

Fig. 27. Charging energy efficiency measurement results of three high voltage converters.

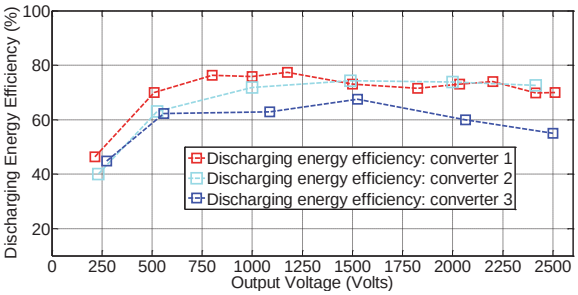

Fig. 28. Discharging energy efficiency measurement results of three high voltage converters.

VI. System Integration

A. *Incremental motion with different speeds*

The integrated system shown in Fig. 23 was tested for its variable speed and repeatability. In Fig. 23, the height and outer diameter of each DEAP actuator are 110 mm and 33 mm, respectively. 100 increments are generated using the digital controller and the total displacement and travel time is recorded. The applied voltage level is fixed to a maximum 1.8 kV to avoid any potential damage to the transducers. Table IV shows the acquired data of the experiments. It can be seen that the system has repeatability within 5% (of stroke) for different speed levels. Moreover, the speed of the system could have been doubled if the maximum operating voltage (2.4 kV) is applied to all actuators, i.e. a maximum speed of 3 mm/s could be achieved.

B. *Bidirectional motion:*

The above test is repeated with a maximum voltage of 1700 V for bidirectional motion at three different speed settings (delay times t_D) in the controller. Table V shows the results which indicate a larger total displacement in the forward motion compared to the reverse motion.

C. *Discussion*

The DEAP incremental actuator system indicated a non-repeatable motion when operated bidirectional resulting in a drift from original position. This drift increased with the number of bidirectional iterations resulting in an even larger drift from original position. Such drift might be primarily caused by non-identical grippers differing in their gripping force. As the extending transducer is activated, it excites both grippers with the same force. The activated gripper should have enough gripping force to not slip backward due to transient forces generated by the extender. If the two grippers have different gripping forces, the one with smaller force will exhibit larger backward slipping resulting cumulatively in a drift of the whole system from the original position.

TABLE IV
Experimental Data of DEAP Incremental Actuator Moving with Different Speeds to Achieve 100 Increments/Steps

Total stroke* (mm)	Actuator total travel time (s)	Delay time t_D (ms)	Average Speed (mm/s)	Increment size/ stroke per step (mm)	Incremental actuation frequency $\Delta f_{increment}$ (Hz)
39	50	50	0.78	0.39	1.53
39	45	40	0.86	0.39	1.68
39	40	30	0.97	0.39	1.87
38	35	20	1.07	0.38	2.11
40	30	10	1.33	0.40	2.41
40	28	5	1.43	0.40	2.60
39	25	2	1.56	0.39	2.73
39	26	1	1.50	0.39	2.78

*All 3 DEAP actuators are driven with a maximum voltage of 1800 V.
Charing time T_{ch}=23 ms, discharging time T_{dch}=36 ms.

TABLE V
Experimental Data from Bidirectional DEAP Incremental Actuator Tests for 100 Increments

Direction of movement	Total stroke* (mm)	Incremental actuator total travel time (s)	Delay time t_D (ms)	Average Speed (mm/s)	Incremental actuation frequency $\Delta f_{increment}$ (Hz)
Forward	40	71	100	0.56	1.08
Forward	44	35	10	1.26	2.60
Forward	43.7	32	1	1.36	3.03
Reverse	37	71	100	0.52	1.08
Reverse	41	41	10	1.00	2.60
Reverse	35	37	1	0.94	3.03

*All 3 DEAP actuators are driven with a maximum voltage of 1700 V.
Charing time T_{ch}=21 ms, discharging time T_{dch}=33 ms.
Forward: positive x-axis direction.
Reverse: negative x-axis direction.

D. Future work

Subsequent iteration of the DEAP incremental actuator will consider the improvement of both the mechanical and electronics concepts. Specific attention will be given to the design of the grippers to, i) achieve a more identical performance, and ii) have enough grip force to overcome the inertial effects and as such increased speed and repeatability. The focus will be given to develop a more compact and autonomous system where the electronics are carried by the actuator. The weight and form factor of DEAP are to be exploited and demonstrated. This is potentially achieved by reducing the actuator size, redesigning the auxiliary mechanics, and integrating the electronics on a single PCB print. Moreover, the form factor can be demonstrated by developing a concept which can travel on curved and inclined paths which is challenging for other technologies to achieve.

VII. Conclusions

A new DEAP incremental actuator concept has been designed, built and tested. It is demonstrated that the DEAP is feasible for providing incremental motion with variable speed and bidirectional motion. Control and high voltage electronics also demonstrated good performance in providing the appropriate stimuli to the transducers with reasonable efficiency and compactness. The conceptual design considerations and control of the DEAP incremental actuator are discussed in detail. Experimental test results with the three high voltage bidirectional dc-dc converter are presented. The maximum charging energy efficiency of converter 2, for a non-optimized flyback transformer was 87 %.

The proposed incremental actuator moves with a maximum velocity of 1.5 mm/s, at 2.78 Hz incremental actuation frequency, when all actuators are driven with 1.8 kV. It is possible to achieve a speed of 3 mm/s, when the actuators are driven by 2.4 kV. The final conclusion is that the proposed new DEAP incremental actuator will have promising and demanding applications in the future.

Acknowledgement

The authors would like to thank the industrial partner Danfoss PolyPower A/S for providing the actuators and system integration set up. The authors would also like to thank Lina Huang and Jonas T. Smith for their help in the system integration.

References

[1] OK Coil, Online available: http://www.okcoil.com/engineer-area/technicle-articles.html [accessed 14 Nov. 2014].

[2] JenaTec, Online available: http://www.jena-tec.co.uk/linear-actuators.php [accessed 14 Nov. 2014].

[3] PI, Online available: http://www.linear-actuator.net/Vacuum_Linear_Actuators.php [accessed 14 Nov. 2014].

[4] AGI American Grippers, Online available: http://localautomation.com/featured/agi-pneumatic-linear-actuator-agi-american-grippers-inc.html [accessed 14 Nov. 2014].

[5] Stemulate, Online available: http://www.stemulate.org/2012/07/02/solid-learning-robot-linear-actuators/ [accessed 14 Nov. 2014].

[6] Y. Bar-Cohen, "Electroactive Polymer [EAP] Actuators as Artificial Muscles: Reality, Potential, and Challenges," 2nd ed. Washington, DC: SPIE, 2004.

[7] R. E. Pelrine, R. D. Kornbluh, Q. Pei, J. P. Joseph, "High-speed electrically actuated elastomers with strain greater than 100%," *Science*, vol. 287, pp. 836–839, 2000.

[8] F. Carpi, D. DE Rossi, R. Kornbluh, R. Pelrine, P. Sommer-Larsen, Eds, "Dielectric Elastomer As Electromechanical Transducers," Amsterdam, The Netherlands: Elsevier, 2008.

[9] Danfoss PolyPower, Denmark, Online available: http://www.polypower.com/ [accessed 20 Oct. 2014].

[10] LEAP Technology, Denmark, Online available: http://leaptechnology.com/ [accessed 20 Oct. 2014].

[11] M. Tryson, H. E. Kiil, M. Benslimane, "Powerful tubular core free dielectric electro active polymer (DEAP) push actuator," in *Proc. SPIE*, vol. 7287, 2009.

[12] R. Sarban, B. Lassen, M. Willatzen, "Dynamic Electromechanical Modeling of Dielectric Elastomer Actuators With Metallic Electrodes," *IEEE/ASME Trans. Mechatronics,* vol. 17, no. 5, pp. 960-967, Oct. 2012.

[13] L. Huang, P. Thummala, Z. Zhang, M. A. E. Andersen, "Battery powered high output voltage bidirectional flyback converter for cylindrical DEAP actuator," in *Proc. IEEE IPMHVC*, pp. 454-457, 3-7 June 2012.

[14] R. D. Kornbluh, R. Pelrine, Q. Pei, R. Heydt, S. Stanford, S. Oh, J. Eckerle, "Electroelastomers: applications of dielectric elastomer transducers for actuation, generation, and smart structures," in *Proc. SPIE*, vol. 4698, pp. 254-270, 2002.

[15] Q. Pei, R. Pelrine, S. Stanford, R. D. Kornbluh, M. S. Rosenthal, K. Meijer, R. J. Full, "Multifunctional electroelastomer rolls and their application for biomimetic walking robots," in *Proc. SPIE*, vol. 4698, 2002.

[16] I. A. Anderson, T. A. Gisby, T. G. McKay, B. M. O'Brien, E. P. Calius, "Multi-functional dielectric elastomer artificial muscles for soft and smart machines," *Journal of Applied Physics*, 112, 041101, 2012.

[17] K. Jung, J. C. Koo, J. -do Nam, Y. K. Lee, H. R. Choi, "Artificial annelid robot driven by soft actuators," *Journal of Bioinspiration and Biomimetics*, vol. 2, pp. S42-S49, 2007.

[18] I. A. Anderson, T. C. H. Tse, T. Inamura, B. M. O'Brien, T. McKay, T. Gisby, "A soft and dexterous motor," *Journal of Applied Physics*, 98, 123704, 2011.

[19] R. Wache, D. N. McCarthy, S. Risse, G. Kofod, "Rotary Motion Achieved by New Torsional Dielectric Elastomer Actuators Design," *IEEE/ASME Trans. Mechatronics*, vol. 99, pp. 1-3, Feb. 2014.

[20] R. J. E. Merry, J. L. Holierhoek, M. J. G. van de Molengraft, M. Steinbuch, "Gain Scheduling Control of a Walking Piezo Actuator," *IEEE/ASME Trans. Mechatronics*, vol. 19, no. 3, pp. 954-962, June 2014.

[21] D. M. Neal, H. H. Asada, "Bipolar Piezoelectric Buckling Actuators," *IEEE/ASME Trans. Mechatronics*, vol. 19, no. 1, pp. 9-19, Feb. 2014.

[22] Y. Jianyong, J. Zongxia, M. Dawei, Y. Liang, "High-Accuracy Tracking Control of Hydraulic Rotary Actuators With Modeling Uncertainties," *IEEE/ASME Trans. Mechatronics*, vol. 19, no. 2, pp. 633-641, April 2014.

[23] P. Thummala, Z. Zhang, M. A. E. Andersen, S. Rahimullah, "Dielectric electro active polymer incremental actuator driven by multiple high-voltage bi-directional DC-DC converters," in *Proc. IEEE ECCE USA,* pp. 3837-3844, 15-19 Sept. 2013.

[24] M. Karpelson, G. Y. Wei, R. J. Wood, "Driving high voltage piezoelectric actuators in microrobotic applications," *Sensors and Actuators A*, vol. 176, pp. 78– 89, 2012.

[25] L. Eitzen, C. Graf, J. Maas, "Cascaded bidirectional flyback converter driving DEAP transducers," in *Proc. IEEE IECON*, pp. 1226-1231, 7-10 Nov. 2011.

[26] L. Eitzen, C. Graf, J. Maas, "Bidirectional power electronics for driving dielectric elastomer transducers," in *Proc. SPIE*, vol. 8340, p. 834018 1-12, 2012.

[27] R. W. Erickson, D. Maksimovic, "Fundamentals of Power Electronics," 2nd ed. New York: Springer, 2001.

[28] N. O. Sokal, R. Redl, "Control algorithms and circuit designs for optimal flyback-charging of an energy storage capacitor (e.g., for flash lamp or defibrillator)," *IEEE Trans. Power Electronics*, vol. 12, no. 5, pp. 885-894, Sep. 1997.

[29] J. Elmes, C. Jourdan, O. Abdel-Rahman, I. Batarseh, "High-Voltage, High-Power-Density DC-DC Converter for Capacitor Charging Applications," in *Proc. IEEE APEC*, pp. 433-439, 2009.

[30] S. K. Chung, H. B. Shin, "High-voltage power supply for semi-active suspension system with ER-fluid damper," *IEEE Trans. Vehicular Technology*, vol. 53, no. 1, pp. 206- 214, Jan. 2004.

[31] T. Bhattacharya, V. S. Giri, K. Mathew, L. Umanand, "Multiphase Bidirectional Flyback Converter Topology for Hybrid Electric Vehicles," *IEEE Trans. Industrial Electronics*, vol. 56, no. 1, pp. 78-84, Jan. 2009.

[32] G. Chen, Y.-S. Lee, S.Y.R. Hui, D. Xu, Y. Wang, "Actively clamped bidirectional flyback converter," *IEEE Trans. Industrial Electronics*, vol. 47, no. 4, pp. 770-779, Aug. 2000.

[33] F. Zhang, Y. Yan, "Novel Forward–Flyback Hybrid Bidirectional DC-DC Converter," *IEEE Trans. Industrial Electronics,* vol. 56, no. 5, pp. 1578-1584, May 2009.

[34] T. Andersen, M. S. Rødgaard, O. C. Thomsen, M. A. E. Andersen, "Low voltage driven dielectric electro active polymer actuator with integrated piezoelectric transformer based driver," in *Proc. SPIE EAPAD*, vol. 7976, p. 79762N, 2011.

[35] P. Thummala, Z. Zhang, M. A. E. Andersen, "High Voltage Bi-directional Flyback Converter for Capacitive Actuator," in *Proc. IEEE EPE,* pp. 3-6 Sept. 2013.

[36] P. Thummala, H. Schneider, Z. Zhang, A. Knott, M. A. E. Andersen, "Optimization of a bi-directional flyback converter for a high voltage capacitor charging application," in *Proc. IEEE APEC*, pp. 2556-2563, 16-20 March 2014.

[37] H. Schneider, P. Thummala, L. Huang, Z. Ouyang, A. Knott, Z. Zhang, M. A. E. Andersen, "Investigation of transformer winding architectures for high voltage capacitor charging applications," in *Proc. IEEE APEC*, pp. 334-341, 16-20 March 2014.

[38] J. P. L. Bigue, J. S. Plante, "Experimental Study of Dielectric Elastomer Actuator Energy Conversion Efficiency," *IEEE/ASME Trans. Mechatronics*, vol. 18, no. 1, pp. 169-177, Feb. 2013.

[39] C. M. Druitt, G. Alici, "Intelligent Control of Electroactive Polymer Actuators Based on Fuzzy and Neurofuzzy Methodologies," *IEEE/ASME Trans. Mechatronics*, vol. 19, no. 6, pp. 1951-1962, Dec. 2014.

[40] P. Thummala, D. Maksimovic, Z. Zhang, M. A. E. Andersen, S. Rahimullah, "Digital control of a high-voltage (2.5 kV) bidirectional DC-DC converter for driving a dielectric electro active polymer (DEAP) based capacitive actuator," in *Proc. IEEE ECCE USA*, 14-18 Sept. 2014.

[41] Linear Technology, "LT3751 High Voltage Capacitor Charger with Regulation," Linear Technology Corporation, USA. http://cds.linear.com/docs/en/datasheet/3751fc.pdf [accessed 20 Oct. 2014].

[42] IXYS, Online available: http://ixapps.ixys.com/DataSheet/DS100214A-(IXTH_V03N400_S).pdf [accessed 20 Oct. 2014].

[43] IXYS, Online available: http://ixapps.ixys.com/DataSheet/DS100498(IXTA-T02N450HV).pdf [accessed 20 Oct. 2014].

Appendix N

Bidirectional Flyback Converter with Multiple Series Connected Outputs for High Voltage Capacitive Charge and Discharge Applications

---

IEEE Applied Power Electronics Conference and Exposition 2015 (APEC)

Bidirectional Flyback Converter with Multiple Series Connected Outputs for High Voltage Capacitive Charge and Discharge Applications

Prasanth Thummala, Henrik Schneider, Zhe Zhang and Michael A. E. Andersen
Electronics Group, Department of Electrical Engineering
Technical University of Denmark
Kongens Lyngby, DK-2800 Denmark
Web: http://www.ele.elektro.dtu.dk/
Email: pthu@elektro.dtu.dk, hensc@elektro.dtu.dk

***Abstract*—This paper evaluates two different implementations of a bidirectional flyback converter for driving a capacitive electro active actuator, which must be charged and discharged from 0 V to 2.5 kV DC and vice versa, supplied from a 24 V battery. In one implementation, a high voltage MOSFET (4 kV) in series with a high voltage blocking diode is added, in parallel with a high voltage freewheeling diode of a conventional flyback topology, to enable bidirectional operation. Experimental result from a digitally controlled bidirectional flyback converter shows that the discharge energy efficiency is limited by the parasitics of the high voltage active components, which also prevent full utilization of valley switching during discharge process. A second implementation is therefore proposed, where the secondary of flyback transformer winding is split into multiple windings which are connected in series by lower voltage rating MOSFETs driven by a gate drive transformer. Simulation results to compare the operation of conventional and proposed converters are provided. The advantages of proposed implementation are improved energy efficiency and lower cost. Experimental results with two series connected secondary windings are provided to validate the proposed implementation.**

NOMENCLATURE

C_{in}/C_{load}	Input capacitance / Load capacitance.
C_{out1}	Balancing capacitor across a series combination of one of the splitted secondary winding and a secondary MOSFET.
C_{ossp}	Output capacitance of the low voltage MOSFET M_p.
C_{osss}	Output capacitance of the high voltage MOSFET M_s.
C_{osss1}	Output capacitance of one of the several series connected MOSFETs (M_{s1}) on the secondary high voltage side.
C_j	Junction capacitance of the high voltage diodes D_2 or D_b.
C_s	Self capacitance of secondary high voltage winding of the flyback transformer.
C_{s1}	Self capacitance of one of the secondary high voltage splitted windings of the flyback transformer.
D_2	High voltage (5 kV) freewheeling diode which conducts while charging the capacitive load.
D_b	High voltage (5 kV) blocking diode which conducts while discharging the capacitive load.
D_{bp}/D_{bs}	Body diode of the MOSFET M_p/M_s.
D_{bs1}	Body diode of one of the several series connected MOSFETs (M_{s1}) on the secondary high voltage side.
$i_{in}/i_p/i_s$	Input / Primary / Secondary current.
i_{load}	Current through the load.
L_{mp}/L_{ms}	Primary / Secondary magnetizing inductance of a non-splitted flyback transformer.
L_{ms1}	Secondary magnetizing inductance of one of the splitted winding of the flyback transformer.
L_{lkp}/L_{lks}	Leakage inductance referred to primary / secondary of a non-splitted flyback transformer.
L_{lks1}	Leakage inductance referred to secondary of one of the splitted winding of the flyback transformer.
M_p/M_s	Low voltage / High voltage (4 kV) MOSFET.
M_{s1}	One of the several series connected MOSFETs on the secondary high voltage side.
n	Turns ratio from secondary to primary of the non-splitted flyback transformer.
n_1	Turns ratio from one of the splitted secondary to primary of the splitted flyback transformer.
N_p/N_s	Number of primary / secondary turns of the non-splitted flyback transformer.
N_{s1}	Number of secondary turns on one of the splitted secondary winding of the flyback transformer.
R_p/R_s	DC resistance of low voltage / high voltage winding of the transformer.
R_{s1}	DC resistance of one of the splitted secondary high voltage winding of the flyback transformer.
V_{Db}/V_{D2}	Voltage across the high voltage (5 kV) blocking / freewheeling diode.
V_{Mp}/V_{Ms}	Voltage across the low voltage / high voltage (4 kV) MOSFET.
V_{Ms1}	Voltage across one of the several series connected MOSFETs (M_{s1}) on the secondary high voltage side.
V_{in}/V_{out}	Input voltage / Output or load voltage.

I. Introduction

Dielectric electro active polymer (DEAP) is an emerging smart material that has experienced substantial improvement and has gained increasing attention over the last decade from the researchers [1]–[3]. The DEAP material is a very thin (40 μm) incompressible silicone elastomer film with a compliant electrode layer on both sides [5], [7]. DEAP can be considered as a pure capacitive load from an electrical perspective [6]. The basic behaviour of the DEAP actuator is the reduction in the polymer thickness and the increment in its area, due to an applied electric field (40-60 V/μm) [7], [8]. The axial DEAP actuator as shown in Fig. 1 is ideally equivalent to a capacitive load. When a DEAP actuator is driven with high voltage (2-2.5 kV), it converts a portion of the electrical energy into mechanical displacement, which is of the order of mm (1-1.5 mm) [4], [5]. Three of such axial DEAP actuators are used to create a DEAP incremental actuator [9] as shown in Fig. 2. DEAP, when used as linear incremental actuators, has the potential to be an effective replacement for many conventional (e.g., piezo, pneumatic and hydraulic) linear actuators due to its unique properties such as large strain, light weight, and high flexibility.

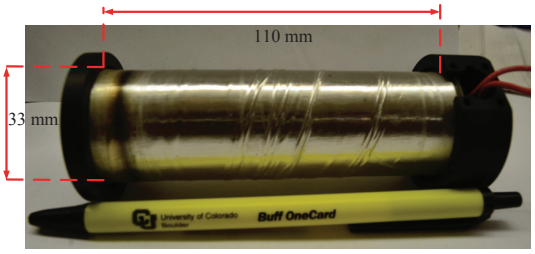

Fig. 1. A linear DEAP actuator manufactured by Danfoss PolyPower A/S.

The DEAP actuator applications [10], [11] require high voltage (HV) bidirectional power electronic converters, to charge and discharge the actuator, and to transfer part of the energy stored in it to the source. Switch-mode power supplies for charging the capacitive loads have been implemented in [12]–[15]. The flyback converter is suitable for low power ($<$ 150 W) and high voltage (2.5 kV) applications, due to its simple structure and low component count [16]. In [17], [30], [32]–[36], [44], [45] bidirectional flyback converters with various power stages and control techniques, for charging and discharging DEAP actuators have been proposed and implemented. The proposed converter with multiple series connected secondary windings is different from aforementioned converters, since it is aimed for bidirectional operation, by replacing the diode with a MOSFET on the secondary HV side. This paper is organized as follows: Section II describes the conventional and proposed HV drivers. Section III provides the simulation results. Section IV discusses the gate driver for the secondary HV side. Section V provides the experimental results and efficiency measurements. Section VI concludes the paper followed by the futur work in Section VII.

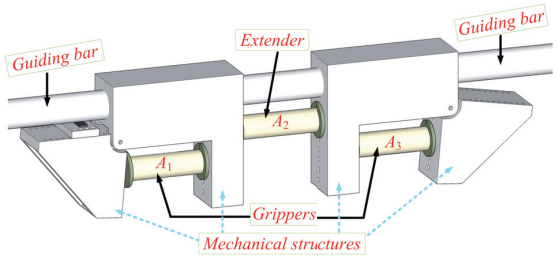

Fig. 2. A DEAP incremental actuator.

II. High Voltage Drivers: Conventional and Proposed

High efficient flyback based converters have been widely investigated and implemented by several researchers [18]–[24]. Several bidirectional flyback converter topolofies have been proposed and implemented in [25]–[29]. The conventional high voltage bidirectional flyback converter [30], [31], for driving (charging and discharging) a DEAP actuator with a certain actuation frequency, is shown in Fig. 3.

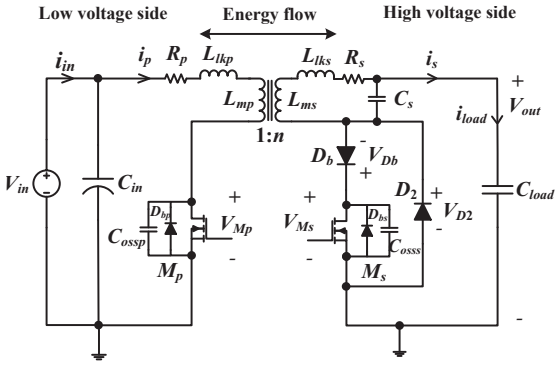

Fig. 3. Conventional HV bidirectional flyback converter.

An efficiency optimization technique has been proposed in [32], [33] to improve the energy efficiency of the converter. Investigation of different transformer winding architectures (TWAs) for the same topology has been proposed in [34]. A new digital control technique to achieve the valley switching during both charge and discharge processes in a bidirectional flyback converter is proposed in [35], for better energy efficiency and improved charge and discharge speed. Primary parallel, secondary series flyback converter with multiple transformers is proposed in [36], to reduce the equivalent self-capacitance on the secondary HV side. The HV converter used in [9], [30], [32], [35], requires a HV (4 or 4.5 kV) MOSFET M_s and two HV (5 kV) diodes D_2 and D_b as shown in Fig. 3.

The 4 kV, 300 mA high voltage IXYS MOSFET [37] has the following features:

- high on-resistance of 290 Ω.
- high output capacitance of 19 pF.
- high reverse recovery time of 2.8 μs.

The 5 kV, 150 mA VMI high voltage diode [38] has the following features:

- on-state voltage drop of 7 V.
- junction capacitance of 3 pF.
- reverse recovery time of 70 ns.

Therefore, using a HV MOSFET M_s and two HV diodes D_2 and D_b on the secondary side of the HV bidirectional DC-DC converter, make it very expensive and inefficient.

To reduce the voltage rating of the high voltage MOSFETs, series input and parallel output DC-DC converters have been proposed and implemented in [39]–[43]. The proposed HV bidirectional flyback converter is shown in Fig. 4. Using this topology, it is possible to series connect several lower voltage ($<$ 4 kV) rated MOSFETs each having a better body diode (with less reverse recovery time).

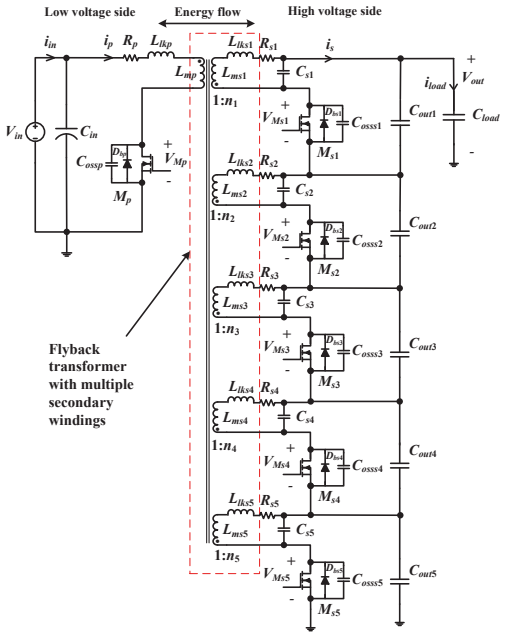

Fig. 4. Proposed HV bidirectional flyback converter with 5 series connected secondary transformer windings and MOSFETs on the secondary HV side.

The advantages of the proposed topology are:

- reduction in the voltage rating and price of the HV MOSFET.
- elimination of blocking and freewheeling HV diodes.
- possibility to achieve perfect valley switching of HV MOSFET, unlike the semi-valley switching [35] (due to series connection of HV diode D_b and HV MOSFET M_s during the discharge process).
- improved overall (charge and/or discharge) energy efficiency.

However, the difficulties associated with the proposed converter are:

- the need of high side gate drivers for driving some of the secondary MOSFETs.
- synchronous switching of secondary MOSFETs.
- voltage sharing among the secondary windings and the secondary MOSFETs.

III. Simulation Results

Simulations have been performed in pSpice software to validate the proposed method, and the results are provided in Figs. 5 and 6.

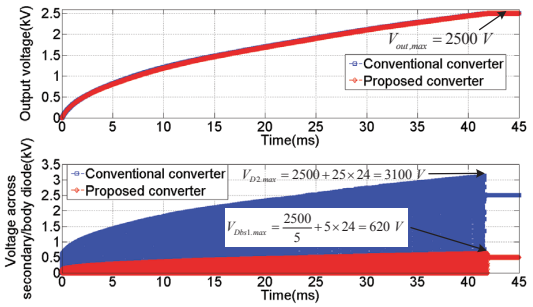

Fig. 5. Simulation results during charge process for $p = 5$ stages.

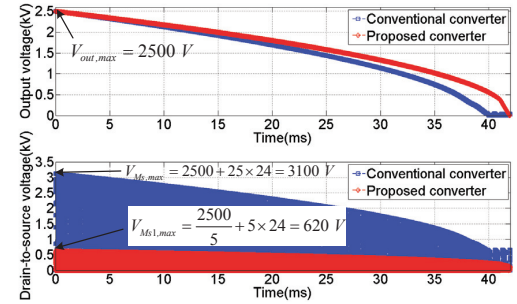

Fig. 6. Simulation results during discharge process for $p = 5$ stages.

The simulation parameters used for the conventional flyback converter (Fig. 3) are: V_{in}=24 V, C_{load}=400 nF, L_{mp}=48 μH, L_{ms}=30 mH, R_p=60 mΩ, n=25, R_s=13 Ω. Peak current control has been implemented during both charge (with current limit 5 A) and discharge (with current limit 200 mA) processes with a fixed time period of 22 μs (switching frequency f_{sw}=45.54 kHz). The simulation parameters used for the proposed flyback converter (Fig. 4) are the same as above, except the turns ratio (n_1=5) and the secondary magnetizing inductance (L_{ms1}=1.2 mH). In the simulations, the leakage inductance and self-capacitance are ignored and ideal switches and diodes are being used. Figure 5, provides the comparison between the output voltages, and the voltage across the secondary HV free wheeling diode V_{D2}, and body diode V_{Ms1}, for the conventional and proposed converters,

during charge process. Figure 6, provides the comparison of the output voltages and the drain-to-source voltage across the secondary MOSFET, for the conventional and proposed converters, during discharge process.

When p series connected transformer and MOSFET stages are used in the secondary HV side of the proposed converter:

- the turns ratio n_1 is reduced by p.
- the magnetizing inductance L_{ms1} is reduced by p^2.
- the drian-to-source across the body diode of the secondary MOSFETs during the charge process is reduced by p.
- the drian-to-source across the secondary MOSFETs during the discharge process is reduced by p.

Hence, to charge and discharge the capacitive load to and from 2.5 kV output voltage, the 4 kV or 4.5 kV MOSFET on the secondary HV side, could be easily replaced by a 800 V MOSFET, when $p = 5$ stages are used in the secondary side.

Table I provides the comparison between the conventional and proposed converters in terms of losses due to the HV active components (at the maximum output voltage during both charge and discharge modes). Table II provides the comparison between the conventional and proposed converters in terms cost and the volume occupied, when the real MOSFETs and HV diodes are used in the converter.

TABLE I. LOSS COMPARISON BETWEEN THE CONVENTIONAL AND PROPOSED CONVERTERS

Converter Type	**Loss during charge process (W)**	**Loss during discharge process (W)**	**Total loss (W)**
Conventional	$L_1 = 0.168$	$L_3 = 0.133$ $L_4 = 4.9$	5.201
Proposed	$L_2 = 0.192$	$L_5 = 0.61$	0.8

TABLE II. COST AND VOLUME COMPARISON BETWEEN THE CONVENTIONAL AND PROPOSED CONVERTERS

Converter Type	**Cost ($)** *low quantity prices	**Volume occupied (mm^3)**	**Total cost ($)**	**Total volume (mm^3)**
Conventional	20 (*10 for each HV diode) *30 (HV MOSFET)	128 (64 each diode) 1034 (MOSFET)	50	1162
Proposed	5 (1 for each MOSFET), 3 (for gate driver)	440 (88 each MOSFET), 560 (gate driver)	8	1000

In Table I the loss expressions are given by:
$L_1 = i_{avgC} V_{onD2}$ (for HV diode D_2);
$L_2 = p i_{avgC} V_{onDbs}$ (for $p = 5$ HV body diodes);
$L_3 = i_{avgD} V_{onDb}$ (for HV diode D_b);
$L_4 = i^2_{rmsD} R_{dsons} + 0.5 C_{osss} V^2_{Ms,max} f_{sw} + V_{gs} f_{sw} Q_{gs}$ (for 4 kV MOSFET M_s);
$L_5 = p(i^2_{rmsD} R_{dsons1} + 0.5 C_{osss1} V^2_{Ms1,max} f_{sw} + V_{gs} f_{sw} Q_{gs1})$ (for $p = 5$ HV MOSFETs M_{si}, $i = 1, 2...5$);

The parameters used are: i_{avgC}= 24 mA, i_{avgD} =19 mA, i_{rmsD}=52 mA, V_{onD2}=V_{onDb}=7 V, V_{onDbs}=1.6 V, R_{dsons} = 290 Ω (4 kV), $R_{dsons1} = 13$ Ω, C_{osss}=19 pF, $C_{osss1} = 9.5$ pF, V_{Ms}=3100 V, V_{Ms1}=620 V, V_{gs}=12 V, Q_{gs}=16.3 nC, Q_{gs1}=7.7 nC;

In the above i_{avgC}, i_{avgD}, i_{rmsD} are the average current during charge and discharge modes, and RMS current during discharge mode, respectively. Those values are extracted from the pSpice simulations. Also V_{onD2}, V_{onDb}, and V_{onDbs} are the on-state diode drops of diodes D_2, D_b and D_{bs1}, respectively.

IV. DRIVING THE SECONDARY SERIES CONNECTED MOSFETS USING A GATE DRIVE TRANSFORMER (GDT)

In the proposed topology as shown in Fig. 4, the secondary HV side MOSFETs, need to be driven with $p-1$ high side gate drivers, for p series connected stages. It is possible to drive all secondary MOSFETs using a gate drive transformer (GDT). Figure 7a) provides the full schematic of the gate driver for 2 series connected stages ($p = 2$). The microcontroller generates enable signals for the dual low-side gate driver, whose outputs are fed to the GDT. The GDT as shown in Fig. 7a) has a single primary and two secondary windings with 1:1 turns ratio.

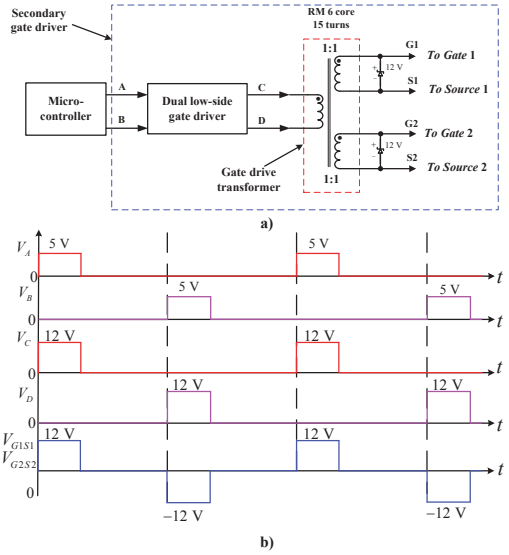

Fig. 7. a) Schematic of the gate driver for driving two secondary series connected MOSFETs; b) Driving signals at different nodes in the gate driver schematic.

The GDT is made using a RM 6 core, each winding has 15 turns with 0.2 mm diameter. The two isolated outputs of the GDT are used to drive the 2 secondary series connected MOSFETs. To protect the secondary MOSFETs from the voltage spikes, a 12 V Zener diode is placed across the gate to source terminals of the two MOSFETs. Driving signals at different nodes in the secondary gate driver are shown in Fig. 7b). The two primary winding terminals of gate drive transformer (nodes C and D) are driven with two out-of-phase signals. Positive signal at the primary dot terminal of GDT (node C), produces positive gate-to-source driving signals, and positive signal at the primary non-dot terminal of GDT (node D), produces negative gate-to-source driving signals, for the two MOSFETs, respectively. In Fig. 7b), G_1, G_2, S_1 and S_2 represents the gate nodes and source nodes of the two MOSFETs, respectively. The idea of driving the two series

connected MOSFETs, using a GDT described above, can be used to drive more than 2 series connected MOSFET stages ($p > 2$). However, the type of core used for the GDT can be changed depending on the number of stages.

V. Experimental Results

The experimental prototype of the conventional HV bidirectional flyback converter is shown in Fig. 8 [35]. The experimental results showing the bidirectional operation at 2.5 kV output voltage are provided in Fig. 9. The primary MOSFET M_p is 250 V, 16 A [FQD16N25CTM], the secondary side MOSFETs are 4 kV, 300 mA, 290 Ω [IXTV03N400S] and 4.5 kV, 200 mA, 750 Ω [IXTA02N450HV], and the HV diodes D_2 and D_b are 5 kV, 150 mA [SXF6525]. However, for evaluating the conventional and proposed converters, only 4 kV MOSFET is considered. The secondary MOSFET used in the proposed converter is 800 V, 1 A, 13 Ω [STN1NK80Z, [46]].

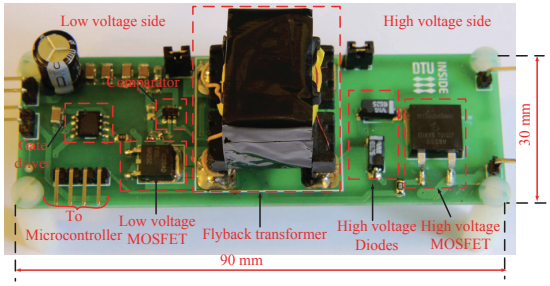

Fig. 8. Experimental prototype of the digitally controlled conventional HV bidirectional flyback converter with 4.5 kV MOSFET on the HV side [35].

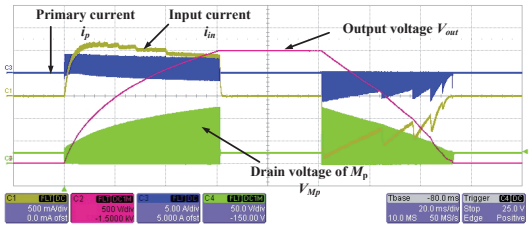

Fig. 9. Experimental results showing a single charge (0 V to 2.5 kV) and discharge cycle (2.5 kV to 0 V) [35]; CH1: 500 mA/div, CH2: 500 V/div, CH3: 5 A/div, CH4: 50 V/div, Time scale: 20 ms/div.

A digital control technique was recently proposed in [35] to achieve valley switching control during both charge and discharge processes. In Fig. 9 a full charge/discharge cycle is shown. Figure 10 confirms the valley switching operation in charge mode. However, during discharge mode the valley voltage of the drain of HV MOSFET M_s is limited by the series connected HV diode D_b as seen in Fig. 11. The energy efficiency measurements during both charge and discharge modes as a function of output voltage are provided in Fig. 12. The proposed converter is expected to achieve ideal valley switching during the discharge process leading to improved energy efficiency.

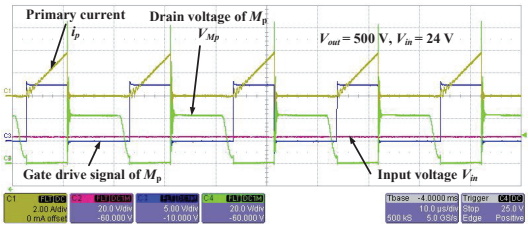

Fig. 10. Experimental waveforms when the converter is operated with valley switching during charge process; CH1: 2 A/div, CH2: 20 V/div, CH3: 5 V/div, CH4: 20 V/div, Time scale: 5 μs/div.

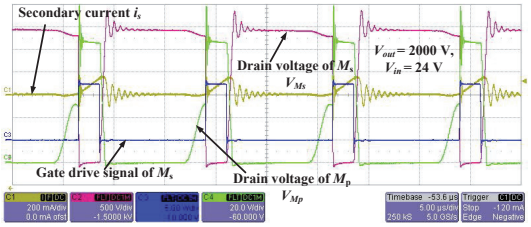

Fig. 11. Experimental waveforms when the converter is operated with valley switching during discharge process; CH1: 200 mA/div, CH2: 500 V/div, CH3: 5 V/div, CH4: 20 V/div, Time scale: 5 μs/div.

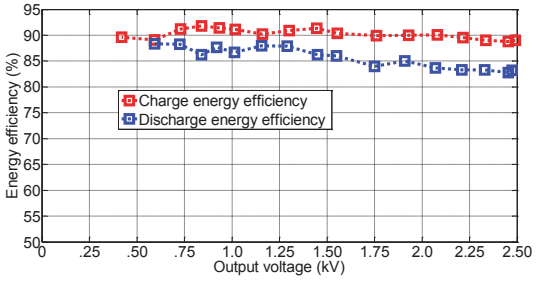

Fig. 12. Energy efficiency measurements with a 4 kV MOSFET on HV side.

The converter specifications are provided in Table III. The details of flyback transformer are shown in Table IV. To verify the concept of proposed converter, only two series connected secondary stages are considered. The 300 secondary turns are split into two for each series connected secondary winding ($N_{s1} = 150$). The parameters of the flyback transformer are provided in Table V. It is a non-optimized (non-interleaved, non-sectioned) transformer.

The flyback transformer used for the experiment is of non-interleaved and non-sectioned, and it is not propoerly optimized. However, for this application, transformer with multiple sections would be better choice to reduce the self-capacitance. The experimental results from the proposed converter with 2 series connected secondary stages ($p = 2$) are shown in Figs. 13, 14 and 15, respectively.

Figure 13 provides a single charge and discharge cycle using the proposed topology, when the capacitor load is charged and discharged from 0 V to 200 V, and vice versa. To verify the

proposed concept, during both charge and discharge processes, the converter is driven with fixed switching frequency. During the charge process the switching time period is 59 μs, and during the discharge process, the switching time period is 100 μs. In Figs. 14 and 15, a comparison of drain-to-source voltage across the two secondary MOSFETs during a charge and discharge swithcing cycle are provided.

TABLE III. CONVERTER SPECIFICATIONS

Parameter	Value
Input voltage	24 V
Capacitance of load	400 nF
On-time of primary MOSFET during the charge process	9 μs

TABLE IV. DETAILS OF THE SPLITTED FLYBACK TRANSFORMER WITH A TURNS RATIO OF 25

Parameter	Value
Number of primary / secondary turns	12 / 300
Diameter of primary / secondary winding	0.5 mm / 0.12 mm
Number of layers of primary / secondary winding	1 / 4
Type of core / material	EF25 / N87

TABLE V. PARAMETERS OF THE SPLITTED FLYBACK TRANSFORMER

Parameter	Value
Primary / Each splitted secondary magnetizing inductance Secondary non-splitted magnetizing inductance	42 μH / 6.3 mH 25 mH
Leakage inductance referred to primary / splitted secondary Leakage inductance referred to non-splitted secondary	1.1 μH / 53 μH 721 μH
Primary / Secondary splitted winding DC resistance Secondary non-splitted winding DC resistance	64 mΩ / 6.3 Ω 12.4 Ω
Self-capacitance of each splitted secondary winding Self-capacitance of non-splitted secondary winding	78.2 pF 37 pF

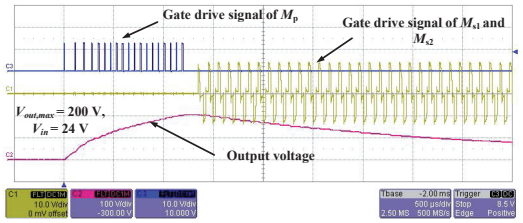

Fig. 13. A charge and discharge cycle with the proposed topology; CH1: 10 V/div, CH2: 100 V/div, CH3: 10 V/div, Time scale: 500 μs/div.

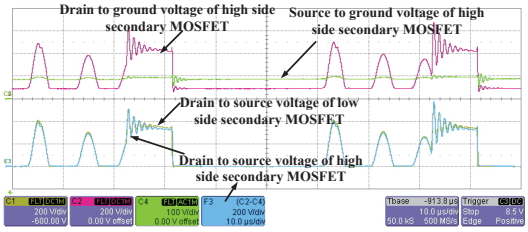

Fig. 14. Comparison of the voltage stress across the two secondary MOSFETs during the charge process using the proposed topology; CH1: 200 V/div, CH2: 200 V/div, CH4: 100 V/div,F3=C2-C4: 200 V/div, Time scale: 10 μs/div.

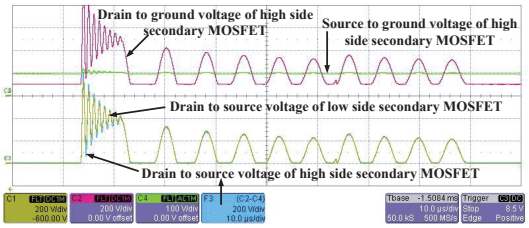

Fig. 15. Comparison of the voltage stress across the two secondary MOSFETs during the discharge process using the proposed topology; CH1: 200 V/div, CH2: 200 V/div, CH4: 100 V/div,F3=C2-C4: 200 V/div, Time scale: 10 μs/div.

VI. CONCLUSION

In this paper, a bidirectional flyback converter with multiple series connected outputs is proposed, for high voltage drive of capacitive DEAP actuators. Simulation results (output voltages and voltage stresses across the secondary MOSFETs/diodes) during both charge and discharge processes are provided, to show a comparison between the proposed and conventional implementations. A theoretical comparison shows that the proposed converter has the potential to improve efficiency and lower the cost. The detailed implementation of secondary gate driver, using a gate drive transformer is provided. Experimental results from the conventional (for full operating voltage range 0-2.5 kV) and the proposed (0-200 V) bidirectional converters are provided. The experimental waveforms of the drain-to-source voltages of the two secondary MOSFETs confirms the voltage sharing across the two MOSFETs.

VII. FUTURE WORK

Due to lack of time the converter operation for full operating voltage range, and with $p = 5$ series connected secondary stages is not verified. However, the future work regarding the proposed converter involves:

- implementing the valley switching control during both charge and discharge processes.
- design and implementation of the gate drive transformer for $p = 5$ stages.
- design of the efficient flyback trasformer with very low self-capacitance.
- investigating the coupling factor of different winding strategies interms of voltage sharing.

REFERENCES

[1] Y. Bar-Cohen, *Electroactive Polymer [EAP] Actuators as Artificial Muscles: Reality, Potential, and Challenges*, 2nd ed. Washington, DC: SPIE, 2004.

[2] R. E. Pelrine, R. D. Kornbluh, Q. Pei, and J. P. Joseph, "High-speed electrically actuated elastomers with strain greater than 100%," *Science*, vol. 287, pp. 836–839, 2000.

[3] F. Carpi, D. DE Rossi, R. Kornbluh, R. Pelrine, and P. Sommer-Larsen, *Dielectric Elastomer As Electromechanical Transducers*, Amsterdam, Netherlands: Elsevier, 2008.

[4] M. Tryson, H. E. Kiil, M. Benslimane, "Powerful tubular core free dielectric electro active polymer (DEAP) push actuator," in *Proc. SPIE*, vol. 7287, 2009.

[5] R. Sarban, B. Lassen, M. Willatzen, "Dynamic Electromechanical Modeling of Dielectric Elastomer Actuators With Metallic Electrodes," *IEEE/ASME Trans. on Mechatronics*, vol. 17, no. 5, pp. 960–967, Oct. 2012.

[6] L. Huang, P. Thummala, Z. Zhang, M. A. E. Andersen, "Battery Powered High Output Voltage Bidirectional Flyback Converter for Cylindrical DEAP Actuator," in *Proc. IEEE IPMHVC*, Jun. 2012, pp. 454–457.

[7] Danfoss PolyPower, http://www.polypower.com/, [accessed 18 Nov. 2014].

[8] LEAP Technology, http://www.leaptechnology.com/, [accessed 20 Nov. 2014].

[9] P. Thummala, Z. Zhang, M. A. E. Andersen, S. Rahimullah, "Dielectric electro active polymer incremental actuator driven by multiple high-voltage bi-directional DC-DC converters," in *Proc. IEEE ECCE USA*, Sept. 2013, pp. 3837–3844.

[10] R. D. Kornbluh, R. Pelrine, Q. Pei, R. Heydt, S. Stanford, S. Oh, J. Eckerle,"Electroelastomers: applications of dielectric elastomer transducers for actuation, generation, and smart structures," in *Proc. SPIE*, vol. 4698, pp. 254-270, 2002.

[11] I. A. Anderson, T. A. Gisby, T. G. McKay, B. M. OBrien, E. P. Calius, "Multi-functional dielectric elastomer artificial muscles for soft and smart machines," *Journal of Applied Physics*, 112, 041101, 2012.

[12] S. K. Chung, H. B. Shin, "High-voltage power supply for semi-active suspension system with ER-fluid damper," *IEEE Trans. Vehicular Technology*, vol. 53, no. 1, pp. 206–214, Jan. 2004.

[13] J. Elmes, C. Jourdan, O. Abdel-Rahman, I. Batarseh, "High-Voltage, High-Power-Density DC-DC Converter for Capacitor Charging Applications," in *Proc. IEEE APEC*, Feb. 2009, pp. 433–439.

[14] T. Andersen, M. S. Rodgaard, O. C. Thomsen, M. A. E. Andersen, "Low voltage driven dielectric electro active polymer actuator with integrated piezoelectric transformer based driver," in *Proc. SPIE Electroactive Polymer Actuators and Devices (EAPAD)*, vol. 7976, pp. 79762N, 2011.

[15] N. O. Sokal, R. Redl, "Control algorithms and circuit designs for optimal flyback-charging of an energy storage capacitor (e.g., for flash lamp or defibrillator)," *IEEE Trans. Power Electronics*, vol. 12, no. 5, pp. 885–894, Sep. 1997.

[16] R. W. Erickson and D. Maksimovic, *Fundamentals of Power Electronics*, 2nd ed. New York: Springer, 2001.

[17] L. Eitzen, C. Graf, J. Maas, "Cascaded bidirectional flyback converter driving DEAP transducers," in *Proc. IEEE IECON*, Nov. 2011, pp. 1226–1231.

[18] S. H. Kang, D. Maksimovic, I. Cohen, "Efficiency Optimization in Digitally Controlled Flyback DCDC Converters Over Wide Ranges of Operating Conditions" *IEEE Trans. Power Electronics*, vol. 27, no. 8, pp. 3734–3748, Aug. 2012.

[19] L. Chen, H. Hu, Q. Zhang, A. Amirahmadi, I. Batarseh, "A Boundary-Mode Forward-Flyback Converter With an Efficient Active LC Snubber Circuit," *IEEE Trans. Power Electronics*, vol. 29, no. 6, pp. 2944–2958, June 2014.

[20] J. Park, Y.-S. Roh, Y.-J. Moon, C. Yoo, "A CCM/DCM Dual-Mode Synchronous Rectification Controller for a High-Efficiency Flyback Converter," *IEEE Trans. Power Electronics*, vol. 29, no. 2, pp. 768–774, Feb. 2014.

[21] Y.-H. Kim, Y.-H. Ji, J.-G. Kim, Y.-C. Jung, C.-Y. Won, "A New Control Strategy for Improving Weighted Efficiency in Photovoltaic AC Module-Type Interleaved Flyback Inverters," *IEEE Trans. Power Electronics*, vol. 28, no. 6, pp. 2688–2699, June 2013.

[22] A. Radic, A. Straka, A. Prodic, "Low-volume stackable flyback converter with near minimum deviation controller," in *Proc. IEEE APEC*, March 2014, pp. 1948–1953.

[23] J.-W. Shin, S.-J. Choi, B.-H. Cho, "High-Efficiency Bridgeless Flyback Rectifier With Bidirectional Switch and Dual Output Windings," *IEEE Trans. Power Electronics*, vol. 29, no. 9, pp. 4752–4762, Sept. 2014.

[24] N. Sukesh, M. Pahlevaninezhad, P. K. Jain, "Analysis and Implementation of a Single-Stage Flyback PV Microinverter With Soft Switching," *IEEE Trans. Industrial Electronics*, vol. 61, no. 4, pp. 1819–1833, April 2014.

[25] K. Venkatesan, "Current mode controlled bidirectional flyback converter," in *Proc. IEEE PESC*, pp. 835–842 vol.2, 26-29 Jun 1989.

[26] T. Bhattacharya, V. S. Giri, K. Mathew, L. Umanand, "Multiphase Bidirectional Flyback Converter Topology for Hybrid Electric Vehicles" *IEEE Trans. Industrial Electronics*, vol. 56, no. 1, pp.78–84, Jan. 2009.

[27] T. Anno, H. Koizumi, "Double Input Bidirectional DC/DC Converter Using Cell Voltage Equalizing with Flyback Transformer," *IEEE Trans. Power Electronics*, April 2014.

[28] G. Chen, Y.-S. Lee, S.Y.R. Hui, D. Xu, Y. Wang, "Actively clamped bidirectional flyback converter," *IEEE Trans. Industrial Electronics*, vol. 47, no. 4, pp. 770–779, Aug. 2000.

[29] F. Zhang, Y. Yan, "Novel ForwardFlyback Hybrid Bidirectional DC-DC Converter," *IEEE Trans. Industrial Electronics*, vol. 56, no. 5, pp. 1578–1584, May 2009.

[30] P. Thummala, Z. Zhang, M. A. E. Andersen, "High Voltage Bidirectional Flyback Converter for Capacitive Actuator," in *Proc. European Power Electronics (EPE) Conference*, Sept. 2013, pp. 1–10.

[31] L. Huang, Z. Zhang, M.A.E. Andersen, "Design and development of autonomous high voltage driving system for DEAP actuator in radiator thermostat," in *Proc. IEEE APEC*, pp. 1633–1640, 16-20 March 2014.

[32] P. Thummala, H. Schneider, Z. Zhang, A. Knott, M. A. E. Andersen, "Optimization of a bi-directional flyback converter for a high voltage capacitor charging application," in *Proc. IEEE APEC*, Mar. 2014, pp. 2556–2563.

[33] P. Thummala, H. Schneider, Z. Zhang, Z. Ouyang, A. Knott, M. A. E. Andersen, "Efficiency Optimization by Considering the High Voltage Flyback Transformer Parasitics using an Automatic Winding Layout Technique," *IEEE Trans. Power Electronics*, accepted, 2014.

[34] H. Schneider, P. Thummala, L. Huang, Z. Ouyang, A. Knott, Z. Zhang, M. A. E. Andersen, "Investigation of transformer winding architectures for high voltage capacitor charging applications," in *Proc. IEEE APEC*, Mar. 2014, pp. 334–341.

[35] P. Thummala, D. Maksimovic, Z. Zhang, M. A. E. Andersen, "Digital control of a high-voltage (2.5 kV) bidirectional DC-DC converter for driving a dielectric electro active polymer (DEAP) based capacitive actuator," in *Proc. IEEE ECCE USA*, Sept. 2014, pp. 3435–3442.

[36] R. Pittini, L. Huang, Z. Zhang, M. A. E. Andersen, "Primary parallel secondary series flyback converter (PPSSFC) with multiple transformers for very high step-up ratio in capacitive load charging applications," in *Proc. IEEE APEC*, Mar. 2014, pp. 1440–1447.

[37] IXYS, Online available, http://ixapps.ixys.com/DataSheet/DS100214A-(IXTH_V03N400_S).pdf, [accessed 18 Nov. 2014].

[38] VMI, Online available, http://www.voltagemultipliers.com/pdf/SXF6521_25.pdf, [accessed 18 Nov. 2014].

[39] J.-W. Kim, J.-S. Yon, B.-H. Ch, "Modeling, control, and design of input-series-output-parallel-connected converter for high-speed-train power system," *IEEE Trans. Industrial Electronics*, vol. 48, no. 3, pp. 536–544, Jun 2001.

[40] R. Ayyanar, R. Giri, N. Mohan, "Active input-voltage and load-current sharing in input-series and output-parallel connected modular DC-DC converters using dynamic input-voltage reference scheme," *IEEE Trans. Power Electronics*, vol. 19, no. 6, pp. 1462–1473, Nov. 2004.

[41] J. W. Kimball, J. T. Mossoba, P. T. Krein, "Control Technique for Series Input-Parallel Output Converter Topologies" in *Proc. IEEE PESC* pp. 1441–1445, June 2005.

[42] X. Ruan, W. Chen, L. Cheng, C.K. Tse, H. Yan, T. Zhang, "Control Strategy for Input-SeriesOutput-Parallel Converters," *IEEE Trans. Industrial Electronics*, vol. 56, no. 4, pp. 1174–1185, April 2009.

[43] H. Fan, H. Li, "A distributed control of input-series-output-parallel bidirectional dc-dc converter modules applied for 20 kVA solid state transformer," in *Proc. IEEE APEC*, pp. 939–945, 6-11 March 2011.

[44] P. Thummala, D. Maksimovic, Z. Zhang, M. A. E. Andersen, R. Sarban, "Design of a High Voltage DC-DC Converter for Driving the Capacitive Incremental Actuators usable in Electric Vehicles (EVs)," in *Proc. IEEE IEVC*, Dec. 2014.

[45] P. Thummala, Z. Zhang, M. A. E. Andersen, R. Sarban, "Parallel input parallel output high voltage bi-directional converters for driving dielectric electro active polymer actuators," in *Proc. SPIE EAPAD*, vol. 9056, pp. 90561N-90561N-15, Mar. 2014.

[46] STM, Online available, http://www.st.com/st-web-ui/static/active/en/resource/technical/document/datasheet/CD00058073.pdf, [accessed 18 Nov. 2014].

Appendix O

Investigation of transformer winding architectures for high voltage capacitor charging applications

---

IEEE Applied Power Electronics Conference and Exposition 2014 (APEC)

Investigation of transformer winding architectures for high voltage capacitor charging applications

Henrik Schneider, Prasanth Thummala, Lina Huang, Ziwei Ouyang, Arnold Knott, Zhe Zhang, Michael A. E. Andersen
Electronics Group, Department of Electrical Engineering
Technical University of Denmark
2800 Kongens Lyngby, Denmark
hensc@elektro.dtu.dk, pthu@elektro.dtu.dk, huang@elektro.dtu.dk

***Abstract*—Transformer parameters such as leakage inductance and self-capacitance are rarely calculated in advance during the design phase, because of the complexity and huge analytical error margins caused by practical winding implementation issues. Thus, choosing one transformer architecture over another for a given design is usually based on experience or a trial and error approach. This work presents equations regarding calculation of leakage inductance, self-capacitance and AC resistance in transformer winding architectures, ranging from the common non-interleaved primary/secondary winding architecture, to an interleaved, sectionalized and bank winded architecture. The analytical results are evaluated experimentally and through FEM simulations. Different transformer winding architectures are investigated in terms of the losses caused by the transformer parasitics for a bi-directional high-voltage (~1500 V) flyback converter used to drive a dielectric electro active polymer based incremental actuator. The total losses due to the transformer parasitics for the best transformer architectures is reduced by more than a factor of ten compared to the worst case transformer architectures.**

I. INTRODUCTION

Dielectric electro active polymer (DEAP) is an emerging smart material that has experienced significant development and has gained increasing attention over the last decade [1], [2]. DEAP, when used as actuators, has the potential to be an effective replacement for many conventional actuators due to its unique properties such as high strain, light weight, low noise operation, low power consumption. However, a compact high voltage driver is required to charge and discharge the DEAP from 0 V to 2500 V DC supplied from a 24 V battery. The DEAP actuator applications require a bi-directional energy transfer capability, to increase the life time of the battery. The flyback converter topology is suitable for low power (< 150 W), and high voltage capacitor charging applications, as it can be made very compact with a low number of components.

The flyback transformer is the most critical component in terms of driver performance. The high voltage requirement demands a high turns ratio which calls for a large number of secondary turns. This may lead to a high winding self-capacitance resulting in severe capacitive switching loss and undesirable, resonating current spikes in the leading edge of the current waveform, which could lead to false triggering of the current limit during the turn-on process.

The leakage inductance of the transformer may cause undesirable voltage spikes on the drains of the primary and secondary MOSFETs during the charge and the discharge processes, respectively, which lead to use of active or passive snubber circuits in the converter. With active snubbers high energy efficiency can be achieved, at the expense of a higher cost and added control complexity whereas the passive snubbers result in switching loss due to the leakage inductance. The AC resistance is also an important parameter to consider, since the AC conduction loss is caused by high frequency skin and proximity effects in a flyback converter operating in boundary conduction mode (BCM) or in discontinuous conduction mode (DCM).

Thus, accurate estimation of the transformer parameters and their associated losses are required, to evaluate different transformer winding architectures (TWAs) from which the best TWA is selected to achieve high energy efficiency. Extensive research has been done on calculating the leakage inductance in conventional transformers [3]-[6], [17], and in [7]-[17], the capacitance calculation methods have been proposed for inductors, power, planar, and high voltage transformers. The influence of transformer parasitics for the low power flyback converter has been discussed in [24]. This paper investigates a number of TWAs providing a deep insight into transformer design and its impact on the total loss contribution of a bi-directional high-voltage flyback converter.

The paper is organized as follows: the TWAs are described and then calculations of self-capacitance, leakage inductance and AC resistance for different TWAs are provided. The calculated transformer parameters are evaluated via FEA simulation using ANSOFT Maxwell and

This work was sponsored by Danish National Advanced Technology Foundation.

the transformer paracitics for all TWAs are presented, followed by the conclusion.

II. TRANSFORMER WINDING ARCHITECTURES

This paper investigates the four known winding schemes (A, B, C and D) as shown in Fig. 1 [14], [16], [26], [27]. Winding scheme A is the most simple to implement since the next layer starts where the previous layer ended. In winding scheme B, the next layer starts just above the starting point of the previous layer. Winding scheme C split the winding into a number of sections that is individually wounded like winding scheme A. In winding scheme D, the turns progress in a vertical back angled way where turns are built on top of previous turns. It seems like winding scheme D achieves as many angled sections as there are turns in a layer without the penalty of reducing the fill factor due to the thickness of the section walls. Another advantage is that winding scheme D can be easily interleaved which is not the case for winding scheme C since it is hard to add section walls in-between windings. The difference in self-capacitance due to the winding schemes is severe because the voltage potentials between the turns in the winding are changed.

Several winding buildups (S/P, S/P/S, S/P/S/P/S/P/S; where S and P are is the secondary and primary windings, respectively) are investigated - see Fig. 2. Based on these configurations, seven high voltage transformer winding architectures (W_1-W_7) are derived and the winding information is summarized in Table 1. In order to simplify the implementation of the windings a low turns ratio of 10 is selected. The TWAs W_1-W_6 are wound with 10 primary turns and 100 secondary turns. W_7 deviates since it is only implemented with 9 primary turns due to the nature of the winding architecture.

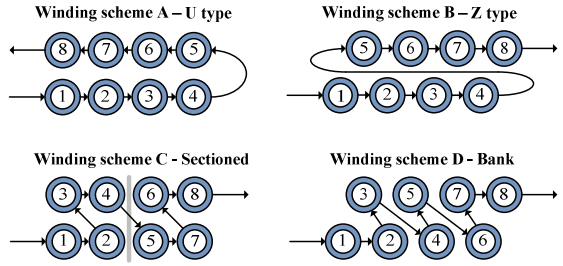

Figure 1. An overview of different winding schemes.

Winding scheme A is employed for the primary winding of all architectures. Moreover, all winding space of the bobbin is utilized to improve the fill factor and to reduce the winding resistance. Equal space allocation for primary and secondary winding is adopted for this investigation, thus the primary winding is wounded with a number of parallel wires.

III. SELF-CAPACITANCE

High voltage transformers tend to have a large number of turns in the high voltage side, which introduces a non-negligible parasitic self-capacitance. It is important to predict the self-capacitance in the design phase in order to avoid severe switching loss. In fact, the winding self-capacitance is a parameter representing the electric field energy stored in the winding and is considered as a shunt lumped element in most cases [14]. Due to a large number of turns per layer, the effect of the turn-to-turn capacitance can be neglected and the main

TABLE I. HIGH VOLTAGE TRANSFORMER ARCHITECTURES

Design	Winding buildup	Secondary winding		Primary winding
		Scheme	Parameters	Parameters
W_1	S/P	A	$N_s = 100$ $d_{is} = 0.3$ mm $d_{os} = 0.32$ mm $p_{TT} = 0.355$ mm $p_{LL} = 0.34$ mm $n_{ls} = 4$ $n_{pars} = 1$ Core / Material used: RM8 / N41	$N_p = 10$ $*d_{ip} = 0.7$ mm $*d_{op} = 0.8$ mm $n_{lp} = 2$ $n_{parp} = 2$
W_2	S/P	B		
W_3	S/P	C		
W_4	S/P	D		
W_5	S/P/S	B		
W_6	S/P/S	D		
W_7	S/P/S/P/S/P/S	B		$N_p = 9$ $*d_{ip} = 0.48$ mm $*d_{op} = 0.5$ mm $n_{lp} = 3$ $n_{parp} = 5$
Parameters interpretation				
N_s / N_p - number of secondary / primary turns; n_{ls} / n_{lp} - number of secondary / primary winding layers; n_{pars} / n_{parp} - number of secondary / primary parallel windings; d_{is} / d_{os} - inner / outer diameter of secondary winding; d_{ip} / d_{op} - inner / outer diameter of primary winding; p_{TT} / p_{LL} - turn-to-turn / layer-to-layer pitch of secondary winding; *In the practical transformer implementation triple insulated (TEX) windings are not used for the primary due to the unavailability of the wires;				

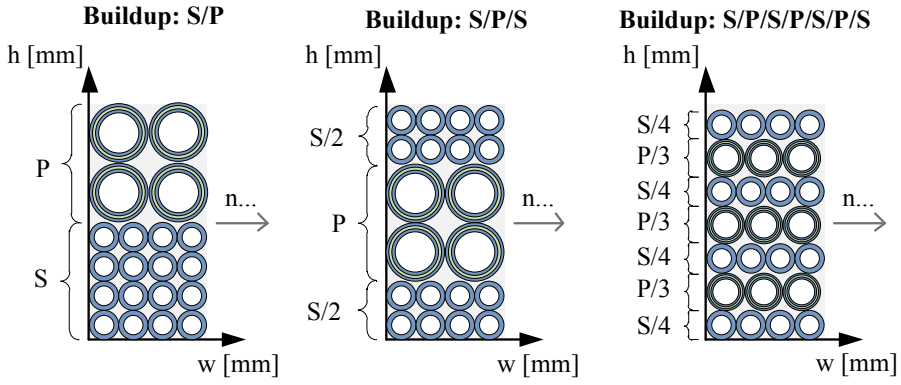

Figure 2. An overview of different winding buildups.

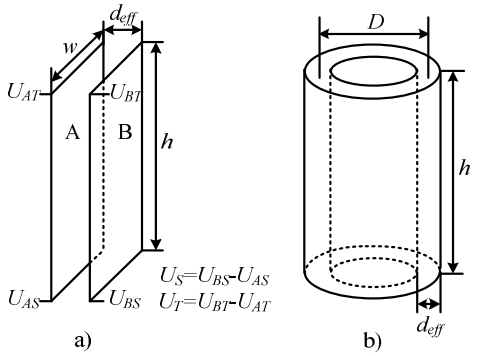

Figure 3. a) Two parallel plates with a linear potential distribution, b) Cylindrical capacitor model

contribution to the self-capacitance comes from the layer-to-layer capacitance, which can be calculated based on the simple parallel-plate or cylindrical capacitor model [14]-[16].

The self-capacitance in the transformer windings can be calculated using the electro static energy stored in the volume between the conductors [14], [16] and is given by

$$E_{Electric} = \frac{1}{2}\iiint_{Vol} \varepsilon\, E^2 dv = \frac{1}{2} C_S U_W^2 \tag{1}$$

where ε is the equivalent dielectric constant of the winding, E is the electric field strength, C_S is the self-capacitance, and U_W is the total voltage across the winding.

The energy stored in two adjacent conductive layers with a linear potential distribution, shown in Fig. 3a, can be calculated by (2), which is derived in [16]. The total stored energy is

$$E_{Stored} = \frac{C_l}{6}\left(U_S^2 + U_S U_T + U_T^2\right) \tag{2}$$

where U_S and U_T are the potential difference between the two surfaces at the bottom and top respectively, and C_l is the capacitance between the two surfaces and is considered as a parallel plate capacitance and can be calculated using (3)

$$C_l = \varepsilon_r \varepsilon_0 \frac{hw}{d_{eff}} \tag{3}$$

where ε_0 is the vacuum permittivity and is 8.854×10^{-12} F/m, ε_r is the relative permittivity of the dielectric material. The parameters h, w represents the dimensions of the plate and d_{eff} is the effective distance between two layers (which needs to be calculated for each TWA) and is given by

$$d_{eff} = p_{LL} - 1.15 d_{is} + 0.26 p_{TT} \tag{4}$$

where p_{LL}, d_{is} and p_{TT} are the layer to layer pitch, inner diameter, and turn to turn pitch, of the secondary winding, respectively. According to the methods given in [16], the expressions for calculating the self-capacitance for all above mentioned TWAs have been derived and are summarized in Table 2. Normally, the cylindrical shape, shown in Fig. 3b, is desired for most winding layers due to the simple winding technique as well as the short mean turn length [14]. If the distance between two layers is much less than the mean diameter for the two layers, the cylindrical capacitor can be considered to be a parallel plate capacitor and (3) can be employed to calculate the capacitance by replacing w with πD (see Fig. 3b).

TABLE II. SELF-CAPACITANCE EXPRESSIONS FOR DIFFERENT TWAS

TWA	Self-capacitance expression
W_1	$4\frac{(n_{ls}-1)}{n_{ls}^2}\frac{C_l}{3}$; $C_l = \varepsilon_r\varepsilon_0\frac{b_w l_{w1}}{d_{eff1}}$; $l_{w1} = \pi\left(D_i + n_{ls}d_{is} + (n_{ls}-1)h_{is}\right)$
W_2	$4\frac{(n_{ls}-1)}{n_{ls}^2}\frac{C_l}{4}$; $C_l = \varepsilon_r\varepsilon_0\frac{b_w l_{w1}}{d_{eff1}}$; $b_w = (T_{ls}-1)p_{TT} + d_{os}$
W_3	$\frac{4(n_{ls}-1)}{q_1 n_{ls}^2}\frac{C_l}{3}$; $C_l = \varepsilon_r\varepsilon_0\frac{\frac{b_{w2}}{q_1}l_{w1}}{d_{eff1}}$
W_4	$\varepsilon_r\varepsilon_0\frac{p_{TT}l_{w1}}{d_{eff2}}\frac{L}{b_w}$; $L = (n_{ls}-1)p_{LL} + d_{os}$ [7]
W_5	$\frac{\varepsilon_r\varepsilon_0 b_w}{n_{ls}^2}\left[\frac{l_{w2}}{d_{eff3}} + \frac{l_{w3}}{d_{eff3}} + \frac{l_{w4}}{d_{eff3} + n_{lp}d_p + (n_{lp}-1)h_{lp}}\right]$
W_6	$\varepsilon_r\varepsilon_0\left[\frac{p_{TT}(l_{w2}+l_{w3})}{d_{eff4}}\frac{L_1}{b_w} + \frac{p_{TT2}l_{w4}}{d_{eff4} + n_{lp}d_p + (n_{lp}-1)h_{ip}}\frac{L_2}{b_w}\right]$; $L_1 = \left(\frac{n_{ls}}{2}-1\right)p_{LL} + d_{os}$; $p_{TT2} = n_{lp}h_p + (n_{lp}-1)h_{lp} + d_{os}$; $L_2 = p_{TT2} + d_{os}$
W_7	$\frac{\varepsilon_r\varepsilon_0 b_w}{n_{ls}^2}\left[\frac{l_{w5}+l_{w6}+l_{w7}}{d_{eff5}}\right]$
Parameters interpretation	
ε_0 / ε_r - relative permittivity of vacuum / dielectric material; $\varepsilon_r = 4$; b_w - the width of the layer; T_{ls} is turns per layer of secondary winding; D_i - inner diameter of the bobbin; $d_{eff1,2,3,4,5}$ - effective thickness of dielectric between two layers [14] [16] for different TWAs; l_{w1} - mean length turn for the TWAs W_1, W_2, W_3 and W_4; l_{w2} / l_{w3} / l_{w4} - mean length turn between most inner two secondary (S_1, S_2) / most outer two secondary (S_3, S_4) / most outer secondary and the most inner secondary (S_2, S_3), layers for W_5 and W_6; l_{w5} / l_{w6} / l_{w7} / l_{w8} / l_{w9} / l_{w10} - mean length turn between most inner two secondary (S_1, S_2) / middle two secondary (S_2, S_3) / most outer two secondary (S_3, S_4) layers for W_7 q_1 - number of sections for structure W_3 and $q_1 = 4$; For remaining abbreviations refer Tables 1 and 3;	

IV. LEAKAGE INDUCTANCE

The leakage inductance in a transformer is calculated using the energy stored in the magnetic field [16]. The total leakage energy stored in the magnetic field is given by

$$E_{Magnetic} = \frac{1}{2}\iiint_{Vol} \mu_0\, H^2\, dv = \frac{1}{2} L_{lk} I_p^2 \tag{5}$$

where H is the magnetic field strength which is proportional to the number of ampere turns linked by the flux path, L_{lk} is the leakage inductance, and I_p is the peak current in the winding. The fundamental principles used to calculate the leakage inductance are thoroughly investigated in [3], [4],

TABLE III. PRIMARY LEAKAGE INDUCTANCE EQUATIONS FOR DIFFERENT TWAS

TWA	Leakage inductance expression
W_1, W_2, W_3, W_4	$\mu_0 l_w N_p^2 \left[\frac{1}{b_w}\left(\frac{n_{lp}h_p}{3} + \frac{(2n_{lp}-1)(n_{lp}-1)}{6}\left(\frac{h_{ip}}{n_{lp}}\right) + h_i \right) + \frac{1}{b_{w2}}\left(\frac{n_{ls}h_s}{3} + \frac{(2n_{ls}-1)(n_{ls}-1)}{6}\left(\frac{h_{is}}{n_{ls}}\right)\right) \right]$ [17]
W_5, W_6	$\frac{\mu_0 l_w N_p^2}{b_w} \left[\frac{n_{ls1}^3 + n_{ls2}^3}{3(n_{ls1}+n_{ls2})^3}\left(n_{lp}h_p + (n_{ls1}+n_{ls2})h_s\right) + \frac{n_{ls1}^2 + n_{ls2}^2}{(n_{ls1}+n_{ls2})^2}h_i \right.$ $\left\{ \frac{n_{ls1}(n_{ls1}-1)(2n_{ls1}-1) + n_{ls2}(n_{ls2}-1)(2n_{ls2}-1)}{6(n_{ls1}+n_{ls2})^2} \right\} h_{is} +$ $\left. \left\{ \left(n_{lp}-1\right)\left(\frac{n_{ls1}n_{lp}}{n_{ls1}+n_{ls2}}\right)^2 + \frac{n_{lp}(n_{lp}-1)(2n_{lp}-1)}{6} - \frac{n_{ls1}^2 n_{lp}(n_{lp}-1)}{n_{ls1}+n_{ls2}} \right\} \frac{h_{ip}}{n_{lp}^2} \right]$
W_7	$\mu_0 \frac{l_w}{b_w} N_p^2 \left[\frac{3h_p + 4h_s}{72} + \frac{7}{36}h_i \right]$
Parameters interpretation	
μ_0 - permeability of free air; l_w - mean length turn (MLT); b_w - width of the layer; b_{w2} - width of the layer excluding the combined with of the sections walls for TWA W_3, $b_{w2} < b_w$; For W_1, W_2 and W_4, $b_w = b_{w2}$; $h_p = d_{op}$ and $h_s = d_{os}$; h_{ip} / h_{is} / h_i - insulation thickness between primary-to-primary layer, secondary-to secondary layer and primary-to-secondary layer; For W_5 and W_6, n_{ls1} and n_{ls2} are the number of secondary layers are at the top and bottom of a primary winding respectively, having n_{lp} primary layers. In Fig. 4c, n_{ls1}=2 and n_{ls2}=2; For remaining abbreviations refer Tables 1 and 2;	

and [16]. Based on those methods, the equations for calculating the leakage inductances for TWAs W_1-W_7 have been derived and are summarized in Table 3 [17]. The MMFs in each primary and secondary layer are $T_{lp}I_p$ and $T_{ls}I_s$, respectively. For the winding buildup shown in Fig. 4a, the energy stored in the magnetic field is derived in (AI) in Appendix.

V. AC RESISTANCE

The AC resistance is calculated using equations commonly found in the literature [18]-[19], [26]. The DC resistance of the primary/secondary winding can be calculated by

$$R_{DC} = \frac{\rho l_w N}{A\, n_{par}},\quad A = \frac{\pi d_i^2}{4} \tag{6}$$

where ρ is the resistivity of copper at room temperature (ρ=17.24 nΩ/m at 20 °C), N is the total number of primary/secondary turns, l_w is the mean length turn of the winding, n_{par} is the number of parallel wires, A is the cross sectional area of the winding and d_i is the inner diameter of the winding excluding the insulation.

The AC resistance per layer of a given winding is given by

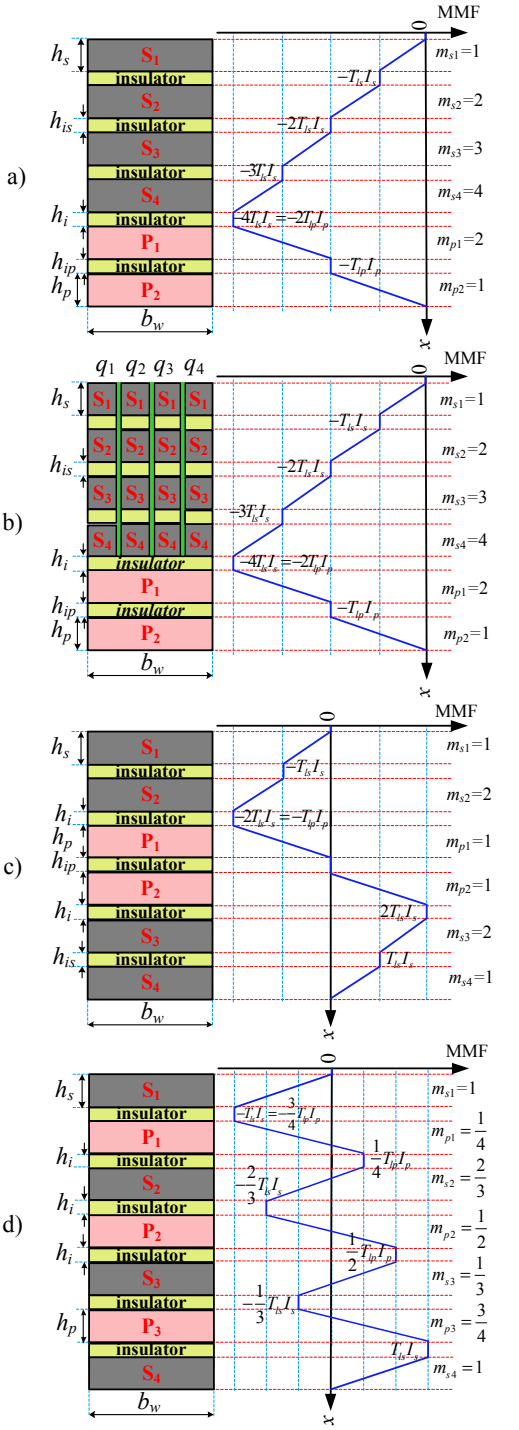

Figure 4. Analytical MMF distribution for, a) non-interleaved structure (S/P – W_1, W_2, W_4), b) non-interleaved structure (S/P – W_3), c) interleaved structure (S/S/P/P/S/S –W_5, W_6), d) fully interleaved structure (S/P/S/P/S/P/S –W_7)

$$R_{AC,\text{layer}} = R_{DC,layer} Q \left\{ \begin{array}{l} \left(2m^2 - 2m + 1\right) \dfrac{\sinh(2Q) + \sin(2Q)}{\cosh(2Q) - \cos(2Q)} - \\ 4\left(m^2 - m\right) \dfrac{\cos(Q)\sinh(Q) - \sin(Q)\cosh(Q)}{\cosh(2Q) + \cos(2Q)} \end{array} \right\} \quad (7)$$

Assume the variables Δ_1, Δ_2, Δ_3, and Δ_4 are assigned as in (8)

$$\Delta_1 = \frac{\sinh(2Q) + \sin(2Q)}{\cosh(2Q) - \cos(2Q)},\ \Delta_2 = \frac{\cos(Q)\sinh(Q) - \sin(Q)\cosh(Q)}{\cosh(2Q) + \cos(2Q)}$$
$$\Delta_3 = \frac{\sinh(Q) + \sin(Q)}{\cosh(Q) - \cos(Q)},\ \Delta_4 = \frac{\sinh(Q) - \sin(Q)}{\cosh(Q) + \cos(Q)} \quad (8)$$

The variable Δ_1 in terms of Δ_3 and Δ_4, and Δ_2 and Δ_4 is given by [19]

$$\Delta_1 = \frac{1}{2}\left(\Delta_3 + \Delta_4\right),\ \Delta_1 = \left(2\Delta_2 + \Delta_4\right) \quad (9)$$

Using (8), (9) in (7), the simplified AC resistance per layer is

$$R_{AC,\text{layer}} = R_{DC,layer} Q \left\{ \Delta_1 + 2\left(m^2 - m\right)\Delta_4 \right\} \quad (10)$$

$$R_{AC,\text{layer}} = R_{DC,layer} \frac{Q}{2} \left\{ \Delta_3 + \left(2m - 1\right)^2 \Delta_4 \right\} \quad (11)$$

The total AC resistance of M layers for the non-interleaved TWAs W_1-W_4 is given by

$$\begin{aligned} R_{AC,\text{total}} &= R_{DC,layer} Q \sum_{m=1}^{M} \left\{ \Delta_1 + 2\left(m^2 - m\right)\Delta_4 \right\} \\ &= \left(R_{DC,layer} M\right) Q \left\{ \Delta_1 + \frac{2}{3}\left(M^2 - 1\right)\Delta_4 \right\} \\ &= R_{DC,\text{total}} Q \left\{ \Delta_1 + \frac{2}{3}\left(M^2 - 1\right)\Delta_4 \right\} \end{aligned} \quad (12)$$

where $R_{DC,layer}$ and $R_{DC,total}$ are the DC resistance per layer and total DC resistance, respectively. The variable m represents the effective number of layers and is given by

$$m = \frac{F(h)}{F(h) - F(0)} \quad (13)$$

where $F(0)$ and $F(h)$ are the magneto motive forces (MMFs) at the start and end of each layer, respectively. The variable Q is the effective layer thickness normalized with the skin depth and is given by

$$Q = \frac{layer\ thickness}{penetration\ depth} = \frac{\frac{\pi}{4}^{3.5} d_i \sqrt{\frac{d_o T_l}{b_w}}}{\sqrt{\frac{\rho}{\pi \mu_0 f}}} \quad (14)$$

where d_i is the bare wire diameter, d_o is the overall wire diameter including insulation, T_l is the turns per layer of the given winding and f is the switching frequency.

To calculate the AC resistance per layer for the interleaved TWAs W_5-W_7, (10) or (11) needs to be used with the corresponding value of m for each layer. The total AC resistance is the sum of all AC resistances in each layer.

The total AC resistance referred to the primary is given by

$$R_{AC} = R_{AC,\text{total, P}} + \frac{R_{AC,\text{total, S}}}{n^2} \quad (15)$$

where n is the transformer turns ratio $R_{AC,total,\text{P}}$ and $R_{AC,total,\text{S}}$ are the total AC resistance of primary and secondary windings, respectively.

TABLE IV. ENERGY LOSS EXPRESSIONS OF TRANSFORMER PARACITICS

Name of energy loss	Loss expressions	
	Charge process (J)	Discharge process (J)
Switching loss due to self-capacitance	$E_{C1} = 0.5 C_P V_{dsP}^2$	$E_{C2} = 0.5 C_S V_{dsS}^2$
Snubber loss due to leakage inductance	$E_{L1} = \dfrac{0.5 L_{lkP} i_{pkP}^2 V_{snLV}}{V_{snLV} - \dfrac{V_{out}}{n}}$	$E_{L2} = \dfrac{0.5 L_{lkS} i_{pkS}^2 V_{snHV}}{V_{snHV} - V_{in} n}$
Winding loss due to AC and DC resistances	$E_{R1} = \left(\left[\begin{matrix} I_{DCP}^2 R_{DCP} + \\ I_{RMSP}^2 R_{ACP} \end{matrix} \right] t_{onC} + \left[\begin{matrix} I_{DCS}^2 R_{DCS} + \\ I_{RMSS}^2 R_{ACS} \end{matrix} \right] t_{offC} \right)$	$E_{R2} = \left(\left[\begin{matrix} I_{DCP}^2 R_{DCP} + \\ I_{RMSP}^2 R_{ACP} \end{matrix} \right] t_{offD} + \left[\begin{matrix} I_{DCS}^2 R_{DCS} + \\ I_{RMSS}^2 R_{ACS} \end{matrix} \right] t_{onD} \right)$

Parameters interpretation

C_P / C_S – self capacitance referred to primary / secondary;
V_{dsP} / V_{dsS} – drain to source voltage of primary / secondary MOSFET;
L_{lkP} / L_{lkS} – leakage inductance referred to primary / secondary;
i_{pkP} / i_{pkS} – primary / secondary peak current;
V_{snLV} / V_{snHV} – RCD snubber capacitor voltage of primary / secondary;
V_{out} / V_{in} – output / input voltage of the converter;
I_{DCP} / I_{DCS} – DC current of primary / secondary;
R_{DCP} / R_{DCS} – DC resistance of primary / secondary;
I_{RMSP} / I_{RMSS} – RMS current of primary / secondary;
R_{ACP} / R_{ACS} – AC resistance of primary / secondary;
t_{onC} / t_{offC} – on / off time of the primary MOSFET during the charge process;
t_{onD} / t_{offD} – on / off time of the HV MOSFET during the discharge process;

VI. FINITE ELEMENT ANALYSES

The different winding architectures are simulated in Ansoft Maxwell to extract the value of the leakage inductance, self-capacitance and AC resistance. In Fig. 5 the electrostatic energy between the windings is shown for winding schemes B and D. It is noted that the energy density is high between layer to layer and low between turn to turn as expected in winding scheme B. In winding scheme D there is less electrostatic energy and thus it has lower self-capacitance.

Fig. 6 shows a close-up of the magneto static energy of the three investigated winding buildups. The leakage flux runs approximately vertically through the windings and the magneto static energy is highest in the space between the primary and secondary windings. The heavy interleaved buildup (S/P/S/P/S/P/S) has very low magneto static energy and thus it will have a very low leakage inductance.

The AC resistance at 100 kHz is also simulated for the three winding buildups. A standard mesh which is very fine compared to the skin depth is used to simulate the eddy effects in the winding. A close up plot of the mesh is shown in Fig. 7.a. The diameter of the secondary winding is 0.3 mm and the skin depth at 100 kHz is approximately 0.2 mm. It is

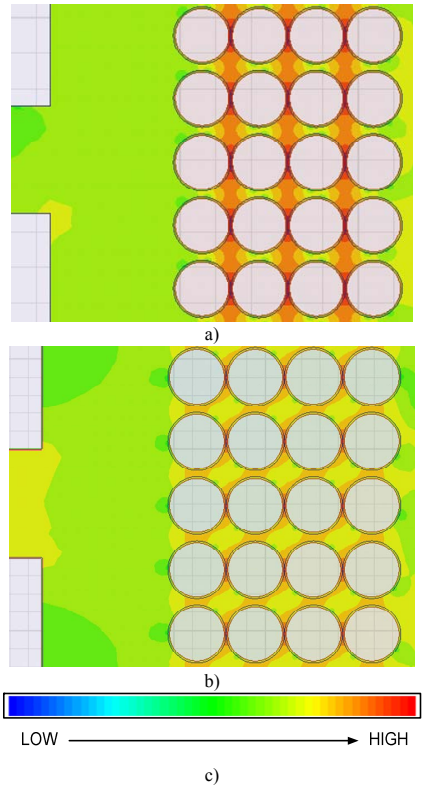

Figure 5. Plots from simulation of self-capacitance.
a) Energy distribution for winding scheme B. b) Energy distribution for winding scheme D. c) Density color bar

noted that the dimensions of the mesh is much lower than the diameter of the winding and the skin depth at 100 kHz. In Fig. 7. b-d, a close up of the current density for the three winding buildups is shown. It is noted that the current density in the non-interleaved buildup is much higher compared to the others and thus the AC resistance will also be higher.

VII. Experimental Results

The simulated, calculated and measured values of the self-capacitance, leakage inductance (measured at 10 kHz frequency using the impedance analyzer PSM1735) and AC resistance for the 7 TWA's are shown in the Tables 5, 6 and 7, respectively, from which it is clear that the measured, calculated and simulated transformer parameters for most of the TWAs closely matches. However, the differences in winding parameters such as an average layer to layer distance and mean length turn may cause errors around ±20 %. The measurement setup with 5 of the transformer prototypes is shown in Fig. 8. The energy loss expressions due to the transformer parasitics are summarized in Table 4. A plot of the loss distribution of the energy losses caused by the transformer parasitics), in a bi-directional flyback converter, used for charging and discharging an incremental DEAP actuator is shown in Fig. 9. The winding loss calculation for the flyback transformer is different from that of normal

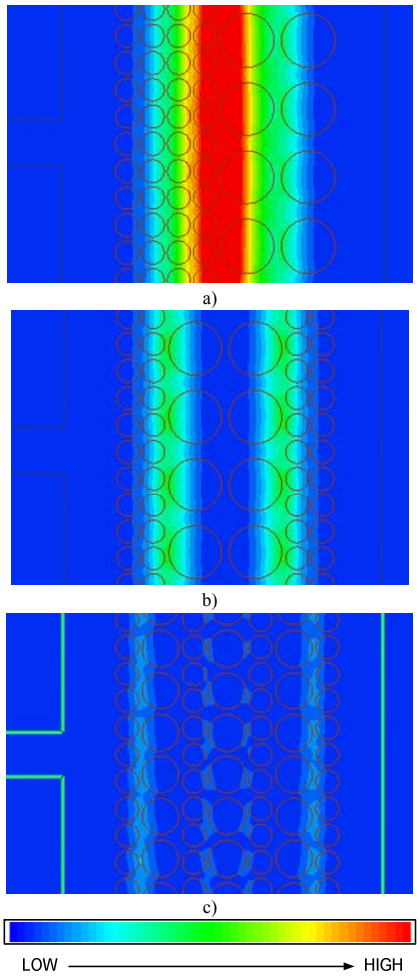

Figure 6. Plots from simulation of leakage inductance.
a) P/S. b) S/P/S. c) S/P/S/P/S/P/S. d) Density color bar.

transformer since the primary and secondary currents are out of phase, in [20] the winding loss is calculated for a flyback transformer with a non-interleaved structure. The same method can be used for the interleaved structures as well. However, due to limited space that is not included in this paper.

The calculated transformer parasitic values are used for calculating all losses, in order to provide a fair and useful comparison of the losses. The following specifications are used to calculate the losses in the bi-directional flyback converter [17], [20]-[23]: input voltage: 24V, output voltage: 1500 V, load capacitance: 200 nF, switching frequency during the charging and discharging process: 20-200 kHz, and 26 kHz, and primary peak current during charge and discharge processes: 2.12 A. The primary magnetizing inductance: 35 μH. From Fig. 9, it is clear that W_6 has the lowest loss among all TWAs followed by W_4, W_7 and W_3.

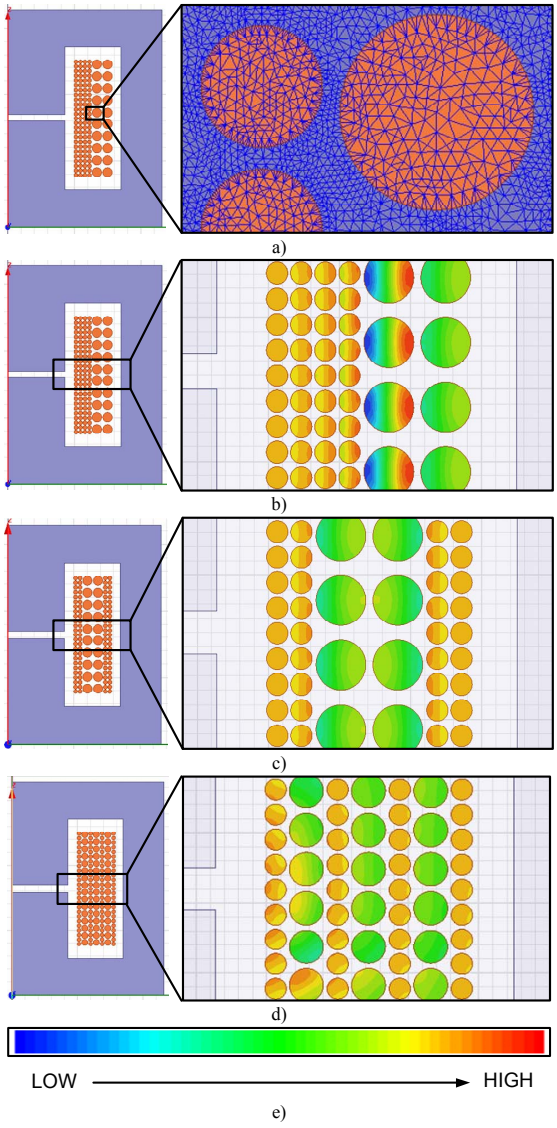

Figure 7. Plots from the simulations of AC resistance.
a) Default mesh, b) Current density of W_1-W_4, c) Current density of W_5-W_6, d) Current density of W_7, e) Density color bar

Thus the structure W_6 is highly recommended for high voltage capacitor charging application.

VIII. Conclusions

The analytical equations for calculating the transformer AC resistance, lekage inductance and self-capacitance for seven different winding architectures have been presented and evaluated experimentally and with FEA simulation. The main contribution to the errors is due to practical winding issues which are not accounted for in the equations. The transformer loss distribution is based on the calculated values, and it clearly shows that transformer winding architectures

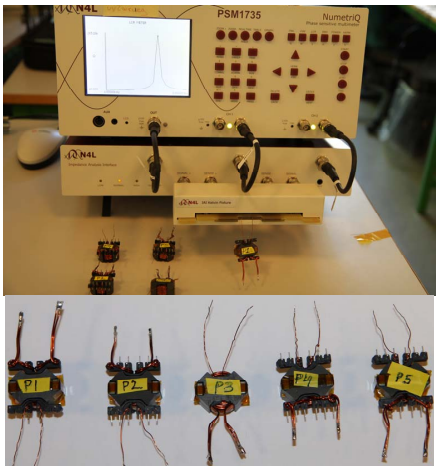

Figure 8. Measurement setup and five transformer prototypes with RM8 core

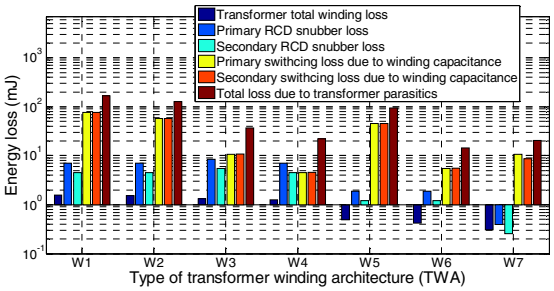

Figure 9. Energy loss distribution of the losses caused by transformer parasitics in the high voltage capacitor charging application.

where the self-capacitance is lowest are particularly suitable for high voltage charging applications. Future work involves the experimental validation of the proposed TWAs in the high voltage bi-directional dc-dc converter.

TABLE V. Self-capacitance of Secondary Winding at Resonance Frequency

TWA	Buildup	Winding scheme	Sim. (pF)	Calc. (pF)	Meas. (pF)
W_1	S/P	A	33	32	28
W_2	S/P	B	25	24	26
W_3	S/P	C	2.4	2	4.2
W_4	S/P	D	1.9	1	1.3
W_5	S/P/S	B	10	20	22
W_6	S/P/S	D	3.3	2.1	6
W_7	S/P/S/P/S/P/S	B	5	3.6	15

TABLE VI. Leakage Inductance Referred to Primary

TWA	Buildup	Winding scheme	Sim. (nH)	Calc. (nH)	Meas. (nH)
W_1	S/P	A	526	590	550
W_2	S/P	B			520
W_3	S/P	C			725
W_4	S/P	D			580
W_5	S/P/S	B	150	152	181
W_6	S/P/S	D			208
W_7	S/P/S/P/S/P/S	B	30	22	74

TABLE VII. AC RESISTANCE REFERRED TO PRIMARY AT 100 KHZ

TWA	Buildup	Winding scheme	Sim. (mΩ)	Calc. (mΩ)	Meas. (mΩ)
W_1	S/P	A	102	110	130
W_2	S/P	B			127
W_3	S/P	C			135
W_4	S/P	D			84
W_5	S/P/S	B	35	37	39
W_6	S/P/S	D			42
W_7	S/P/S/P/S/P/S	B	23	18	22

REFERENCES

[1] R. E. Pelrine, R. D. Kornbluh, Q. Pei, and J. P. Joseph, "High-speed electrically actuated elastomers with strain greater than 100%," in Proc. *Science*, vol. 287, pp. 836–839, 2000.

[2] R. E. Pelrine, R. D. Kornbluh, and J. P. Joseph, "Electrostriction of polymer dielectric with compliant electrodes as a means of actuation," in Proc. *Sens. Actuators A*, vol. 64, pp. 77–85, 1998.

[3] W. G. Hurley and D. J. Wilcox, "Calculation of leakage inductance in transformer windings," in Proc. *IEEE Trans. Power Electronics*, vol. 9, pp. 121-126, 1994.

[4] Z. Ouyang, Z. Zhang, O. C. Thomsen and M. A. E. Andersen, "Planar-integrated magnetics (PIM) module in hybrid bidirectional DC-DC converter for fuel cell application," in Proc. *IEEE Trans. Power Electronics*, vol.26, pp. 3254-3264, 2011.

[5] S. R. Cove, M. Ordonez, F. Luchino, and J. E. Quaicoe, "Applying Response Surface Methodology to Small Planar Transformer Winding Design," in Proc. *IEEE Trans. Industrial Electronics*, vol. 60, pp. 483-493, 2013.

[6] J. Zhang, Z. Ouyang, M. Duffy, M. A. E Andersen and W. G. Hurley "Leakage inductance calculation for planar transformer with magnetic shunt", in Proc. *ECCE USA* 2013.

[7] F. Blache, J-P. Keradec, B. Cogitore, "Stray capacitances of two winding transformers: equivalent circuit, measurements, calculation and lowering," in Proc. *IEEE Industry Applications Society Annual Meeting,* pp. 1211-1217 vol. 2, 2-6 Oct. 1994.

[8] W. T. Duerdoth, "Equivalent capacitance of transformer windings," in Proc. *Wireless Eng.*, vol. 23, pp. 161–167, Jun. 1946.

[9] A. Massarini and M. K. Kazimierczuk, "Self-capacitance of inductors," in Proc. *IEEE Trans. Power Electron.*, vol. 12, no. 4, pp. 671–676, Jul. 1997.

[10] T. Duerbaum and G. Sauerlander, "Energy based capacitance model for magnetic devices," in Proc. *APEC*, vol. 1, pp. 109–115, 2001.

[11] W. T. Duerdoth, "Equivalent capacitance of transformer windings," in Proc. *Wireless Eng.,* vol. 23, pp. 161–167, Jun. 1946.

[12] T. Duerbaum, "Capacitance model for magnetic devices," in Proc. *Power Electron. Spec. Conf.*, vol. 3, pp. 1651–1656, 2000.H. Y. Lu, J. Zhu, S. Y. R. Hui, and V. S. Ramseden, "Measurement and Modeling of stray capacitances in high frequency transformers," in Proc. *Power Electron. Spec. Conf.*, pp. 763–769, 1999.

[13] H. Y. Lu, J. G. Zhu, and S. Y. R. Hui, "Experimental determination of stray capacitances in high-frequency transformers," in Proc. *IEEE Trans. Power Electron.*, vol. 18, no. 5, pp. 1105–1112, Sep. 2003.

[14] L. Dalessandro, F. da Silveira Cavalcante, J. W. Kolar, "Self-Capacitance of High-Voltage Transformers," in Proc. *IEEE Trans. Power Electronics,* vol. 22, no. 5, pp. 2081-2092, Sept. 2007.

[15] J. Biela, J. W. Kolar, "Using Transformer Parasitics for Resonant Converters—A Review of the Calculation of the Stray Capacitance of Transformers," in Proc. *IEEE Trans. Industry Applications,* vol. 44, no. 1, pp. 223-233, 2008.

[16] E. C. Snelling, *Soft Ferrites-Properties and applications,* 2nd ed. London, UK, Butterworth, 1988.

[17] P. Thummala, H. Schneider, Z. Ouyang, Z. Zhang, M. A. E. Andersen, "Estimation of transformer parameters and loss analysis for high voltage capacitor charging application," in Proc. *IEEE ECCE Asia,* pp. 704-710, 3-6 Jun. 2013.

[18] W.G. Hurley, E. Gath, J. G. Breslin, "Optimizing the AC resistance of multilayer transformer windings with arbitrary current waveforms," in Proc. *IEEE Trans. Power Electronics*, vol. 15, no. 2, pp. 369-376, Mar 2000.

[19] J. A. Ferreira, "Improved analytical modeling of conductive losses in magnetic components," in Proc. *IEEE Transactions on Power Electronics*, vol. 9, no. 1, pp.127,131, Jan 1994.

[20] P. Thummala, H. Schneider, Z. Zhang, A. Knott, M. A. E. Andersen, "Optimization of a Bi-Directional Flyback Converter for a High Voltage Capacitor Charging Application," in Proc. *IEEE APEC,* pp., 16-20 Mar. 2014.

[21] K. Venkatesan, "Current Mode Controlled Bidirectional Flyback Converter," in Proc. *IEEE PESC*, pp. 835-842, 1989.

[22] T. Bhattacharya, V. S. Giri, K. Mathew, L. Umanand, "Multiphase Bidirectional Flyback Converter Topology for Hybrid Electric Vehicles,", in Proc. *IEEE Transactions on Industrial Electronics*, vol. 56, no.1, pp.78-84, Jan. 2009.

[23] P. Thummala, Z. Zhang, M. A. E. Andersen, "High Voltage Bi-directional Flyback Converter for Capacitive Actuator," in Proc. *European Power Electronics Conference (EPE),* pp. 3-6th Sept. 2013.

[24] G. Chen, Y.-S. Lee, S.Y.R. Hui, D. Xu, Y. Wang, "Actively clamped bidirectional flyback converter," in Proc. *IEEE Trans. Industrial Electronics*, vol. 47, no. 4, pp. 770-779, Aug. 2000.

[25] M. J. Prieto, A. Fernandez, J. M. Diaz, J. M. Lopera, J. Sebastian, "Influence of transformer parasitics in low-power applications," in Proc. *IEEE APEC*, vol. 2, pp. 1175-1180, 14-18th Mar. 1999.

[26] R. W. Erickson and D. Maksimovic, "Fundamentals of Power Electronics," 2nd ed. New York: Springer, 2001.

[27] John R. Barnes, "Robust electronic design reference book," Volume 1, Springer, 2004.

APPENDIX

$$E_{Mag}=\frac{\mu_0}{2}l_w b_w\int H^2(x)\,dx=\frac{\mu_0}{2}l_w b_w K_1;\; K_1=\left[\sum_{u=1}^{n_{ls}}\int_0^{h_s}H_{su}^2\,dx+\sum_{v=1}^{n_{lp}}\int_0^{h_p}H_{pv}^2\,dx+\sum_{a=1,b=a+1}^{n_{ls}-1}H_{sab}^2\,h_{is}+\sum_{c=1,d=c+1}^{n_{lp}-1}H_{pcd}^2\,h_{ip}+H_{sp}^2h_i\right]$$

$$H_{su}=\left[-\frac{(u-1)T_{ls}I_s}{b_w}-\frac{T_{ls}I_s}{b_w}\frac{x}{h_s}\right];H_{pv}=\left[-\frac{(n_{lp}-v+1)T_{lp}I_p}{b_w}+\frac{T_{lp}I_p}{b_w}\frac{x}{h_p}\right];H_{sab}=-\frac{uT_{ls}I_s}{b_w};H_{pcd}=-\frac{vT_{lp}I_p}{b_w};H_{sp}=-\frac{n_{ls}T_{ls}I_s}{b_w};$$

$$K_1=\left[\begin{array}{l}\int_0^{h_s}\left(-\frac{T_{ls}I_s}{b_w}\frac{x}{h_s}\right)^2dx+\int_0^{h_s}\left(-\frac{T_{ls}I_s}{b_w}-\frac{T_{ls}I_s}{b_w}\frac{x}{h_s}\right)^2dx+\int_0^{h_s}\left(-\frac{2T_{ls}I_s}{b_w}-\frac{T_{ls}I_s}{b_w}\frac{x}{h_s}\right)^2dx+\int_0^{h_s}\left(-\frac{3T_{ls}I_s}{b_w}-\frac{T_{ls}I_s}{b_w}\frac{x}{h_s}\right)^2dx+\left(-\frac{T_{lp}I_p}{b_w}\right)^2h_{ip}\\+\left[\left(-\frac{T_{ls}I_s}{b_w}\right)^2+\left(-\frac{2T_{ls}I_s}{b_w}\right)^2+\left(-\frac{3T_{ls}I_s}{b_w}\right)^2\right]h_{is}+\int_0^{h_p}\left(-\frac{2T_{lp}I_p}{b_w}+\frac{T_{lp}I_p}{b_w}\frac{x}{h_p}\right)^2dx+\int_0^{h_p}\left(-\frac{T_{lp}I_p}{b_w}+\frac{T_{lp}I_p}{b_w}\frac{x}{h_p}\right)^2dx+\left(-\frac{2T_{lp}I_p}{b_w}\right)^2h_i\end{array}\right] \quad \text{(AI)}$$

$$=\left(\frac{T_{ls}I_s}{b_w}\right)^2\left[4^3\frac{h_s}{3}+14h_{is}\right]+\left(\frac{T_{lp}I_p}{b_w}\right)^2\left[2^3\frac{h_p}{3}+h_{ip}+4h_i\right]=\left(\frac{N_pI_p}{b_w}\right)^2\left[\frac{2h_p+4h_s}{3}+\frac{7h_{is}}{8}+\frac{h_{ip}}{4}+h_i\right];\;\begin{array}{l}n_{lp}T_{lp}I_p=n_{ls}T_{ls}I_s;\\N_pI_p=N_sI_s;\end{array}$$

Appendix P

Optimization of bi-directional flyback converter for a high voltage capacitor charging application

---

IEEE Applied Power Electronics Conference and Exposition 2014 (APEC)

Optimization of bi-directional flyback converter for a high voltage capacitor charging application

Prasanth Thummala, Henrik Schneider, Zhe Zhang, Arnold Knott, Michael A. E. Andersen
Electronics Group, Department of Electrical Engineering
Technical University of Denmark
2800 Kongens Lyngby, Denmark
pthu@elektro.dtu.dk, hensc@elektro.dtu.dk

Abstract—This paper presents an optimization technique for a flyback converter with a bidirectional energy transfer. The main goal is to optimize the converter for driving an incremental dielectric electro active polymer actuator, which must be charged and discharged from 0 V to 2500 V DC, supplied from a 24 V battery. The proposed optimization routine sweeps through a database of low voltage switching devices, and transformer core types and sizes. For each core, important winding parameters such as, the vertical winding space allocation for primary and secondary windings, and the spacing between the secondary windings layers are also swept. This enables the optimization routine to calculate and optimize the losses caused by transformer parasitics such as leakage inductance, self-capacitance and AC resistance which is crucial in achieving a high energy efficiency and high power density required for this application. The efficiency and loss distribution results provided by the optimization routine provide a deep insight into the transformer design and its impact on total converter efficiency. Finally, experimental work on a prototype of the bi-directional flyback converter is presented. The maximum charging and discharging energy efficiencies of the optimized design, are 96.1% and 85%, respectively.

I. INTRODUCTION

Dielectric electro active polymer (DEAP) is an emerging smart material that has experienced substantial development and has gained increasing attention over the last decade [1]-[4]. The DEAP technology can be used in actuator, sensor and energy harvesting applications. Bidirectional power electronics are of particular interest in DEAP actuator applications since the potential of the material needs to be high (charged) to expand and low (discharged) to retract. In Fig. 1, an illustration of an incremental actuator using two DEAPs as grippers and one DEAP as an extender is shown. DEAP, when used as incremental actuators, has the potential to be an effective replacement for many conventional incremental actuators due to its unique properties, such as large strain, light weight, low power consumption, and high flexibility. The DEAP technology has the potential to be used in various industries, e.g. automotive, aeronautics, space and medicine. In order to take full advantage of the DEAP potential, the drivers for the DEAP's need to have a low volume to be utilized in small spaces and the weight and energy efficiency influence the achieved traveling distance when powered from a battery.

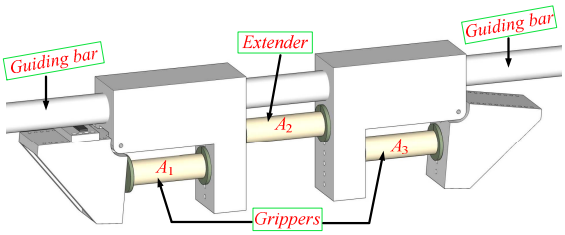

Figure 1. Incremental DEAP actuator [24].

The flyback topology is selected for the high voltage driver since it is suitable for low power (< 150 W) and has a low component count. High voltage switch-mode power supplies for charging the capacitive loads have been implemented in [5]-[12]. The design methodologies for transformers used in conventional switch mode power supplies are well documented in the literature. However, the procedures are conservative and are based on some assumptions in order to provide a simple, low risk and fast design phase. Often, the size of a suitable core is calculated based on assumptions such as constant switching frequency, a guess of the total converter efficiency, transformer conduction loss and core loss based on sinusoidal excitation and estimation of the winding current density. Thus, more complex and customized design procedures tailored for specific applications are needed to achieve efficient transformer designs. In this paper, an unconventional optimization routine is developed and tailored for bi-directional flyback converters, for high voltage capacitor charging and discharging applications, since literature regarding for this application is very limited [21]. The transformer optimization procedures for the switch-mode DC-DC converters have been discussed in [13]-[20]. The efficiency optimization method of the digitally controlled flyback converter for wide operating conditions is given in [15]. Analytical optimization of solid round wire conductors is

This work was sponsored by Danish National Advanced Technology Foundation.

proposed in [16]. In [17], a weighted efficiency oriented design methodology is proposed for a flyback inverter. The optimization routine is different from most methods since it does not depend on any guess work, estimations or rule of thumb approaches in order to achieve the transformer design. Instead, advanced algorithms for calculating the transformer parasitics are used in combination with a comprehensive loss model in order to evaluate the converter efficiency and other key parameters for a wide range of implementation possibilities. The loss model takes into account that the waveforms in the flyback converter are not sinusoidal in both the conduction and switching loss calculations. The optimization routine provides the designer with the necessary practical details of the chosen design such as core size, core material, wire sizes, number of winding layers, etc. In order to provide a high level of driver design flexibility for different DEAP applications, the driver efficiency and its size/weight can be weighted. The main idea behind the optimization routine can easily be adapted to fit other topologies and applications.

II. Optimization Routine

The optimization routine is described as follows: first, a drain to source voltage of the primary MOSFET is selected from a range of voltage levels. Then the turns ratio, magnetizing inductance, peak primary current, and primary and secondary turns are calculated using the converter specifications (input and maximum output voltages, charging time). Next, a primary MOSFET rated for the selected drain to source voltage is selected from a range of MOSFETs with varying parameters such as MOSFET package type, on-resistance and gate charge, etc. Next a transformer core is selected, followed by the choice of winding space allocation and layer to layer spacing. A dynamic winding function is used to design the transformer enabling the calculation of transformer parameters. Finally, losses in all components of the bi-directional flyback converter [6], in both charging and discharging modes are calculated [12] and added to represent the total estimated loss for that specific design. The optimization routine iterates through all design possibilities and in this case presents two solutions: one for the smallest transformer (limited by a temperature limit), and another for the most efficient solution (limited by an increase in converter efficiency vs. increase in transformer size). In the following sections, the challenges faced in the optimization routine are described, and solutions are presented.

A. Dynamic transformer design

Well into the optimization routine when the design parameters such as the number of turns and the allocated winding space is locked a winding implementation need to be found. In order to simplify that task the huge design space is limited - see Table 1. The core types are limited to 5 types. It is hard to predict which core type is most suitable for any application. In a flyback converter, a long transformer window width is often preferred to minimize the leakage inductance and AC resistance by providing a close coupling between windings and decrease the amount of winding layers. For high voltage converters, this could be different, since the winding self-capacitance on the high voltage side has a significant impact on the performance of the converter. Only the N87 core material and a simple non-interleaved winding structure (S-P) are used to limit complexity of the proposed optimization method. However, the optimization method can be easily adopted for an interleaved winding structure. Single insulated solid wire is used for the secondary winding since a

TABLE I. High voltage transformer structures and winding information

Description	Design decision	Advantages
Core type	ETD, EFD, E, RM and PQ	Round and square center leg ease the analytical complexity.
Core material	N87	Suitable for high frequency of operation.
Winding structure	P / S	Simple implementation and decreases analytical complexity.
Primary winding type	Solid wire	Flexible in terms of design and different winding structures.
Primary winding insulation	Triple insulation	Avoid edge tape to achieve a higher fill factor. More flexible in terms of implementation.
Secondary winding type	Solid wire	Suitable winding type, for a large number of turns. Flexible in terms of design, prototyping and different winding structures.
Secondary winding insulation	Single insulation	Minimum insulation thickness for a large number of turns.
Air gap	All legs	Simplifies the prototyping.
Maximum transformer temperature	140 °C	With an estimated ambient temperature of 40 °C, this enables a transformer temperature rise of 100 °C.

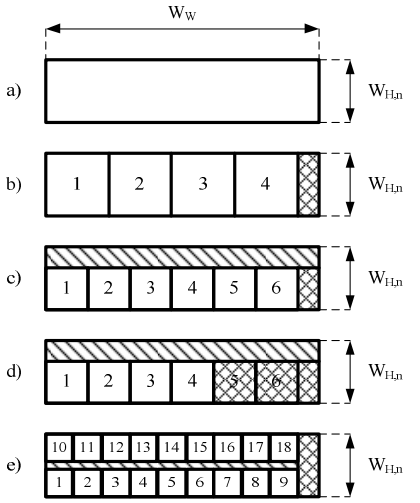

Figure 2. Cases from the dynamic transformer design. a) Allocated winding area. b) Initial starting point (Square width = area height). c) Unused space above and beside the squares (fill factor < 1). d) Squares not used (fill factor << 1). e) Close to ideal winding implementation (All squares used for the windings, horizontal space used as spacing between layers, high fill factor).

lot of turns are needed. The proper insulation between primary and secondary windings are achieved using a triple insulated solid wire for the secondary winding, which has proven to increase the winding fill factor and thus the efficiency and/or size of the transformer. The air gap is provided in all legs of the core, and the maximum air gap length is limited to 20% of the center leg length/window width, to avoid the loss due to the fringing field. A maximum transformer temperature limit of 140 °C is chosen. These limitation values can be altered based on the experience of the designer or the initial design specifications.

In this section, different cases about the dynamic transformer design are explained. The concept is best understood with the help of visualization. In Fig. 2.a, the space allocation for a given winding is shown. The width of the available area is the width of the bobbin window W_W and the height of the area is the allocated height for the winding $W_{H,n}$. The first step is to split the area into squares with a square width (W_{sq}) equal to the allocated height for the winding. It is $\alpha W_{H,n}$ for secondary and $(1-\alpha)W_{H,n}$ for the primary winding, with being the space allocation factor for secondary. In this case, it results in 4 squares and a non-square area that is considered as an unusable area as shown in Fig 2.b. In each square, a solid round wire could be placed with a diameter equal to the width of the square or a bundle of round wires with an outside bundle diameter equal to the width of the square. In this work, only the first option has been considered since the high number of needed secondary turns result in very thin wire diameter compared to the skin depth. If the number of turns required is 4 or less, this case will be considered as a valid solution and saved for later comparison with other found solutions. If a single turn is needed, then four squares could be utilized by 4 round wires in parallel and only the non-square area would not be used. The wire diameter may not be optimal compared to the skin depth which is why more solutions need to be considered and validated. This is achieved by splitting the winding area into smaller and smaller squares. The width of the squares for the secondary winding is limited by the smallest practical feasible diameter of a solid round wire (0.08 mm). In Fig. 2.c, the square size limits the use of the shaded area above the squares. However, that area can be set free for another winding thus improving the overall fill factor. The case shown in Fig. 2.d, illustrates, how the fill factor of a winding is reduced if not all squares are utilized as a turn. Fig. 2.e, illustrates how an optimum winding solution could look like if 18 turns were needed and the width of the square was optimum in terms of skin depth. Note that non-square horizontal area is utilized as spacing between the layers. The spacing distance is swept in order to balance the transformer parameters and the converter performance.

In Fig. 3, a flowchart of the dynamic transformer winding design is shown. The gray arrows point to a set of variables that are calculated during each iteration viz, squares per column (Sq_{Column}), squares per row (Sq_{Row}), total squares (Sq_{Total}), squares in parallel ($Sq_{Parallel}$), number of layers (N_{Layers}), total squares used (Sq_{Used}), last or final layer fill factor ($FF_{LastLayer}$) and spacing between the layers ($Space_{Layers}$). These variables are calculated from the equations (1)-(9). As explained earlier, the design phase starts by defining a square

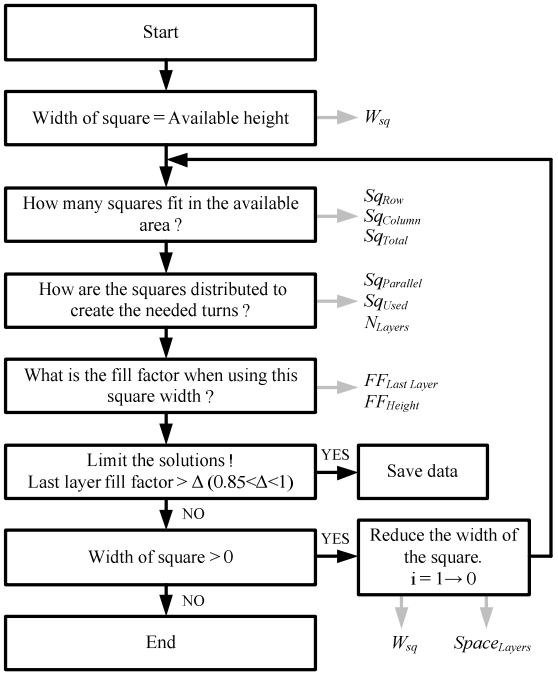

Figure 3. Flowchart of dynamic winding design.

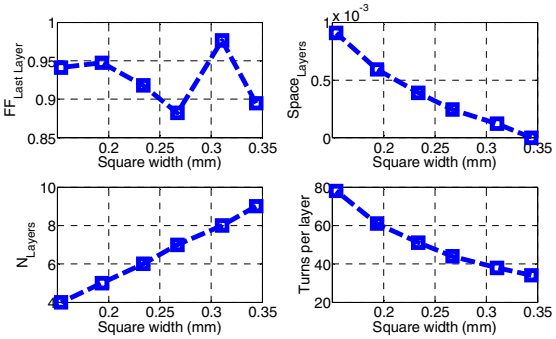

Figure 4. Results of the dynamic winding design for optimized core.

sized based on the allocated height for a given winding. Then important information about how many squares that can fit into the available area is calculated. The actual number of squares used to construct the winding is then determined based on the number of turns needed. The calculated variables are saved if the fill factor of the final layer is above 85 percent. This limit is implemented since the calculations of the transformer parameters are based on fully occupied layers.

$$W_{Sq} = \alpha \cdot W_{H,n} \cdot i \tag{1}$$

where the variable i varies from 1 to 0 in small steps.

$$Sq_{Column} = floor\left(\frac{\alpha W_{H,n}}{W_{Sq}}\right) \tag{2}$$

$$Sq_{Row} = floor\left(\frac{W_w}{W_{Sq}}\right) \tag{3}$$

$$Sq_{Total} = Sq_{Column} \cdot Sq_{Row} \tag{4}$$

$$Sq_{Parallel} = floor\left(\frac{Sq_{Total}}{N}\right) \tag{5}$$

where N is the number of turns of that particular winding for which the dynamic winding design is applied.

$$Sq_{Used} = N \cdot Sq_{Parallel} \tag{6}$$

$$N_{Layers} = ceil\left(\frac{Sq_{Used}}{Sq_{Row}}\right) \tag{7}$$

$$FF_{Last\ Layer} = \left[\frac{N}{Sq_{Row}} - floor\left(\frac{N}{Sq_{Row}}\right)\right] \tag{8}$$

$$Space_{Layers} = \frac{W_{H,n} - N_{layers} W_{sq}}{\left(N_{layers} - 1\right)} \tag{9}$$

In the above equations $ceil(x+\Delta x)=x+1$ and $floor(x+\Delta x)=x$ with $0<\Delta x<1$.

B. *Estimation of transformer parasitics and comprehensive loss model*

The outputs of the dynamic transformer design are used to calculate the transformer parasitics [12] such as DC and AC resistances, leakage inductance and self-capacitance. The loss model has been verified in [12]. In this paper, the winding loss calculations are calculated accurately, since the primary and secondary currents are 180° out of phase.

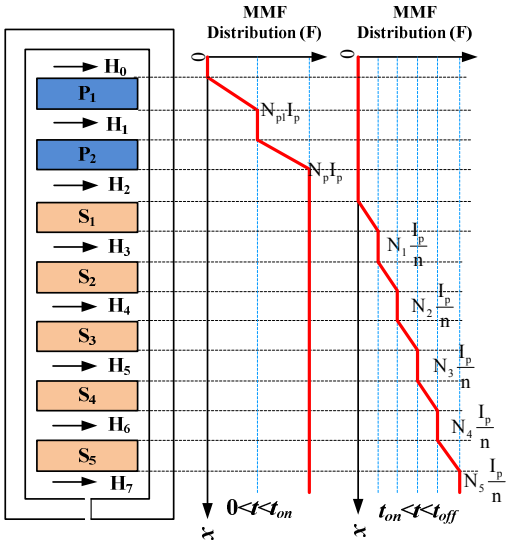

Figure 5. MMF distribution of the non-interleaved (P-P-S-S-S-S-S) structure with respect to space (secondary winding is wounded on the bobbin first).

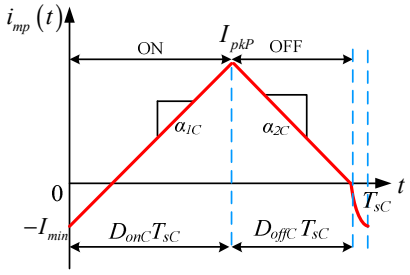

Figure 6. Magnetizing current during the charge process.

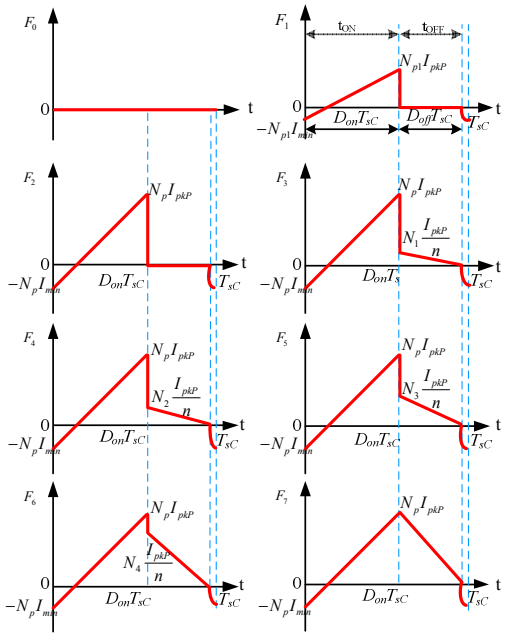

Figure 7. MMF distribution of the non-interleaved (P-P-S-S-S-S-S) structure with respect to time during the charge process.

1) Flyback transformer winding loss during charge process:

The high voltage bi-directional flyback converter proposed in [6], [12], operates in boundary conduction mode (BCM) with variable switching frequency during the charge process and in discontinuous conduction mode (DCM) during the discharge process. The winding loss in a flyback transformer is calculated using the MMF analysis presented in [22]. For the winding loss modeling, a non-interleaved transformer with 2 layers on the primary side and 5 layers on the secondary side is considered as an example. The MMF distribution in a flyback transformer is different from that of a normal transformer [22]. Fig. 5 shows different MMF distributions during both turn-on ($0<t<t_{on}$) and turn-off ($t_{on}<t<t_{off}$) periods in a non-interleaved flyback transformer. The magnetizing current and the time variation of the MMF at the boundary of each layer during the charging process are shown in Figs. 6 and 7, respectively. As the output voltage increases, the magnitude of the minimum negative current $-I_{min}$, in Fig. 6

increases with the switching frequency during the charge process [6], [12].

In Fig. 7, since the negative MMF is presented at the end of each switching cycle for very short time compared to the switching period, it can be neglected in the loss calculation. In Fig. 5, N_{p1} and N_p, are the number turns in the primary layer 1 and the total primary turns. The terms N_1, N_2, N_3, N_4, N_5 are defined as follows: $N_1=N_{s1}$, $N_2=N_{s1}+N_{s2}$, $N_3=N_{s1}+N_{s2}+N_{s3}$, $N_4=N_{s1}+N_{s2}+N_{s3}+N_{s4}$, and $N_5=N_{s1}+N_{s2}+N_{s3}+N_{s4}+N_{s5}=N_s$ where N_{s1}, N_{s2}, N_{s3}, N_{s4}, N_{s5} and N_s are the number of turns in the secondary layers 1, 2, 3, 4, 5, and total secondary turns, respectively.

The magnetizing current and the time variation of the MMFs at the boundary of each layer during the discharging process are shown in Figs. 8 and 9, respectively. Even though the magnetizing current is negative during the discharging process compared to that in the charging process, for the convenience the MMF waveforms are drawn as positive (since the power loss is a function of square of the MMFs, see (10)).

The MMF distribution in each transformer winding layer in the time domain is decomposed into sinusoidal harmonics by Fourier series analysis. The power loss is then computed for each harmonic, and the power loss densities over all harmonics are summed to find the power dissipated in each layer. The corresponding loss model in each layer (P_{layer}) is given by [22], [23]

$$P_{\text{layer}} = \frac{R_{layer}}{2N_l^2}\sum_{i=1}^{\infty}\varepsilon_i\begin{bmatrix}\left(\left|F_i(h)\right|^2+\left|F_i(0)\right|^2\right)G_1(\varepsilon_i)\\ -4\left|F_i(h)\right|\left|F_i(0)\right|\cos(\Delta\theta)G_2(\varepsilon_i)\end{bmatrix} \tag{10}$$

$$\delta_i = \sqrt{\frac{\rho}{\pi\mu_0 i f_{si}}} \tag{11}$$

$$\varepsilon_i = \left(\frac{\pi}{4}\right)^{0.75}\sqrt{\frac{N_l}{w_w}}\left(\frac{d^{1.5}}{\delta_i}\right) \tag{12}$$

$$G_1(\varepsilon_i) = \frac{\sinh(2\varepsilon_i)+\sin(2\varepsilon_i)}{\cosh(2\varepsilon_i)-\cos(2\varepsilon_i)} \tag{13}$$

$$G_2(\varepsilon_i) = \frac{\sinh(\varepsilon_i)\cos(\varepsilon_i)+\cosh(\varepsilon_i)\sin(\varepsilon_i)}{\cosh(2\varepsilon_i)-\cos(2\varepsilon_i)} \tag{14}$$

$F_i(h)$ and $F_i(0)$ are the MMF amplitudes of the i^{th} harmonic at $x=0$ and $x=h$ respectively, assuming h as the thickness of each layer, with the suffix i being the harmonic number. For example for layer 1, $F_i(h)=F_1$ and $F_i(0)=F_0$; for layer 2, $F_i(h)=F_2$ and $F_i(0)=F_1$, and so on. R_{layer} is the resistance of each layer, T_l is the number of turns in each layer, δ_i is the skin depth of the conductor material, ε_i is the ratio of conductor diameter to the effective skin depth, G_1 and G_2, which are functions of ε_i, are given by (13) and (14) [22].

The amplitude and phase of i^{th} harmonic of the MMF during the charge process are given by

$$|F_i| = \sqrt{a_i^2+b_i^2} \tag{15}$$

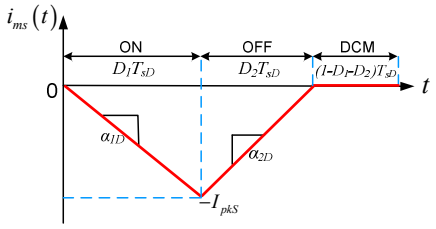

Figure 8. Magnetizing current during the discharge process.

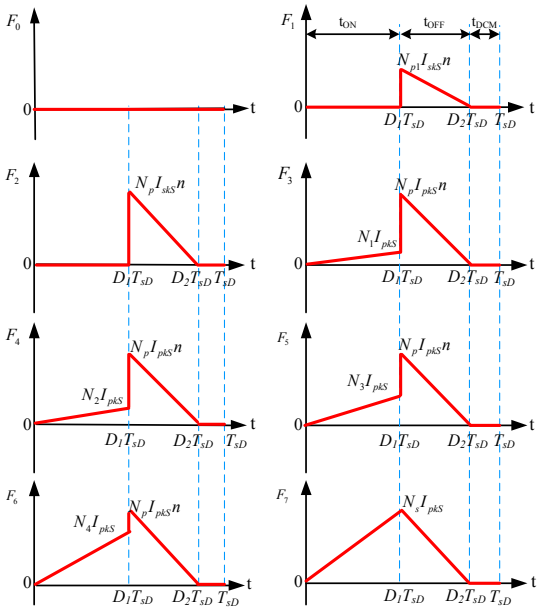

Figure 9. MMF distribution of the non-interleaved (P-P-S-S-S-S-S) structure with respect to time during the discharge process.

$$\theta_i = \begin{cases}\tan^{-1}\left(-\dfrac{b_i}{a_i}\right), & \text{if } a_i \geq 0\\ \pi+\tan^{-1}\left(-\dfrac{b_i}{a_i}\right), & \text{if } a_i < 0\end{cases} \tag{16}$$

$$\Delta\theta = \theta_i(0)-\theta_i(h) \tag{17}$$

The coefficients of the Fourier series of each MMF, during the charging process are given by

$$a_i = \frac{2}{T_{sC}^2 w_i^2}\begin{bmatrix}(\alpha_{1C}-\alpha_{2C})\cos(D_{onC}T_{sC}w_i)+\alpha_{2C}-\alpha_{1C}+\\ w_i(F_{f1}-F_{i2})\sin(D_{onC}T_{sC}w_i)\end{bmatrix} \tag{18}$$

$$b_i = \frac{2}{T_{sC}^2 w_i^2}\begin{bmatrix}(\alpha_{1C}-\alpha_{2C})\sin(D_{onC}T_{sC}w_i)-\alpha_{1C}+\\ w_i(F_{i2}-F_{f1})\cos(D_{onC}T_{sC}w_i)-w_iF_{i1}\end{bmatrix} \tag{19}$$

$$w_{iC} = \frac{2\pi i}{T_{sC}} \tag{20}$$

where w_{iC} the frequency of the i^{th} harmonic, T_{sC} is the switching period, and α_{1C}, α_{2C} are the on-time and off-time slopes of the corresponding MMFs, during the charging process, respectively. F_{i1}, F_{f1}, F_{i2} and F_{f2}, are the initial and final MMFs of the MMF waveform during the turn-on and turn-off processes, respectively.

The expression for the total winding loss in a flyback transformer during the charge process is

$$P_{winding,\,flyback} = I_{DC,P}^2 R_{DC,P} + I_{DC,S}^2 R_{DC,S} + \sum_{k=1}^{n_{ls}+n_{lp}} P_{\text{layer}}(k) \tag{21}$$

where n_{ls}, n_{lp}, $I_{DC,P}$, $I_{DC,S}$, and $R_{DC,P}$, $R_{DC,S}$ are the number of primary, secondary layers, primary, secondary DC current, primary, secondary DC resistances, during the charge process, respectively.

2) Flyback transformer winding loss during discharge process:

The winding loss during the discharge process is calculated similar to that of the charge process, hence equations are avoided.

C. Evaluating simulated results

Table 2 provides a comparison of the smallest core (D_1) and optimized core (D_2) designs. Dynamic winding design discussed in Section 2 has been employed for both designs D_1 and D_2. All losses in the bi-directional flyback converter have been calculated in Matlab. For the winding loss calculation, 30 harmonics are considered.

TABLE II. DESIGN SPECIFICATIONS FOR D_1 AND D_2

Design specifications: V_{in}=24V; V_{out}=2500V; C_{out}=400nF;B_{sat}=0.3T; T_{ch}=50ms	**D_1**	**D_2**
Primary MOSFET	IPB600N25N3 G 250V, 25A, 60 mΩ	IPB600N25N3 G 250V, 25A, 60 mΩ
Core type	E16	PQ 20/20
Core volume	750 mm^3	2850 mm^3
Total turns primary / secondary	29 / 720	12 / 300
Layers primary / secondary	2 / 8	1 / 4
Turns per layer of primary / secondary	15 / 90	12 / 75
Wire diameter Primary/ secondary	0.4 mm / 0.1 mm	(0.5+0.2) mm / 0.143 mm
Primary magnetizing inductance	40 µH	44 µH
Peak primary current charge / discharge	4.24 A / 5.3 A	4.24 A / 5.3 A
Space allocation secondary (α)	0.6	0.8
Spacing between the secondary layers (mm)	60 μm	0.9 mm
Transformer weight	35 grams	120 grams
Transformer maximum temperature rise (°C)	71	30

The minimum turns ratio is calculated using the following equation

$$n_{\min} = \frac{N_p}{N_s} > \frac{\left(V_{out} + V_{HVdiodedrop}\right)}{\beta_1\left[\left(V_{BVpri}\ \beta_2\right) - V_{in}\right]} \tag{22}$$

where V_{in}, $V_{HVdiodedrop}$, N_p, N_s, β_1, and β_2 are the input voltage, high voltage diode drop, number of primary and secondary turns, leakage factor for primary, and margin factor for primary MOSFET drain to source voltage, respectively. The constants, β_1 and β_2 are chosen as 1.75 and 0.8, respectively, which results $n_{\min}$ as 25. In the optimized core, for primary winding TEX-E triple insulated winding has been used. For the smallest core, normal wire with single insulation is used, as the triple isolated wire has an insulation thickness of 0.2 mm, due to which lower diameter wire needs to be used for a

TABLE III. ENERGY LOSS DISTRIBUTION FOR D_1 AND D_2

Different energy losses in the bi-directional flyback converter (mJ)	**Charging E_{losse} (mJ)**		**Discharging E_{lossd} (mJ)**		**Total (mJ)**	
During charging: Output energy E_{out} = 1250 mJ; $\eta_{charge}=E_{out}/(E_{out}+E_{losse})$ During discharging: Input energy E_{in}= 1250 mJ; $\eta_{discharge}=(E_{in}-E_{lossd})/E_{in}$	**D_1**	**D_2**	**D_1**	**D_2**	**D_1**	**D_2**
Energy loss due to transformer paracitics	371.6	105.8	426	96	798	201.8
Winding loss due to resistance	31	12.3	3.75	2.37	34.8	14.67
Loss due to leakage inductance	126	25.7	284	56.4	410	82.1
Capacitive switching loss due to self-capacitance	207.6	57.1	132	37.3	340	94.4
Core loss (Power loss / switching frequency)	7	10.7	5.96	13.9	13	24.6
Converter energy losses	65.4	58.7	168	154		
Primary MOSFET conduction loss	6.1	6.1	--	--		
Secondary MOSFET conduction loss	--	--	6.97	7.4		
Primary MOSFET switching loss	44	38.5	--	--		
Secondary MOSFET switching loss	--	--	129	115	233	212
HV diode conduction loss	2.3	2.5	--	--		
Primary body diode loss	--	--	14.3	16		
Gate drive loss	1	0.9	0.4	0.3		
IC power consumption	9.5	8.2	16.8	15		
Loss due to primary current sense resistor	2.5	2.5	--	--		
Total energy loss	437	164.5	594	250	1031	413.8
Energy efficiency (%)	74	88.43	52.3	80	39	70.8

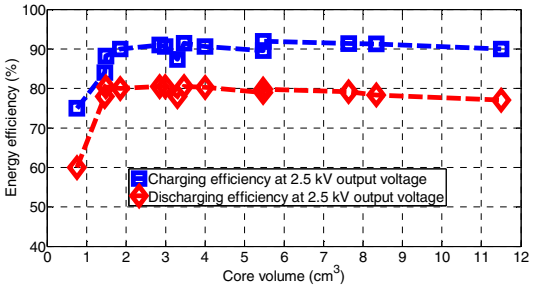

Figure 10. Calculated optimized efficiency at 2.5 kV vs. core volume.

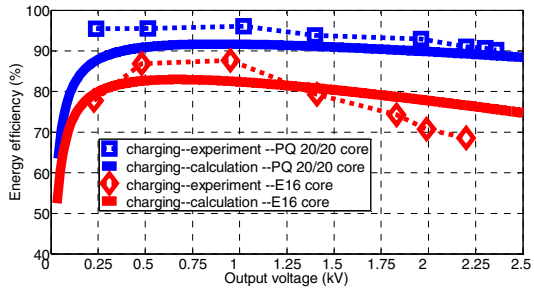

Figure 11. Comparison of calculated and measured charging energy efficiencies for optimized PQ 20/20 and smallest core E16

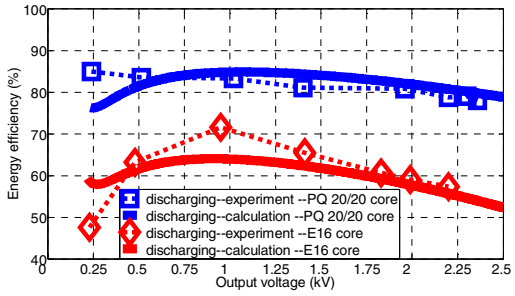

Figure 12. Comparison of calculated and measured discharging energy efficiencies for optimized PQ 20/20 and smallest core E16

given window width. But that results in higher DC resistance for the primary winding and may exceed the transformer temperature limit. Figure 10 shows the charging and discharging energy efficiency variation at 2.5 kV output voltage with respect to different core volumes. The core which has reasonably good energy efficiency with low volume is selected as the optimized core. From Fig. 10, the core which has a volume of 2.85 cm^3 is selected as an optimized core which is PQ 20/20. The smallest core is E 16, and is selected as the core which has low volume and whose temperature doesn't exceed the maximum temperature limit.

III. EXPERIMENTAL RESULTS

The comparison of the measured and calculated charging energy efficiency for the smallest and optimized cores is given in Fig. 11. Figure 12 shows the comparison of the measured and calculated discharging energy efficiency for the smallest

TABLE IV. COMPARISON OF CALCULATED AND MEASURED TRANSFORMER PARAMETERS FOR DESIGNS D_1 AND D_2

Parameter	D_1		D_2	
	Meas.	Calc.	Meas.	Calc.
Leakage inductance referred to primary (secondary shorted)	3.3 μH	3.22 μH	857 nH	804 nH
Leakage inductance referred to secondary (primary shorted)	2.23 mH	2.14 mH	550 μH	502 μH
Self-capacitance of secondary without core (primary opened)	18.61 pF	16.24 pF	3.06 pF	3.3 pF
Self-capacitance of secondary with core (primary opened)	21.62 pF	18.1 pF	6.23 pF	5.5 pF
DC resistance of primary (secondary opened)	182 mΩ	186 mΩ	74 mΩ	58.8 mΩ
DC resistance of secondary (primary opened)	44 Ω	46.54 Ω	18.2 Ω	15.3 Ω
AC resistance referred to primary at 100 kHz (secondary shorted)	370 mΩ	463 mΩ	125 mΩ	108 mΩ
AC resistance referred to secondary at 100 kHz (primary shorted)	190 Ω	358 Ω	73.6 Ω	68 Ω
AC resistance of primary at 100 kHz (secondary opened)	2.45 Ω	--	190 mΩ	--
AC resistance of secondary at 100 kHz (primary opened)	242 Ω	--	85 Ω	--
Primary resonance frequency with core	217 kHz	--	335 kHz	--
Secondary resonance frequency with core	238 kHz	--	360 kHz	--
Secondary resonance frequency without core	776 kHz	--	1.08 MHz	--

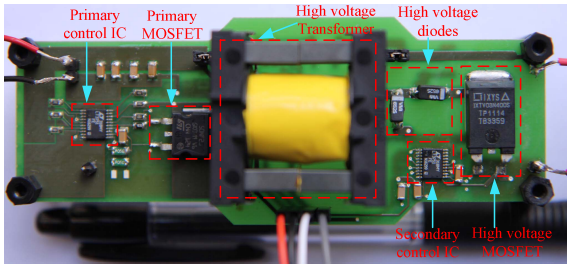

Figure 13. Experimental prototype of the bi-directional flyback converter with ETD 29 transformer

and optimized cores. The experimental prototype of the bi-directional flyback converter is shown in Figure 13. Table 3 shows the loss distribution of the optimized and smallest core designs, from which it is clear that the total losses due to transformer parasitics for design D_1 is higher than that of D_2, and the other losses from the converter remains the same for both designs. Comparison of measured and calculated transformer parameters, and resonant frequencies for both designs are provided in Table 4. The loss distributions of the

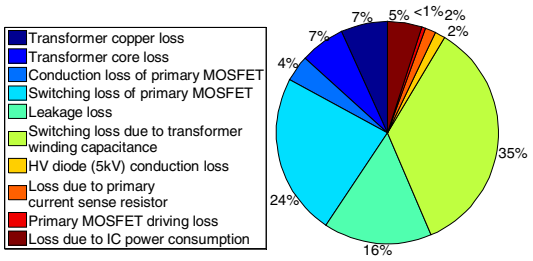

Figure 14. Energy loss distribution during charge process with optimized core.

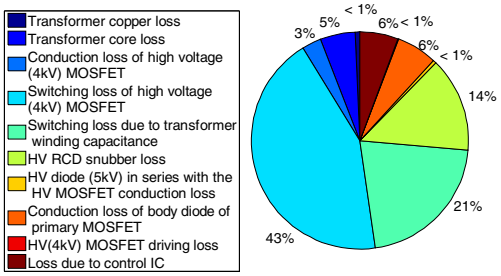

Figure 15. Energy loss distribution during discharge process with optimized core.

optimized design during charge and discharge processes are shown in Figs. 14 and 15, respectively.

IV. CONCLUSIONS

In this paper, a new dynamic transformer winding design concept is introduced. An optimization algorithm for minimizing the total energy loss of a bi-directional flyback converter for a high voltage capacitor charging application is presented. Winding loss calculation for a flyback transformer, with a simple non-interleaved structure is discussed. The proposed optimization technique is experimentally validated on a bi-directional flyback converter, and high efficiency (>90%) is achieved during the charge process. The proposed dynamic winding design can be easily extended to other transformer structures and for other applications.

REFERENCES

[1] R. E. Pelrine, R. D. Kornbluh, Q. Pei, and J. P. Joseph, "High-speed electrically actuated elastomers with strain greater than 100%," in Proc. *Science*, vol. 287, pp. 836–839, 2000.

[2] R. E. Pelrine, R. D. Kornbluh, and J. P. Joseph, "Electrostriction of polymer dielectric with compliant electrodes as a means of actuation," in Proc. *Sensors and Actuators A*, vol. 64, pp. 77–85, 1998.

[3] M. Tryson, H. E. Kiil, M. Benslimane, "Powerful tubular core free dielectric electro active polymer (DEAP) push actuator," in Proc. *SPIE Electroactive Polymer Actuators and Devices (EAPAD)*, vol. 7287, 2009.

[4] R. Sarban, B. Lassen, M. Willatzen, "Dynamic Electromechanical Modeling of Dielectric Elastomer Actuators With Metallic Electrodes," in Proc. *IEEE/ASME Transactions on Mechatronics,* vol. 17, no. 5, pp. 960-967, Oct. 2012.

[5] L. Eitzen, C. Graf, J. Maas, "Cascaded bidirectional flyback converter driving DEAP transducers," in Proc. *IECON*, pp. 1226-1231, 7-10 Nov. 2011.

[6] P. Thummala, Z. Zhang, M. A. E. Andersen, "High Voltage Bi-directional Flyback Converter for Capacitive Actuator," in Proc. *European Power Electronics Conference (EPE),* pp. 3-6th Sept. 2013.

[7] L. Eitzen, T Hoffstadt, J. Maas, "Power electronics concepts for driving EAP actuators," in Proc. *SPIE Electroactive Polymer Actuators and Devices (EAPAD)*, pp. 86870D, 2013.

[8] P. Thummala, Z. Zhang, M. A. E. Andersen, O. C. Thomsen, "A high voltage DC-DC converter driving a Dielectric Electro Active Polymer actuator for wind turbine flaps," in Proc. *IEEE UPEC,* pp. 1-7, 4-7 Sept. 2012.

[9] J. Elmes, C. Jourdan, O. Abdel-Rahman, I. Batarseh, "High-Voltage, High-Power-Density DC-DC Converter for Capacitor Charging Applications," in Proc. *IEEE APEC*, pp. 433-439, 2009.

[10] T. Andersen, M. S. Rødgaard, O. C. Thomsen, M. A. E. Andersen, "Low voltage driven dielectric electro active polymer actuator with integrated piezoelectric transformer based driver," in Proc. *SPIE Electroactive Polymer Actuators and Devices (EAPAD),* vol. 7976, pp. 79762N, 2011.

[11] S. K. Chung, H. B. Shin, "High-voltage power supply for semi-active suspension system with ER-fluid damper," in Proc. *IEEE Transactions on Vehicular Technology*, vol. 53, no. 1, pp. 206- 214, Jan. 2004.

[12] P. Thummala, H. Schneider, Z. Ouyang, Z. Zhang, M. A. E. Andersen, "Estimation of transformer parameters and loss analysis for high voltage capacitor charging application," in Proc. *IEEE ECCE Asia,* pp. 704-710, 3-6 Jun. 2013.

[13] R. Prieto, J.A. Cobos, O. Garcia, R. Asensi and J. Uceda, "Optimizing the winding strategy of the transformer in a flyback converter," in Proc. *IEEE Power Electronics Specialists Conference (PESC)*, vol. 2, pp. 1456-1462, 1996.

[14] C. R. Sullivan, T. Abdallah, T. Fujiwara, "Optimization of a flyback transformer winding considering two-dimentional field effects, cost and loss," in Proc. *IEEE APEC*, vol.1, pp.116-122, 2001.

[15] H. K. Sang, D. Maksimovic, I. Cohen, "Efficiency Optimization in Digitally Controlled Flyback DC–DC Converters Over Wide Ranges of Operating Conditions," in Proc. *IEEE Transactions on Power Electronics*, vol. 27, no. 8, pp. 3734-3748, Aug. 2012.

[16] R. P. Wojda, M. K. Kazimierczuk, "Analytical Optimization of Solid–Round-Wire Windings," in Proc. *IEEE Transactions on Industrial Electronics*, vol. 60, no. 3, pp. 1033-1041, March 2013.

[17] A.C. Nanakos, E.C. Tatakis, N.P Papanikolaou, "A Weighted-Efficiency-Oriented Design Methodology of Flyback Inverter for AC Photovoltaic Modules," in Proc. *IEEE Transactions on Power Electronics*, vol. 27, no. 7, pp. 3221-3233, July 2012.

[18] C. Marxgut, J. Muhlethaler, F. Krism, J.W. Kolar, "Multiobjective Optimization of Ultraflat Magnetic Components With PCB-Integrated Core," in Proc. *IEEE Transactions on Power Electronics*, vol. 28, no. 7, pp. 3591-3602, July 2013.

[19] J. Mühlethaler, "Modeling and Multi-Objective Optimization of Inductive Power Components,", Ph.D. Theis, Dept. Information Technology and Electrical Engineering, ETH Zurich, Switzerland 2012.

[20] Z. Ouyang, "Planar Magnetics for High Grade Converter," Ph.D. Theis, Dept. Electrical Engineering, Technical University of Denmark, Denmark 2011.

[21] N. O. Sokal, R. Redl, "Control algorithms and circuit designs for optimal flyback-charging of an energy storage capacitor (e.g., for flash lamp or defibrillator)," in *Proc. IEEE Transactions on Power Electronics*, vol. 12, no. 5, pp. 885-894, Sep. 1997.

[22] J. Vandelac, P. D. Ziogas, "A Novel Approach for Minimizing High-Frequency Transformer Copper Losses," *IEEE Trans. on Power Electronics,* vol. 3, no. 3, pp. 266-277, Jul 1988.

[23] S. H. Kang, "Efficiency Optimization in Digitally Controlled Flyback DC-DC Converters Over Wide Ranges of Operating Conditions," Ph.D. Theis, Dept. Electrical, Computer and Energy Engineering, University of Colorado Boulder, USA 2011.

[24] P. Thummala, Z. Zhang, M. A. E. Andersen, S. Rahimullah, "Dielectric electro active polymer incremental actuator driven by multiple high-voltage bi-directional DC-DC converters," in Proc. *IEEE ECCE USA,* pp. 3837-3844, 15-19 Sept. 2013.

Appendix Q

Estimation of Transformer Parameters and Loss Analysis for High Voltage Capacitor Charging Application

---

IEEE Energy Conversion Congress and Exposition ASIA 2013 (ECCE)

Estimation of Transformer Parameters and Loss Analysis for High Voltage Capacitor Charging Application

Prasanth Thummala, Henrik Schneider, Ziwei Ouyang, Zhe Zhang, and Michael A. E. Andersen
Electronics Group, Department of Electrical Engineering
Technical University of Denmark
Oersteds Plads, Building 349, Kongens Lyngby, Denmark
Email: pthu@elektro.dtu.dk , Homepage: http://www.dtu.dk/centre/ele/English.aspx

Abstract—**In a bi-directional DC-DC converter for capacitive charging application, the losses associated with the transformer makes it a critical component. In order to calculate the transformer losses, its parameters such as AC resistance, leakage inductance and self capacitance of the high voltage (HV) winding has to be estimated accurately. This paper analyzes the following losses of bi-directional flyback converter namely switching loss, conduction loss, gate drive loss, transformer core loss, and snubber loss, etc. Iterative analysis of transformer parameters viz., AC resistance, leakage inductance and stray capacitance of the HV winding will lead to a considerable reduction in converter losses. In this work, a 24 V to 2.5 *k*V bi-directional flyback converter has been implemented and the same has been used for loss calculation.**

Keywords— *high voltage bi-directional converter, capacitive load, AC resistance, core loss, stray capacitance, leakage inductance*

I. INTRODUCTION

High voltage switch mode power converters are used in a wide variety of capacitive charging applications. Typical applications include pulsed lasers, dielectric electro active polymer (DEAP) actuators, pulsed sonar equipment, photo flash systems, electric fences, and plasma research. Our research focus is to develop high voltage DC-DC power supplies as a driving mechanism for DEAP actuator applications [1]-[4].

The DEAP material requires a high electric field strength of 60 V/μm and the thickness of polymer film is 40 μm therefore, a high voltage is needed for the DEAP actuator (is a pure capacitive load with very low leakage current) to achieve a reasonable actuation stroke. Thus specific component used in this study requires high voltage in the range of kilovolts (~ 2.5 *k*V) at relatively low current. However, with the advanced research and development in high voltage devices like MOSFETS and diodes, it is possible to implement efficient and compact high voltage drivers, to drive and fulfil the requirements of DEAP actuator applications. An incremental DEAP actuator (Fig. 1) which consists of 3 sub-actuators (2 grippers and 1 extender), is the load which needs to be driven by high voltage DC-DC converters.

Danish National Advanced Technology Foundation (*sponsor*).

The common goals of high voltage DC-DC power supplies are reliability, high efficiency, low cost, size and weight. The flyback topology is suitable for low power (< 150 W) and high voltage applications, as it can be made very compact with a low number of components. The magnetic transformer is the most critical component in the HV flyback converter, its leakage inductance causes undesirable voltage spikes, and winding capacitance result in the undesirable current spikes, distortions in the waveforms of the converter, and slow rise times. These non-idealities in the transformer can lead to increased capacitive switching loss, snubber loss, winding loss due to skin and proximity effects, and variable core loss at high and variable frequency of operation, which might lead to reduced converter efficiency and reliability. So, accurate estimation of the transformer parameters, and individual losses in the converter are required to achieve an optimized design for this demanding application.

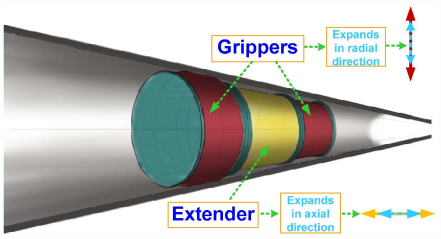

Fig. 1. Incremental DEAP actuator.

The converter efficiency can be improved by optimizing the whole converter design as well as with the proper selection of the control strategy. There is only limited research available in the literature, for an in depth optimization of a flyback transformer for the capacitive load charging and discharging application. In the future an efficiency optimization for this application will be carried out as an extension to the present research work.

This paper is organized as follows. Section II describes the estimation of the HV transformer parameters. Section III summarizes the power loss modelling. Section IV discusses the details of the HV transformer design and the calculations are validated with measured data. Section V shows the experimental and simulation results, followed by the conclusion in Section VI.

II. HV TRANSFORMER PARAMETERS ESTIMATION

A. DC and AC resistances

An increase in the switching frequency of the converter increases the transformer winding losses due to the skin and proximity effects. Since the converter operates under boundary mode during charging and in discontinuous conduction mode (DCM) during discharging, the AC conduction loss cannot be ignored and may dominate the total winding loss. The AC conduction loss is caused by high frequency skin and proximity effects, as well as the fringing effect. Due to its complexity fringing effect is not considered in this paper.

The DC resistance of the primary winding can be calculated by

$$R_{DCP} = \frac{\rho l_{TP}}{A_P},\ A_P = \frac{\pi {d_P}^2}{4} \tag{1}$$

where, ρ is the resistivity of copper at room temperature, N_P is the number of primary turns, l_{TP} is the total length of the primary winding, and d_P is the diameter of the primary winding.

The AC resistance of each harmonic in the current waveform can be calculated as [4], [5],

$$F_{RPn} = \frac{R_{ACP}}{R_{DCP}} = F_{Skin} + F_{Prox} = \varepsilon_P \sqrt{n} \left\{ \frac{sinh\left(2\varepsilon_P\sqrt{n}\right) + sin\left(2\varepsilon_P\sqrt{n}\right)}{cosh\left(2\varepsilon_P\sqrt{n}\right) - cos\left(2\varepsilon_P\sqrt{n}\right)} + \frac{2}{3}\left(m_P^2 - 1\right)\frac{sinh\left(\varepsilon_P\sqrt{n}\right) - sin\left(\varepsilon_P\sqrt{n}\right)}{cosh\left(\varepsilon_P\sqrt{n}\right) + cos\left(\varepsilon_P\sqrt{n}\right)} \right\}$$

$$\varepsilon_P = \left(\frac{\pi}{4}\right)^{\frac{3}{4}} \left(\frac{d_P}{\delta_P}\right) \sqrt{\frac{d_i}{d_o}} \tag{2}$$

where, n is the harmonic number, m_p is the number of layers of the primary winding and ε_P is the primary winding conductor thickness normalized with respect to the conductor skin depth at the switching frequency for a round conductor, δ_P is the skin depth at the fundamental frequency, and d_i / d_o is the porosity factor of the primary winding.

B. Leakage Inductance

In the flyback converter the leakage inductance causes voltage spikes on the drain of low voltage and the high voltage MOSFETs, and may cause significant loss if the flyback transformer is not properly designed.

1) Without interleaving: The leakage inductance for the winding structure shown in Fig. 2a referred to primary is calculated using the energy stored in the magnetic field.

$$E_{Mag} = \frac{1}{2}\int_{Vol} B \cdot H \cdot dv = \frac{1}{2} L_{lk} {I_{pk}}^2 \tag{3}$$

The general expression for the leakage inductance referred to the primary winding for a non-interleaving winding structure having n_{lp} primary layers and n_{ls} secondary layers (with equal turns per layer) is derived in this work and is given by

$$L_{lkp} = \mu_o \frac{l_w}{b_w} {N_p}^2 \left[\frac{n_{lp} h_p + n_{ls} h_s}{3} + \frac{\left(2n_{lp} - 1\right)\left(n_{lp} - 1\right)}{6}\left(\frac{h_{ip}}{n_{lp}}\right) + \frac{\left(2n_{ls} - 1\right)\left(n_{ls} - 1\right)}{6}\left(\frac{h_{is}}{n_{ls}}\right) + h_i \right] \tag{4}$$

where μ_o is the permeability of free air, l_w is the mean length turn (MLT), b_w is the width of the bobbin window excluding the edge isolation tape width, n_{lp} / n_{ls} is the number of primary/secondary layers, and h_{ip} / h_{is} is the insulation thickness between the primary/secondary layers, and h_i is the insulation thickness between the primary and secondary layers, and N_p is the number of primary turns.

The leakage inductance of transformer for the structure shown in Fig. 2 referred to primary is given by [6], [7]

$$L_{lkp} = \mu_o \frac{l_w}{b_w} {N_p}^2 \left[\frac{h_p + 5h_s}{3} + \frac{6}{5} h_{is} + h_i \right] \tag{5}$$

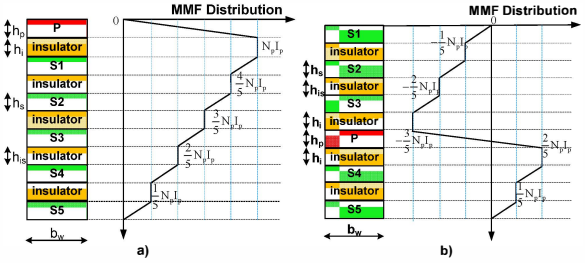

Fig. 2. Analytical MMF distribution for non-interleaving structure P-S-S-S-S-S (left) and interleaving S-S-S-P-S-S (right) structure.

2) With interleaving: Practical experience revealed that interleaving the primary and secondary windings reduces the leakage inductance, self capacitance, and increases the interwinding capacitance. A transformer that is used in the HV application will have a lot of secondary windings, the interleaving structure with the secondary windings sandwiched between the primary winding as shown in Fig. 2b is typical for the high voltage DC-DC converter application.

The general expression for the leakage inductance referred to the primary, for an interleaving winding structure where n_{ls1} and n_{ls2} secondary layers are at the top and bottom of a primary winding respectively, having n_{lp} primary layers (with equal turns per layer of both, and no insulation between the primary layers) is derived in this work and is given by

$$L_{lkp} = \frac{\mu_o l_w {N_p}^2}{b_w} \left[\frac{{n_{ls1}}^3 + {n_{ls2}}^3}{3\left(n_{ls1} + n_{ls2}\right)^3}\left[n_{lp} h_p + \left(n_{ls1} + n_{ls2}\right) h_s \right] + \frac{n_{ls1}\left(n_{ls1} - 1\right)\left(2n_{ls1} - 1\right) + n_{ls2}\left(n_{ls2} - 1\right)\left(2n_{ls2} - 1\right)}{6\left(n_{ls1} + n_{ls2}\right)^2} h_{ls} + \frac{{n_{ls1}}^2 + {n_{ls2}}^2}{\left(n_{ls1} + n_{ls2}\right)^2} h_i \right] \tag{6}$$

The leakage inductance of the HV transformer for a simple interleaving structure shown in Fig. 2b is calculated using (7).

$$L_{lkp} = \frac{\mu_o}{2}\frac{l_w}{b_w} N_p^{\,2}\left[\frac{7h_p + 35h_s}{75} + \frac{6}{25}h_{is} + \frac{13}{25}h_i\right] \tag{7}$$

C. Stray Capacitance

The stray capacitance is another important parameter in the HV transformer because it contributes to capacitive switching loss. The stray capacitance is calculated using the energy stored in the electric field [8]

$$E_{Ele} = \frac{1}{2}\int_{Vol} D \cdot E \cdot dv = \frac{1}{2} C \cdot \Delta V^2 \tag{8}$$

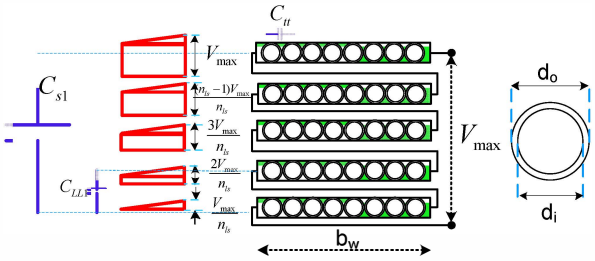

Fig. 3. Voltage distribution in the secondary HV winding with the layers wounded in the same direction

The turn to turn capacitance per unit length of the non-interleaved HV winding with a round conductor is given by

$$C_{tt} = \varepsilon_0\left(\varepsilon_r \theta \cdot \ln^{-1}\left(\frac{d_o}{d_i}\right) + \cot\left(\frac{\theta}{2}\right) - \cot\left(\frac{\pi}{12}\right)\right) \tag{9}$$

where $\theta = \cos^{-1}\left(1 - \frac{1}{\varepsilon_r}\ln\left(\frac{d_o}{d_i}\right)\right)$, ε_0 is the air permitivity, ε_r is the dielectric constant of the insulation of the winding, d_o / d_i is the outer/inner diameter of the HV winding conductor. The layer to layer capacitance is given by

$$C_{LL1} = \frac{T_{Ls}(T_{Ls}+1)(2T_{Ls}+1)}{6T_{Ls}^{\,2}} C_{tt} l_w \tag{10}$$

where T_{Ls} is the turns per layer of the HV winding.

The self capacitance of the HV winding for the winding configuration shown in Fig. 3 is given by

$$C_{S1} = \frac{C_{LL1}}{4}(n_{ls}-1)\left(\frac{2}{n_{ls}}\right)^2 \tag{11}$$

For the HV winding structure shown in Fig. 4, the layer to layer capacitance is given by [9], [10]

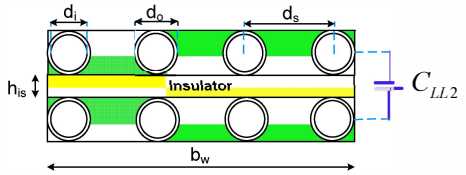

Fig. 4. A random HV winding arrangement.

$$C_{LL2} = \varepsilon_o \varepsilon_r \frac{l_w b_w}{d_{eff}} \tag{12}$$

where $d_{eff} = h_{is} + (d_o - 1.15d_i + 0.26d_s)$ is the effective distance between the two layers, d_s is the spacing between the centers of adjacent turns. The self capacitance of the HV winding for the winding structure shown in Fig. 4, and with the winding connections as shown in Fig. 3 is given by

$$C_{S2} = \frac{C_{LL2}}{4}(n_{ls}-1)\left(\frac{2}{n_{ls}}\right)^2 \tag{13}$$

D. Trade-off between AC resistance, leakage inductance and stray capacitance for HV application

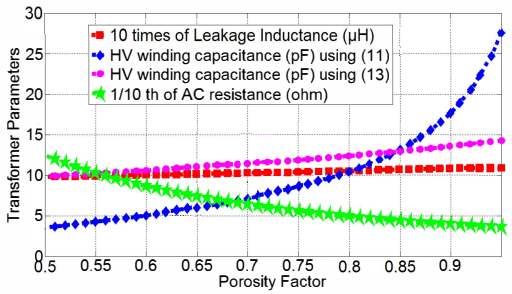

Fig. 5. Trade-off between the primary leakage inductance, secondary stray capacitance and the secondary AC resistance with a change in the porosity factor (d_i/d_o).

Fig. 5 shows the trade-off between the transformer parameters by changing the porosity factor. To show all the parameters in a single plot, the leakage inductance is multiplied by 10 and the AC resistance is divided by 10. The porosity factor (d_i / d_o) is changed from 0.95 to 0.5 and the calculated parameters are shown in Fig. 5. It is observed that the AC resistance increases, and the self capacitance of the HV winding drops as the porosity factor is decreased.

III. Loss Modeling of the Converter

In order to investigate the bi-directional converter efficiency, it is necessary to estimate the losses associated with each one of the circuit components in the converter. The schematic of the bi-directional flyback converter is shown in Fig. 6. The detailed analysis of the same converter is discussed in [13]. Different losses contributed from the transformer of the bi-directional flyback converter are given below.

A. Transformer winding loss

The flyback converter operates in boundary mode with variable switching frequency, while charging the capacitive load [13]. The primary winding power loss is given by [5]

$$P_{wP} = R_{DCP} I_{DCP}^2 + \frac{1}{2} R_{DCP} \sum_{n=1}^{\infty} F_{RPn} I_{Pn}^{\,2} \tag{14}$$

By applying the Fourier series expansion for the primary current waveform shown in Fig. 7 the following equations are obtained:

$$I_{DCP} = \frac{\left(I_{pk} - I_{min}\right)}{2} D_{onC} \tag{15}$$

$$I_{Pn} = \sqrt{a_n^{\,2} + b_n^{\,2}} \tag{16}$$

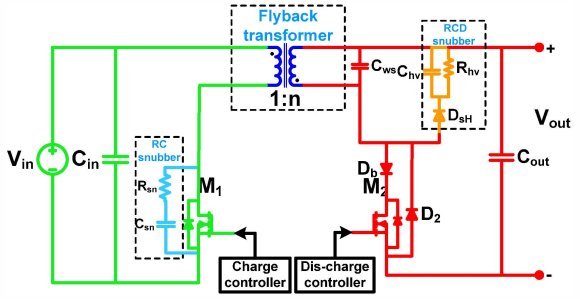

Fig. 6. Bi-directional flyback converter for capacitive load [13].

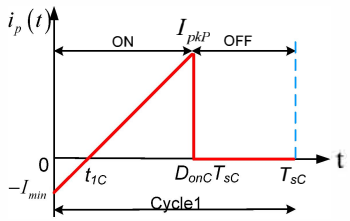

Fig. 7. Primary current waveform while charging the capacitive load.

$$a_n = \left\{ \frac{-I_{min}}{\pi n} sin\left(2\pi n D_{onC}\right) + \frac{I_{pk} + I_{min}}{2\pi^2 n^2 D_{onC}} \times \left[cos\left(2\pi n D_{onC}\right) - 1 + \left(2\pi n D_{onC}\right) sin\left(2\pi n D_{onC}\right) \right] \right\} \tag{17}$$

$$b_n = \left\{ \frac{I_{min}}{\pi n} cos\left(2\pi n D_{onC}\right) + \frac{I_{pk} + I_{min}}{2\pi^2 n^2 D_{onC}} \times \left[sin\left(2\pi n D_{onC}\right) - \left(2\pi n D_{onC}\right) cos\left(2\pi n D_{onC}\right) \right] \right\} \tag{18}$$

where I_{DCP}, I_{pkP}, I_{min}, R_{DCP}, I_{RMSP} and R_{ACP} are the primary winding DC current, peak current, negative current at the beginning of the turn-on process, DC resistance, rms current, and AC resistance (given by (2)) respectively. I_{Pn} is the current amplitude of the n^{th} harmonic. D_{onC} is the on-time duty cycle during charging process. The secondary winding power loss can also be calculated using the above approach.

The negative current at the beginning of the turn-on process (Fig. 7.) is because of the HV winding capacitance. When the secondary winding current becomes zero, the drain to source voltage tends to drop. Since the control IC LT3751 [14] that is used, operates under boundary mode control, the next switching cycle starts before the HV winding capacitance completely discharges. So current flows in the negative direction to discharge the HV winding capacitance at the start.

B. *Transformer core loss*

The core loss calculation during the charging process needs to take care of the variable switching frequency of operation. The most commonly used expression for the time-average core loss calculation per unit volume, for the sinusoidal excitation is the Steinmetz equation given by

$$P_v = k f^{\alpha} \left(\Delta B/2\right)^{\beta} \tag{19}$$

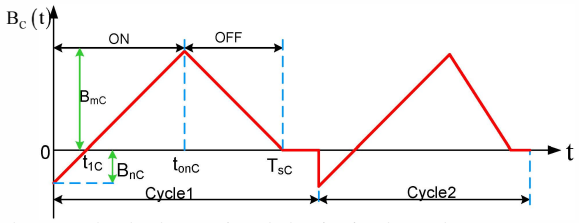

Fig. 8. Flux density waveform during the charging mode.

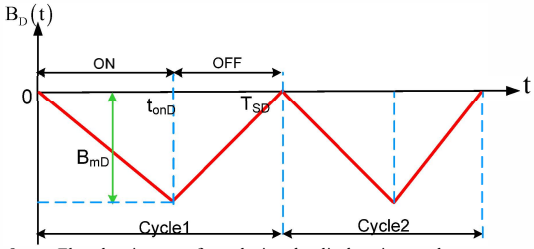

Fig. 9. Flux density waveform during the discharging mode.

The core loss per unit volume due to non-sinusoidal excitation is calculated using the improved generalized Steinmetz equation (IGSE) [10] which is given by

$$P_v = \frac{1}{T}\left[\int_0^T k_i \left|\frac{dB(t)}{dt}\right|^{\alpha} (\Delta B)^{\beta-\alpha}\, dt\right],\ k_i = \frac{k}{(2\pi)^{\alpha-1} \int_0^{2\pi} |cos\,\theta|^{\alpha}\, 2^{\beta-\alpha}\, d\theta} \tag{20}$$

where k, α and β are the constants provided by the manufacturer, ΔB is the peak-to-peak flux density of the current excitation. The angle θ represents the phase angle of the sinusoidal waveform. Figs. 8 and 9 show the flux density waveforms during charging and discharging modes.

The core loss per unit volume during the charge operation in each switching cycle is given by

$$P_{vC} = \frac{k_{iC}}{T_{sC}}\left[\left(B_{mC} + B_{nC}\right)^{\beta_C} \cdot t_{onC}^{\,1-\alpha_C} + B_{mC}^{\,\beta_C} \cdot t_{offC}^{\,1-\alpha_C}\right] \tag{21}$$

Similarly the core loss per unit volume during the discharge operation in each switching cycle is given by

$$P_{vD} = \frac{k_{iD} B_{mD}^{\,\beta_D}}{T_{sD}}\left[t_{onD}^{\,1-\alpha_D} + t_{offD}^{\,1-\alpha_D}\right] \tag{22}$$

with $k_{iC}, \beta_C, \alpha_C, T_{sC}, B_{mC}, t_{onC}, t_{offC}$ / $k_{iD}, \beta_D, \alpha_D, T_{sD}, B_{mD}, t_{onD}, t_{offD}$ as the core loss constants, switching period in each cycle, peak flux density, on-time and off-time in each switching cycle during charging/discharging modes respectively.

C. *Losses in the bi-directional flyback converter excluding the magnetic losses*

Different losses associated with the bi-directional flyback converter are provided in Table I. The loss distribution can be made after calculating all those losses. The results of the loss analysis are shown in Section V.

TABLE I. DIFFERENT LOSSES IN THE BI-DIRECTIONAL FLYBACK CONVERTER DURING CHARGE AND DISCHARGE OPERATIONS

Type of power loss			Power loss expression	Abbreviations *The subscript 'P' / 'S' or 'C' / 'D' in any variable represents that variable is being referred to primary / secondary side or that variable during charging and discharging modes*
Switching loss	Low voltage MOSFET		$P_{swP} = \frac{f_{swC}}{2}\left[(C_{wP}+C_{ossP})V_{dsP}^2 + V_{dsP} I_{pkPC}\left(t_{if}+t_{vr}\right)\right]$	C_{wP}/C_{wS} - self capacitance of the transformer primary/secondary C_{ossP}/C_{ossS} - output capacitance of the primary/secondary MOSFET V_{dsP}/V_{dsS} - primary/secondary MOSFET drain to source voltage $V_{dsP} = V_{in} + V_{out}/n$; $V_{dsS} = V_{out} + nV_{in}$ f_{swC} / f_{swD} - switching frequency during charging/discharging operation n - turns ratio of the transformer from secondary to primary t_{if} / t_{vr} - current fall/voltage rise transition times of the corresponding MOSFETs
	HV MOSFET		$P_{swD} = \frac{f_{swD}}{2}\left[(C_{wS}+C_{ossS})V_{dsP}^2 + V_{dsS} I_{pkSD}\left(t_{if}+t_{vr}\right)\right]$	
Conduction loss	Low voltage MOSFET		$P_{cP} = I_{RMSPC}^2 r_{dsonP}$ $I_{RMSPC}^2 = \frac{I_{pkPC}^2}{3}\left(\frac{D_{onC}T_{sC}-t_1}{T_{sC}}\right) + \frac{I_{min}^2}{3}\left(\frac{t_1}{T_{sC}}\right)$	r_{dsonP}/r_{dsonS} - on-resistance of the primary/secondary MOSFET I_{RMSPC}/I_{RMSSC} - primary/secondary rms current during charging mode I_{RMSPD}/I_{RMSSD} - primary/secondary rms current during discharging mode I_{min} - negative current at the beginning of the turn-on process V_{f_D} - HV diode forward voltage drop I_{DCSC} / I_{RMSSC} - average/rms current through the HV diode D_2 during charging I_{DCSD} / I_{RMSSD} - average/rms current through the HV diode D_b during discharging r_D - HV diode on resistance $V_{f_{M_1}}$ - forward voltage drop of body diode of M_1 I_{DCPD} - average current through primary during discharging D_{onC} / D_{onD} - on-duty cycle during charging/discharging
	Sense resistor on the primary side		$P_{sensePC} = I_{RMSPC}^2 r_{senseP}$ $P_{sensePD} = I_{RMSPD}^2 r_{senseP}$	
	HV MOSFET		$P_{cS} = I_{RMSSD}^2 r_{dsonS}$ $I_{RMSSD}^2 = \frac{I_{pkSD}^2}{3} D_{onD}$	
	HV diode	Diode D_2	$P_{cD_2} = V_{f_D} I_{DCSC} + r_D I_{RMSSC}^2$	
		Diode D_b	$P_{cD_b} = V_{f_D} I_{DCSD} + r_D I_{RMSSD}^2$	
	Body diode of low voltage MOSFET		$P_{cBDM_1} = V_{f_{M_1}} I_{DCPD}$	
Reverse recovery loss of HV diode			$P_{rrC} = Q_{rr}\left(V_{out} + nV_{in}\right) f_{swC}$ $Q_{rr} = \int_t^{t+t_{rr}} -i_s \, dt$	Q_{rr}/t_{rr} - reverse recovery charge/time in the high voltage diode D_2 i_s - secondary current, V_{out}/V_{in} - output/input voltage of flyback converter
Gate driver loss			$P_{Gate} = V_{GS}\left(Q_{GM_2} f_{swD} + Q_{GM_1} f_{swC}\right)$	V_{GS} - gate drive voltage of the MOSFET Q_{GM_2}/Q_{GM_1} - gate charge for high voltage/low voltage MOSFETS
Snubber loss	RC snubber across primary MOSFET		$P_{snLV} = C_{sn} V_{dsP}^2 f_{swC}$	C_{sn} -snubber capacitance in the RC snubber V_{clamp} - clamping voltage of the RCD snubber
	RCD snubber across secondary winding		$P_{snHV} = \frac{1}{2} L_{lkS} I_{pkSD}^2 \frac{V_{clamp}}{V_{clamp} - nV_{in}} f_{swD}$	
Power consumption in the two control IC's			$P_{Controller} = 2V_{cc} I_Q$	V_{cc} - IC supply voltage I_Q - quiescent current of V_{cc}

IV. HV TRANSFORMER DESIGN: COMPARISON OF MEASUREMENTS AND CALCULATIONS

Since the proposed DC-DC converter operates in a wide output voltage range (0-2.5 *k*V), to charge and discharge the DEAP actuator employed in a specific application, different components of the converter have to be designed for different operating points. High voltage capacitor charging application requires proper design of the transformer, otherwise significant amount of energy is lost and efficiency will suffer.

The parameters that significantly affect the efficiency of the converter for capacitor charging application are the peak current, MOSFET type, transformer type and size, magnetizing

inductance, the turns ratio, air-gap length, AC resistance, leakage inductance, and HV winding capacitance.

V. Experimental and Simulation Results

The specifications of the bi-directional flyback converter and the components used in it are provided in Tables II and III respectively. The flyback transformer parameters are shown in Tables V. The experimental prototype is shown in Fig. 11. A boundary mode controller LT3751 has been used for performing both charging and discharging operations. The bi-directional flyback converter charge and discharge cycles are controlled using a microcontroller. Table IV presents the components used in the bi-directional flyback converter. Fig. 10 shows the comparison of the calculated and measured charging and discharging energy efficiencies of the converter. The energy efficiency definitions can be obtained from [13].

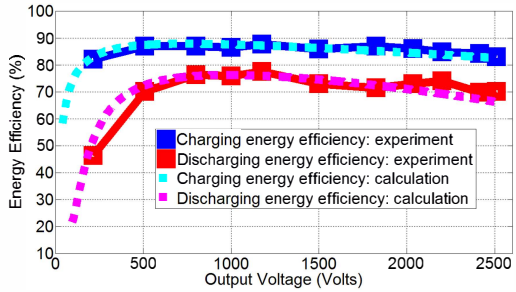

Fig. 10. Comparison of the experimental and the calculated charging and discharging energy efficiencies for a non-interleaved transformer.

TABLE II. Bi-Directional Flyback Converter Specifications

Parameter	Value
Input voltage	24 V
Output voltage	0-2500 V
Stored energy in the load at 2.5 *kV* output voltage	0.625 J
Capacitance of the film capacitive load	200 *nF*
Primary peak current during charging/discharging	4.24 A / 5.3 A

TABLE III. Components Used in the Bi-Directional Flyback Converter

Component	Name
Low voltage MOSFET	STB50NF25 [250 V, 45 A, 55 *mΩ*]
HV MOSFET	IXTV03N400S [4 *kV*, 300 *mA*, 290 Ω]
HV diode	SP5LFG [5 *kV*, 400 *mA*, 50 *ns*(t_{rr})]
Film capacitor load	WIMA [200 *nF* , 3 *kV*]
Analog control IC	LT 3751

TABLE IV. Comparison of HV Transformer Parameters

Parameter	Calculation		Measurement
DC resistance of secondary winding of transformer (Ω)	23		27.5
Leakage inductance of primary winding of transformer (*μH*)	1.09		1.11
Self capacitance of HV winding (*pF*)	**Eq. (11)**	**Eq. (13)**	16.29
	17.65	13.58	

TABLE V. Flyback Transformer Parameters with Non-Interleaving Structure

Parameter	Value
Flyback transformer core type / Material	EF20 / N87
Primary (L_{mP}) / Secondary magnetizing inductance (L_{mS})	28 *μ*H / 15.3 *m*H
Primary turns (N_P) / Secondary turns (N_S)	16 / 375
Leakage inductance of transformer primary (L_{lkP}) / secondary (L_{lkS})	1.11 *μ*H / 633 *μ*H
Secondary winding self (C_s) / Interwinding capacitance (C_{int})	16.29 *p*F / 41 *p*F
DC resistance of primary (R_{dcP}) / secondary winding (R_{dcS})	62 *m*Ω / 28.5 Ω
Primary (n_{lp}) / Secondary layers (n_{ls})	1 / 5
Turns per layer of primary (T_{Lp}) / secondary (T_{Ls})	16 / 75
Each layer primary (h_p) / secondary winding thickness (h_s)	0.5 *mm* / 0.1 *mm*
Insulation thickness between secondary layers (h_{is})	0.1 *mm* (Kapton Tape)
Insulation thickness between the primary layer and the adjacent secondary layer (h_i)	0.3 *mm*
Transformer edge isolation tape width	1.6 *mm* So, $b_w = b_w - 2\times1.6$ *mm*
Dielectric constant of the insulation of the HV winding (ε_r)	3.5

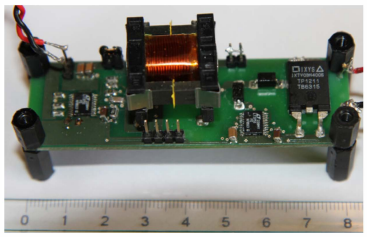

Fig. 11. Picture of the experimental setup.

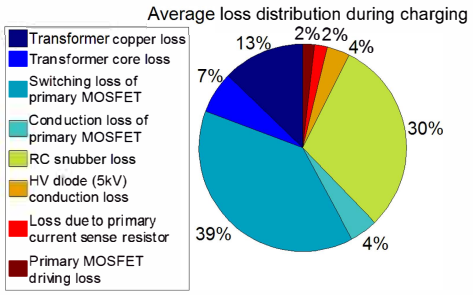

Fig. 12. Average loss distribution during charging of capacitive load.

All loss calculations are done in Matlab. The average loss distributions of the bi-directional flyback converter during charging and discharging modes are shown in Figs. 12 and 13 respectively. Fig. 14 provides the comparison of the average power losses during charging and discharging modes. The peak current of the primary MOSFET has been changed, and

the charging energy efficiency variation has been provided in Fig. 15. In Fig. 16 we show the variation of the energy efficiency with the porosity factor. At high porosity factor the HV winding capacitance is high, so the discharging energy efficiency at 2.5 *k*V is low compared to that at medium porosity factor. However, at low porosity factor, the AC/DC resistance increases, so both charging and discharging energy efficiencies will drop.

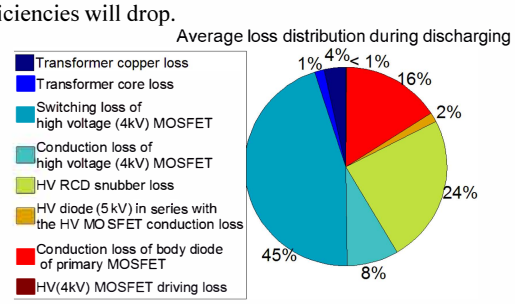

Fig. 13. Average loss distribution during discharging of capacitive load.

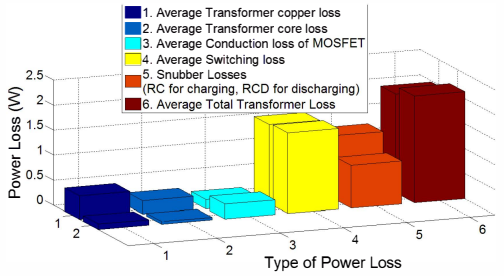

Fig. 14. Comparison of the average loss; On Y-axis, 1 and 2-corresponds to power loss during charging and discharging respectively.

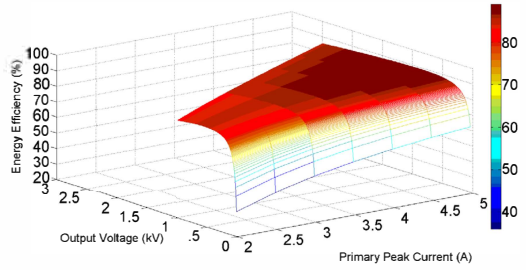

Fig. 15. 3D plot showing how the peak current affects the charging energy.

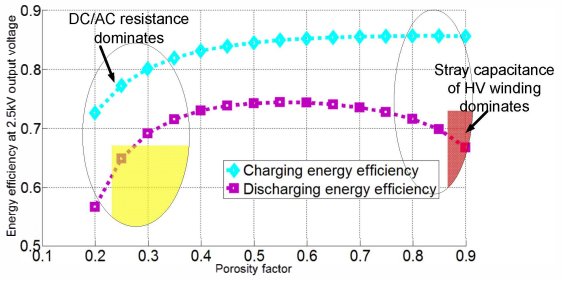

Fig. 16. Variation of energy efficiency at 2.5 *k*V with porosity factor (d_i/d_o)

VI. Conclusion

The power losses in the bi-directional flyback converter for the capacitor charging application has been analyzed in detail. Due to the variable switching frequency and non-sinusoidal waveforms, it is very difficult to accurately compute the core and winding losses. The core loss was accurately calculated during charge and discharge operations, using piecewise linear approximation of the IGSE model.

Estimation of the leakage inductance for a non-interleaved structure and an interleaved winding structure has been discussed. Stray capacitance calculation for a typical HV winding structure is discussed. Trade-off between the different transformer parameters has been made with respect to porosity factor. Comparison of the measurement efficiency and the calculated efficiency shows the accuracy of the proposed loss analysis.

The future work involves the optimization of the whole converter with mostly focusing on transformer optimization.

References

[1] R. Pelrine, P. S. Larsen, R. Kornbluh, R. Heydt, G. Kofod, Q. Pei, P. Gravesen, "Applications of dielectric elastomer actuators," in *Proc. SPIE*, vol. 4329, pp. 335-349, 2001.

[2] M. Tryson, H. E. Kiil, and M. Benslimane, "Powerful tubular core free dielectric electro activate polymer (DEAP) push actuator," in *Proc. SPIE* vol. 7287, p. 72871F, 2009.

[3] P. Thummala, L. Huang, Z. Zhang and M. A. E. Andersen, "Analysis of Dielectric Electro Active Polymer Actuator and its High Voltage Driving Circuits," in *Proc. IPMHVC*, pp. , Jun. 4-7, 2012.

[4] P. Thummala, Z. Zhang, M. A. E. Andersen, O. C. Thomsen, "A high voltage DC-DC converter driving a Dielectric Electro Active Polymer actuator for wind turbine flaps," in *Proc. UPEC* pp.1,7, 4-7 Sept. 2012.

[5] W.G. Hurley, E. Gath, J. G. Breslin, "Optimizing the AC resistance of multilayer transformer windings with arbitrary current waveforms," *IEEE Trans. Power Electronics*, vol.15, no.2, pp.369-376, Mar 2000.

[6] D. Murthy-Bellur, M. K. Kazimierczuk, "Winding losses caused by harmonics in high-frequency flyback transformers for pulse-width modulated dc-dc converters in discontinuous conduction mode," *IET Trans. Power Electronics*, vol.3, no.5, pp.804,817, September 2010.

[7] J. Zhang, Z. Ouyang, M. Duffy, M. A. E Andersen and W. G. Hurley "Leakage inductance calculation for planar transformer with magnetic shunt", in *Proc. ECCE USA* 2013 (accepted).

[8] Z. Ouyang, O. C. Thomsen, M. A. E. Andersen, "The analysis and comparison of leakage inductance in different winding arrangements for planar transformer", *in Proc. IEEE PEDS*, pp. 1143-1148, Nov. 2009.

[9] L. Dalessandro, F. da Silveira Cavalcante, J. W. Kolar, "Self-Capacitance of High-Voltage Transformers," *IEEE Trans. On Power Electronics*, Vol. 22, no.5, pp. 2081-2092, Sept. 2007.

[10] J. Biela, J. W. Kolar, "Using Transformer Parasitics for Resonant Converters—A Review of the Calculation of the Stray Capacitance of Transformers," *IEEE Trans. on Industry Applications*, , vol. 44, no.1, pp. 223-233, 2008.

[11] E. C. Snelling, *Soft Ferrites-Properties and applications*, 2nd ed. London, UK, Butterworth, 1988.

[12] K. Venkatachalam, C. R. Sullivan, T. Abdallah, and H. Tacca, "Accurate prediction of ferrite cores loss with nonsinusoidal waveforms using only Steinmetz parameters," in *Proc. IEEE Workshop Comput. Power Electron.*, pp. 36–41, 2002.

[13] P. Thummala, Z. Zhang and M. A. E. Andersen, "Bi-directional Flyback Converter for Capacitive Actuator", in *Proc. EPE* 2013 (accepted).

[14] LT3751, "High voltage capacitor charger controller with regulation," datasheet.

www.elektro.dtu.dk

Department of Electrical Engineering
Electronics Group (ELE)
Technical University of Denmark
Oersteds Plads bygning 349
DK-2800 Kgs. Lyngby
Denmark
Tel: (+45) 45 25 25 25
Fax: (+45) 45 88 01 17
Email: info@elektro.dtu.dk